NASA CONTRACTOR
REPORT

EXPERIMENTAL AND THEORETICAL INVESTIGATION OF THREE-DIMENSIONAL TURBULENT BOUNDARY LAYERS AND TURBULENCE CHARACTERISTICS INSIDE AN AXIAL FLOW INDUCER PASSAGE

A. K. Anand and B. Lakshminarayana

Prepared by
PENNSYLVANIA STATE UNIVERSITY
University Park, Pa. 16802
for Lewis Research Center

1. Report No. NASA CR-2888	2. Government Accession No.	3. R

4. Title and Subtitle EXPERIMENTAL AND THEORETICAL INVESTIGATION OF THREE- DIMENSIONAL TURBULENT BOUNDARY LAYERS AND TURBULENCE CHARACTERISTICS INSIDE AN AXIAL FLOW INDUCER PASSAGE	5. Report Date August 1977
	6. Performing Organization Code

7. Author(s) A. K. Anand and B. Lakshminarayana	8. Performing Organization Report No. None
	10. Work Unit No.

9. Performing Organization Name and Address Pennsylvania State University 233 Hammond Building University Park, Pennsylvania 16802	11. Contract or Grant No. NGL-39-009-007
	13. Type of Report and Period Covered Contractor Report

12. Sponsoring Agency Name and Address National Aeronautics and Space Administration Washington, D. C. 20546	14. Sponsoring Agency Code

16. Abstract

Analytical and experimental investigations of the characteristics of three-dimensional turbulent boundary layers in a rotating helical passage of an inducer rotor are reported. Expressions are developed for the velocity profiles in the inner layer, where the viscous effects dominate, in the outer layer, where the viscous effects are small, and in the interference layer, where the end walls influence the flow. The prediction of boundary layer growth is based on the momentum integral technique. The equations derived are general enough to be valid for all turbomachinery rotors with arbitrary pressure gradients. The experimental investigations are carried out in a flat plate inducer 3 feet in diameter. The mean velocity profiles, turbulence intensities and shear stresses, wall shear stress, and limiting streamline angles are measured at various radial and chordwise locations by using rotating probes. The measurements are in general agreement with the predictions. The radial flows are well represented by an expression which includes the effect of stagger angle and radial pressure gradient. The radial flows in the rotor channel are higher than those on a single blade. The law of the wall is valid up to $y^+ \sim 200$. The collateral region exists only very near the blade surface. The radial component of turbulence intensity is higher than the streamwise component because of the effect of rotation. Both the turbulence intensity and stresses increase on approach to a blade surface and are minimum in the free stream region except near the hub and annulus wall regions, because of the end wall effects. Flow near the blade tip is highly complex because of the interaction of the blade boundary layers and the annulus wall, which results in an appreciable radial inward flow as well as a defect in the main-stream velocity near the midpassage. A wall shear stress correlation, which includes the effects of both Reynolds number and rotation parameter, valid for the flow in a rotating channel is derived from the measured data.

17. Key Words (Suggested by Author(s)) Three-dimension turbulent boundary layer Rotating turbulent boundary layer Axial flow inducer Turbomachinery	18. Distribution Statement Unclassified – unlimited STAR category 02

19. Security Classif. (of this report) Unclassified	20. Security Classif. (of this page) Unclassified	21. No. of Pages 217	22. Price* A10

TABLE OF CONTENTS

LIST OF TABLES

$a_o, a_1, \ldots a_n$ constant coefficients in the expansion of variable B in Equation (50)

b   universal constant in skin friction coefficient Equation (79)/temperature coefficient of the electrical resistivity of the hotwire

c   chord length

C_E entrainment coefficient

$Co(\omega)$ Cospectrum

C_f skin friction coefficient $(2\tau_o/\rho U_e^2)$

d   diameter of hotwire sensor

e   output a.c. voltage of anemometer

e_c conversion constant between heat and electrical energies

E   output d.c. voltage of anemometer/entrainment function

E_o output d.c. voltage of anemometer at zero flow velocity

f,g   functions representing the crossflow and chordwise velocity profiles in Equation (14)

F   absolute tangential velocity component in the 'interference region'

h   static head

h_o stagnation head measured by pitot hole in the disk probe

H   shape factor (δ_1^*/θ_{11})

$H_{\delta-\delta_1^*}$ head's form of shape parameter $((\delta-\delta_1^*)/\theta_{11})$

J,L,M,N   functions of shape factor (H) relating crossflow to mainstream flow in Equation (77)

k $U_e/\Omega r$

K_1 Karman constant

κ wave number

ℓ length of hotwire sensor

p   static pressure

$p*$ reduced pressure $(p+\rho gh - \frac{1}{2}\rho \ (\vec{\Omega} x \ \vec{r}) \cdot (\vec{\Omega} \ x \ \vec{r})$

P_o stagnation pressure

q   fluctuating component of effective cooling velocity

Q   mean component of effective cooling velocity

r   radial distance

r^+ normalized radial distance $(u_* r/\nu)$

r_c critical radius above which the interference region exists

R   nondimensional radial distance (r/r_t)

R_c nondimensional critical radius (r/r_c)

$R_{\theta_{11}}$ Reynolds number based on boundary layer edge velocity and local momentum thickness θ_{11}

R_o electrical resistance of hotwire at $0^o C$

R_x Reynolds number based on free stream velocity and distance from the leading edge

RG   Normalized radial pressure gradient parameter $(R/U_e)(\partial U_e/\partial R)$

S_1, S_2, S_3, S_4 series defined by Equation (23)

TG   normalized tangential pressure gradient parameter $(r/U_e \ \partial U_e/\partial x)$

u', v', w' fluctuating velocity components in x,y,r directions respectively

u,v,w   velocity components in the reference coordinate system in x,y,r directions respectively (Figure 3)

$\overline{u_i' \ u_j'}$ fluctuating velocity correlations

U_e main flow velocity component at the edge of the boundary layer

U   local total relative flow velocity

u_* friction velocity $(\sqrt{\tau_o/\rho}\ )$

U_{bt}	blade velocity at tip
v_o	flow velocity in y direction at tip radius and midpassage in the interference region
V_θ	absolute tangential velocity component
$\vec{W}$	total relative flow velocity vector
W_θ	relative tangential velocity component
x,y,r	orthogonal curvilinear coordinate system in rotating frame of reference (Figure 3)
r,θ,z	cylindrical polar coordinate system in rotating frame of reference
y^+	nondimensional distance (u_*y/ν)

Greek Symbols

α,β,γ	direction cosine functions (Appendix A)
$\alpha_1,\beta_1,\gamma_1$	universal constants in Equation (79)
α	angle between the relative streamline and cylindrical plane
α_w	limiting streamline angle
β	stagger angle measured from the axial direction
β_2	air exit angle (absolute) measured from axial direction
δ	boundary layer thickness defined as the distance from blade where $\partial u/\partial y \equiv 0$ first occurs
$\delta_1^*,\ \delta_2^*$	boundary layer displacement thickness (Equation 72)
Δ	$\theta_{11}R_x^{1/5}$
ε_w	limiting streamline parameter $(\tan \alpha_w)$
θ	angular variable (Figure 3)/temperature
θ_{11}	main stream momentum thickness (Equation 72)
$\theta_{12},\theta_{21},\theta_{22}$	momentum thickness parameters due to cross flow (Equation 72)

ν	kinematic viscosity
ρ	nondimensional distance from the wall $(\frac{y}{\delta})$
τ	shear stress
τ_x, τ_r	shear stress components inside the boundary layer
Ω	angular velocity of rotation
ω	Cole's wake function, frequency
ψ_s	blade static pressure coefficient $(gh/\frac{1}{2}\rho\ U_{bt}^2)$
ψ_t	stagnation pressure coefficient
π	Cole's parameter for imposed pressure gradients on the boundary layer
Ω^o	$\Omega\nu\ \sin\ \beta/u_*^2$
ϕ	flow coefficient
$\Phi(\omega)$	amplitude of spectrum at frequency ω
$\phi(\kappa)$	amplitude of spectrum in wave number space
χ	nondimensional normal distance in y direction from midpassage

Subscripts

e	value in the flow external to the boundary layer
f	fluid conditions
i,j,k	indices with values 1, 2, and 3
ℓ,m	indices representing the particular wire ℓ,m = 1, 2, or 3 for 3 sensor probe
h	integer representing a particular observation point in a set
s	static conditions
t	tip/transition
w	hotwire conditions

x, y, r   values in the coordinate directions

1, 2, 3   components in x, y, r directions respectively

o   value at the wall/value at zero flow

Superscripts

−   passage averaged values/time averaged values

'   fluctuating quantity unless otherwise stated

I. INTRODUCTION

1.1 Objectives and General Relevance of the Study

Three dimensional turbulent boundary layers are experienced in a
wide variety of flows over both stationary and rotating bodies, such as
the blades of fluid machinery. The crossflows, even though in some cases
small, significantly affect the boundary layer growth and its structure.
In cases where the flow undergoes large turning and has crosswise
pressure gradients (e.g. on the leading or the trailing edge of a stator
blade) or experiences in addition rotation effects (e.g. rotor blades),
the cross flows are large and any two-dimensional simplification of the
flow will be grossly in error.

In addition to producing cross flows, the rotation and curvature of
a body alter the basic turbulence structure of the flow. For example on
the convex surface of a bend, the flow tends to stabilize and even
re-laminarize for large values of curvature. On the other hand, the
flow is destabilized on a concave surface and may even separate for
large values of curvature. Similarly rotation also stabilizes or
destabilizes the flow, depending upon its direction with respect to the
flow.

Lack of knowledge on these three-dimensional turbulent boundary
layers, especially those with rotation and curvature, has hampered the
technological progress in areas such as the fluid machinery (e.g.
compressors, pumps, propellers, turbines, etc.). The rotation induced
coriolis and centrifugal forces generate spanwise flows inside the
blade boundary layer, the magnitude of which depends on the angular
velocity of the blade, the flow coefficient, the rotor blade geometry

and its cascade parameters such as space/chord ratio, aspect ratio, stagger angle, etc. This spanwise migration of the flow results in a decrease of the boundary layer growth near the hub and an increase near the tip, an increase in skin friction and changes in the turbulent characteristics of the flow.

The flow losses due to blade boundary layers form a major portion of the total aerodynamic losses in the turbomachinery stage. It varies directly with free stream velocity, boundary layer thickness, skin friction coefficient, magnitude of cross flow inside the boundary layer and location of flow separation point (if any). All these variables in turn are strongly dependent on the three-dimensionality of the flow. Hence omission of the three-dimensional effects due to rotation and curvature in the prediction of aerodynamic efficiency on the basis of stationary two-dimensional boundary layer theories and cascade data is entirely inadequate.

In addition, near the tip, complex flow interactions take place between the blade boundary layer and the annulus wall. The outward spanwise flow in the blade boundary layer is deflected inward by the annulus wall to the center of the passage. This results in an inward spanwise flow with a marked reduction of mainstream velocity. The shape of velocity profiles in this "interference layer" (so named, because it is formed by the interference between the annulus wall boundary layer and the blade boundary layer flow near the tip) is unconventional and resembles a wake. The radial inward flow component increases and the mainstream flow component decreases with increase in distance from the blade. The direction of turbulent shear stresses is likewise found to reverse in accordance with the mean velocity gradients, and the turbulent

intensity level also increases with distance from the blade. This results in an increase in the mixing losses and the turbulence generated broad band noise in rotating fluid machinery. It also explains some of the discrepancy in the end wall loss correlations between the measurements in a rotor and correlations based on stationary cascade data.

It is thus obvious that flow analysis and measurements in an actual rotating fluid machinery are essential, both in studying the effects of rotation and curvature on three-dimensional turbulent boundary layers with arbitrary pressure gradients, and in incorporating their effects in the design of turbomachinery blading. An extensive and systematic investigation was therefore conducted to study these important and basic differences between stationary and rotating turbulent boundary layers on the blades of an axial flow fluid machinery rotors, and in particular, on the blades of an axial flow rocket pump inducer. An inducer has long and narrow blade passages and therefore represents the worst case of three-dimensional effects. The previous study was performed on a single helical blade of large chord length, rotating in a fluid, otherwise at rest, and enclosed in an annulus. This represents a study of three-dimensional boundary layers with zero pressure gradients and includes the effects of rotation and curvature only. The interference due to adjacent blade boundary layer and the annulus wall in the ducted rotating passages formed by the rotor blades in actual fluid machinery could not be simulated. The present study was conducted inside the straight helical channel formed by the blades of a four bladed flat plate axial flow inducer. Even though the direct effects of cambered blades of actual turbomachinery blading could not be investigated experimentally, the theoretical analysis presented here is valid for

3

axial flow fluid machinery rotors with arbitrary blade geometry and blade loading.

The following objectives were kept in mind in conducting the study:

1. To study the effects of rotation and curvature on three-dimensional turbulent boundary layer characteristics such as mean velocity profiles, skin friction, turbulence structure, boundary layer growth, etc. in a rotating channel with arbitrary pressure gradients.

2. To study the interference effects due to the presence of an annulus wall or adjacent blade on rotating blade boundary layers in an actual fluid machinery.

3. To develop calculation methods (e.g. integral method) to predict the gross three-dimensional boundary layer parameters θ_{11}, ϵ_w and H. These are essential for calculating the boundary layer flow losses and in predicting the overall aerodynamic performance of fluid machinery.

4. To develop probes, probe traversing device, signal processing system and instrumentation for accurate measurement of boundary layer flow characteristics in a rotor frame of reference.

1.2 Statement of the Problem

This is an experimental and analytical study of the effects of rotation and curvature on the three-dimensional turbulent boundary layer flow characteristics in a rotating channel with arbitrary pressure gradients. The following characteristics of the boundary layers are studied throughout the rotating channel except where otherwise stated:

1. Mean velocity profiles

2. Turbulent intensity and shear stress components

4

3. Spectral distribution of all six turbulent correlations of Reynolds stress tensor (at mid-chord and near the blade tip only)

4. Growth of boundary layer momentum thickness

5. Limiting streamline angle or skew angle

6. Shape parameter

7. Skin friction and its correlation with other boundary layer parameters (θ_{11}, ϵ_w and H).

In addition, the interference effects on the boundary layers due to the presence of end walls and boundary layers on the adjacent blades are also studied.

1.3 Previous Related Work

Exact solutions of Navier-Stokes equations for rotating bodies have been obtained only for the simplest cases of three-dimensional rotating laminar boundary layers. Karman (1) obtained the complete solution for laminar flow over a rotating infinite disk immersed in an infinite stationary fluid using similarity analysis for the velocity profiles. Barna (2) and Benton (3) have obtained the laminar solution in rotating pipes by assuming the flow to be a small perturbation of Hagen-Poiseuille flow, and found that the friction factor "f" is increased by rotation given by $f/f_{\Omega=0} = f(Re_h, \sqrt{Ro_d})$, where Ro_d is a rotation parameter $= \Omega d/U_c$ and Re_h is Reynolds number based on hydraulic diameter and centerline velocity U_c, d is the pipe diameter and Ω is the angular velocity of rotation. Experimental results of Treffethen (4) in the range of $2 \times 10^2 < Re_h$, $Ro_d < 3 \times 10^3$ confirmed the above conclusion. The stability analysis of Chawla (5) for laminar rotating boundary layers has shown that the Tollmein-Schlichting waves are not affected by

5

rotation but Taylor-Görtler vortex cells are damped and the transition to turbulence is delayed.

Horlock and Wordsworth (6) and Banks and Gadd (7) investigated the three-dimensional laminar boundary layer characteristics on a turbomachinery blade. Similar investigations on a helicopter blade have been reported by Fogarty (8) and McCroskey and Yaggy (9). Effects of curvature and pressure gradients are neglected and small cross flow assumptions are made. They conclude that the rotation decreases the boundary layer growth compared to the stationary case, primarily due to spanwise migration of the flow.

For turbulent boundary layers on rotating bodies, lack of information on the exact nature of turbulent shear stress terms in the equations of mean motion (known as the closure problem in turbulent flows) has eluded an exact solution even in the simplest case of incompressible flow over a rotating disk. Approximate solutions based on momentum integral technique have been obtained for a few cases but the empiricism involved is based on scarce experimental data in rotating systems. The procedure involves the integration of the differential equations of motion across the boundary layer and thus eliminates the need for the nature of turbulent stresses which vanish both at the wall and outside the boundary layer. The final equations contain momentum thickness parameters, which are related to each other and solved by assuming similarity in velocity profiles and an empirical relation for the skin friction. The following studies of this nature have been made:

Turbulent Boundary Layers on Axisymmetric Bodies. Karman (1) was first to obtain a solution for turbulent boundary layer growth on a rotating disk. He used 1/7th profile for the mainstream velocity, skin friction

coefficient based on stationary flat plate data and a constant value
of ε_w, the limiting streamline parameter. The parameter ε_w is defined
as the tangent of the angle which the local streamline makes with the
inviscid free streamline, as the distance of the former from the blade
surface approaches zero. Cham and Head (10) obtained a numerical
solution of the momentum integral equations for turbulent boundary layer
growth on an axisymmetric disk and concluded that ε_w is nearly invariant
with radius. The atmospheric turbulent boundary layer (11) also falls
in this category. Solutions have been obtained (e.g. Blackadar and
Tennekes (12)) by assuming that the Rossby Number is very large. The
Rossby Number, Ros, is the inverse of rotation number Ro and for
atmospheric boundary layers, its value is indeed very large compared to
one. However, in most of the flows in laboratory and industrial
rotating equipment, the Rossby number is small and the large Rossby
number assumption presents a serious limitation on the practical
application of this theory.

Turbulent Boundary Layers in Centrifugal Impellers. The axis of
rotation in centrifugal impellers is perpendicular to the mainstream
flow direction and hence large Coriolis forces are produced normal to
the plane containing the axis of rotation and the flow. Hill and Moon
(13), Moon (14), Moore (15), Haleen and Johnston (16) have investigated
such flows. Moon's (14) result for rectangular channel rotating about
an axis perpendicular to the flow showed that the boundary layer growth
on the low pressure side is increased substantially and the velocity
profiles are of power law type, while on the high pressure side the
boundary layer is much thinner and the velocity profiles fit the
universal law of the wall. Skin friction measurements showed a decrease

7

on the suction side and substantial increase on the pressure side.
Moore (15) studied the flow on the center line of the rotating ducts of
various aspect ratios (ratio of the two sides of the rectangular section)
ranging from 0.5 to 7.33. His results show an increase in friction
factor of ~20% on the leading side and a similar decrease on the trailing
side. However uncertainty in data is too high to allow generalization to
predict the effects of rotation in such flows. Haleen and Johnston (16)
did a detailed experimental study on the structure of turbulent boundary
layers in a rotating rectangular duct. Using hydrogen bubble technique,
they showed that on the suction side, a tendency toward supression of
turbulence exists and the tendency increases with rotation number and
for very large Reynolds number, the turbulent flow may even re-laminarize.
The rotation number, Ro_δ, is defined here as $Ro_\delta = 2\Omega\delta/U_\infty$ where Ω is the
magnitude of angular velocity of rotation, δ is the boundary thickness
and U_∞ is the free stream velocity. The rotation number is the inverse
of Rossby number ($Ros = U/2\Omega L$). The former is more convenient to use in
turbomachinery applications, while the latter is well known for its
application in the geostrophic flows.

Turbulent Boundary Layers in Axial Flow Machines. To date, very
little work has been done to investigate the characteristics of rotating
turbulent boundary layers on the blades of an axial flow fluid machinery.
In many cases where the blade chord and the stagger angle are small,
the main stream flow direction is almost parallel to the direction of
rotation. The Coriolis force is small and very little secondary flows
are developed due to rotation. However if the blade chord and the
stagger angle are large, the boundary layers are thick. The secondary
flows are large and the effect of Coriolis force cannot be neglected.

8

Banks and Gadd (7) investigated the turbulent boundary layer growth near the leading edge of a single helical blade of large stagger rotating in a stationary fluid. They approximate the blade by a flat sector of a disk with leading and trailing edges. The two momentum integral equations were solved by assuming a series solution, small cross flow and 1/7th profile for the mainstream velocity. Later, Lakshminarayana et al. (17) conducted an extensive experimental and analytical investigation of the three-dimensional turbulent boundary layer growth on a single rotating helical blade of a rocket pump inducer. Using the momentum integral approach, they predicted the boundary layer growth and the limiting stream line angle of the flow over the entire blade. They also obtained the nature of mean velocity profiles in the outer part of the turbulent boundary layer and a skin friction correlation to show the direct effects of rotation. The skin friction stress was found to increase with rotation according to the formula

$$c_f/c_{f_{\Omega=0}} = 1 + c_1 \quad (\varepsilon_w \, x \, /r)$$

where ε_w is the limiting streamline angle and x is the distance from the leading edge.

Effect of Curvature in Boundary Layers. The effect of curvature on boundary layers has been discussed by Bradshaw (18), Stratford et al. (19). Stratford et al. proposed an expression for the change in mixing length, based on classical mixing length arguments, whereas Bradshaw drew an analogy between streamline curvature and buoyancy. A first order effect of curvature, suggested by Bradshaw on the basis of Monin-Oboukhov meteorological formula is

$$\frac{\ell}{\ell_{Ri=0}} = 1 - \beta Ri$$

9

where $\ell = |\tau_0/\rho|^{1/2}/(\partial u/\partial y)$. Ri is the Richardson Number = 2s(1 + s) where s = (u/R/$\partial u/\partial y$) and β is a constant. Bradshaw suggests a value of $\beta = 7$ for the convex surfaces and $\beta = 4$ for the concave surfaces. Bradshaw applied the same analogy to turbulent flows with rotation and concluded that the equivalent Richardson number for the case of rotation can be written by replacing (u/R) with 2Ωy, i.e.

$$Ri = - (2\Omega y)/(\partial u/\partial y)$$

where Ωy is the component of rotation vector $\vec{\Omega}$ normal to the plane of mean rate of strain. Experimental data of Haleen and Johnston (16) for the rotating case agree fairly well with Bradshaw's predictions. The combined effects of rotation and curvature on turbulent quantities can be predicted by using a combination Richardson number.

The experimental data of various authors (14, 15, 16, 17, 20) in the rotor blade passages of centrifugal and axial-flow turbomachinery has clearly shown that rotation and curvature greatly modify the boundary layer growth, turbulence and skin friction characteristics. But a generalized analytical and experimental study to explain these changes in flow behaviour, especially in mean velocity profiles and turbulence quantities which are so important in predicting the aerodynamic and acoustical performance of a turbomachinery rotor, was lacking and prompted this investigation.

1.4 Method and Means of Investigation

As discussed in previous sections, three-dimensional flow analysis and measurements in an actual fluid machinery are essential to study the combined effects of rotation and curvature on the characteristics of three-dimensional turbulent blade boundary layers with arbitrary pressure

gradients. Analytical expressions for mean velocity profiles are
derived in Chapter II for the inner, outer and interference regions of
the boundary layer in generalized orthogonal curvilinear rotating
coordinate system suitable for an axial flow turbomachinery rotor with
arbitrary blade geometry, cascade parameters and blade loading. Boundary
layer growth, limiting streamline angle and shape factor are predicted
throughout the rotor channel using the momentum integral technique and
by solving the resulting three first order partial differential equations
simulatneously (two momentum integral equations and an auxiliary
entrainment equation) by a finite difference scheme.

The experimental work is carried out in a four bladed flat plate
inducer at a Reynolds number of 6.67×10^5 (based on peripheral velocity
and radius at the tip), which assures that the flow is turbulent over
most portions óf the blade channel. Experimental test facility, data
transmission and instrumentation are described in Chapter III. Extensive
three-dimensional flow measurements of the blade static pressure,
limiting streamline angle, mean velocity profiles, turbulence intensities,
turbulent shear stresses, skin friction have been made throughout the
rotor channel. Data reduction procedures and methods of measurements are
reported in Chapter IV.

Measurements were performed both at open throttle and partially
throttled conditions. The former gave mild chordwise pressure gradients
so that the major effects of rotation and curvature could be discerned.
With throttling, large pressure gradients are produced with flow condi-
tions comparable to an actual fully loaded axial flow rocket pump inducer
studied by Lakshminarayana (21). Laminar to turbulent transition and
spectral measurements of all the turbulent quantities at mid chord and

near the tip are reported. Performance characteristics and exit flow measurements have also been conducted and the experimental results of all measurements are reported in Chapter V. They are compared with theoretical predictions of Chapter II. Subsequent chapters include discussion, conclusions and recommendations for future work and methods of incorporating these effects in design of turbomachine blading. Direction cosines and dimensions of sensors, supports, etc. of the special boundary layer triple sensor hotwire probe, response characteristics of two dual channel hotwire anemometers and turbulent scales of the flow ect. are discussed in Appendix A. A systematic analysis of errors in measurements, their elimination and the accuracy of data is given in Appendix B. The equations of Reynolds stresses in reference rotating coordinate system (x, y, r) and the qualitative effects of rotation and curvature are reported in Appendix C.

II. THEORETICAL ANALYSIS

2.1 Qualitative Nature of the Flow

Extensive flow visualization inside the blade passages of an axial flow inducer, reported by Lakshminarayana (22), show that the qualitative nature of the flow in rotating passages is different from their stationary counterpart. Inside the boundary layer of a rotating blade, there is an imbalance between the radial pressure gradient and the centrifugal force. This produces radial outward or inward flow depending on whether the latter force in a fluid machine is larger than the former or vice versa.

In pumps, compressors, etc., (Figure 1) the absolute and relative tangential velocities are in opposite direction. The centrifugal force is therefore larger than the radial pressure gradient inside the blade boundary layer and hence outward radial flows are produced. On some locations of a turbine blade or stator blade, the centrifugal force is smaller than the absolute tangential velocity component and hence radial inward flows are produced. The inducer, which has the absolute and relative tangential velocities in opposite direction represents the first case, consequently, the radial flow in its blade boundary layers is outward. This spanwise migration of the flow, produces thinner boundary layers near the hub and thicker boundary layers near the tip. Since the blade passages of an inducer are long and narrow (chord/ spacing ≃ 3.6), the inducer represents the worst case of the three-dimensional boundary layer. The cross flows are large and limiting streamline layers are thick and merge with each other after midchord at most of the radial locations. Near the tip, due to the interference

13

Interference Region

Radial
Flow

A

Blade
Boundary
Layer
Region

Core
Region

Blade
Boundary
Layer
Region

A

B

B

Ω

90°

Radial Inward
Flow Region

r

Region IV

(b)

Velocity Profile
Along A-A

x

Region IV

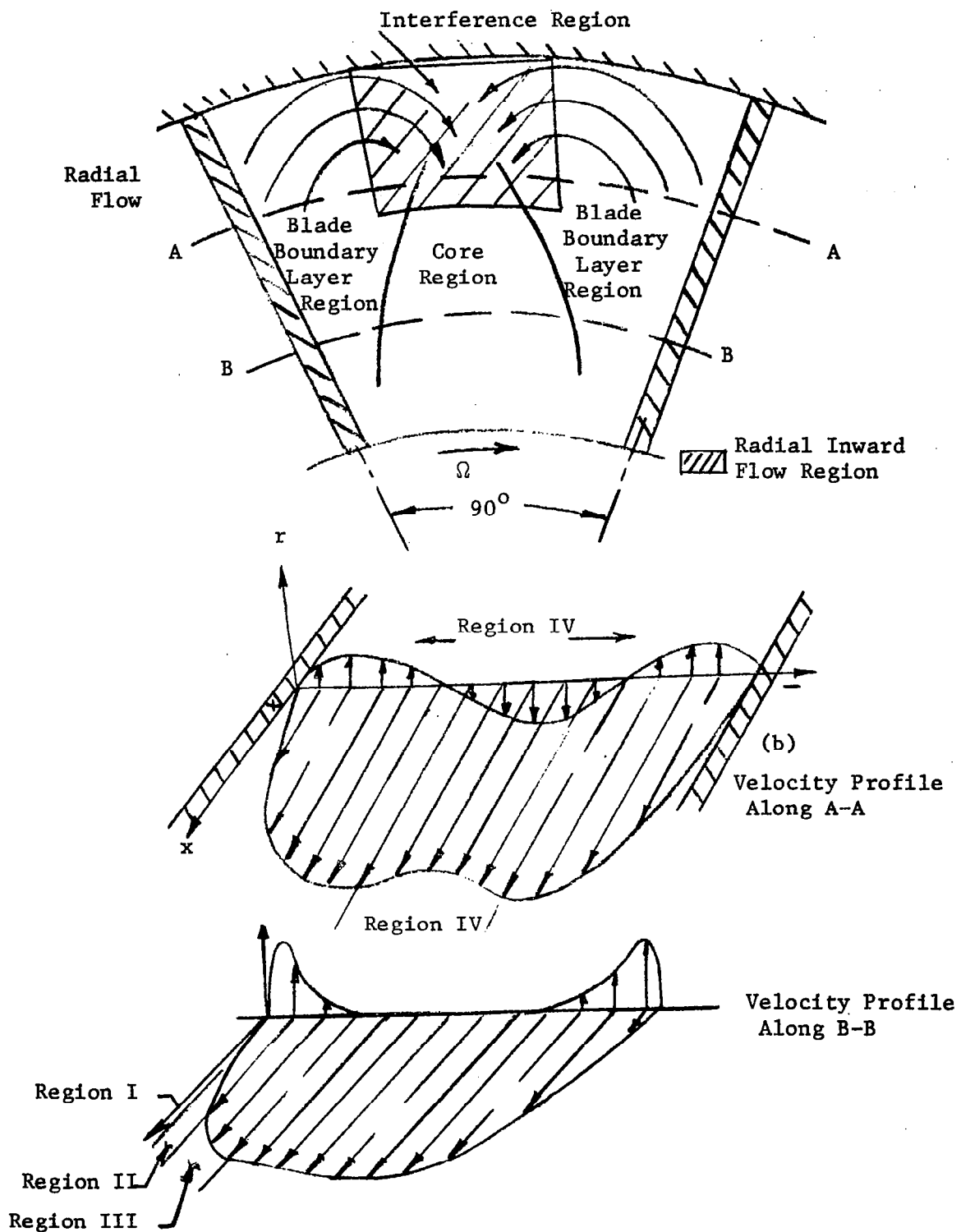Velocity Profile
Along B-B

Region I

Region II

Region III

Figure 2.   Qualitative Nature of Velocity Profiles in a Rotating Channel.

1. The Inner Layer – $y^+ < 10$, where the viscous forces dominate and the inertia forces can be neglected.

2. The Buffer Layer/Inertial Sublayer – $10 < y^+ < 10^3$, where all the forces including inertia, viscous and turbulent forces are important. A knowledge of the nature of turbulent quantities, especially the turbulent stresses is required to predict even the mean velocity profiles of the flow field.

3. Outer Layer – $y^+ > 10^3$, where viscous and turbulent stress gradients may be neglected.

4. Interference Layer – It is formed near the tip in the central region of the channel section due to the interaction of blade boundary layers with the annulus wall. The outward radial flow near the blade surfaces is deflected inward by the annulus wall, to the center of the channel section. The resulting inward radial flow interacts with the mainflow, causing a reduction in streamwise velocity. Thus the shape of the mean velocity profiles is reversed in this region compared to those near the blade surface.

2.2 Flow Model and Governing Equations

The flow of a Newtonian fluid is governed by the Navier-Stokes equations. In the boundary layer on a rotating blade of a turbomachinery, the flow is inherently unsteady when viewed from a stationary coordinate system. It is steady, in the absence of inlet distortions, when viewed from a non-inertial coordinate system rotating at the same angular velocity as the rotor. The rotation introduces two additional acceleration terms viz. Coriolis acceleration ($2\vec{\Omega}\times\vec{W}$) normal to both the

17

relative flow velocity vector $(\vec{W})$ and the rotation vector $(\vec{\Omega})$, and centrifugal acceleration $(\nabla(\frac{1}{2} (\vec{\Omega}x\vec{r}) \cdot (\vec{\Omega}x\vec{r})$.

The Navier-Stokes equation in rotating frame of reference is,

$$\frac{D\vec{W}}{Dt} + 2\vec{\Omega}x\vec{W} = - \nabla p*/\rho - \nu\nabla x(\nabla x\vec{W}) \tag{1}$$

where $p* = p + \rho gh - (\rho/2) (\vec{\Omega}x\vec{r}) \cdot (\vec{\Omega}x\vec{r})$, is known as the reduced pressure and $\vec{W}$ is total relative flow velocity vector, g is the acceleration due to gravity, and h is the height of the fluid element from a reference axis.

The Coriolis and centrifugal forces modify the local force balance between inertia, pressure and viscous forces on a fluid element and are responsible for the observed changes in the mean velocity profiles, boundary layer growth, turbulent structure, skin friction stresses, etc., compared to an equivalent stationary flow system.

The generalized equations given below are based on the following assumptions. These equations are not necessarily restricted to inducer blades and are valid for any axial-flow turbomachine with arbitrary pressure gradients.

(a) The flow is incompressible, homogeneous, single phase and steady in a relative frame.

(b) The blade elements are nearly radial; leading to the choice of curvilinear orthogonal coordinate system (x, y, r) shown in Figure 3. x is along the blade in the direction of the inviscid streamline and y is normal to the blade. Both x and y are curved and orthogonal to each other as well as the radial coordinate r. (i.e. x and y lie in the co-axial cylindrical plane of the machinery). This system is related to cylindrical coordinate system through the equations,
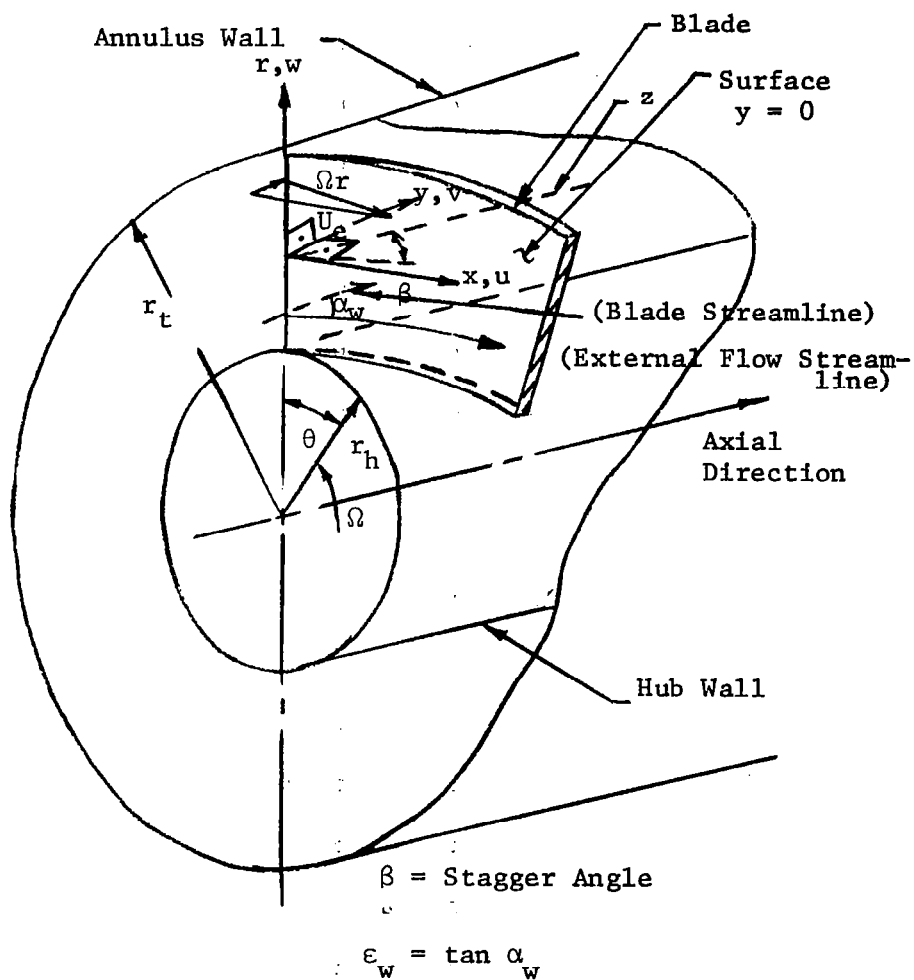
18

Figure 3. Rotating Curvilinear Orthogonal Coordinate System.

β = Stagger Angle

$\varepsilon_w = \tan \alpha_w$

(only one blade is shown for clarity)

$$dx = rd\theta \sin\beta + dz \cos\beta$$
$$dy = -rd\theta \cos\beta + dz \sin\beta$$

(2)

(c) Only the dominant shear stresses are retained and the usual boundary layer approximations are made.

Hence the principal curvatures encountered in this flow system are

$$K_{xr} = \frac{\sin^2\beta}{r} \ , \ K_{yr} = \frac{\cos^2\beta}{r}$$

(3)

$$K_{xy} = \frac{\partial\beta}{\partial x} \quad , \ K_{yx} = \frac{\partial\beta}{\partial y}$$

where, for example, K_{xr} is the principal curvature on the surface r = constant in the direction of the parameter x. β is the streamline angle (x direction) measured from the axial direction (z). With the usual boundary layer approximations, the time averaged equation of mean motion in a rotating (x, y, r) system can be written as (Figure 3),

X momentum: $u \dfrac{\partial u}{\partial x} + v \dfrac{\partial u}{\partial y} + w \dfrac{\partial u}{\partial r} + \sin^2\beta \dfrac{uw}{r} - 2\Omega \ w \ \sin\beta$

(4)

$$+ \frac{\partial\beta}{\partial x} \ uv = - \frac{1}{\rho} \ \frac{\partial p^*}{\partial x} + \frac{1}{\rho} \ \frac{\partial\tau_x}{\partial y}$$

r momentum: $u \dfrac{\partial w}{\partial x} + v \dfrac{\partial w}{\partial y} + w \dfrac{\partial w}{\partial r} - \sin^2\beta \dfrac{u^2}{r} + 2\Omega \ u \ \sin\beta$

(5)

$$- 2\Omega \ v \ \cos\beta = - \frac{1}{\rho} \frac{\partial p^*}{\partial r} + \frac{1}{\rho} \frac{\partial\tau_r}{\partial y}$$

continuity: $\dfrac{\partial u}{\partial x} + \dfrac{\partial v}{\partial y} + \dfrac{\partial w}{\partial r} + \dfrac{w}{r} + \dfrac{\partial\beta}{\partial y} \ u + \dfrac{\partial\beta}{\partial x} \ v = 0$ (6)

where p*, the reduced pressure, neglecting the term due to gravity
($\rho g h$), is

$$p^* = p - \frac{1}{2} \rho \ (\vec{\Omega} x \vec{r}) \cdot (\vec{\Omega} x \vec{r})$$

u, v, w are mean velocities in x, y, and r directions, $\vec{\Omega}$ is the angular
velocity, τ_x and τ_r are total viscous and turbulent shear stresses in
x and r directions respectively. For small cambered blades or the flat
plate inducer used in the experimental program, retaining the principal
curvature term $K_{xr} = \sin^2\beta/r$ equations (4), (5), and (6) are simplified
to:

$$u \frac{\partial u}{\partial x} + v \frac{\partial u}{\partial y} + w \frac{\partial u}{\partial r} -2\Omega w \sin \beta + \sin^2\beta \ \frac{uw}{r} - U_e \frac{\partial U_e}{\partial x} = \frac{1}{\rho} \frac{\partial \tau_x}{\partial y} \qquad (7)$$

$$u \frac{\partial w}{\partial x} + v \frac{\partial w}{\partial y} + w \frac{\partial w}{\partial r} + (U_e^2 - u^2) \ \frac{\sin^2\beta}{r} - 2\Omega(U_e - u) \ \sin\beta =$$

$$\frac{1}{\rho} \frac{\partial \tau_r}{\partial y} \qquad (8)$$

$$\frac{\partial u}{\partial x} + \frac{\partial u}{\partial y} + \frac{\partial w}{\partial r} + \frac{w}{r} = 0 \qquad (9)$$

The pressure gradient term ($\partial p^*/\rho \partial x$) is replaced by its value in
the external stream ($U_e \ \partial U_e/\partial x$). Similarly, the term $\partial p^*/\rho \partial r$ is
replaced by ($U_e^2 \sin^2\beta/r - 2\Omega U_e \sin\beta$). The velocity U_e and its gra-
dient has to be derived from a three dimensional inviscid program
(e.g. Cooper and Bosch (24)).

A complete solution of these highly nonlinear equations has not been
tried due to lack of knowledge of the nature of turbulent stresses in
the rotating three-dimensional turbulent boundary layers. However, a

possible approach using Bradshaw's three-dimensional boundary layer program (25) is outlined in Chapter VI and explained by Anand et al. (20). It is hoped that the present experimental data and that of Gorton (23) on turbulent stresses would provide a basis to check this approach and supply the required information for the complete solution of the equations of motion.

In the following section, a solution for the nature of mean velocity profiles in the inner, outer, and interference layers of a rotating turbulent boundary layer is derived from the equations (7) to (9) using the previous qualitative and quantitative information on such boundary layers. The buffer layer, which requires a complete solution of equations of motion is not tried due to lack of knowledge of the nature of turbulent stresses in this region.

2.3 Velocity Profile Relationship

Since the cross flow velocity component (w) is coupled to the main stream velocity component (u) through the equations of motion, it is anticipated that similarity in velocity profiles should exist if the velocities are normalized by the local velocity scale, and distances by the proper length scale. The two convenient local parameters of the flow are τ_0 (the shear stress at the wall) and U_e (the local mainstream velocity at the edge of the boundary layer). Using the properties of the fluid ρ and μ, a length scale (ν/u_*) is used, where ν is the kinematic viscosity and u_* is the shear velocity defined as $u_* = \sqrt{\tau_0/\rho}$. For the case of inner layer (being closest to the surface), the proper normalizing velocity scale is the shear velocity u_* and for the outer layer (nearest to the inviscid free stream region, Figure 2), it is the

22

local free stream velocity U_e. If similarity exists, the normalized velocity components would be unique functions of normalized distance $y^+ = u_* y / \nu$ from the surface. Analytical relationship between the two velocity components in these regions follows:

2.3.1 Inner Layer (Region I – Figure 2)

In the inner layer (I), close to the wall ($y^+ < 10$) viscous forces dominate and due to the no slip condition at the wall, the inertia terms in the momentum equations (7) and (8) become very small and are therefore neglected. Therefore in this region, the Coriolis force and the pressure gradient balance the shear stress gradient. Equations (7) and (8) are simplified to

$$- 2\Omega w \sin\beta - U_e \frac{\partial U_e}{\partial x} = \frac{1}{\rho} \frac{\partial \tau_x}{\partial y} \qquad (10)$$

$$2\Omega u \sin\beta - \frac{U_e^2}{r} \left(\frac{2\sin\beta}{k} - \sin^2\beta \right) = \frac{1}{\rho} \frac{\partial \tau_r}{\partial y} \qquad (11)$$

where $k = U_e / \Omega r$. If we assume that the stresses are completely laminar, the stresses can be replaced by mean velocity gradients. This is true in the case of a laminar boundary layer and the laminar sublayer ($y^+ \leq 5$) of a turbulent boundary layer. However, contribution due to gradient of turbulent shear stresses is negligible in this region. The logarithmic law of the wall which is experimentally shown to be valid for $y^+ \leq 200$, gives a zero contribution to the shear stress gradients in this region, if the estimate is based on the mixing length hypothesis, given by

$$\tau_{x_t} = \ell^2 \left(\frac{\partial u}{\partial y} \right)^2 \text{ and } \tau_{r_t} = \ell^2 \left(\frac{\partial w}{\partial y} \right)^2 . \qquad (12)$$

with $\qquad \ell = ky$ and $u/u_* = 1/\kappa_1 \ln y^+ + C \qquad (13)$

23

$\partial \tau_{x_t}/\partial y \equiv 0$. Here the subscript t denotes turbulent. Similarly $\partial \tau_{r_t}/\partial y \equiv 0$. The proper velocity and length scales in this region are u_* and ν/u_*. Assuming similarity in velocity profiles, w and u may be written as:

$$w/u_* = f(y^+),\tag{14}$$

$$u/u_* = g(y^+)$$

where $y^+ = u_* y/\nu$ is the Reynolds number based on shear velocity.

Replacing the stresses by corresponding velocity gradients and using Equation (14), Equations (10) and (11) become,

$$-2\,\Omega^o\,f - TG/r' = g''\tag{15}$$

$$2\,\Omega^o\,g - (2\sin\beta/k - \sin^2\beta)/r' = f''\tag{16}$$

where $\Omega^o = \Omega\nu\sin\beta/u_*^2$, $r' = r^+(u_*/U_e)^2$ and $TG = (r/U_e)\partial U_e/\partial x$. At the wall, shear stress gradient must be completely balanced by the pressure gradient. This and the no slip condition results in the following boundary conditions on the blade surface.

1. $f(o) = g(o) = 0$
2. $f'^2(o) + g'^2(o) = 1$
3. $f''(o) = -(2\sin\beta/k - \sin^2\beta)/r'$
4. $g''(o) = -TG/r'$

The solution of f and g is obtained in a series form by writing

$$f = a_o + a_1 y^+ + a_2 y^{+2} + a_3 y^{+3} + \ldots + b_1/y^+ + b_2/y^{+2} + \ldots\tag{17}$$

$$g = \ell_o + \ell_1 y^+ + \ell_2 y^{+2} + \ell_3 y^{+3} + \ldots + m_1/y^+ + m_2/y^{+2} + \ldots\tag{18}$$

The various constants in Equations (17) and (18) are evaluated from the boundary conditions by substituting for f and g. This gives,

$$a_o = b_1 = b_2 = m_1 = m_2 = \ell_o \equiv 0$$

$$f'(o) = a_1 = \epsilon_w / \sqrt{1+\epsilon_w^2}$$

$$g'(o) = \ell_1 = \frac{1}{\sqrt{1+\epsilon_w^2}}$$

$$f''(o) = 2a_2 = - (2\sin /k - \sin^2 \beta)/r'$$

$$g''(o) = 2\ell_2 = -TG/r'$$

(19)

where $\epsilon_w = \tan \alpha_w$, α_w = limiting streamline angle as defined in Figure 3.

By successive differentiation of Equations (15) and (16), it is found that the nth derivative is related to lower derivatives as follows:

$$g^n = (-2\Omega^o) f^{n-2} = -(2\Omega^o)^2 g^{n-4}$$

$$(n > 2) \qquad (n > 4)$$

(20)

and

$$f^n = (+2\Omega^o) g^{n-2} = -(2\Omega^o)^2 f^{n-4}$$

$$(n > 2) \qquad (n > 4)$$

All the coefficients of f and g can be determined by taking the nth derivative at the wall and relating it to known coefficients. Solution of f and g can be expressed as

25

$$f = \frac{w}{u_*} = \frac{\varepsilon_w \, S_1}{\sqrt{2\Omega^o} \, \sqrt{1+\varepsilon_w^2}} - \frac{(2\sin\beta/k - \sin^2\beta)}{2\Omega^o r'} S_2 + \frac{S_3}{\sqrt{2\Omega^o} \, \sqrt{1+\varepsilon_w^2}} - \frac{TG \, S_4}{2\Omega^o r'}$$

(21)

and

$$g = \frac{u}{u_*} = \frac{S_1}{\sqrt{2\Omega^o} \, \sqrt{1+\varepsilon_w^2}} - \frac{TG \, S_2}{2\Omega^o r'} - \frac{\varepsilon_w \, S_3}{\sqrt{2\Omega^o} \, \sqrt{1+\varepsilon_w^2}} + \frac{(2\sin\beta/k - \sin^2\beta)}{2\Omega^o r'} S_4$$

(22)

where S_1, S_2, S_3, and S_4 are convergent series given by

$$S_1 = \sum_{p=1}^{\infty} \frac{\eta^{4p-3}}{(4p-3)!} \, , \quad S_2 = \sum_{p=1}^{\infty} \frac{\eta^{4p-2}}{(4p-2)!} \, , \quad S_3 = \sum_{p=1}^{\infty} \frac{\eta^{4p-1}}{(4p-1)!} \, , \quad S_4 = \sum_{p=1}^{\infty} \frac{\eta^{4p}}{4p!}$$

(23)

and $\eta = \sqrt{2\Omega^o} \, y^+$; $o < \eta \le 1$. η is a dimensionless variable which gives the maximum value of distance from the wall (y^+_{max}) up to which the solution is applicable for a given value of the angular velocity of rotation. For a typical flow in turbomachinery, $\Omega^o \sim 10^{-3}$, $r' \sim 10^2$. The approximate orders of magnitude of the first four terms are 1, $5 \times 10^{-3} \, y^+/\varepsilon_w$, $3 \times 10^{-4} \, y^{+2}/\varepsilon_w$, $8 \times 10^{-7} \, TG \, y^{+3}/\varepsilon_w$ for radial velocity profile and 1, $5 \times 10^{-3} \, TG \, y^+$, $3 \times 10^{-4} \varepsilon_w y^{+2}$, $8 \times 10^{-7} \, y^{+3}$ for streamwise velocity profile respectively.

Very near the wall, it is sufficient to retain only the terms of the order η, η^2, and η^3. Hence the velocity profiles near the wall can be represented by

$$\frac{w}{u_*} = \frac{\varepsilon_w y^+}{\sqrt{1+\varepsilon_w^2}} - \frac{(2\sin\beta/k - \sin^2\beta)}{r'} \frac{y^{+2}}{2} + \frac{\Omega^o}{\sqrt{1+\varepsilon_w^2}} \frac{y^{+3}}{3}$$

(24)

26

$$\frac{u}{u_*} = \frac{y^+}{\sqrt{1+\varepsilon_w^2}} - \frac{TG}{r'} \frac{y^{+2}}{2} - \frac{\varepsilon_w \Omega^o}{\sqrt{1+\varepsilon^2}} \frac{y^{+3}}{3} \qquad (25)$$

Thus, the velocity profiles in the inner layer are functions of β, TG, k, Ω^o and r'.

The results from Equations (24) and (25), for k = 1.0, $\beta = 0°$, $30°$, $45°$, $90°$, $\Omega^o = 10^{-3}$, $r' = 10^{+2}$, TG = 0, $\pm$ 1.0 plotted in Figures 4 and 5 indicate that the flow is collateral, approximately up to $y^+ = 10$ or $u/u_* = 8$. When $\beta = 0$ (i.e. axial blading), both the radial and stream-wise velocity profiles are collateral for zero chordwise pressure gradient (TG = 0.0) and the velocity profiles follow the three-dimensional solution in stationary boundary layers with zero streamwise pressure gradients. For $\beta > 0°$, the flow is not collateral. The departure is large for radial velocity profile and increases with β, reaching a maximum for $\beta = 90°$ (flat sector). Effect of chordwise pressure gradient parameter (TG) is large on the streamwise velocity profile and negligible on the radial velocity profile. The radial pressure gradient parameter (k) has the opposite effect. The departure for the radial velocity profile is large and increases with a decrease in k and is negligible for a streamwise velocity profile.

The effect of rotation parameter Ω^o is to increase the radial velocity and decrease the streamwise velocity, compared to the no rotation case. It also has a large effect on the thickness of the inner layer. For lower values of Ω^o, the inner layer is thicker. The effect of r', which varies directly with Reynolds number is to reduce the departure from collateral behavior. In the limit r' increases to infinity, the flow becomes collateral.
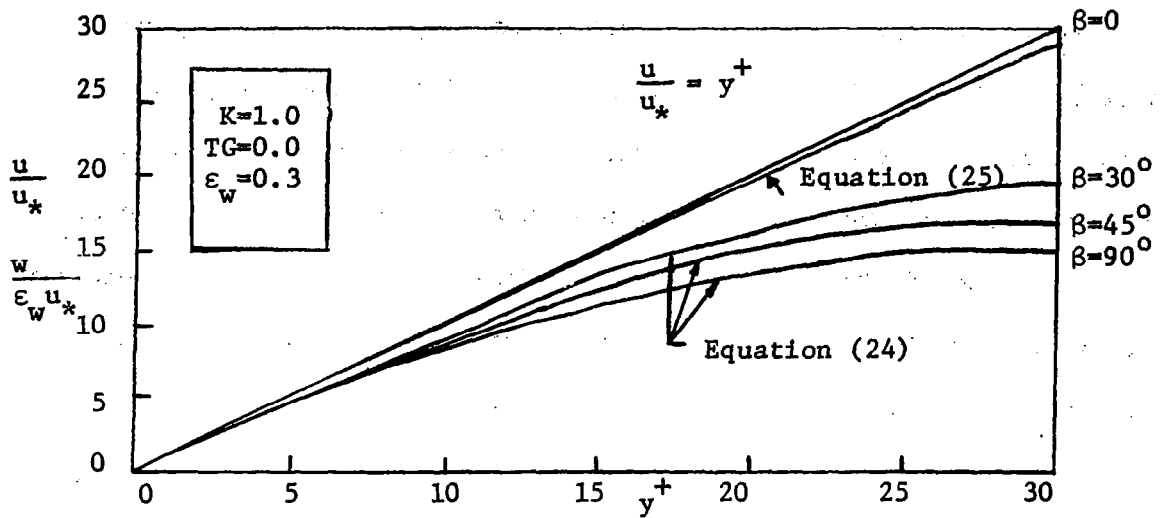
Figure 4. Velocity Profiles in the Laminar Sublayer of the Turbulent Blade Boundary Layer and Laminar Blade Boundary Layer.
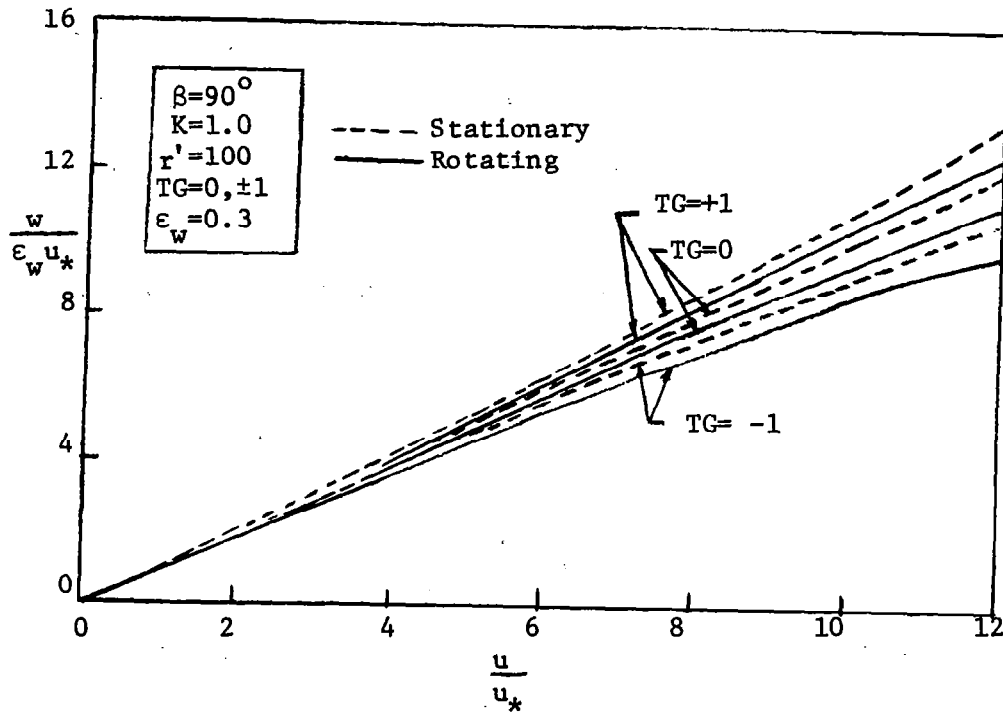

Figure 5. Hodograph Plot of Velocity Profiles in the Laminar Sublayer of the Turbulent Blade Boundary Layer and in Laminar Blade Boundary Layer.

It is thus evident that the collateral region exists only very near the wall for flows with radial or chordwise pressure gradient. This is true for the boundary layer on both rotating and stationary channel. In the absence of these pressure gradients, the collateral regions extend farther from the wall. These conclusions, unfortunately, cannot be verified experimentally since measurements very close to the wall are difficult to make and are inaccurate.

2.3.2 Outer Layer (Region III - Figure 2)

In the outer part of the boundary layer (i.e. for $y^+ > 10^3$), both the turbulent and viscous stresses in Equations (7) and (8) are small. Correlation between the two velocity components is mainly governed by inertia, pressure and Coriolis force terms in the momentum equations. Neglecting the shear stresses, eliminating v from the two equations and writing

$$w/U_e = f(u/U_e) \qquad (26)$$

the resulting equation can be written as (the procedure is similar to the one carried out by Lakshminarayana et al. (17))

$$ff' \left\{ \frac{u}{U_e} (\sin^2\beta + RG) - \frac{2\sin\beta}{k} \right\} - f'\left\{ 1 - (\frac{u}{U_e}) + f \frac{u}{U_e} \right\} TG$$

$$- f^2 RG + \sin^2\beta (1 + \frac{u}{U_e})(\frac{2}{k\sin\beta} - 1 - \frac{u}{U_e}) = 0 \qquad (27)$$

where $RG = \frac{R}{U_e} \frac{\partial U_e}{\partial R}$ is a radial pressure gradient parameter and $R = r/r_t$ is the nondimensional radius. Equation (27) indicates that, in general, f is not only a function of $\frac{u}{U_e}$ but pressure gradient parameters RG and TG also. For $U_e = \Omega r$ (or $k = 1.0$) and $\sin\beta = 1$, the above equation is satisfied, if

$$\frac{w}{U_e} = f = \sqrt{1 - (\frac{u}{U_e})^2} \qquad (28)$$

even in the developing region of the turbulent boundary layer with free stream pressure gradients in x-direction. This expression is identical to that derived by Senoo and Nishi (26) for a three-dimensional turbulent boundary layer in a stationary curved duct.

When TG = 0 (i.e. no chordwise pressure gradient) which is nearly so for a fully developed channel flow (in the absence of interference effect near the outer and inner walls) or for very lightly loaded blading, Equation (27) can be simplified to

$$g' + \frac{g\{2RG/(RG+\sin^2\beta)\}}{\{\frac{2\sin\beta}{k(RG+\sin^2\beta)} - \frac{u}{U_e}\}} = \frac{2\sin^2\beta}{(RG+\sin^2\beta)} \cdot \frac{(1- \frac{u}{U_e})(\frac{2}{k\sin\beta} - 1 - \frac{u}{U_e})}{\{\frac{2\sin\beta}{k(RG+\sin^2\beta)} - \frac{u}{U_e}\}} \qquad (29)$$

Where $g = f^2$. Since k, RG and β are now functions of r only, the above equation can be solved to give

$$g = f^2 = C_1[(\frac{u}{U_e}) - \frac{2\sin\beta}{k(RG+\sin^2\beta)}]^{(2RG/RG+\sin^2\beta)}$$

$$+ (\frac{2}{k} - \sin\beta)\frac{\sin\beta}{RG} - (\frac{u}{U_e})^2 \qquad (30)$$

where C_1 is a constant. The value of constant C_1 is obtained from the fact that solution (30) must be identical to general solution (28) when $\sin\beta = k = 1$ i.e. $C_1 \equiv 0$. Hence the cross flow profile in the outer layer of the fully developed boundary layer in the channel is given by

$$\frac{w}{U_e} = \pm \sqrt{(\frac{2}{k} - \sin\beta)\frac{\sin\beta}{RG} - (\frac{u}{U_e})^2} \qquad (31)$$

Thus the cross-flow in the outer layer is not a simple function of the streamwise velocity, but of pressure gradient parameters k and RG and the blade stagger angle β also. It should be pointed out that k, RG

and β are inter-related by the local velocity triangle for a machine (as shown in Figure 1) and therefore can result in radial outward or inward flow according as the centrifugal force is larger or smaller than radial pressure gradient ($\sim V_\theta^2/r$) respectively.

In cases where the radial flow changes sign in a boundary layer, (e.g. $k > 1$ or when $(2/k - \sin\beta) \sin \beta/RG < (u/U_e)^2$), Equation (30) is not valid, because the turbulent shear stress gradients are not negligible when the cross flow velocity changes its sign inside the boundary layer. This has been confirmed by turbulent shear stress measurements in the interference region reported in Chapter V where the radial flow velocity changes sign (i.e. from outward to inward) and turbulent intensity and stress gradients are not negligible.

Equation (31) indicates that the radial flow in rotating turbulent blade boundary layers increases if the factor $(2/k - \sin\beta) \dfrac{\sin\beta}{RG}$ increases and is zero only in case $k = \sin\beta = 1.0$ i.e. when the centrifugal force is exactly balanced by the radial pressure gradient (V_θ^2/r) at the edge of the boundary layer.

2.3.3 Interference Layer

Near the blade tip the rotation induced outward radial flow inside the blade boundary layer is deflected by the annulus wall, producing an inward radial flow. This region is designated as the "interference region" and is shown in Figure 2. The extent of this region increases downstream of the blade passage, particularly when the flow becomes fully developed, resulting in a large decrease of streamwise velocity component u. The flow in this region is complex due to the interference effects of the annulus wall and adjoining blade boundary layers.

31

The intense mixing resulting from the interaction produces large shear stresses and so viscous and turbulence effects cannot be neglected. Turbulent stress measurements in this region reported in Chapter V show that the stresses are not constant but vary linearly with distance from the blade surfaces. Based on these observations, an asymptotic solution is derived below.

Since the flow is assumed to be fully developed, the velocity components u, v, and w do not vary with x, i.e.

$$u = u\ (r,\ y)$$
$$v = v\ (r,\ y) \tag{32}$$
$$w = w\ (r,\ y)$$

For the case of an inducer, $\beta \simeq 80^{\circ} - 84^{\circ}$ (i.e. $\sin\beta \simeq 1$). The equations of motion (7) to (9) with the usual boundary layer assumptions and for a fully developed flow are simplified to,

$$w\ (\frac{\partial u}{\partial r} + \frac{u}{r} - 2\Omega) + v\ \frac{\partial u}{\partial y} = \frac{1}{\rho}\ \frac{\partial \tau_x}{\partial y} - \frac{1}{\rho}\ \frac{\partial p}{\partial x} \tag{33}$$

$$w\ \frac{\partial w}{\partial r} + v\ \frac{\partial w}{\partial y} - \frac{1}{r}\ (\Omega r - u)^2 = - \frac{1}{\rho}\ \frac{\partial \tau_r}{\partial y} - \frac{1}{\rho}\ \frac{\partial p}{\partial r} \tag{34}$$

$$\frac{\partial w}{\partial r} + \frac{w}{r} + \frac{\partial u}{\partial y} = 0 \tag{35}$$

The left hand side of Equations (33) and (34) are functions of r and y only; therefore, the right hand side must also be independent of x. Using the assumption that turbulent shear stresses are linear with y, and pressure variation with y in the boundary layer can be neglected, Equations (33) and (34) can be simplified by differentiating partially with respect to y and using the continuity Equation (35) to give,

$$w \left\{ \frac{\partial^2 (Fr)}{\partial r \partial y} - \frac{1}{r} \frac{\partial (Fr)}{\partial y} \right\} + \frac{\partial w}{\partial y} \frac{\partial (Fr)}{\partial r} - \frac{\partial w}{\partial r} \frac{\partial (Fr)}{\partial y} + v \frac{\partial^2 (Fr)}{\partial y^2} = 0 \qquad (36)$$

and

$$w \left\{ \frac{\partial^2 w}{\partial r \partial y} - \frac{1}{r} \frac{\partial w}{\partial y} \right\} - \frac{2}{r^3} Fr \frac{\partial (Fr)}{\partial y} + v \frac{\partial^2 w}{\partial y^2} = 0 \qquad (37)$$

where $F = \Omega r - u$.

Equations (35), (36) and (37) can be solved by the method of separation of variables by writing,

$$w = A(r) \ B(y)$$

$$Fr = C(r) \ D(y) \qquad (38)$$

$$v = E(r) \ F(y)$$

The resulting equations are:

$$AB \left\{ C'D' - \frac{1}{r} C D' \right\} + A B'C'D - A'B C D' + E F C D'' = 0 \qquad (39)$$

$$AB \left\{ A'B' - \frac{1}{r} A B' \right\} - 2 \frac{CD}{r^3} C D' + E F A B'' = 0 \qquad (40)$$

$$\frac{F'}{B} = \left(\frac{A' + A/r}{E} \right) = C_4 \qquad (41)$$

Here (') refers to total derivative of a function with respect to its variable. The Interference Flow Regime for the inducer channel is shown in Figure 6. The tip clearance and leakage flows are neglected and the annulus wall is assumed to rotate with the blade. The action of the annulus wall is assumed to deflect the outward radial flow jet near the blades, by $180°$ inviscidly, to the main stream at the center of the section. The jet mixes with the flow and penetrates up to the radius r_c. The boundary conditions are:

$$\frac{\partial w}{\partial y} = \frac{\partial u}{\partial y} = v \equiv 0 \text{ at } y = s$$

$$\qquad (42)$$
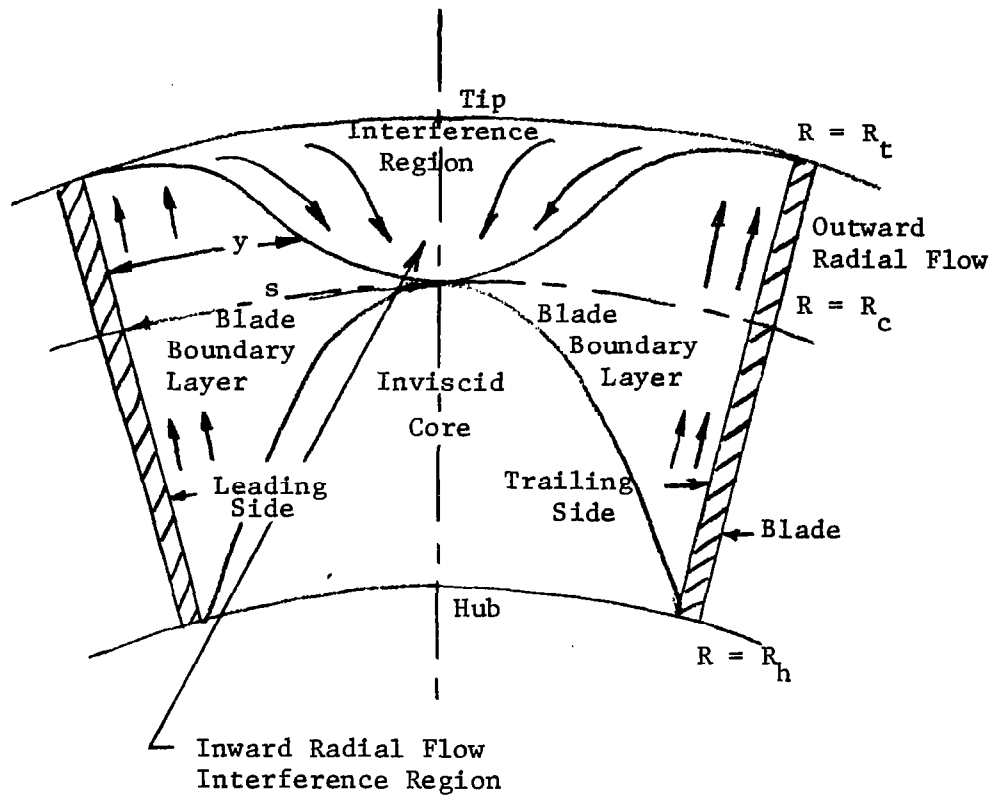
$$w = 0 \qquad \text{ at } r = r_c$$

33

Figure 6. Cross-Section of Inducer Channel Showing "Interference Region".

2s is the channel width as shown in Figure 6. The boundary conditions (42) in terms of new variables (Equation (38)) are:

$$B' = D' = F \equiv 0 \text{ at } y = s$$
$$\text{and} \qquad\qquad\qquad\qquad\qquad\qquad\qquad (43)$$
$$A = 0 \qquad\qquad \text{at } r = r_c$$

Equations (39) and (40) can be separated only if

$$B \ D' = c_5 B' \ D = c_6 \ f \ D'' \qquad\qquad (44)$$

and

$$B \ B' = c_7 D \ D' = c_8 F \ B''$$

where c_5, c_6, c_7, and c_8 are constants.

Equation (44) shows that

$$D = c_9 \ B \qquad\qquad (45)$$

where c_9 is a constant. Also

$$c_5 = 1, \ c_6 = c_8, \ c_7 = 1/c_9^{\,2} \qquad\qquad (46)$$

From Equations (41) and (44), it is clear that,

$$c_8 c_4 \ B \ B'' + B \ B' \ \frac{B'''}{B''} = (B \ B'' + B'^2) \qquad\qquad (47)$$

It is assumed that B can be written as a polynomial series of y as follows:

$$B = b_0 + b_1 \ (y-s) + b_2 \ (y-s)^2 + b_3 \ (y-s)^3 + \ . \ . \ . + b_{-1} \ (y-s)^{-1} + \ .$$
$$(48)$$

where b_0, b_1, b_2, b_{-1} are constant coefficients. Since B is finite at $y = s$, b_{-1}, b_{-2}, . . . b_{-n} terms are all zero. Also B is symmetric about $y = s$, hence

$$b_3 = b_5 = \ . \ . \ . = b_{2n+1} = 0 \qquad\qquad (49)$$

where n is an integer. Using the boundary condition $B'(y=s)=0$,

$$b_1 = 0$$

Therefore B can be reduced to the following simplified form:

$$B = a_o + a_2 \chi^2 + a_4 \chi^4 + \ldots + a_{2n} \chi^{2n} + \ldots \qquad (50)$$

where $\chi = (\frac{Y-s}{s})$. Substituting for B from Equation (50) in Equation (44), following relation between coefficients is obtained:

$$2a_o a_2 + (2a_2^2 + 4a_o a_4) \chi^2 + \ldots + \sum_{m=0}^{n} (2n+2-2m) \, a_{2m} a_{(2n+2-2m)} \chi^{2n}$$

$$= c_4 c_8 [+2a_o a_2 + (\frac{2a_2^2}{3} + 12 a_o a_4) \chi^2 + \ldots \sum_{m=0}^{n} \frac{(2n+2-2m)(2n+1-2m)}{(2m+1)} a_{2m} a_{2n+2-2m} \chi^{2n}$$

$$(51)$$

where $m = 0, 1, 2 \ldots$ etc.

Comparing the coefficients of χ of same index,

$$c_4 c_8 = 1$$

$$2a_2^2 + 4a_o a_4 = \frac{2a_2^2}{3} + 12 \, a_o a_4 \qquad (52)$$

For general case

$$\sum_{m=0}^{n} (2n+2-2m) \, a_{2m} a_{2n+2-2m} = \sum_{m=0}^{n} \frac{(2n+2-2m)(2n+1-2m)}{(2m+1)} a_{2m} a_{2n+2-2m} \qquad (53)$$

This is simplified to give

$$\sum_{m=0}^{n} \frac{(2n+2-2m)(2n-4m)}{(2m+1)} a_{2m} a_{2n+2-2m} = 0 \qquad (54)$$

Using Equation (54) all the coefficients of B can be found,

$$a_4 = \frac{1}{6} (\frac{a_2^2}{a_o}), \quad a_6 = \frac{1}{90} (\frac{a_2^3}{a_2^2}), \quad a_8 = \frac{1}{2520} (\frac{a_2^4}{a_o^3}) , \ldots$$

The solution of B in Equation (50) can be written as

$$B = a_o [1 + (\frac{a_2}{a_o}) \chi^2 + (\frac{a_2}{a_o})^2 \frac{\chi^4}{6} + (\frac{a_2}{a_o})^3 \frac{\chi^6}{90} + \ldots] \qquad (55)$$

Substituting for B in Equation (45), D becomes

$$D = c_9 B = c_9 a_o [1 + (\frac{a_2}{a_o}) \chi^2 + (\frac{a_2}{a_o})^2 \frac{\chi^4}{6} + \ldots] \tag{56}$$

Solution for F is obtained by integrating Equation (41) with respect to χ, using the Equation (55) for B and the boundary condition F = 0 at $\chi = 0$.

$$F = c_4 a_o [\chi + (\frac{a_2}{a_o}) \frac{\chi^3}{3} + (\frac{a_2}{a_o})^2 \frac{\chi^5}{30} + (\frac{a_2}{a_o})^3 \frac{\chi^7}{630} + \ldots] \tag{57}$$

Substituting for E from Equation (41) and using Equation (44), the two Equations (39) and (40) are reduced to

$$AC' - \frac{AC}{r} + AC' - A'C + (A' + A/r) \, C = 0 \tag{58}$$

and

$$AA' - \frac{A^2}{r} - \frac{2}{3} \frac{2}{r} C^2 c_9^2 + (A' + A/r) \, A = 0 \tag{59}$$

Equation (58) gives $2AC' = 0$. Since $A \neq 0$,

$$C = c_{10} \tag{60}$$

where c_{10} is a constant. Equation (59) gives,

$$2AA' - (2/r^3) C^2 c_9^2 = 0 \tag{61}$$

Substituting for C from Equation (60) and integrating A, is obtained as

$$A^2 = - c_{10} c_9^2 / r^2 + c_{11} \tag{62}$$

where c_{11} is an integration constant. Since A = 0 at $r = r_c$, A is given by,

$$A = c_9 c_{10} \sqrt{(\frac{1}{r_c^2}) - (\frac{1}{r^2})} \tag{63}$$

Substituting for A from Equation (63) in Equation (41), E is obtained as follows

$$E = \frac{2 \, c_9 c_{10}}{r_c^2} \{(r/r_c)^2 - 1\}^{-1/2} \tag{64}$$

The solution of u, v, and w is obtained by substituting the expressions for A, B, C, D, E, and F from Equations (63), (55), (60), (56), (64), and (57) respectively as follows:

$$\frac{w}{w_t} = \frac{1}{R} \left\{ \frac{R^2-R_c^2}{1-R_c^2} \right\}^{1/2} \left\{ 1 + \left(\frac{a_2}{a_o}\right) \chi^2 + \left(\frac{a_2}{a_o}\right)^2 \frac{\chi^4}{6} + \left(\frac{a_2}{a_o}\right)^3 \frac{\chi^6}{90} + \dots \right\} \qquad (65)$$

$$\left(\frac{\Omega r - u}{\Omega r_t - u_t}\right) = \frac{1}{R} \left\{ 1 + \left(\frac{a_2}{a_o}\right) \chi^2 + \left(\frac{a_2}{a_o}\right)^2 \frac{\chi^4}{6} + \left(\frac{a_2}{a_o}\right)^3 \frac{\chi^6}{90} + \dots \right\} \qquad (66)$$

$$\frac{v}{v_o} = \left\{ \frac{R^2-R_c^2}{1-R_c^2} \right\}^{-1/2} \left\{ \chi + \left(\frac{a_2}{a_o}\right) \frac{\chi^3}{3} + \left(\frac{a_2}{a_o}\right)^2 \frac{\chi^5}{30} + \left(\frac{a_2}{a_o}\right)^3 \frac{\chi^7}{630} + \dots \right\} \qquad (67)$$

where w_t and u_t are the radial and chordwise velocities at the tip at y = s (i.e. $\chi = 0$). v_o is a constant. The ratio $(a_2/a_o) \equiv (\partial^2 w/\partial \chi^2/2w)$ at $\chi = 0$ is a negative constant because w is negative and has a minima at y = s. Its value is to be determined from the experimental data. From Equations (65), (66), and (67) the following correlations between u, v, and w are obtained;

$$\frac{w}{\Omega r - u} = \left(\frac{w_t}{\Omega r_t - u_t}\right) \left\{ \frac{R^2-R_c^2}{1-R_c^2} \right\}^{1/2} = \varepsilon_{max} \left\{ \frac{R^2-R_c^2}{1-R_c^2} \right\}^{1/2} \qquad (68)$$

and

$$\frac{v}{w} = \frac{v_o R}{w_t} \left\{ \frac{1-R_c^2}{R^2-R_c^2} \right\} \left(\frac{y-s}{s}\right) \left\{ 1 - \frac{2}{3} \left(\frac{a_2}{a_o}\right) \frac{(y-s)^2}{s^2} + \dots \right\} \qquad (69)$$

where ε_{max} is the maximum radial inward flow angle at the tip. The results of Equations (65-69) plotted in Figure 7 show the following properties of the velocity profiles in the interference layer:

$$\frac{(\Omega r - u)}{U_{bt}} \quad \text{(Eqn. 66)}$$

$$\chi = \frac{(y-S)}{S}$$

$$\frac{w}{U_{bt}} \quad \text{(Eqn. 65)}$$
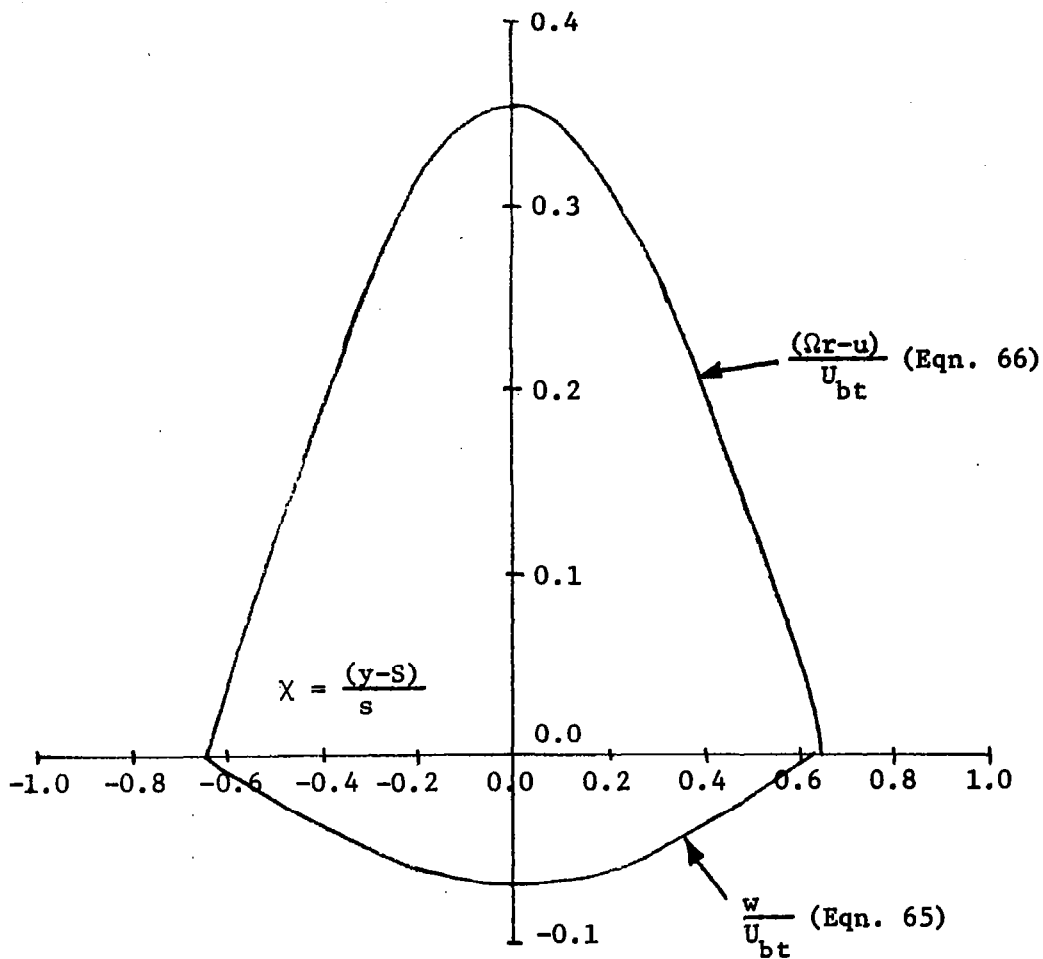
a. Velocity Profiles at R = 0.98, x/c = 0.9, (a_2/a_o = 3.0, R_c = 0.8, Open Throttle Data in Figures 26 and 32).

$$(\Omega r - u)/U_{bt}$$

R=0.80

R=0.86

R=0.93

R=0.98

$$\frac{w}{U_{bt}}$$
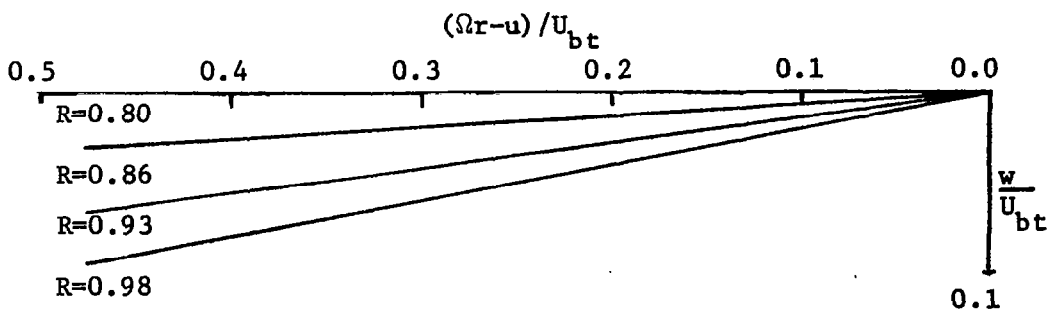
b. Hodograph Plot of Radial Velocity Versus Streamwise Velocity Defect.

Figure 7. Velocity Profiles in the Interference Region.

1. The radial inward flow is maximum near the tip and decrease to zero at a radius r_c. Its profile is an even polynomial in terms of distance (y-s) from the center of the channel and is approximately parabolic. The ratio (a_2/a_o) is given by $(\partial^2 w/\partial \chi^2/w)$ at $\chi = 0$ (i.e. y = s) and is directly related to ratio of shear stress gradient to the magnitude of velocity in the radial direction at the center of the channel.

2. The velocity defect in streamwise velocity varies directly with radial velocity at any radius.

3. The velocity normal to the blade v is zero at mid channel, increases with distance away from centerline and is directly proportional to the product of radial velocity and distance from the center of the channel.

2.4 Momentum Integral Analysis

In the field of turbomachinery, it is important to know the gross boundary layer growth characteristics in a rotating passage. In particular, for a turbomachinery designer it gives an estimate of aerodynamic losses, regions of separation (if any) and the severity of the three dimensionality of the flow. The earlier analysis in section 2.3 is aimed towards an understanding of the structure of the boundary layer. This has both scientific and engineering relevance, whereas the immediate need of a turbomachinery engineer is to know the boundary layer growth parameters viz. the momentum thickness, the limiting streamline angle and the shape factor, which are necessary in predicting the overall aerodynamic performance of a turbomachine. The following momentum integral analysis enables the calculation of turbulent boundary

layer growth in a rotating blade passage. The chief virtue of an integral method for turbulent boundary layers lies in the implicit and global manner in which the effects of turbulence are incorporated.

The method is an extension of Lakshminarayana et al.'s (17) method for predicting the boundary layer growth on a single rotating helical blade. It includes the effect of the pressure gradients imposed by the inviscid external flow. The two momentum integral equations (one in the mainstream and the other in radial flow direction) are reduced to two first order partial differential equations using a power law profile for the mainstream velocity, Mager's profile for the cross-flow and a skin friction relation based on the experimental data of Anand and Lakshminarayana (27). The skin friction coefficient is a modification of Ludwig and Tillmann's (28) skin friction correlation for two-dimensional flows to three-dimensional turbulent boundary layers with pressure gradients, including the effect of rotation. The exponent of the power law for the streamwise velocity component is a function of the local shape parameter (H), which is defined as the ratio of streamwise displacement thickness to streamwise momentum thickness. It thus represents the shape of the streamwise velocity profile.

In turbomachinery blade passages, the flow experiences large pressure gradients. These pressure gradients cause large changes in velocity profiles and consequently in the shape parameter H. The variation of H cannot be neglected and an additional equation is required.

Out of the available auxiliary equations described by Kline et al. (29), only the "energy integral equation" and the "entrainment equation" have been found suitable for the turbulent boundary layers. The former involves more empiricism in calculating the dissipation integral term,

41

and assumes the shear stress distribution in the turbulent boundary layer. Since the shear stress variation differs largely from flow to flow, especially those under the influence of rotation and curvature, the entrainment equation rather than energy integral equation is used. The entrainment equation is derived from the concept that a turbulent boundary layer grows by a process of "entrainment" of the inviscid fluid at the edge of the boundary layer into the turbulent region and has been found to give good predictions in a variety of flows as demonstrated by Kline et al. (29). The momentum equations and the entrainment equation are solved numerically by a finite scheme to predict the three most important boundary layer parameters viz. θ_{11}, ε_w, and H, of the flow.

The following two momentum equations in rotating coordinate system (x, y, r) can be derived from Equations (7) to (9) in a manner similar to Mager (30),

$$\frac{\partial \theta_{11}}{\partial x} + (2+H) \frac{\theta_{11}}{r} TG + (2 \frac{\theta_{12}}{r} - \frac{\delta_2^*}{r}) RG + \frac{\partial \theta_{12}}{\partial r} + (1+\sin^2\beta) \frac{\theta_{12}}{r}$$

$$+ \frac{\delta_2^*}{r} \sin\beta (\frac{2}{k} - \sin\beta) = \frac{C_{fx}}{2} \tag{70}$$

$$\frac{\partial(r\theta_{22})}{r \partial r} + 2 \frac{\theta_{22}}{r} RG + 2 \frac{\theta_{21}}{r} TG + \frac{\partial \theta_{21}}{\partial x} + \frac{\theta_{11}\sin^2\beta}{r}$$

$$- \frac{\delta_1^*}{r} \sin \beta (\frac{2}{k} - \sin\beta) + \varepsilon_w \frac{C_{fx}}{2} = 0 \tag{71}$$

where θ_{11}, θ_{22} etc. are momentum thicknesses, δ_1^*, δ_2^* are displacement thicknesses in mainstream and cross flow directions defined as follows,

$$\theta_{11} = \int_0^\delta \frac{u}{U_e} (1 - \frac{u}{U_e}) dy, \qquad \delta_1^* = \int_0^\delta (1 - \frac{u}{U_e}) dy$$

$$\theta_{12} = \int_0^\delta \frac{w}{U_e} (1 - \frac{u}{U_e}) dy, \qquad \delta_2^* = \int_0^\delta \frac{w}{U_e} dy \qquad (72)$$

$$\theta_{21} = \int_0^\delta \frac{uw}{U_e^2} dy \qquad \theta_{22} = \int_0^\delta (\frac{w}{U_e})^2 dy$$

where $C_{fx} = 2\tau_{x_o}/\rho U_e^2$, τ_{x_o} is the streamwise component of surface shear stress, $\tau_{r_o} = \epsilon_w \tau_{x_o}$ (the flow is assumed to be collateral near the surface) and $k = U_e/\Omega r$, U_e is the velocity in mainstream direction at the edge of the boundary layer and C_f = skin friction coefficient.

The assumed mainstream velocity profile is

$$\frac{u}{U_e} = (y/\delta)^{(H-1)/2} = (\eta)^{(H-1)/2} \qquad (73)$$

where δ is the local boundary layer thickness, defined as the normal distance from the blade surface, where the streamwise velocity reaches its first maxima. H is the local shape factor and η is the nondimensional y coordinate. The assumed cross-flow profile is (Mager (30))

$$\frac{w}{u} = \epsilon_w (1-\eta)^2 \qquad (74)$$

where ϵ_w is the limiting streamline parameter (tan α_w) as defined in Figure 3.

Equations (73) and (74) simplify Equations (70) and (71) in terms of four parameters θ_{11}, ϵ_w, H, and C_{fx}. The resulting equations are:

43

$$\frac{\partial \theta_{11}}{\partial x} + (2+H) \frac{\theta_{11}}{r} TG + J \left[\frac{\epsilon_w \theta_{11}}{r} (1+\sin^2\beta+2RG) + \frac{\partial}{J\partial r} (J\theta_{11}\epsilon_w) \right]$$

$$+ L(\frac{2\sin\beta}{k} - \sin^2\beta - RG) \frac{\epsilon_w \theta_{11}}{r} = \frac{C_{fx}}{2} \qquad (75)$$

and

$$N\{\frac{\partial}{N\partial x} (\epsilon_w \theta_{11} N) + 2 \frac{\epsilon_w \theta_{11}}{r} TG\} + \theta_{11} \frac{\sin^2\beta}{r} + M\{2RG \frac{\epsilon_w^2 \theta_{11}}{r}$$

$$+ \frac{\partial}{Mr\partial r} (r\epsilon_w^2 \theta_{11} M)\} - H(\frac{2\sin\beta}{k} - \sin^2\beta) \frac{\theta_{11}}{r} + \epsilon_w \frac{C_{fx}}{2} = 0 \quad (76)$$

where

$$J = \frac{\theta_{12}}{\epsilon_w \theta_{11}} = \frac{(30+14H)}{(H+2)(H+3)(H+5)} \; , \; L = \frac{\delta_2^*}{\epsilon_w \theta_{11}} = \frac{16H}{(H-1)(H+3)(H+5)} \qquad (77)$$

$$M = \frac{\theta_{22}}{\epsilon_w \theta_{11}} = \frac{24}{(H-1)(H+2)(H+3)(H+4)}, \; N = \frac{\theta_{21}}{\epsilon_w \theta_{11}} = \frac{2}{(H-1)(H+2)}$$

The skin friction coefficient C_{fx} is related to the other three parameters θ_{11}, ϵ_w, and H on the basis of experimental data by Lakshminarayana et al. (17) and Anand and Lakshminarayana (27). In flows with zero or mild pressure gradients the skin friction correlation based on the experimental data of turbulent boundary layer on a single rotating blade by Lakshminarayana et al. (17) is

$$C_{fx} = 0.0582 \; R_x^{-1/5} (1 + 0.85 \sqrt{(\epsilon_w x/r)}) \text{ in the developing} \qquad (78a)$$

region and

$$C_{fx} = 0.079 \; R_r^{-1/5} \text{ for fully developed region} \qquad (78b)$$

where R_x and R_r are Reynolds numbers, both based on the local streamwise velocity at the edge of the boundary layer and distance x from the leading edge for R_x and radius r for R_r respectively. The skin friction relation for flows with large pressure gradients is based on the

44

experimental data for a turbulent boundary layer flow in a rotating channel, described by Anand and Lakshminarayana (27),

$$C_{fx} = \alpha_1 \, R_{\theta_{11}}^{-b} \, 10^{-\gamma_1 H} \, (1+B_1 \sqrt{\varepsilon_w(x-x_t)/c} \,) \tag{79}$$

where α_1, b, γ_1 and β_1 are universal constants. $R_{\theta_{11}}$ is the Reynolds number based on the streamwise velocity at the edge of the boundary layer and streamwise momentum thickness (θ_{11}), and x_t is the chordwise distance of the transition line from the leading edge.

2.4.1 Two Equation Model – Mild Pressure Gradients

For zero or mild pressure gradients in the streamwise direction, the shape factor H, may be assumed constant (H = 1.286) and the number of variables are reduced by one. The two momentum equations together with the assumed skin friction relations 78(a) and 78(b) are sufficient to solve for θ_{11} and ε_w and there is no need for an additional equation for H. Equations (75) and (76) using C_f from Equations (78a) and (78b) and Equation (77) with H = 1.286 are reduced to:

$$\frac{\partial \Delta}{\partial x} + 0.542 \, \varepsilon_w \, \frac{\partial \Delta}{\partial r} + \Delta \, \{3.285 \, \frac{TG}{r} + 0.543 \, \frac{\partial \varepsilon_w}{\partial r} +$$

$$\frac{\varepsilon_w}{r} \, (\frac{5.349}{k} \sin\beta - 1.59 \, RG - 2.134 \, \sin^2\beta) + 0.335 - 0.2/x\} - .0296A = 0 \tag{80}$$

and

$$\varepsilon_w \, \frac{\partial \Delta}{\partial x} + 0.530 \, \varepsilon_w^2 \, \frac{\partial \Delta}{\partial r} + \Delta\{\frac{\varepsilon_w^2}{r} \, (0.318 + 1.05 RG) + \varepsilon_w(\frac{2TG}{r} - \frac{0.2}{x}$$

$$+1.059 \, \frac{\partial \varepsilon_w}{\partial r}) + \frac{\partial \varepsilon_w}{\partial x} \, (0.715 \, \sin^2\beta - 0.8\sin\beta/k)\} + 0.014\varepsilon_w \, A = 0 \tag{81}$$

where J = 0.542, L = 2.673, M = 1.129 and N = 2.13 are used in the above equations, for H = 1.286.

For the present case of inducer, the radial coordinate is normalized by tip radius (r_t = 1.5 feet). The above equations are further simplified to,

$$\frac{\partial \Delta}{\partial x} + 0.362 \; \varepsilon_w \frac{\partial \Delta}{\partial R} + \Delta\{2.19 \frac{TG}{R} + 0.362 \frac{\partial \varepsilon_w}{\partial R} + \frac{\varepsilon_w}{R} (\frac{3.566}{k} \sin\beta$$

$$-1.06RG-1.423\sin^2\beta) + 0.223-0.2/x\}-0.0296A = 0 \tag{82}$$

and

$$\varepsilon_w \frac{\partial \Delta}{\partial x} + 0.353 \; \varepsilon_w^2 \frac{\partial \Delta}{\partial R} + \Delta\{(0.212+0.7RG) \frac{\varepsilon_w^2}{R} + \varepsilon_w(1.33 \frac{TG}{R} - \frac{0.2}{x}$$

$$+ 0.706 \frac{\partial \varepsilon_w}{\partial R})+ \frac{\partial \varepsilon_w}{\partial x} +(0.715\sin^2\beta - \frac{0.8\sin\beta}{k})\}+0.014\varepsilon_w \; A = 0 \tag{83}$$

where

$\Delta = \theta_{11} R_x^{1/5}$ is the momentum thickness parameter, and $A = 1+0.85 \sqrt{(\varepsilon_w x/r)}$ is a rotation parameter which gives the direct effect of rotation on skin friction as explained by Lakshminarayana et al. (17). The boundary conditions are:

1. At the leading edge, $\Delta(0,R) = \varepsilon_w(0,R) = 0$

2. At the hub, $\Delta(x,0.5)$ and $\varepsilon_w(x,0.5)$ are determined from single blade solution which is modified to include pressure gradient parameters RG and TG.

The flow near the leading edge is found to be laminar and its extent (x_t) has been determined by experiment. Banks and Gadd's (7) analysis is used to predict θ_{11} and ε_w in the laminar region up to the point of transition. It is to be noted that this analysis is valid for the laminar boundary layer over a single rotating blade, and so does not take into account the effect of imposed pressure gradients on the boundary layer. Since the actual pressure gradients in this region are very small for the present case, neglecting this effect may be

justified. For $x > x_t$, the flow is assumed to be turbulent and the turbulent flow Equations (82) and (83) are used to predict θ_{11} and ε_w.

The partial differential Equations (82) and (83) are solved numerically using fourth order finite difference scheme. The values of TG, RG are assumed to be known from the inviscid analysis of the channel flow. For the case of rotating helical channel used in this investigation, these values are derived from the measured blade pressure distribution. The convergency criteria used in the numerical analysis are

$$|\Delta_{i,j}^{(n)} - \Delta_{i,j}^{(n-1)}| \leq 10^{-4} \text{ feet}$$

$$\tag{84}$$

$$|\varepsilon_{i,j}^{(n)} - \varepsilon_{i,j}^{(n-1)}| \leq 10^{-3} \text{ radians}$$

where n and n-1 are nth iteration and (n-1) iteration respectively. A zero order solution is obtained by solving for Δ from Equation (82) by neglecting terms containing ε_w and its derivatives. This is used as initial data for Equation (83) to solve for ε_w and thereafter Equations (82) and (83) are successively iterated till convergency, according to the criteria of Equation (84).

The numerical solution of flow over a single rotating helical blade was also obtained and found to agree with the analytical solution obtained by Lakshminarayana et al. (17), where radial variation of ε_w is neglected. The radial variation of ε_w was found to be negligibly small for a single blade and justifies its neglect for that case.

2.4.2 Three Equation Model - Large Pressure Gradients

For boundary layers with large imposed pressure gradients which normally occur in a turbomachinery operating at the design and off

47

design flow conditions, variation of shape factor (H) is large and an additional equation to account for its variation is required. The entrainment equation, which as described earlier is better than other auxiliary equations (Kline et al. (29)) and has the least empiricism, is derived below.

The entrainment equation is obtained from the integration of continuity equation from blade surface (y = 0) to the edge of the boundary layer (y = δ). The continuity Equation (9) is the same both in the rotating and stationary coordinate system (x, y, r).

Following Nash and Patel (31), its integral form can be written as

$$\frac{\partial}{\partial x} \{U_e(\delta-\delta_1^*)\} + \frac{\partial}{r\partial r} \{U_e r\delta_2^*\} = U_e \frac{\partial\delta}{\partial x} + W_e \frac{\partial\delta}{\partial r} - V_e = E \qquad (85)$$

where δ_1^* and δ_2^* are displacement thickness parameters in streamwise and cross flow directions respectively and are defined in Equation (72). E on the right hand side represents the volume flow rate per unit area through the surface $\delta(x,r)$ and is the rate of entrainment of inviscid external flow into the boundary layer.

The entrainment process is a highly complex and inherently unsteady phenomena and its direct measurement is difficult. The entrainment rate depends both on the mean flow parameters, such as the streamwise velocity defect, the rate of boundary layer growth, streamwise velocity, displacement thickness etc., as well as on the turbulent quantities such as turbulence intensities and stresses in the outer layer. The streamwise velocity defect in turn is directly related to streamwise velocity, the shape factor, the magnitude of cross flow and the blockage effects due to confinement of external inviscid flow in the channel.

48

The effect of streamwise velocity and the shape factor on the
entrainment rate have been extensively studied, resulting in Head's
(32) entrainment equation,

$$E = U_e \ F(H_{\delta-\delta_1}{}^*) \qquad\qquad (86)$$

where $H_{\delta-\delta_1}{}^*$ is a shape parameter, defined by $H_{\delta-\delta_1}{}^* = (\delta-\delta_1{}^*)/\theta_{11}$ and
uniquely related to the shape factor H. For one parameter main velocity
profile (according to Head (32)) the equation for shape parameter is,

$$H_{\delta-\delta_1}{}^* - 1.535(H-0.7)^{-2.715} + 3.3 \qquad\qquad (87)$$

and

$$F(H_{\delta-\delta_1}{}^*) = C_E \ (H_{\delta-\delta_1}{}^* - 3.0)^{-0.653} \qquad\qquad (88)$$

where C_E is the entrainment coefficient. Its value for two-dimensional
boundary layers is 0.0306. Qualitatively, it is known (Kline et al.
(29)) that the effect of an increase in turbulence level in the external
stream is to increase the entrainment rate. On the other hand, an
increase in cross flow causes a reduction in boundary layer thickness
and hence its growth rate in streamwise direction. Since the entrainment
rate is directly proportional to boundary layer growth rate, consequently
an increase in cross flow causes a decrease in it. Assuming that the
variation of entrainment rate with $H_{\delta-\delta_1}{}^*$ follows the same relationship
even for three-dimensional flows, e. g. Cham and Head (10), Lewkowicz
(33), the effects of turbulence level and cross flow can be incorporated
by assuming that $C_E = C_E \ (q_e, \ \varepsilon_w)$, where q_e is the free stream turbulence
level. Hence the total entrainment rate can be written as follows:

$$E = U_e C_E(q_e, \ \varepsilon_w)(H_{\delta-\delta_1}{}^* - 3.0)^{-0.653} \qquad\qquad (89)$$

Substituting for E in Equation (85), the auxiliary or entrainment equation becomes

$$\frac{\partial}{\partial x}\{U_e(\delta-\delta_1^*)\} + \frac{\partial}{r\partial r}\{U_e r\delta_2^*\} = U_e C_E(q_e,\epsilon_w)(H_{\delta-\delta_1}^*-3.0)^{-0.653} \qquad (90)$$

Writing in terms of three variables θ_{11}, ϵ_w, and H, the equation becomes:

$$\frac{\partial}{\partial x}\{U_e\theta_{11}H_{\delta-\delta_1}^*\} + \frac{L}{r}\frac{\partial}{\partial r}\{U_e L r\theta_{11}\epsilon_w\} = U_e C_E(q_e,\epsilon_w)(H_{\delta-\delta_1}^*-3.0)^{-0.653} \qquad (91)$$

The entrainment Equation (91) is further simplified to give a direct equation for the shape parameter $H_{\delta-\delta_1}^*$,

$$\frac{\partial H_{\delta-\delta_1}^*}{\partial x} + H_{\delta-\delta_1}^*[\frac{TG}{r} + \frac{1}{\theta_{11}}\frac{\partial\theta_{11}}{\partial x}] = \frac{C_E}{\theta_{11}}(H_{\delta-\delta_1}^*-3.0)^{-0.653}$$

$$- \frac{1}{r}[\epsilon_w(1+RG + \frac{r}{\theta_{11}}\frac{\partial(\theta_{11}L)}{\partial r}) + r\frac{\partial\epsilon}{\partial r}] \qquad (92)$$

The two momentum integral Equations (75) and (76), together with the expression (79) for skin friction and the entrainment Equation (91), constitute a set of four equations for four variables θ_{11}, ϵ_w, H and C_f. C_f can be eliminated from (75) and (76) by substituting (79) and these equations are simplified to:

$$\frac{\partial\Delta}{\partial x} + J\epsilon_w\frac{\partial\Delta}{\partial r} + \frac{\Delta}{r}[TG\{(2+H)(1+b)-b\} + (1+b)r\frac{\partial(\epsilon J)}{\partial r} +$$

$$\epsilon_w\{\frac{2L(1+b)\sin\beta}{k} - RG(L(1+b)-J(2+b)-\sin^2\beta(L-J)(1+b)+J(1+b))\}]$$

$$- \frac{\alpha_1}{2}A^*(1+b) = 0 \qquad (93)$$

and

$$\varepsilon_w \frac{\partial \Delta}{\partial x} + \frac{M}{N} \varepsilon_w^2 \frac{\partial \Delta}{\partial r} + \frac{\Delta}{r} [\varepsilon_w^2 \frac{M}{N} \{(1+b)+RG(2+b)\} + \varepsilon_w \{TG(2+b) +$$

$$\frac{2}{N}(1+b) \ r \ \frac{\partial(\varepsilon_w M)}{\partial r}\} + \frac{(1+b)}{N} \ \frac{\partial(\varepsilon_w N)}{\partial x} + \frac{(1+H)}{N} (Hb)\sin^2\beta - \frac{2H(1+b)}{N} \frac{\sin\beta}{k}]$$

$$+ \frac{\alpha_1(1+b)}{2N} \ \varepsilon_w A^* = 0 \qquad\qquad (94)$$

where $\Delta = \theta_{11} R_{\theta_{11}}^b$ is a new variable for momentum thickness and

$$A^* = 10^{-\gamma_1 H} (1+\beta_1 \ \sqrt{\varepsilon_w/(x-x_t)/e})$$

The experimental data of Anand and Lakshminarayana (27) indicate that the values of $b = +0.268$, $\gamma_1 = 0.678$, $\beta_1 = 0.52$, $\varepsilon_1 = 0.172$. Equations (93) and (94) are to be solved simulatneously for θ_{11} and ε_w, using the same finite difference scheme as described in the section 2.4.1 and assuming initially a constant value of H. These values are to be used in Equation (92) to find a new value of H. Thus Equation (92) is to be solved successively with Equations (93) and (94) till the convergency criterion (84) for Δ and ε_w together with the following criterion for H is reached.

$$\left| H^{(n)} - H^{(n-1)} \right| \leq 0.001 \qquad\qquad (95)$$

where $H^{(n)}$ and $H^{(n-1)}$ are values of the shape factor H at nth and (n-1)th iterations respectively. The boundary conditions and the procedure for incorporating laminar solution are same as described in section 2.4.1

Since an expression for C_E for three-dimensional flow is not yet available, no numerical solutions are given in the thesis, even though the computer programming has been completed.

III. TEST FACILITY AND DATA ACQUISITION EQUIPMENT

3.1 Experimental Test Facility

All the measurements reported in later chapters were performed using the NASA Axial-Flow Inducer Test Facility, shown in Figure 8 and located in the Turbomachinery Laboratory of the Department of Aerospace Engineering at The Pennsylvania State University. A 5 hp Polydyne Adjustable Speed Motor (speed range 286-2000 rpm) drives the rotor through a belt and pulley system. An aerodynamically designed throttle can vary the flow rate through the machine, so that the rotor can be operated at different flow coefficients on the performance map. The annulus has a well designed bell mouth inlet so as to give uniform axial flow at the inlet to the rotor. The facility has a number of test windows and static pressure holes so that a comprehensive flow survey is possible. Extensive flow visualization and quantitative measurements of the flow field were performed upstream, inside and at the exit of an axial flow inducer rotor (references 17, 21, 22, 23, 34) by varying the number of blades from 1 to 4 and at different flow coefficients. These measurements would be compared to the data obtained with the four bladed flat plate inducer described below.

Rotor Facility. The rotor consists of four equally spaced transparent plexiglass helical blades of constant thickness (0.5 inch), an axial advance of 10 inches and an angular extent of 300 degrees. The blade stagger angle varies from 78° at the hub to 84° at the tip. Other dimensions of the rotor and facility are shown in Figure 9. Both the leading and trailing edges of the blade are shaped to form a symmetric rfoil shape to ensure smooth flow at both the edges. The blade
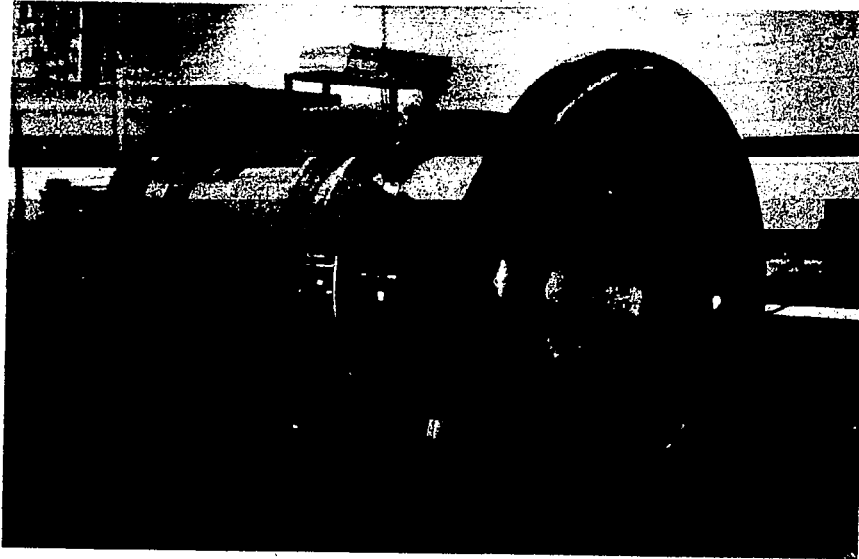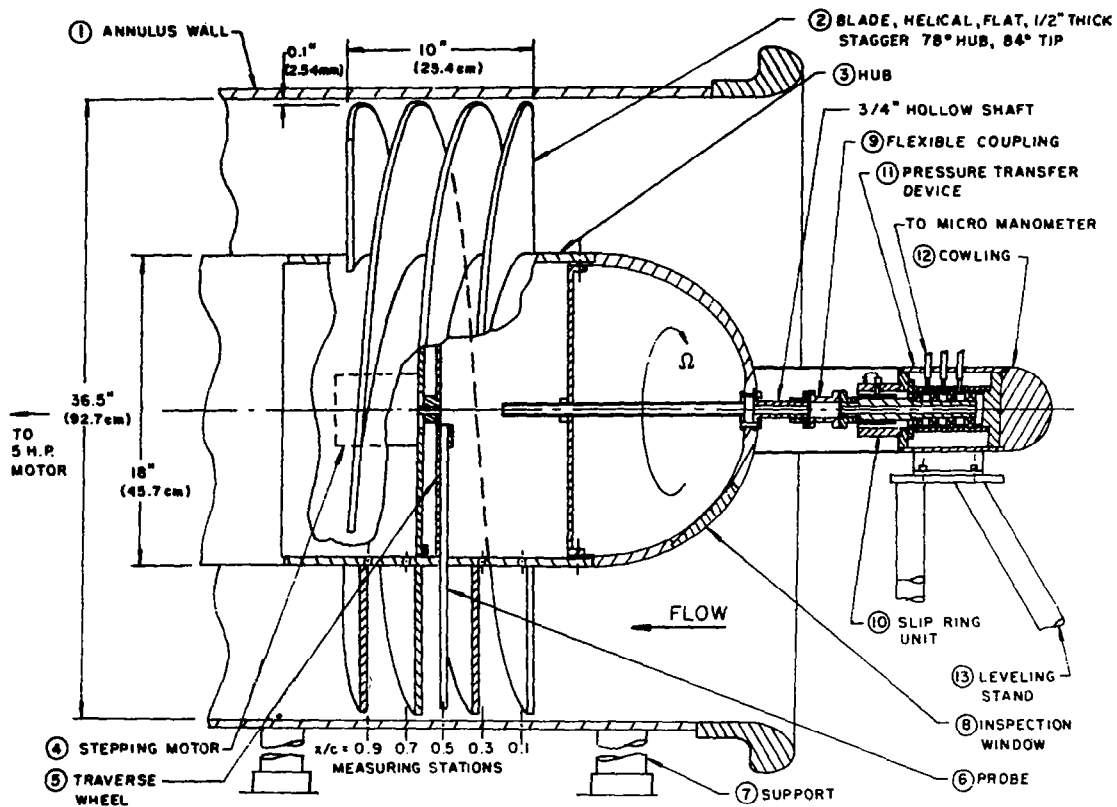
Figure 8.   Inducer Test Facility

53

Figure 9. Four Bladed Rotor and Probe Traversing Facility

surface can be considered hydraulically smooth in the operating range because $u_*\lambda/\nu < 2.5$ where λ is the mean height of the surface roughness.

To facilitate blade static pressure and limiting streamline angle measurements, the adjoining blades of the channel have ten static pressure taps at each of the five axial locations. The rotor is statically and dynamically balanced before installation in the inducer test facility to reduce vibrations.

One unique feature of this facility is the traverse unit for the rotating probe measurements. Referring to Figure 9, it consists of a light traverse disk driven by a fractional horse power step motor. The probe holder and the probe is mounted on the traverse disk. The probe, which is located inside the passage, traverses in a slot in the hub. The traverse disk and the probe can be traversed circumferentially in steps of 1.8° by the stepping motor, thus enabling accurate location and measurement of the flow characteristics inside the blade boundary layers. The motor is powered and controlled by a stationary traverse indexing device through an eight channel slip ring unit. The traverse unit and the probe are locked, except when indexed. Thus the circumferential traverse can be accomplished, through the remotely controlled index device, without stopping the rotor. The radial movement of the probe is carried out manually. Once all the radial and circumferential traverses have been completed, the entire traverse assembly is moved to a different axial location and the measurements repeated. The instrument package, consisting of commerical slip ring unit, mercury slip ring unit, and a pressure transfer device is housed in a stationary cowling attached to the nose cone as shown in Figure 9. In order to eliminate possible transmission of the rotor assembly vibrations to the instrument

packages a flexible rubber coupling is used. All the measurements have been carried out at the rotational speed of 450 rpm corresponding to a Reynolds number of 6.7×10^5, based on the tip radius. The speed of the inducer is maintained constant up to an accuracy of 0.1 rpm by means of a photocell circuit with a 60 slot calibrated disk mounted on the rotor shaft and displayed on an electronic counter. For checking the probe position and for photographing the flow in rotor passages, when rotating, a high intensity strobeflash unit is used. A schematic of the experimental setup is shown in Figure 10. The following devices are used for measurements in rotating system.

3.2 Data Transmission Devices

Three Channel Pressure Transfer Device (PTD). The pressure transfer device (PTD) has three channels, each of which is made airtight by using double sealed ball bearings. Pressure leakage along the cylinder is prevented by the use of O-rings and the plastic sealers. Pressure from the rotating system is transferred to the pressure transverse device through a hollow shaft which is fastened to the nose cone, and is measured by a micro-manometer. In order to reduce the possible interference on the incoming flow, the pressure transfer device is housed inside a streamlined cowling.

Ammonia Transfer Device (ATD). The direction of the flow near the blade surface is determined by means of the ammonia streak method, i.e., by releasing a small amount of ammonia gas through the holes drilled on the blade surfaces and measuring the resulting ammonia trace on an ozalid paper strip attached radially on the blade surface adjacent to
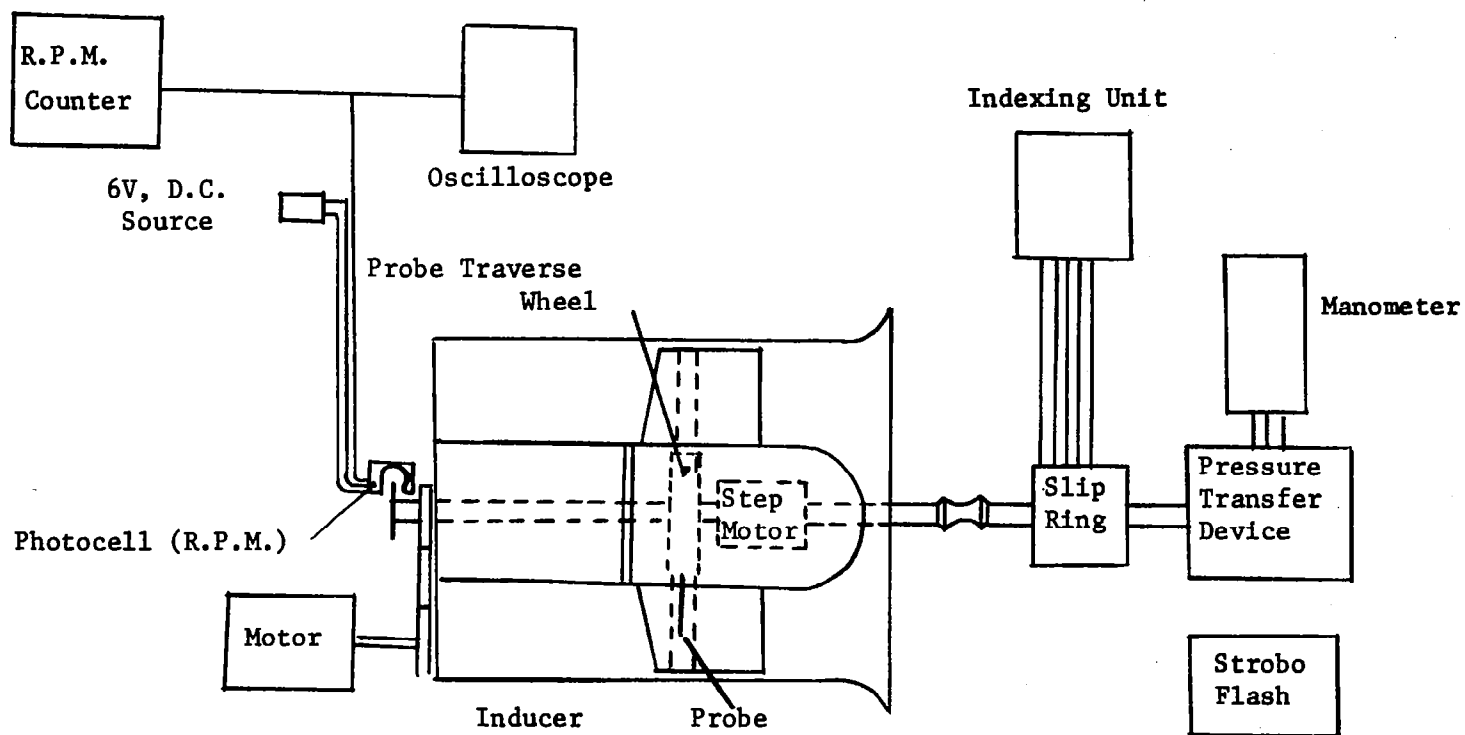
Figure 10.   Experimental Set Up (Open Throttle Measurements).

the measuring station. ATD transfers ammonia gas from the stationary system to the rotating system. The ATD is mounted on the stand outside the rotor assembly.

Slip-Ring Unit. A commercial eight channel slip-ring unit is used to conduct electrical signals from the stationary reference frame to the rotating reference frame of the rotor traverse unit. Electrical continuity is provided by carbon brushes in contact with a rotating commutator aligned along the inducer's rotational axis. The slip-ring unit is mounted on the pressure transfer device, and all electrical and pressure connections were transferred through a hollow shaft and flexible couplings to the nose cone of the inducer.

Mercury Slip-Ring Unit. A six channel mercury slip-ring unit (Rotocon, MSD #6, Meridian Lab.) is utilized in transmitting the hotwire signals from the rotating reference frame of the inducer to the stationary hotwire anemometers. The slip-ring unit exhibits the smallest and most stable resistance in the transfer of measuring signals from the rotating electrical elements to the stationary electrical conductors. Contact between the rotating wires and the stationary contact screws is made through a round contact disc to which the rotating wire is connected, rotating in mercury. Triple-distilled mercury is used to provide the greatest conductivity and the lowest noise level distortion possible. The slip-ring is mounted on a four arm vibration damper and thus eliminates any spurious electrical signals due to possible transmission of rotor assembly vibrations to its electrical contacts.

3.3 Instrumentation and Probes

3.3.1 Measuring Equipment

All the pressure sensitive signals are measured with a Meriam Micro-manometer. All the pressure measurements lie in the range 0.05 - 1.1" of water. The minimum accuracy in pressure measurement is 2%.

Two dual channel constant temperature hotwire anemometers are used to provide the three channel capability necessary for the three-dimensional turbulence measurements. The original anemometer circuitry has been designed by Lumley (35) to give a flat response (Appendix A) up to 50 KHz even for large turbulence signal levels (up to as high as 20%). Operating characteristics of the circuitry are described in Appendix A. The anemometer power supply is kept on for 24 hours before taking data to minimize the voltage drift. The number of ground loops with the connected circuitry are minimized to prevent surging in the anemometer circuitry and to reduce the electrical noise from power supply and other electrical equipment in the room. A schematic of the hotwire set up is shown in Figure 11.

3.3.2 Probes

A three hole probe disk type (Figure 12) is used to measure the total pressure and radial flow angle (defined as the angle which the local streamline makes with the streamline at the edge of the boundary layer) inside the rotor blade passages in a measuring grid of 5 x 5 x 40 in tangential, radial and blade to blade directions respectively. The probe is 1/4 inch in diameter and 1/16 inch thick. Three holes 1/32 inch diameter each, drilled circumferentially on the disk and 45° to each other form the sensing area. The disk probe has a number of
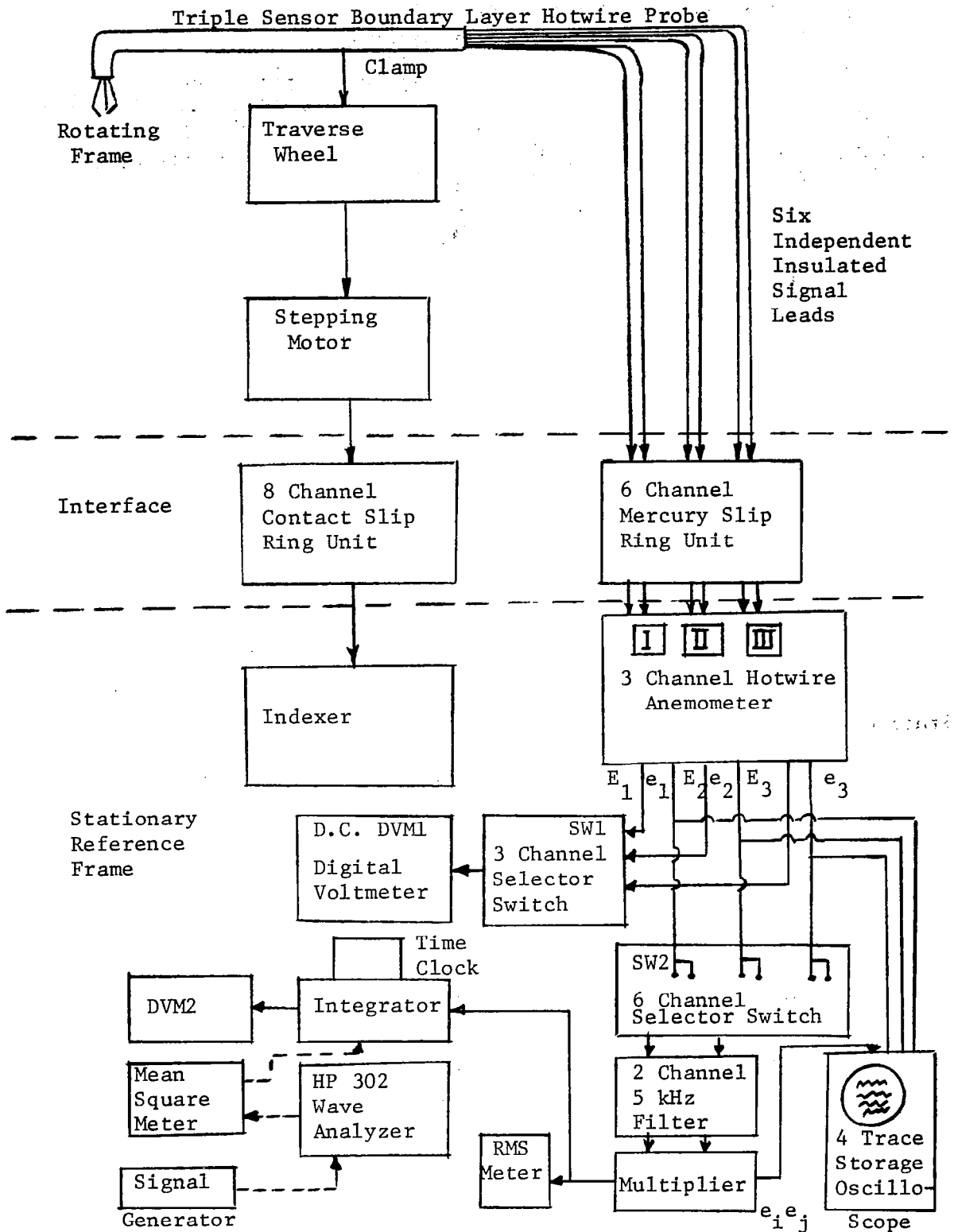
59

Figure 11.   Schematic for Hotwire Measurements.

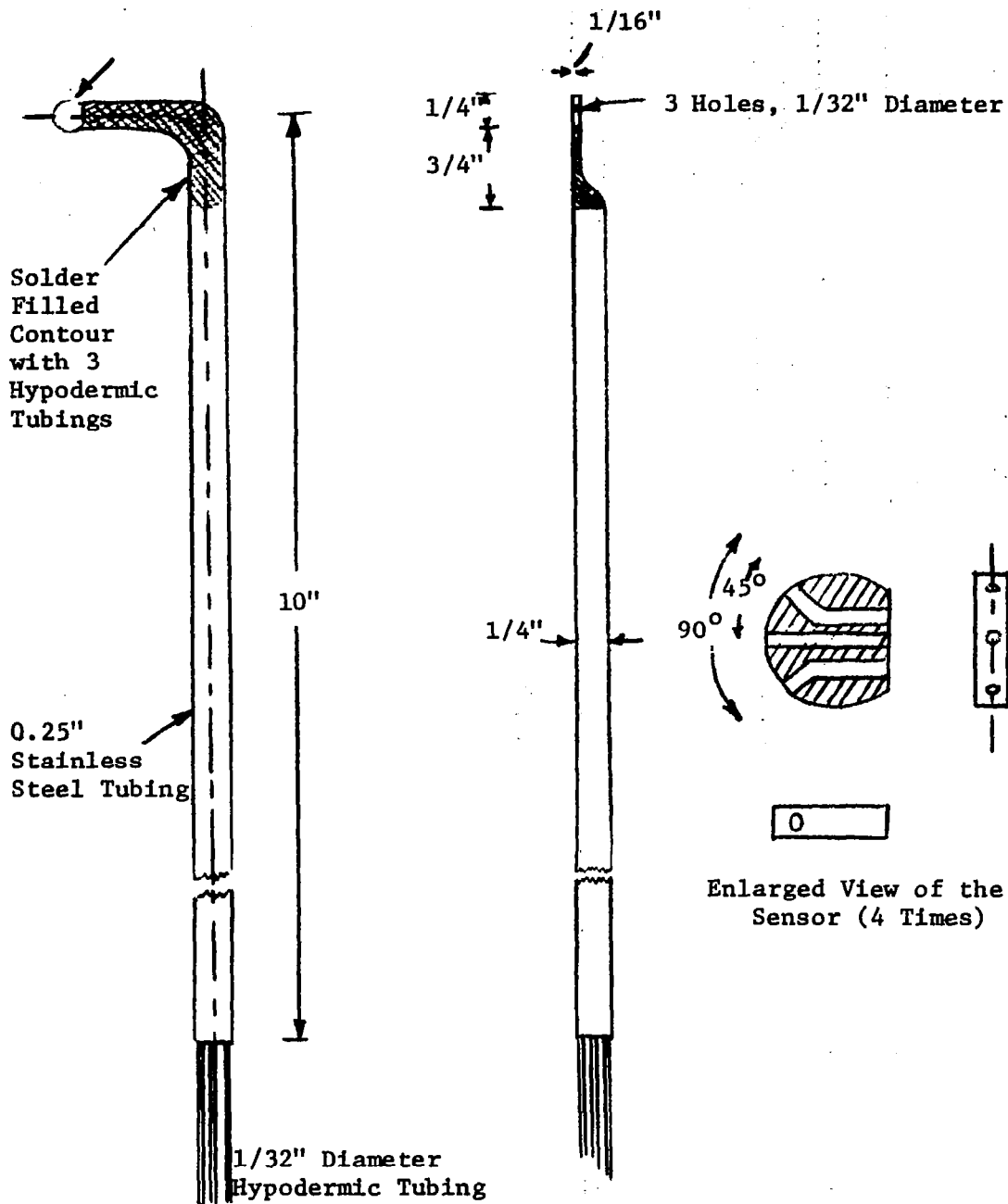1/4" Diameter, 1/16" Thick Disk Sensors
with 3 Holes Drilled 45° to Each Other

1/16"

1/4"

3/4"

3 Holes, 1/32" Diameter

Solder
Filled
Contour
with 3
Hypodermic
Tubings

10"

1/4"

45°

90°

0.25"
Stainless
Steel Tubing

Enlarged View of the
Sensor (4 Times)

1/32" Diameter
Hypodermic Tubing

Figure 12.   Disk Type Boundary Layer Probe.

61

advantages over a conventional yaw probe for measurements close to a blade. It can be easily aligned parallel to a blade surface, produces less flow distortion and has a wide linear flow angle measuring range ($\pm 20^\circ$) as shown in the calibration curve (Figure 13). The calibration curve is later corrected for total pressure and flow angle using the Open Jet Tunnel Facility as described in Appendix B.

Two Preston tubes of outside diameters 0.028 inch and 0.065 inch are used to measure the total wall shear stress by placing them flush with the blade in the direction of measured limiting streamline angle at that location.

A special three sensor boundary layer hotwire probe (Thermosystems Inc.), shown in Figure 14, is used in all rotating hotwire measurements to obtain the mean velocity components and the turbulent quantities from the direct measurement of the three mean sensor output voltages, $\overline{E_1}$, $\overline{E_2}$ $\overline{E_3}$ and the six products of fluctuating voltages $\overline{e_1^2}$, $\overline{e_2^2}$, $\overline{e_3^2}$, $\overline{e_1 e_2}$, $\overline{e_1 e_3}$, $\overline{e_2 e_3}$. The orientation of the sensors is also shown in Figure 14 with respect to the reference coordinate system x, y, r. Sensors 1 and 2 are in the xy plane and are orthogonal to each other. Sensor 1 makes an angle α_1 with the x-axis. Sensor 3 is located midway between 1 and 2 and is at angle γ_1 to the xy plane (i.e. the plane containing sensors 1 and 2). The direction cosines, the dimensions of sensors and the support needles etc. are given in Appendix A. All six needles and their electrical connections are insulated from each other so that each wire can be operated independently of others. The probe body has an elliptic cross section (1/8" x 1/4") and therefore can be used for measurements as close as 1/16" from the blade surface without touching it. The experimental set up for hotwire measurements is shown in Figure 15.
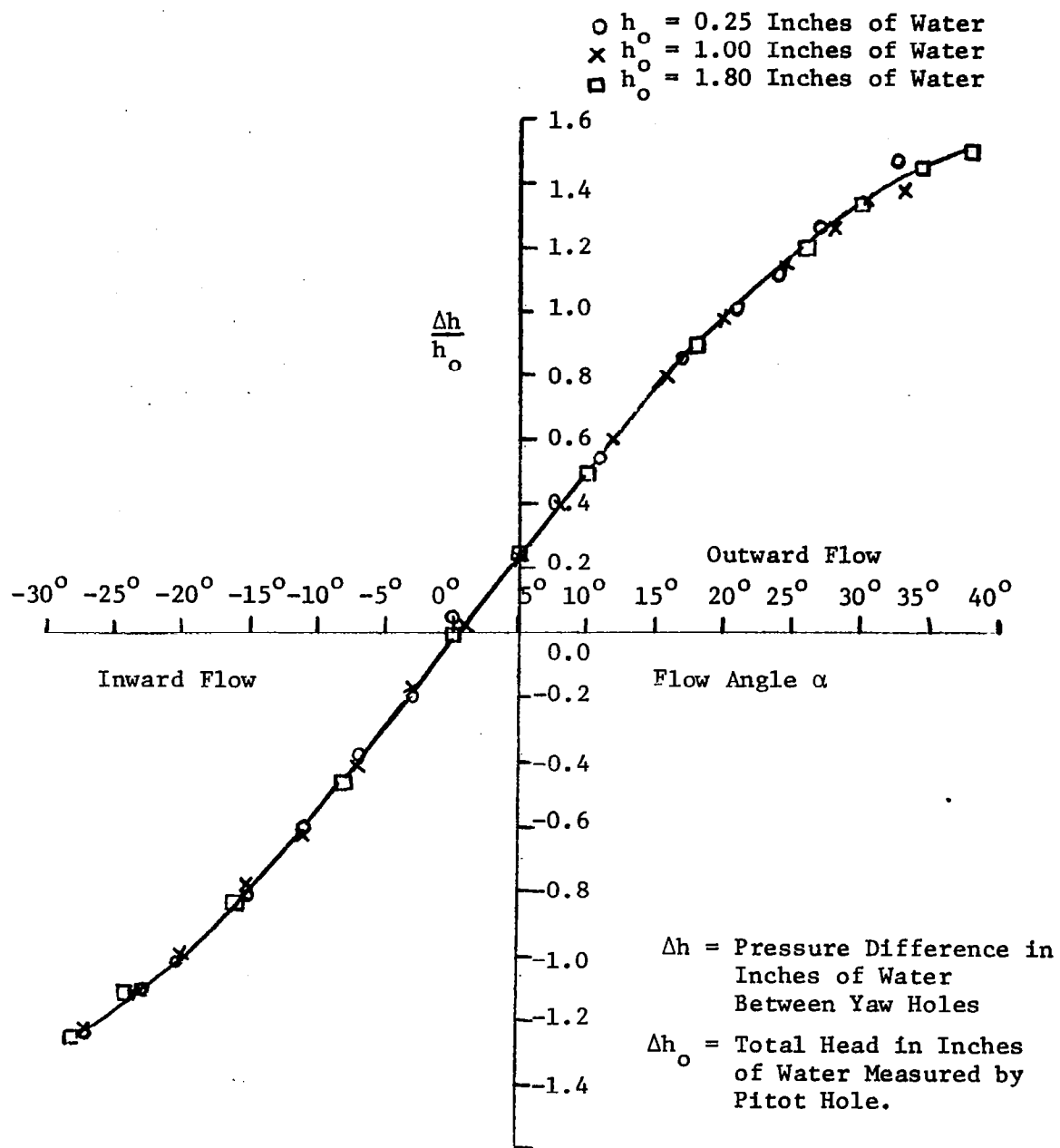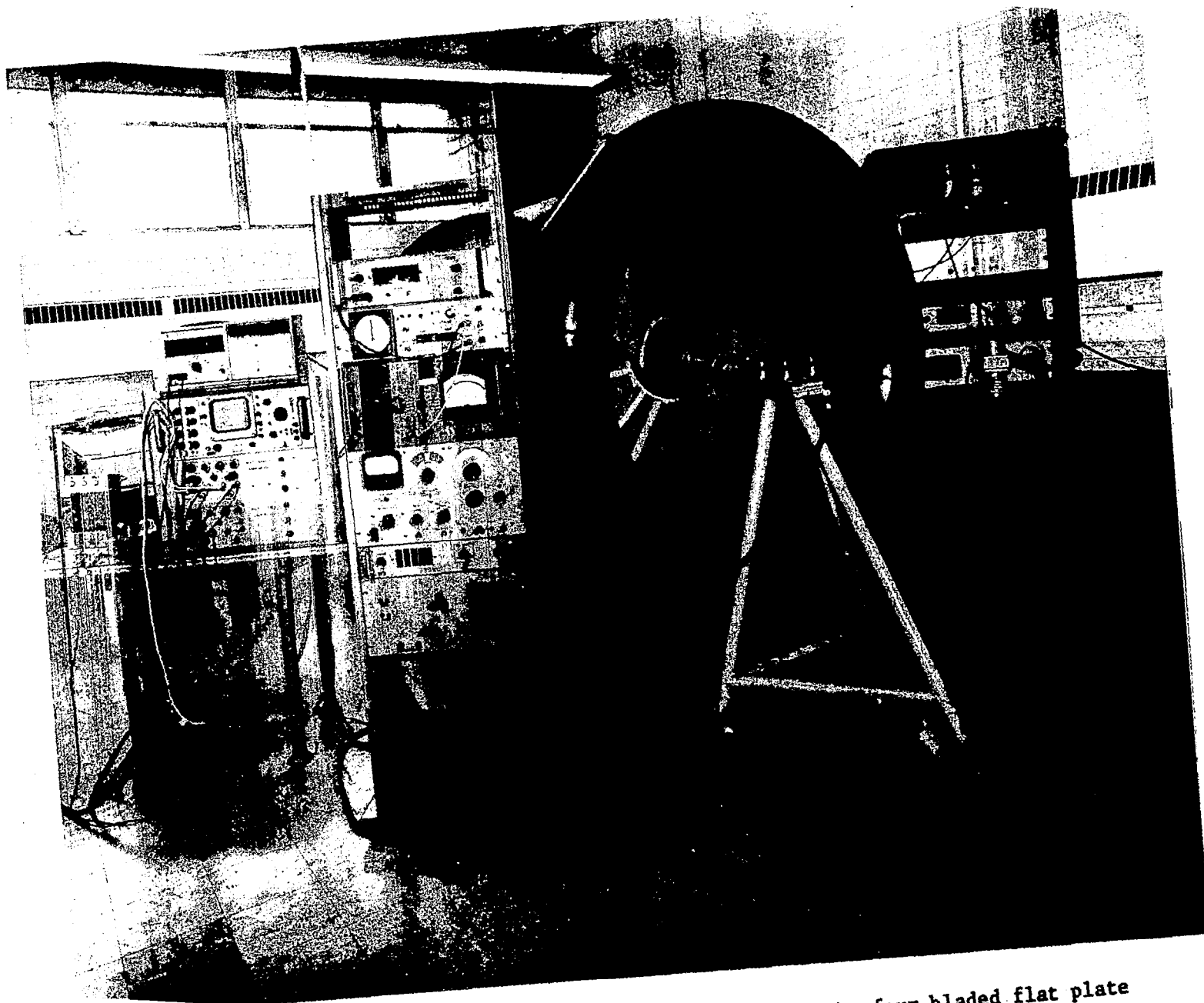
Figure 13. Calibration Curve for Disk Probe.

Figure 14. Three Sensor Hotwire Boundary Layer Probe.

...raph is replaced by four bladed flat plate

3.3.3 Signal Processing Equipment

The output of the anemometer consists of three fluctuating a.c. and three d.c. signals. The d.c. signals are measured with a 3430A Hewlett Packard Digital Voltmeter up to an accuracy of 1 mv, through a three channel selector switch. The a.c. signals are passed through a multichannel selector switch. This switch has six input channels. Each two of these are connected to one of the three a.c. signals. The switch has two output channels and therefore gives any desired dual combination of the three instantaneous signals (i.e. e_1^2, e_2^2, e_3^2, e_1e_2, e_1e_3, e_2e_3).

The signals are now filtered through a dual channel 5 kHz low pass filter-amplifier circuit. Both the turbulent spectral measurements without the filter and the frequency corresponding to Kolmogorov scale (maximum of 3.5 kHz at x/c = 0.1) show that the signal is either of the order of or less than the electrical noise signal above 5 kHz and thus governed the choice of 5 kHz filter. The signals are multiplied in the Model 520 Analog Devices Multiplier Unit and integrated in an integrator up to an accuracy of 1 mv for a large integrating time (45 seconds for each observation) using a synchronized stop clock. The integrator is calibrated to have an integration factor of unity between input and output. The integrated output is read through a 3440 A Hewlett Packard Digital Voltmeter with a 3444 A Multifunction unit, up to an accuracy of 1 mv. A schematic of the hotwire set up for measurements of mean and turbulent quantities is shown in Figure 11.

A type 55D35 DISA RMS unit with variable integration time is used for overall turbulence level measurements. A 302A Hewlett Packard Wave Analyzer is used for spectral measurements. The wave analyzer has a carrier frequency of 100 kHz and a bandwidth of 7 Hz for its narrow band

66

frequency selector filter. Its output is squared and amplified using a
Weston Model 1056, Ballantine Laboratories Mean Square Meter, integrated
for 60 seconds in the integrator and the final output is read on the
3440 A Hewlett Packard Digital Voltmeter. Figure 11 also shows a
schematic of experimental set up for spectral measurements.

A four channel type 3A74 Four Trace Tektronix Storage Oscilloscope
is used in all the hotwire measurements to visualize the magnitude of
all three turbulent signals and their multiplied output. A Model 200CD
Hewlett Packard Wide Band Signal Generator is used to calibrate the
Wave Analyzer and to find the gain of individual components in the
hotwire circuitry, except the hotwire anemometer channels, which are
calibrated individually in the calibration tunnel described along with
other peripheral equipments in the following section.

3.4 Peripheral Equipment

A low turbulence calibration tunnel is used for the hotwire
calibration. The horizontal wind tunnel has a square test section with
each side of one and a half inch and operates within the range of air
velocities of 0-300 feet per second. The calibration velocities are
measured with a United Sensor 1/8 inch pitot-static tube and the micro-
manometer described previously.

Pressure sensitive probes (e.g. cobra probe, total pressure probe,
etc.) are also calibrated in the same tunnel.

A one-foot diameter open jet tunnel of the Garfield Thomas Water
Tunnel Research Facility of The Pennsylvania State University is used
to calibrate the three hole disk probe for total pressure and flow angle
at different velocities. The calibration curves are given in Appendix B.

The local hotwire making facility enables sensor replacement in a comparatively short time. The probe is mounted on a small table vice with sensor area facing an adjustable focus tilting microscope. The new wires are soldered using a special solder iron and etched to required resistance by a dilute nitric acid solution. The desired resistance of the hotwire and the associated "over heat ratio of resistances" of the hotwire anemometer are measured up to an accuracy of 0.1 ohm using a null galvanometer.

An optical profile projector of the Applied Research Laboratory is used to measure the geometry of probe needles and the dimensions of hotwire sensors. It also measures the wire angles with respect to the reference coordinate system (x, y, r).

IV. EXPERIMENTAL TECHNIQUES

4.1 Limiting Streamline Angle Measurement

The limiting streamline angles on a rotating body can be determined from the ammonia streak method described in Reference 36. A small amount of ammonia gas is released through the blade static pressure taps, while the rotor is in motion, and the trace of the gas is recorded on an ozalid paper. It is important to realize that, in order for the above procedure to be valid, the ammonia gas must remain in the collateral region, which means that the ammonia gas coming from the orifice on the blade surface must have a very low velocity. Typical traces of limiting streamlines derived by this method are given by Jabbari (37).

Measurements of the limiting streamline angle are carried out at the predetermined tangential locations which coincided with the locations of the blade static pressure taps. At each tangential location, two measurements are made. Variation between the two measurements is found to be very small. The experimental accuracy of angle measurements is about 2° and for small cross flows which for example occur in the channel for open throttle case, the percentage error can be large ($\sim 10\%$).

4.2 Blade Static Pressure

The flow in a channel differs from those around a single blade in two aspects: (a) The pressure gradient that exists in a channel changes the boundary layer behavior, local shear stress, limiting streamline angle, etc. (b) The interaction between the boundary layers on the two adjoining surfaces gives rise to complicated profiles arising out of mixing. In view of this it is important to have a knowledge of the

69

static pressure measurements on the blade. Blade static pressure taps are connected to PTD by vinyl tubing and the static head measured by the micro-manometer. A centrifugal force correction term is required to determine actual blade static pressure.

If h_m is the height of water column measured by the manometer, the actual static head (h) is given by

$$h = h_m + \frac{\rho_{air}}{\rho_m} \frac{\Omega^2}{2g_o} (r^2 - r_o^2) \tag{96}$$

where ρ_m is the density of manometer fluid, r_o is the radius of rotating shaft (1") used in PTD, and r is the radius of the static pressure tap under consideration.

The blade static pressure measurements were carried out at ten radii and at five chordwise locations, x/c = 0.1, 0.3, 0.5, 0.7, and 0.9 on both leading and trailing surfaces of the blade.

4.3 Transition

The boundary layer near the leading edge is laminar. The extent of the laminar region and the location of transition is determined by the "China Clay Technique". The blade surface is coated with a smooth, thin white film of china clay dissolved in acetone solution. The film is sprayed with ether by a spray gun and the rotor is brought to design speed. The evaporation takes place faster in the turbulent region than in the laminar region and is indicated by the whiteness of the former region compared to darkness of the latter region. The rotor is stopped after about three minutes and the laminar-turbulent transition line is obtained. Details of this method are described by Jabbari (37). The

results are shown in Figure 16 for the case, when the rotor is operated
at large pressure gradients (with the throttle at a flow coefficient of
0.05).

4.4 Skin Friction Coefficient

One of the most important problems in the three-dimensional boundary
layer flow investigations is the determination of the wall shear stress.
In two-dimensional boundary layer flows, the wall shear stress has been
determined by various direct and indirect methods. The frequently used
direct methods include the Preston tube method, the heated element method
(HEM) and the floating element method (FEM).

Because of the presence of the centrifugal force, vibrations in
rotation, use of FEM and HEM methods are severely limited in its
application for wall shear stress measurements on a rotating blade.

The wall shear stress is therefore evaluated by means of the
Preston tube method. Validity of its use for three-dimensional rotating
turbulent boundary layer flows is discussed below.

Following Preston (38) when a total pressure pitot tube (whose
diameter is smaller than the extent of validity of the law of the wall)
is used, the wall shear stress can be related to the dynamic pressure
ΔP recorded by the pitot tube through the following relationship.

$$\frac{\tau_o d^2}{4\rho\nu^2} = F\ (\frac{\Delta P\ d^2}{4\rho\ \nu^2}) \qquad\qquad (97)$$

where d is the diameter of the Preston tube.

This shows that the wall shear stress can be determined by the
local dynamic pressure, once the function F is known. Experimental
verification of the validity of this approach to stationary three-

71

Leading Edge

Flow

T

Tip

Hub

9"

18"
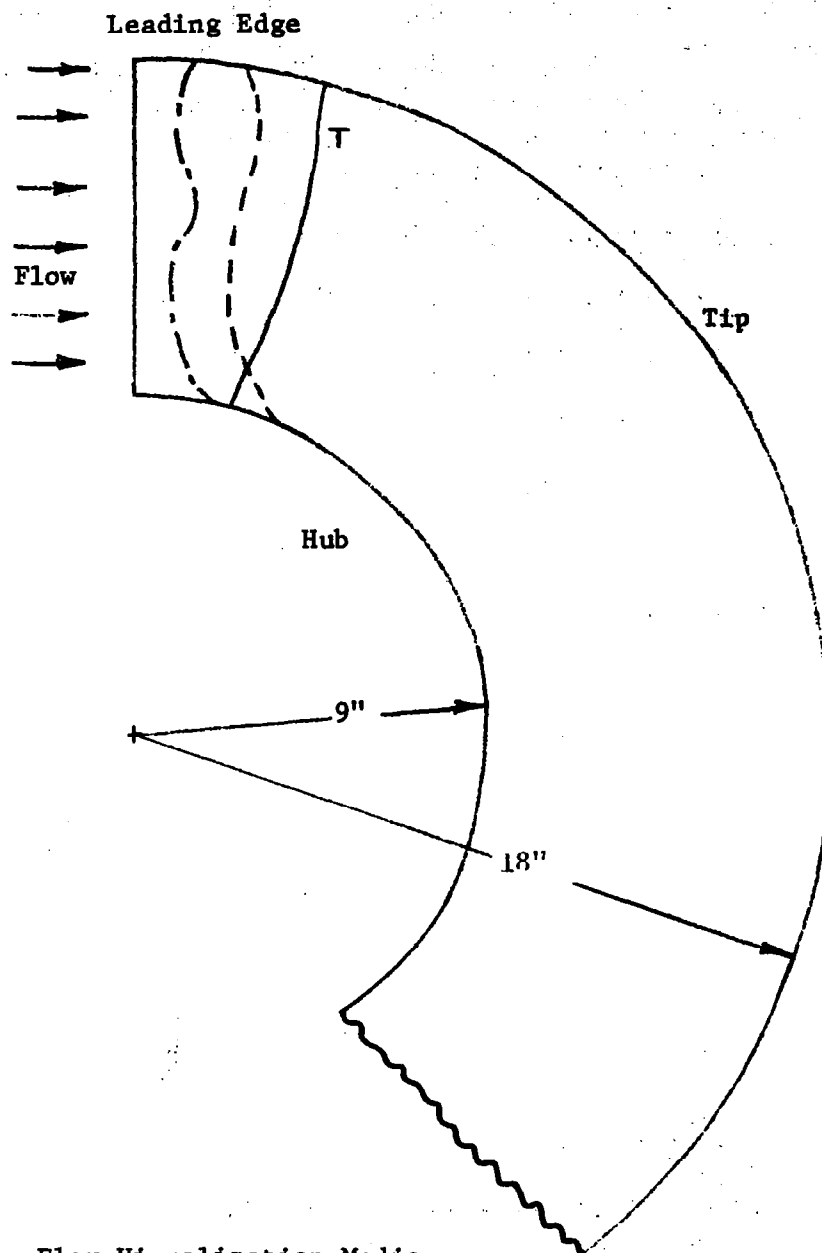
Flow Visualization Media

(a) Camphor and Petroleum Ether (Evaporator)
——————— Trailing Side
(b) China Clay and Petroleum Ether
— — — Trailing Side —— — —— Leading Side

Figure 16. Transition Measurements (Throttled Case).

72

dimensional turbulent boundary layer flows was carried out by Pierce and Krommenhoek (39). Results obtained by the Preston tube method were compared with those obtained by the floating element method which gave the direct measurement of the shear force, and good agreement was reported.

In the present case of rotating three-dimensional turbulent boundary layers, the law of wall $(u/u_* = 1/\kappa_1 (\log y^+ + C))$ is experimentally shown to exist (Chapter V). Skin friction coefficients obtained from the Caluser Plot of the data in Chapter V agree very well with those obtained from Preston tube measurements and hence justify its use.

For the evaluation of the local total pressure, two different sizes of the pitot tubes (one of .028 inch outside diameter with 0.6 diameter ratio, and the other .065 inch in outside diameter with .07 diameter ratio) are used. Both are approximately 1.5 inches in length.

Measurements of the total pressure near the wall are carried out at five tangential locations, $x/c = 0.1$, 0.25, 0.5, 0.75, and 0.9 on both leading and trailing surfaces of the blade. At each tangential location measurements are carried out at four radial positions, $r = 11$, 13, 15, and 17 inches. The tip of the pitot tube is placed flush to the blade surface approximately 1/8 inch upstream of the blade static pressure hole aligned in the direction of the measured limiting stream-line angle. The other end of the tube is connected with a plastic tube to the pressure transfer device through the hole on the hub and the total pressure is recorded by the manometer. Using the blade static pressure, the local dynamic pressure is obtained. Following the calibration procedure given by Patel (40), the local dynamic pressure is related to the wall shear stress.

All measurements at open throttle are carried out using both tubes, and the results are compared. They are shown in Figure 17. It is seen that the two probes give almost identical values indicating that the diameter of the tube does not affect the calculated value of shear stress. All the subsequent measurements are therefore performed using a 0.065 inch diameter Preston tube.

4.5 Mean Velocity Components

Both three hole disk and the triple sensor hotwire rotating probes described in Chapter III are used for the measurement of mean velocity components. In the case of open throttle, only the disk probe is used. For the throttled case with large pressure gradients, a hotwire probe is used at all the measuring stations and the disk probe is used only at $x/c = 0.9$ to compare the two methods of measurement.

In Case I (Open Throttle) the mean flow velocity profiles inside the rotor blade passage are obtained by measuring total pressure and the radial flow angle (α) with the three hole disk probe. Measuring grid is 5 x 5 x 40 in tangential, radial, and blade to blade directions respectively.

The chordwise velocity component u (parallel to the blade surface) and the radial velocity component w (cross flow) are:

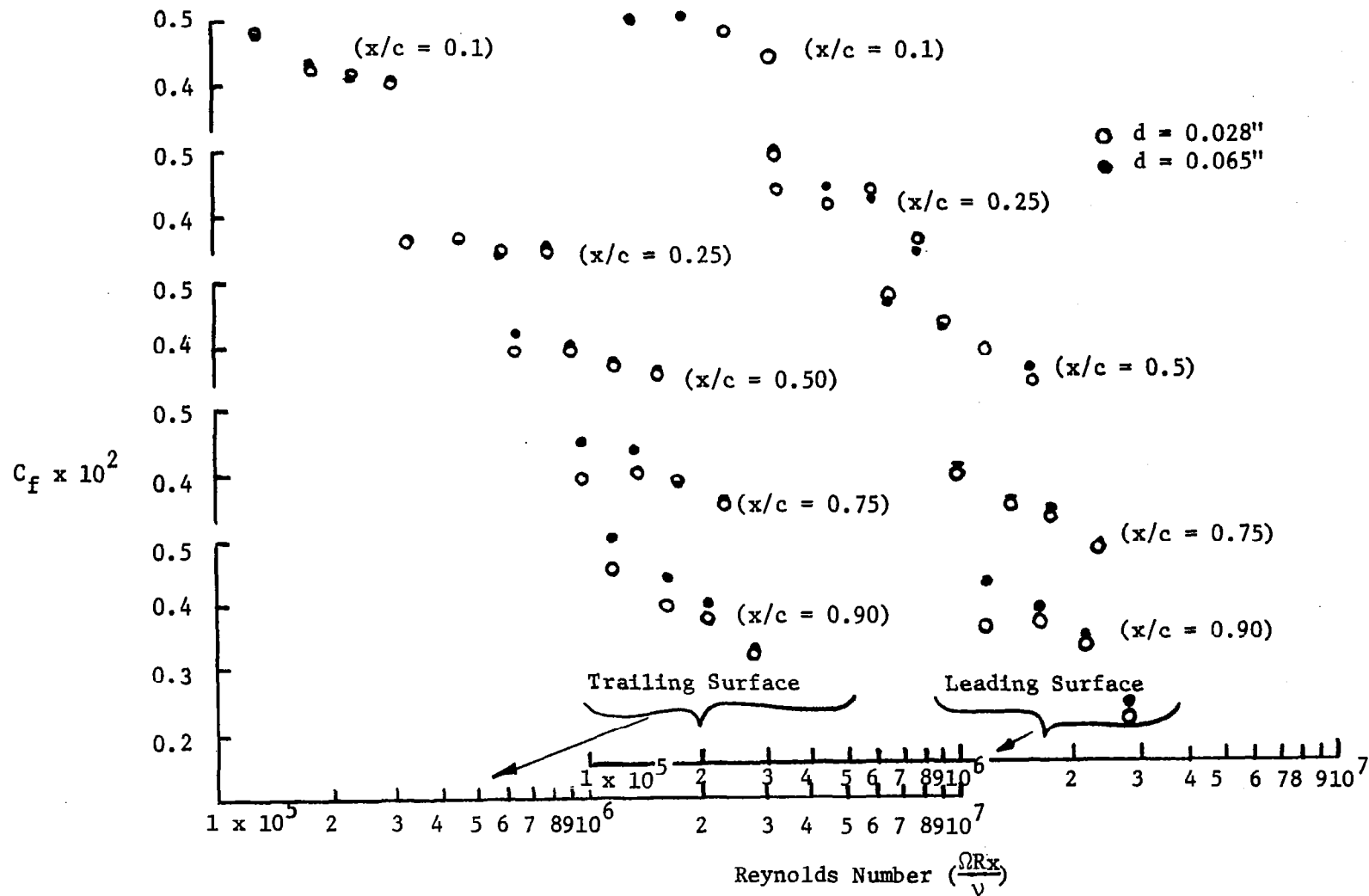$$\frac{u}{U_{bt}} = \sqrt{\frac{(P_o - p)}{\frac{1}{2} \rho U^2_{bt}}} \; \cos \alpha$$

and

Figure 17. Radial and Chordwise Distribution of Skin Friction Coefficient (C_f) on Leading and Trailing Surfaces of Flat Plate Inducer Described in Section 3.1 (Open Throttle).

75

$$\frac{w}{U_{bt}} = \sqrt{\frac{(p_o - p)}{\frac{1}{2}\rho U^2_{bt}}} \ \sin \alpha \qquad (98)$$

where U_{bt} is the blade speed at the tip and p is the static pressure interpolated linearly from the blade static pressure measurements.

For the throttled case, all the three mean velocity components u, v, and w are obtained by using the three sensor boundary layer hotwire probe described in Chapter III. The measured output voltages of the three channel hotwire anemometer, used in the hotwire setup (Figure 15) are solved numerically for the mean velocity components u, v, and w using the appropriate calibration curves and the constitutive equations of the hotwires. The equations and the detailed method of solution is given by Gorton (23). The method essentially relates the actual flow velocity components to the total effective cooling velocity on a finite heated wire in an arbitrary orientation of axes. The effective cooling velocity is further related to output voltage of the anemometer through the use of King's (41) Law. The equations of mean velocity components may be written in matrix form as:

$$\{Q_{\ell n}\}_{(3,N)} = \{\alpha_{\ell i}\}_{(3,3)} \ x \ \{u_{in}\}_{(3,N)} + \{\beta_{\ell i j}\}_{(3,3)} \ x \ \{\frac{u_{in} u_{jn}}{u_{1n}}\}_{(3,N)} \qquad (99)$$

and

$$\{E^2_{\ell n}\}_{(3,N)} = \{E^2_{o\ell}\}_{(3,N)} + \{B_\ell(n)\}_{(1,3)} \ x \ \{\sqrt{Q_{\ell n}}\}_{(3,N)} \qquad (100)$$

where, subscripts ℓ, n, and i denote the wire, the observation point and the velocity component in the reference coordinate system respectively. u_{1n} is the principal component of flow velocity, which in the present

76

coordinate system is in the streamwise direction x. $\alpha_{\ell i}$ and $\beta_{\ell i j}$ are functions of direction cosines of the ℓth wire which includes the correction factor for deviation from the Cosine Law (k_1). E_o is the output D.C. voltage at zero flow velocity, $E_{\ell n}$, $B_{\ell}(n)$ and $Q_{\ell n}$ are the measured values of voltage, slope of the hotwire calibration curve and effective mean cooling velocity for the ℓ wire and at nth observation point. u_i is the mean velocity component (e.g. u, v, w). The numbers in parenthesis outside of a matrix represent its dimensions, e.g. $\{Q_{\ell n}\}_{(3,N)}$ is a matrix with three rows and N columns. N is the total number of observation points in a measuring set. Indices i, j, ℓ can take values 1, 2, and 3. α_{11}, α_{12}, α_{13} correspond to Gorton's terms a_5, a_6, and a_7 for $\ell = 1$ and $\beta_{22} = a_8$, $\beta_{33} = a_9$ and $\beta_{23} = a_{10}$. All other coefficients are zero. The values of functions $\alpha_{\ell i}$ and $\beta_{\ell i j}$ for the hotwire probe used in all measurements, are given in Appendix A.

The computer program of Gorton (23), valid for a three sensor hotwire probe in a generalized non-orthogonal coordinate system is used. The program is modified to incorporate the following corrections to the hotwire data. The correction for deviation from the Cosine Law has already been included by Gorton (23).

1. Effect of changes in ambient fluid temperature during the course of the experiment and in calibration: The ambient temperature drifts as much as $10^{\circ}F$ in a measuring set and significantly affects the hotwire measurements. The hotwire equations are modified to include this correction as described in Appendix B.

2. Effect of finite distances between three wires in a non-uniform flow: This effect is due to spatial resolution of the probe and can be quite significant in non-uniform flows, such as boundary layers and

wakes. Since the measurements have been done at more than one location in a traverse, this correction is incorporated by interpolating measurements from adjacent points.

3. Effect of the variation of the slope of the calibration curve due to the deviation of hotwire equations from King's Law: The hotwire output voltage does not follow King's Law exactly i.e. the slope of the calibration curve is not constant with effective cooling velocity but varies according to the magnitude of cooling velocity. Since the calibration is performed over the entire range of effective cooling velocity anticipated in the measurements (0-80 ft/sec) this correction is incorporated by using the local slope, corresponding to the effective cooling velocity of a hotwire at any observation point.

4. Effect of probe slip-ring contact resistance: It is small but can be incorporated if the anemometer output D.C. voltage is known at zero velocity, with and without the probe slip-ring contact resistance. The hotwire constants of King's Law are modified by a factor $(E_{02}/E_{01})^2$, where E_{02} and E_{01} are D.C. output voltages of the anemometer at zero velocity, with and without the probe slip-ring contact resistance.

5. Effect of the deterioration of the wires due to oxidation and prolonged use: This error can be made very small by operating the wire at optimum overheat ratio. An overheat ratio of 0.8 suggested by Wyngaard and Lumley (42) for velocity measurements is used. The wires are calibrated before and after each set. The variations in constants of the hotwire equations is found to be negligible.

6. Effect of misalignment of the probe in the reference direction (x): This error is due to inaccuracy in aligning the probe in the reference direction. For boundary layer flows, this error can be

minimized by using the well known fact that the velocity normal to the surface is very small and goes to zero at the surface. The reference axis is shifted by a small angle such that this velocity goes to zero for measurements nearest to the surface.

A detailed discussion of these and other errors in hotwire measurements is given in Appendix B. In addition the computation time was improved by a factor of 10, by improving the convergency rate and optimizing the calculation procedure.

4.6 Turbulence Intensity and Shear Stress Components

All the six components of Reynolds stress tensor $(\overline{u_i' u_j'})$ at any point in the rotor passage in the rotating coordinate system (x, y, r) are obtained from the six measured values of the fluctuating voltage correlations $\overline{e_i e_j}$ and the three mean D.C. voltages E_i, (i, j = 1 to 3), using the computer program of Gorton (23). The fluctuating component of effective cooling velocity q_ℓ for ℓth wire at nth data point may be written as:

$$\{q_{\ell n}\}_{(3,N)} = (\alpha_{\ell i} + \Gamma_{\ell i j} \frac{u_{jn}}{u_{1n}})_{(3,3)} u_{in}'_{(3,N)} + \{\beta_{\ell i j}\}_{(3,3)} (\frac{u_{in}' u_{jn}'}{u_{1n}} - \frac{\overline{u_{in}' u_{jn}'}}{u_{1n}})_{(3,N)}$$

$$(101)$$

The coefficients $\alpha_{\ell i}$ and $\beta_{\ell i j}$ are same as occurring in Equation (99) for mean effective cooling velocity Q. The corresponding coefficients $\{\Gamma_{\ell i j}\}$, for $\ell = 1$ in Gorton's form are given by

$\Gamma_{22} = a_{11}$, $\Gamma_{33} = a_{12}$, $\Gamma_{23} = \Gamma_{32} = a_{13}$ and all other Γ's are zero.

The coefficients of the first term can be symbolically expressed as,

$$\alpha_{\ell i} + \Gamma_{\ell i j} \frac{u_{j n}}{u_{i n}} = \gamma_{\ell i} \quad \text{(summation of j is implied)} \tag{102}$$

Neglecting the last term in Equation (101) which is of second order, the matrix equation for Reynolds stress components is:

$$\{\overline{q_{\ell n} q_{mn}}\}_{(6,N)} = \{\gamma_{\ell i} \gamma_{mj}\}_{(3,6)} \times \{\overline{u'_{in} u'_{jn}}\}_{(6,N)} \tag{103}$$

where quantity $(q_{\ell n} q_{mn})$ is the correlation between fluctuating cooling velocities of ℓth and mth wires at nth observation point and is related to output a.c. and d.c. voltages as follows:

$$(\overline{q_{\ell n} q_{mn}}) = \frac{16 \; \overline{E_{\ell n}} \; \overline{E_{mn}}}{B_\ell(n) B_m(n)} \sqrt{Q_{\ell n} \; Q_{mn}} \; (\overline{e_{\ell n} e_{mn}}) \tag{104}$$

The quantities $\overline{E_{\ell n}}$, $B_\ell(n)$ and $Q_{\ell n}$ etc. are respectively mean D.C. voltage, slope and mean effective cooling velocity of the ℓth wire at the nth data point and N is the total number of data points in a measuring set.

The matrix Equations (99), (100), (103), and (104) are solved successively using the known values of voltages and calibration data, by using Newton-Raphson convergency scheme as described by Gorton (23) until the convergency criteria given below is reached.

$$\left| u_i^{(p)} - u_i^{(p-1)} \right| \leq 0.005 \; U_{bt} \tag{105}$$

where $u_i^{(p)}$ and $u_i^{(p-1)}$ are values of a mean velocity component u_i at pth and (p-1)th iteration respectively and U_{bt} is the peripheral velocity of the rotor blade at the tip.

4.7 Spectrum of Turbulent Stress Correlations

The spectrum of a Reynolds stress is defined as

$$\overline{u_i' u_j'} = \int_{-\infty}^{+\infty} Co(\omega) \, d\omega \qquad (106)$$

where ω is the filtering frequency and $Co(\omega)$ is the amplitude of
Reynolds stress at that frequency. It is therefore a measure of the
contribution of various frequencies to the correlation and can also be
used to check the contribution due to any spurious signal such as those
caused by variation in main line frequency, probe variation, etc. The
spectrum of all components of stress tensor $\overline{u_i' u_j'}$ are obtained by
using the Hewlett Packard 302A Wave Analyzer and Balantyne Mean Square
Meter in the hotwire set up (Figure 11). The spectrum in wave number
space ($\kappa = 2\pi\omega/U$) is given by

$$\overline{u_i' u_j'} = \int_{-\infty}^{+\infty} \phi(\kappa) \, d\kappa \qquad (107)$$

where $\phi(\kappa)$ is related to the measured $Co(\omega)$ by

$$\phi(\kappa) = (U/2\pi) \, Co(\omega) \qquad (108)$$

U is the total mean velocity of the flow in the reference coordinate
system (x, y, r).

The experimental value of Cospectrum at any frequency is obtained
by filtering both u_i' and u_j' at the same frequency, multiplying and
averaging to give (Margolis (43)),

$$\left| \overline{u_i' u_j'} \right|_{\omega} = \phi_{ij}(\omega) \, d\omega \qquad (109)$$

where $\phi_{ij}(\omega)$ is the amplitude of the spectrum given in general by

$$\phi_{ij}(\omega) = Co_{ij}(\omega) - i \, Q_{ij}(\omega), \text{ where } i = \sqrt{-1} \qquad (110)$$

Co_{ij} is therefore the real part of the spectrum and the imaginary part Q_{ij} is called the quadrature spectrum. Since the time delay in u_i' and u_j' is zero in the present case, $Q_{ij} = 0$, therefore,

$$\phi_{ij}(\omega) = Co_{ij}(\omega) = \text{Measured Amplitude of } \phi \text{ at } \omega. \qquad (111)$$

$\phi_{ij}(\omega)$ is calculated from the corresponding output voltages $(\overline{e_i e_j})$ filtered and integrated at various frequencies, using equations (109) and (99) to (104) as described in Section 4.6 for the measurement of Reynolds stresses. The same computer program can therefore be used to obtain the spectrum of all turbulence quantities $(\overline{u_i' u_j'})$.

The spectral measurements are carried out only at midchord and at a radius of 17.25 inches. The main objective of the spectral measurements is to detect if there is any contribution to the electrical output signals from the spurious signals such as line frequency, blade passing frequency and its harmonics, natural frequency of the probe, etc. It is also required for the determination of the cutoff frequency (so as to eliminate contribution from the electrical noise above that frequency) of the filtering circuit in the hotwire set up (Figure 11). It is found from the spectral measurements reported in Chapter V that there is no significant contribution to the hotwire output signals from the above mentioned spurious electrical signals.

V. EXPERIMENTAL RESULTS AND COMPARISON WITH PREDICTIONS
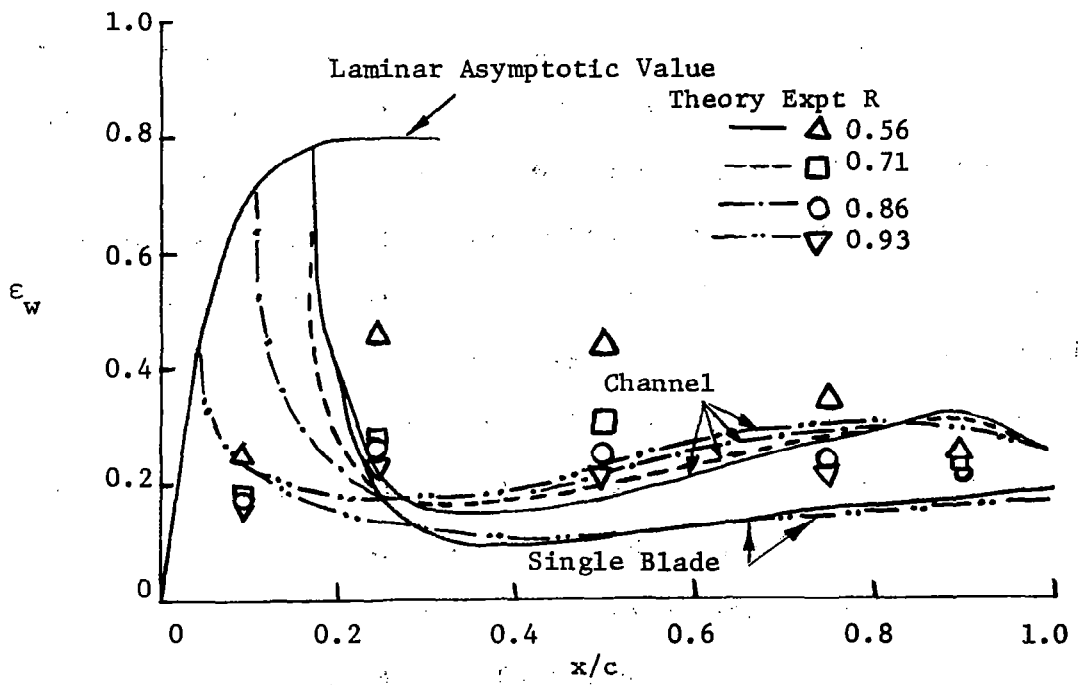
5.1 Data Without Throttle

The experimental data is first obtained by operating the rotor
at the maximum flow rate, i.e. without using a throttle at the exit.
The flow in the rotor channel, therefore experiences only small pressure
gradients and the major effects of rotation can be studied. The
limiting streamline angle, blade static pressure and skin friction
coefficient are measured both on leading and trailing blade surfaces.
The mean velocity profiles are measured inside the rotor channel in a
measuring grid of 5 x 5 x 40 in chordwise (x), radial (r) and blade to
blade (y) directions respectively. For this case, only the mean
quantities which define the three-dimensional mean flow field have been
measured and are described below.

5.1.1 The limiting Streamline Angle.

Radial variation of the limiting streamline angle is shown in
Figure 18 for various chordwise locations. It is seen that, except near
the trailing edge, the limiting streamline angle on the leading blade
surface behaves quite differently from that on the trailing blade
surface. It is interesting to note that at x/c = 0.1, the limiting
streamline angles on the leading surface is nearly twice the value on
the trailing surface. As x increases, this trend reverses itself, and
at x/c = 0.5, the limiting streamline angle on the leading surface
becomes smaller than that on the trailing surface. The flow is laminar
for x/c < 0.1, where the limiting streamline angles are larger than the
turbulent region (x/c > 0.1). The limiting streamline angles are

83

Laminar Asymptotic Value

Theory	Expt	R
——	▲	0.56
– – –	■	0.71
– · – ·	●	0.86
– · · – ·	▼	0.93

Channel

Single Blade

ε_w

x/c

(a) Leading Side

Laminar Asymptotic Value

Theory	Expt	R
——	△	0.56
– – –	□	0.71
– · –	○	0.86
– · · –	▽	0.93

Channel

Single Blade

ε_w

x/c
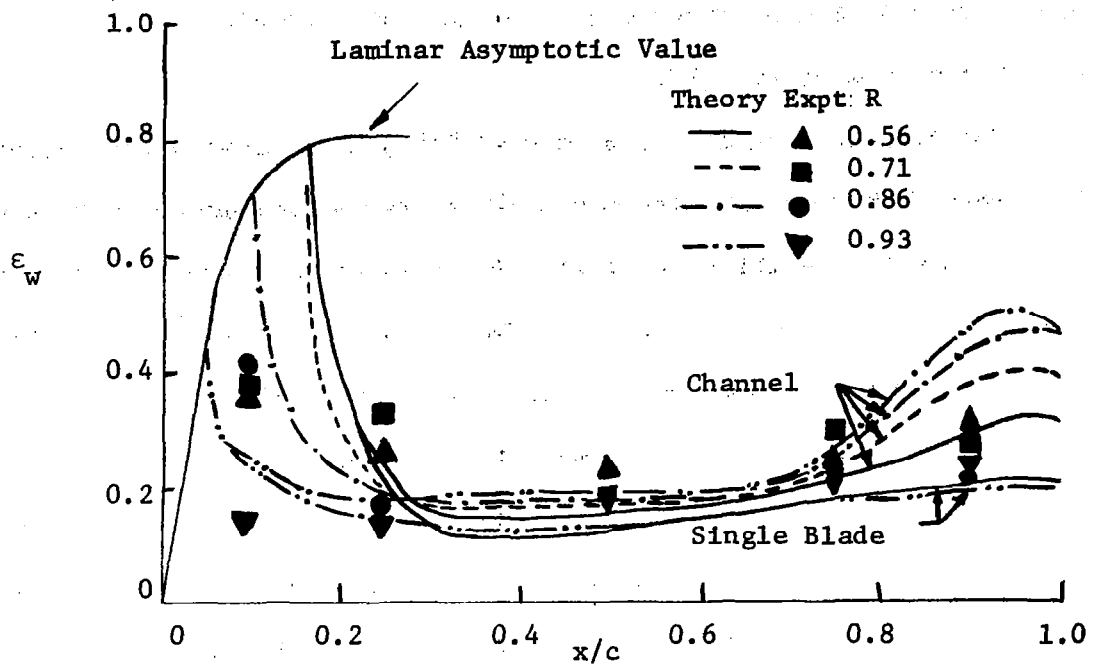
(b) Trailing Side

Figure 18. Radial and Chordwise Distribution of the Limiting
Streamline Angle (Open Throttle).

generally higher than those for a single blade reported by Lakshminarayana et al. (17).

The chordwise variation of the limiting streamline angle (Figure 18) shows that near the tip, the limiting streamline angle increases as x increases on the trailing surface while it takes a nearly constant value on the leading surface. For the radial distance less than 16 inches, the behavior of the limiting streamline angle is different from that very near the tip. As x increases, ε_ω increases to reach a maximum value and then decreases on the trailing surface. This behavior is quite different from the behavior of the limiting streamline angle for a single rotating helical blade which showed that the limiting streamline angle increased monotonically with increase in x.

It must be pointed out here that for a single rotating helical blade the chordwise pressure gradient is zero, and the experimental investigation of Lakshminarayana et al. (17) showed this to be the case. For the present investigation, blade static pressure measurements (Figure 19) have shown that there exist pressure gradients, throughout the passage. It is interesting to note that the behavior of the limiting streamline angle is similar to the behavior of the blade static pressure. This can be seen when Figure 18 is compared with Figure 19. This may be interpreted as the indication that the limiting streamline angle is closely related to the blade static pressure distribution. Thus, in order to evaluate the limiting streamline angle it is necessary that the pressure gradients be known.
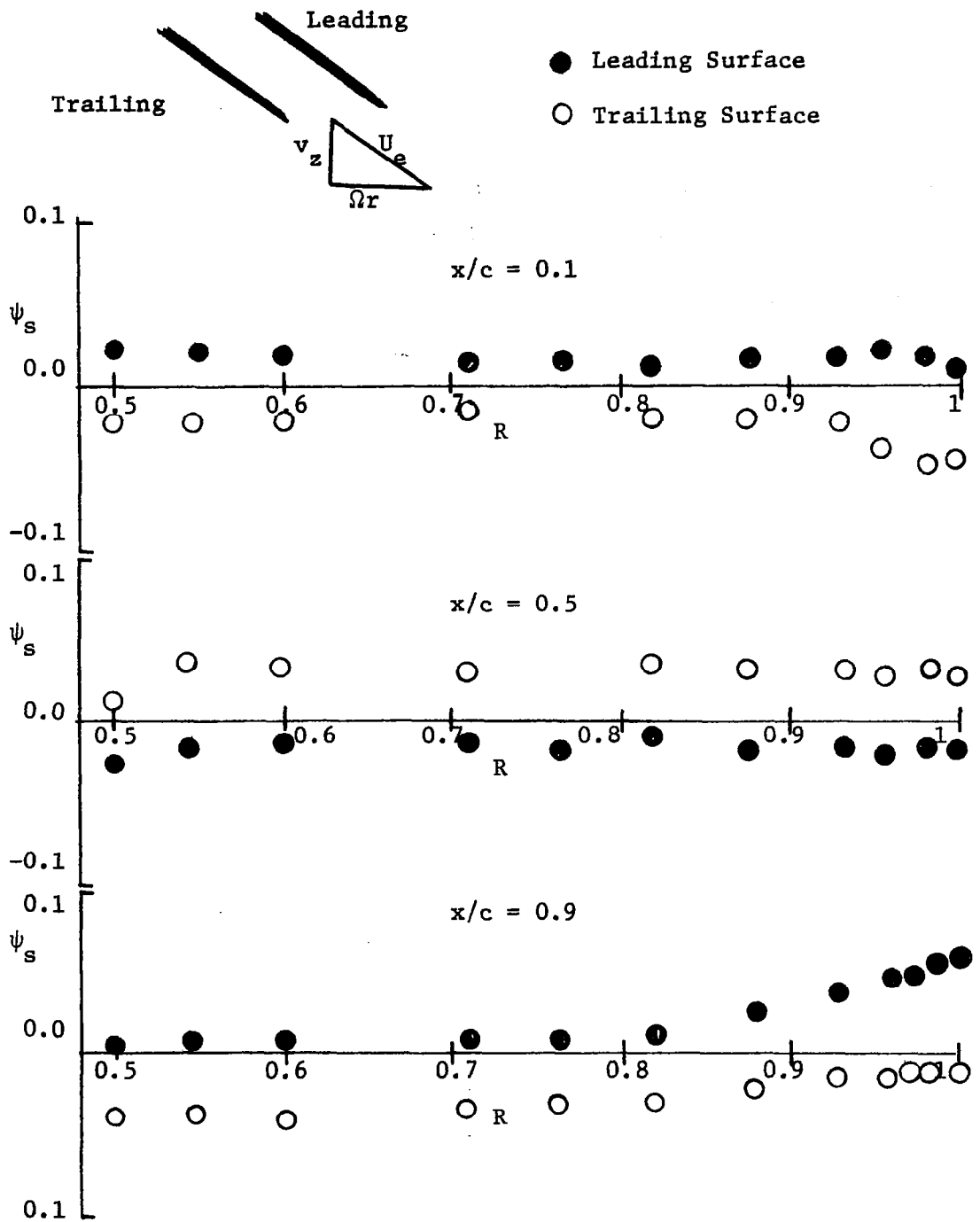
Figure 19. Radial and Chordwise Distribution of Blade Static Pressure Coefficient (Open Throttle).

5.1.2 Blade Static Pressures.

The blade static pressure measurements are carried out at 11 radii and at five chordwise locations, $x/c = 0.1$, 0.25, 0.5, 0.75, and 0.9 both on leading and trailing surfaces of the blade. The results are plotted in Figure 19 for $x/c = 0.1$, 0.5, and 0.9.

The radial variation of the blade static pressure coefficient at various chordwise locations shows that ψ_s takes nearly a constant value except near the tip where it changes considerably, especially near the trailing edge.

The chordwise variation of the blade static pressure coefficient shows that the static pressure distributions on the leading surface behaves quite differently compared to that on the trailing surface. While ψ_s takes the minimum value at the midchord location on the leading surface, it takes the maximum value on the trailing surface.

The existence of a finite loading on the blades can be explained on the basis of the fact that the boundary layers on the leading and trailing surfaces grow differentially giving rise to asymmetrical flow around the blade chord.

5.1.3 Skin Friction Coefficient

The skin friction coefficient is obtained from blade shear stress measurements carried out at five radii ($r = 11$, 13, 15, 17, and 18 inches) and on both surfaces. The five chordwise locations ($x/c = 0.1$, 0.3, 0.5, 0.7, and 0.9) both on leading and trailing blade surfaces are shown in Figure 17.

The skin friction coefficients derived from the velocity profile measurements reported in the next section, are plotted in Figure 20 in
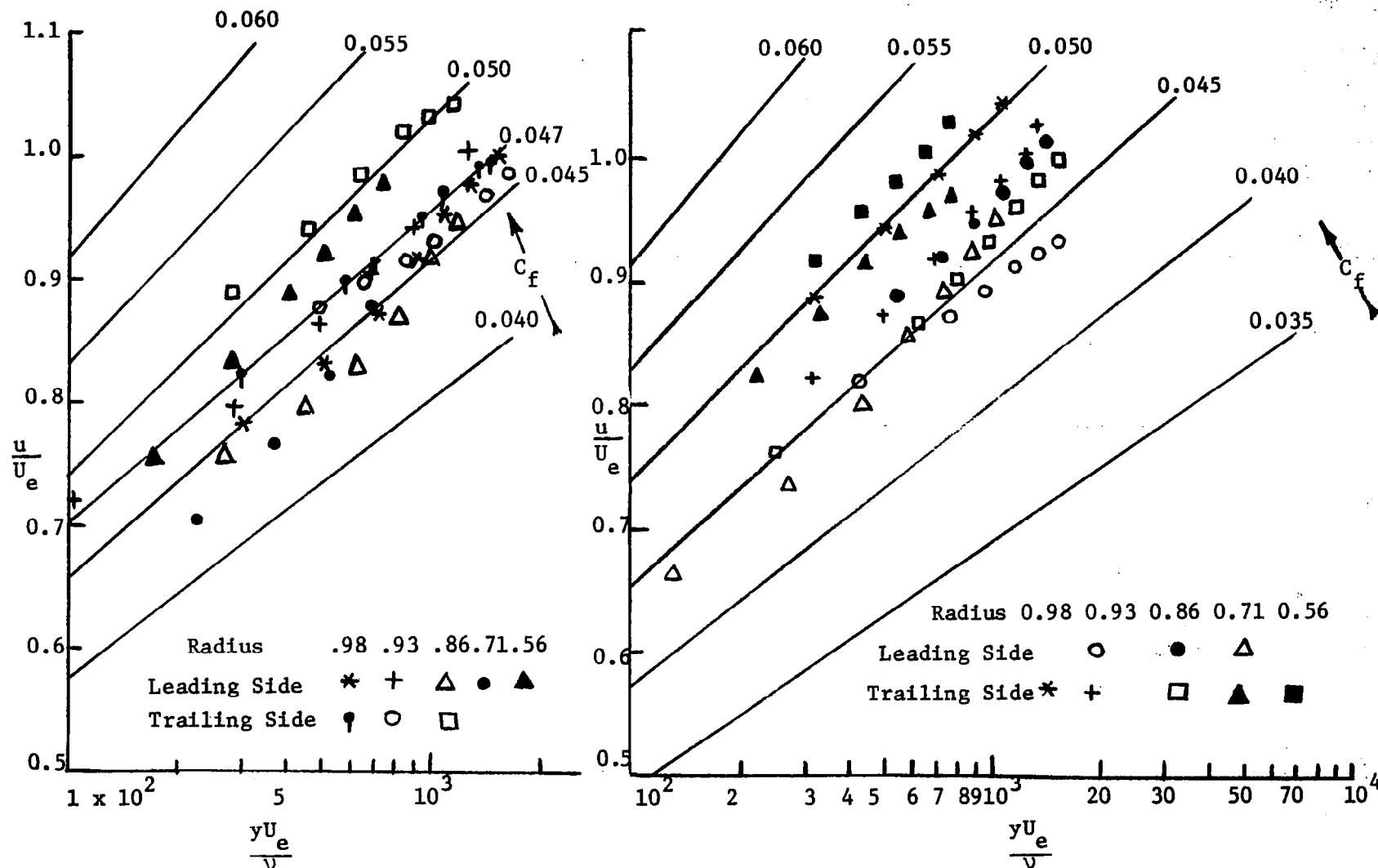
Figure 20. Clauser Plot of Velocity Profiles (Open Throttle).

88
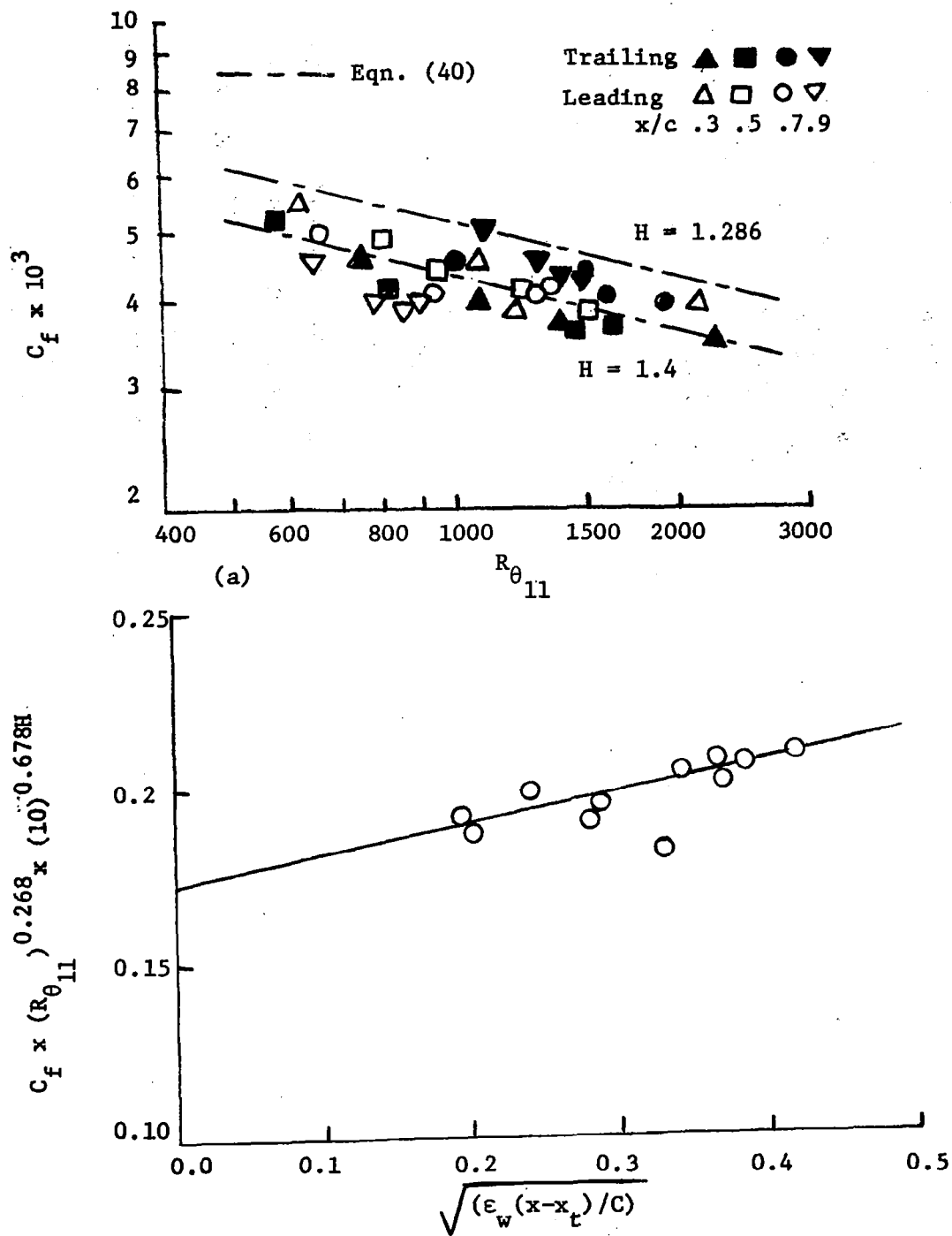
Figure 21. Skin Friction Correlation and Variation of Skin Friction in the Channel (Open Throttle).

Caluser Chart form i.e. u/u_e versus y^+ at $x/c = 0.3$ and 0.5. These values are in close agreement with the values derived from the direct measurements shown in Figure 17.

The skin friction coefficients are plotted as a function of Reynolds number based on local momentum thickness θ_{11} in Figure 21(a). The skin friction coefficient is found to decrease with Reynolds number $R_{\theta_{11}}$ as a power law of index (-0.268). Effect of the limiting streamline angle (ε_w) and the shape factor (H) is best represented by the expression

$$c_f \ \alpha \ (10)^{-0.678H} \quad (1+0.52 \ \sqrt{\varepsilon_w (x-x_c)/c} \ )$$

as shown in Figure 21. Thus the skin friction coefficient correlation for rotating turbulent boundary layers with mild pressure gradients are best represented by the following formula

$$c_f = 0.172 \ (R_{\theta_{11}})^{-0.268} \quad (10)^{-0.678H} \quad (1+0.52 \ \sqrt{\varepsilon_w (x-x_c)/c} \ ) \tag{112}$$

where

$$c_f = \tau_o/(1/2)\rho U_e^2 \ .$$

It should be noted that this correlation is similar to that of a single rotating disk of Lakshminarayana et al (17), where the effect of rotation parameter $(\varepsilon_w \ x/c)^{1/2}$ is discussed. The term in the bracket in Equation (112) represents the effect of three-dimensionality in the flow. It should be noted that this correlation is similar to Ludwig and Tillmann's (28) correlation for a stationary turbulent boundary layer with pressure gradients i.e.

$$c_f = 0.246 \quad (10)^{-0.678H} \quad (R_{\theta_{11}})^{-0.268} \tag{113}$$

90

Equation (112) has a different constant and an additional parameter $(1 + 0.52 \sqrt{\epsilon_w (x-x_t)/c})$. However, it should be noted that since θ_{11} is found to decrease appreciably in the rotating case due to an increased radial migration of the flow, $R_{\theta_{11}}$ is much less for the same free stream velocity U_e and the pressure gradients and therefore the effect of rotation is to increase the skin friction coefficient through a decrease of $R_{\theta_{11}}$ compared to the equivalent stationary case.

5.1.4 Mainstream Velocity Profile.

Figures 22-26 show the distribution of chordwise velocity component 'u' across the passage at various radial and chordwise locations. From the profile distribution at $x/c = 0.1$, it is evident that the flow has already become turbulent over most of the radial locations. The boundary layer is thicker on the trailing side (as much as one inch near the tip). This may be due to inlet flow incidence. The boundary layer is thin and laminar near the hub on the leading surface (at the hub, the Reynolds number based on the peripheral velocity, Ωr and distance from leading edge is approximately 0.8×10^5).

The profile distribution at subsequent downstream measuring stations, (Figures 23 - 26) shows that the boundary layer is turbulent at all the radial locations on both the surfaces and grows rapidly downstream. It should be remarked that the free stream velocity, unless the two boundary layers have merged is found to be the same as the blade speed (Ωr).

The boundary layers at the tip grow rapidly due to radial flow migration. Fully developed flow occurs at $x/c = 0.30$ for $R = 0.98$ and this region extends inward as the flow travels downstream. One of the
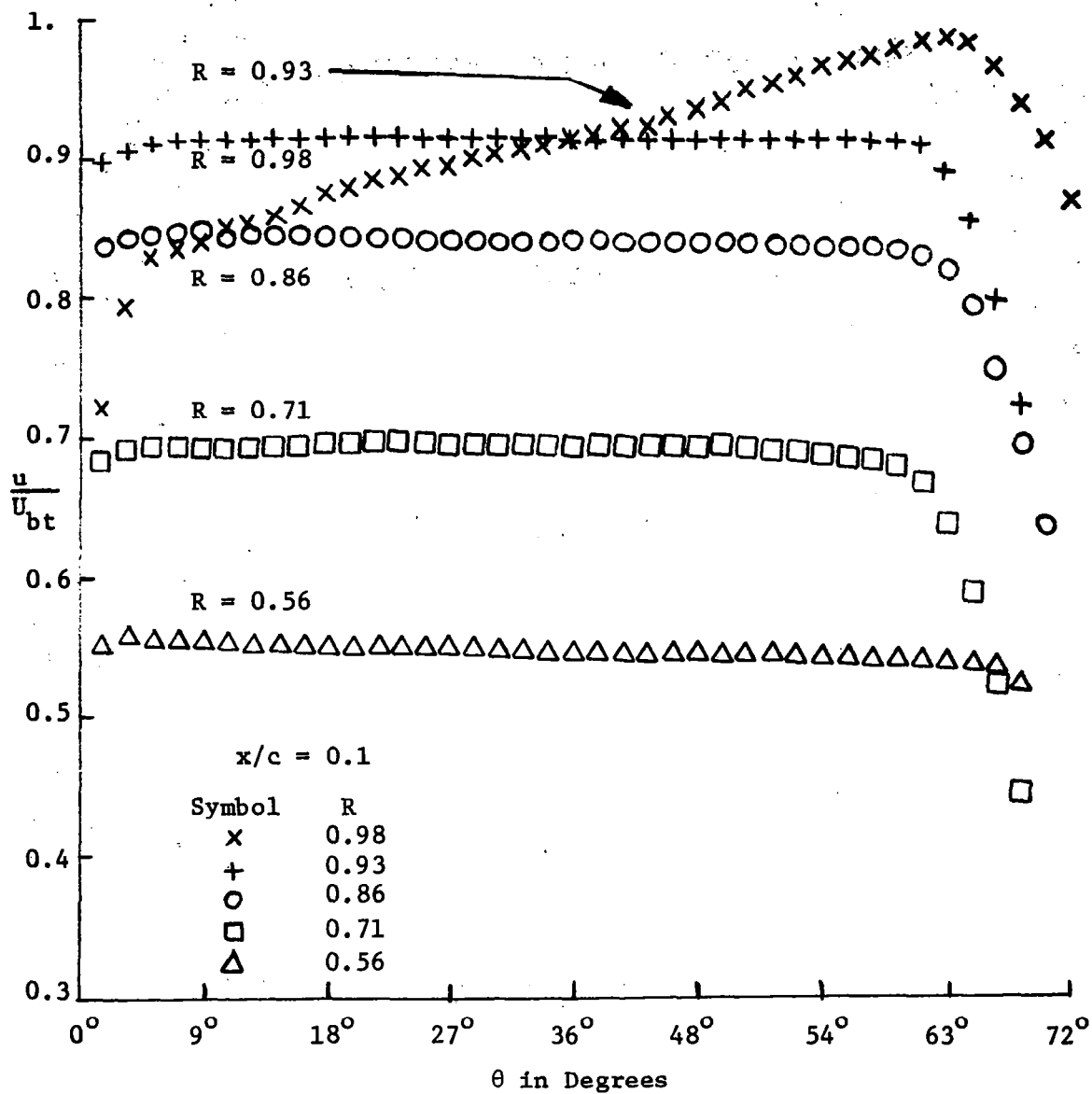
Figure 22. Blade to Blade Distribution of Streamwise
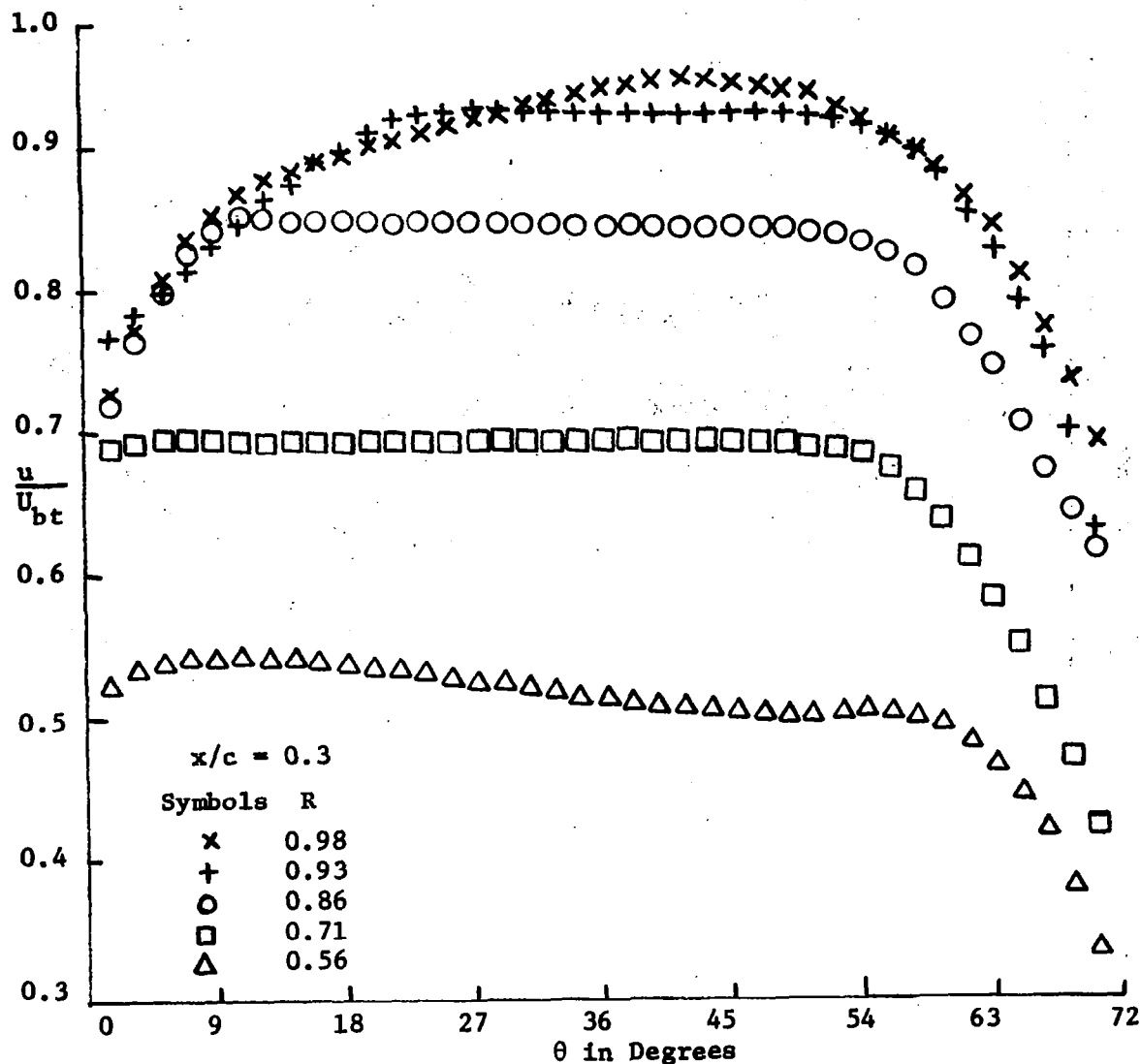Velocity Component at x/c = 0.1 (Open Throttle).

Figure 23.   Blade to Blade Distribution of Streamwise
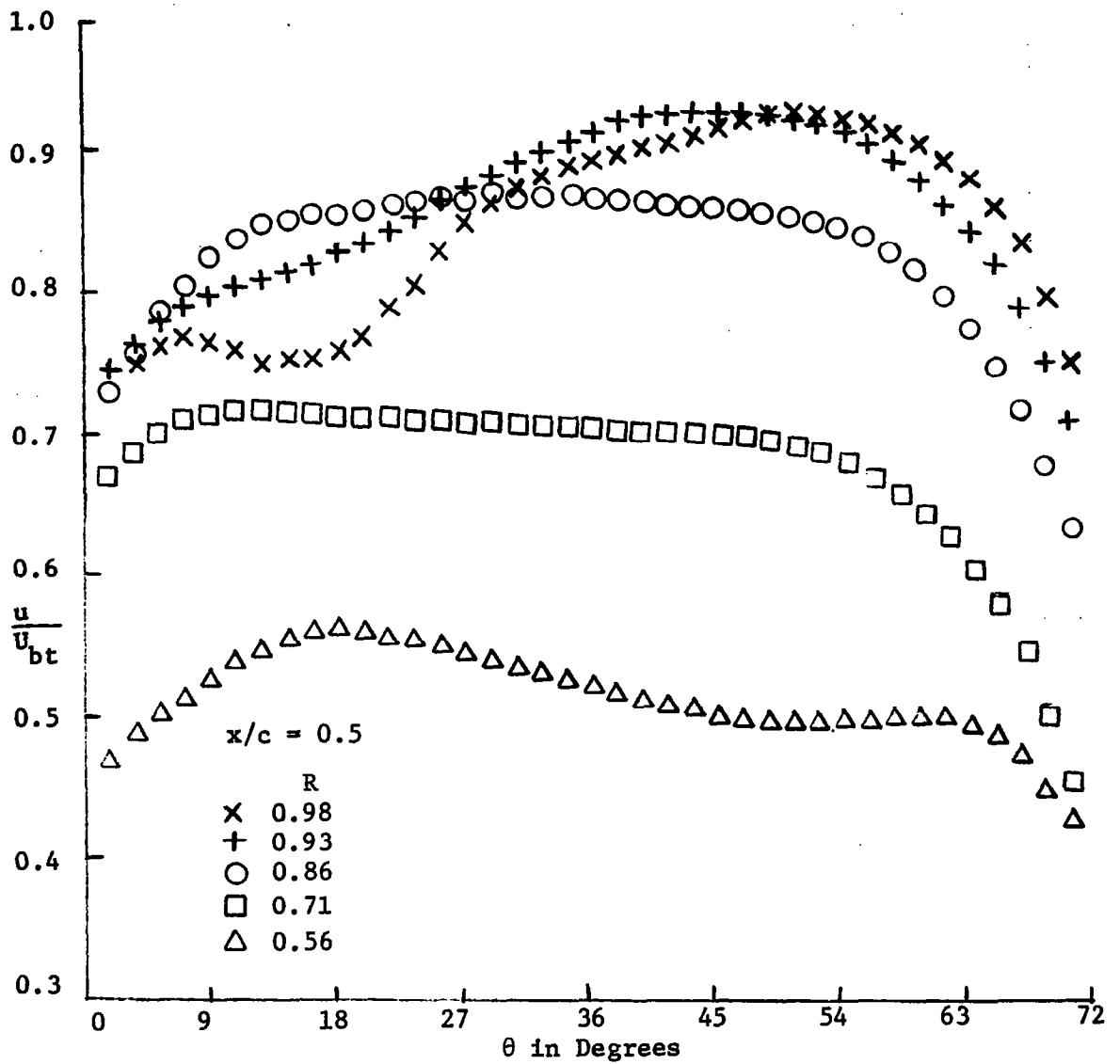Velocity Component at x/c = 0.3 (Open Throttle).

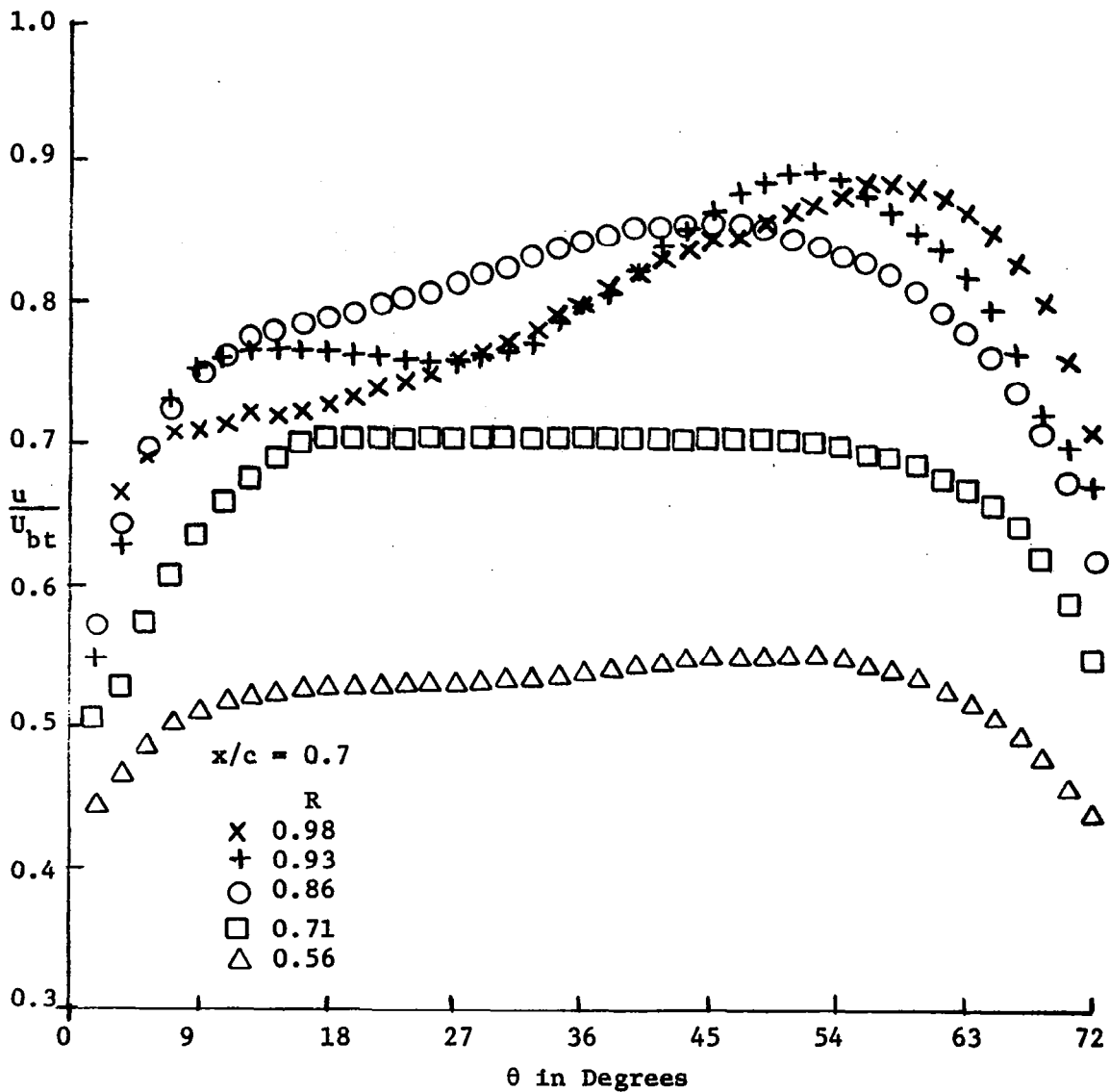Figure 24. Blade to Blade Distribution of Streamwise Velocity
Component at x/c = 0.5.

Figure 25. Blade to Blade Distribution of Streamwise
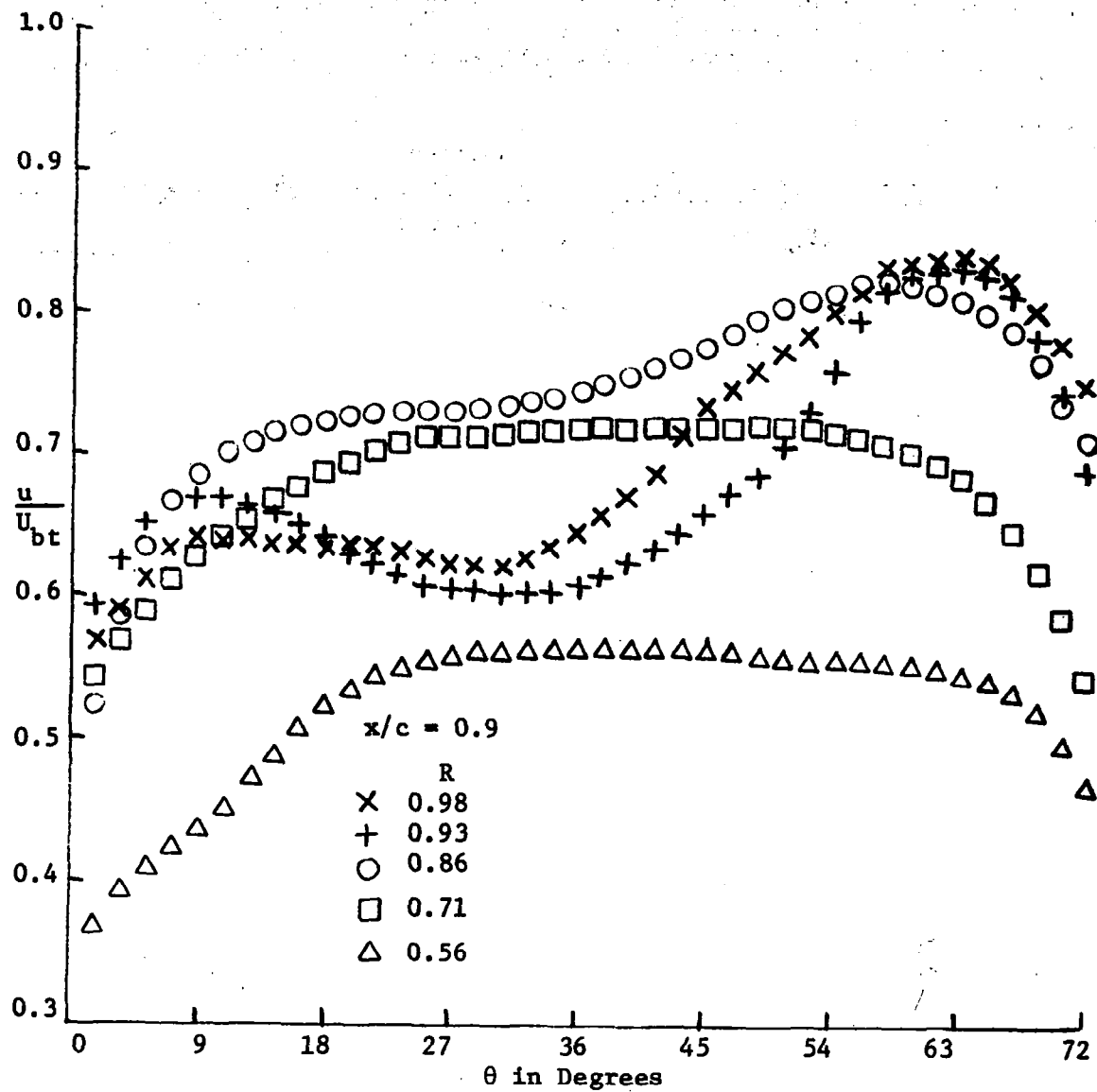Velocity Component at x/c = 0.7 (Open Throttle).

Figure 26. Blade to Blade Distribution of Streamwise
Velocity Component at x/c = 0.9 (Open Throttle).

unique features of the channel flow is the interference region, where the boundary layer profiles are unconventional. This can be discerned for x/c > 0.3, near the tip (Figure 26). A wake type of profile exists near the midpassage. As explained earlier in Chapter II, this is brought about mainly by the interaction of blade boundary layers and the annulus wall. The resulting inward flow near the midpassage (Figure 2) produces this type of profile. The inviscid flow region disappears and therefore no definite boundary layer characteristics can be obtained in terms of boundary layer thickness parameters (δ, δ_1^*, θ_{11}, H, etc.). It is obvious that in this region the momentum integral technique can only give a qualitative picture of the flow.

The boundary layer is generally thicker near the trailing surface except near the trailing edge (Figure 26).

5.1.5 Comparison with Power Law Profile.

In Figure 27, the mainstream velocity (u/U_e) is plotted against the nondimensional distance from the blade wall (y/δ). Comparing this with the Power Law profile of appropriate index ($u/U_e = (y/\delta)^{1/n}$) it appears that the experimental data fits this representation reasonably well. The agreement is poor near the tip because the boundary layer here is affected by the tip clearance and the annulus wall effects. The value of exponent varies from 1/6 to 1/11, except near the hub at x/c = 0.3 where the values are 1/4 and 1/5. Here the boundary layer appears to be in transition (Reynolds number based on peripheral velocity and distance from the leading edge is 3×10^5).

Comparison with Cole's Profile: In Figure 28, the mainstream velocity component u is plotted in the form of Cole's Law,
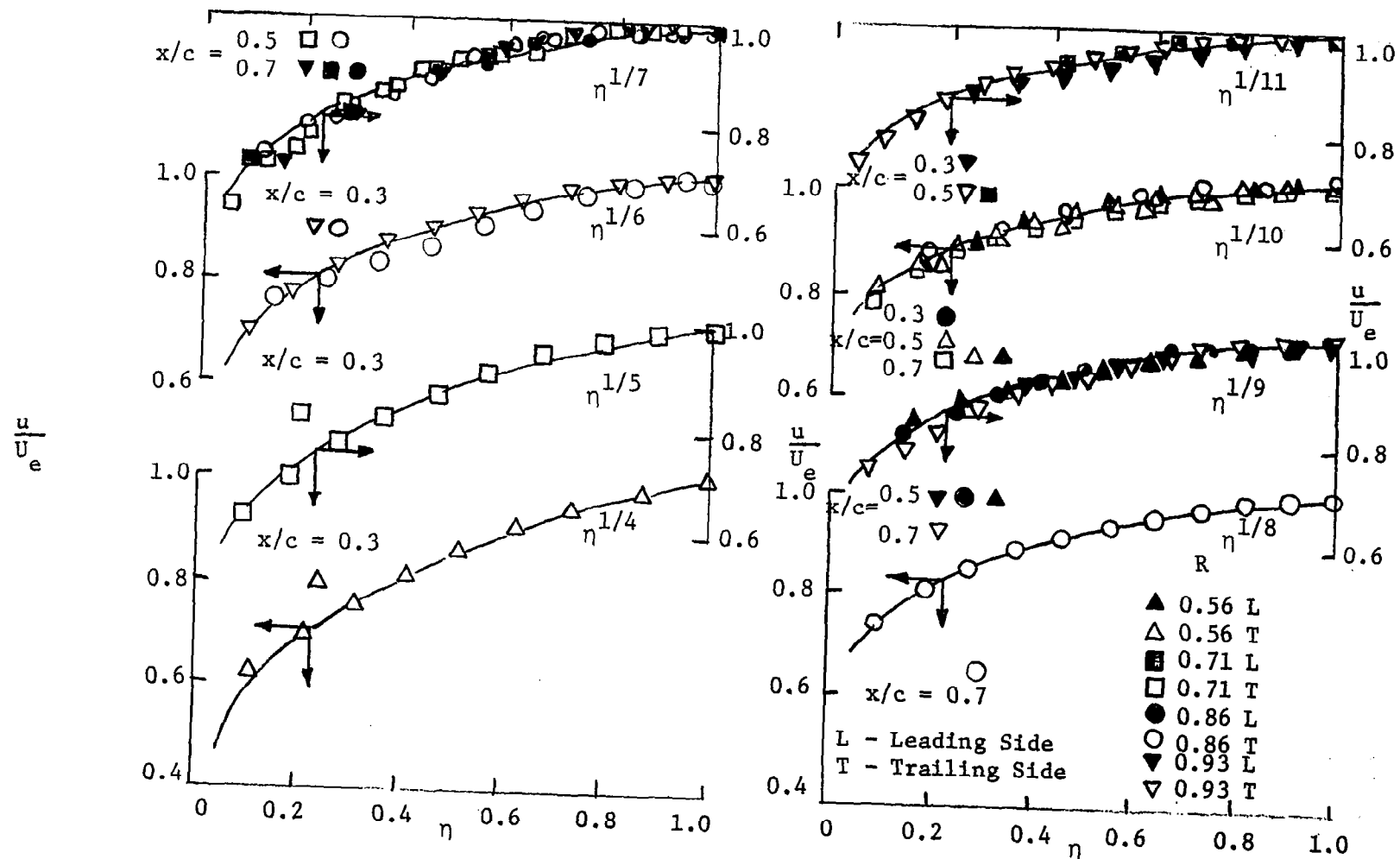
97

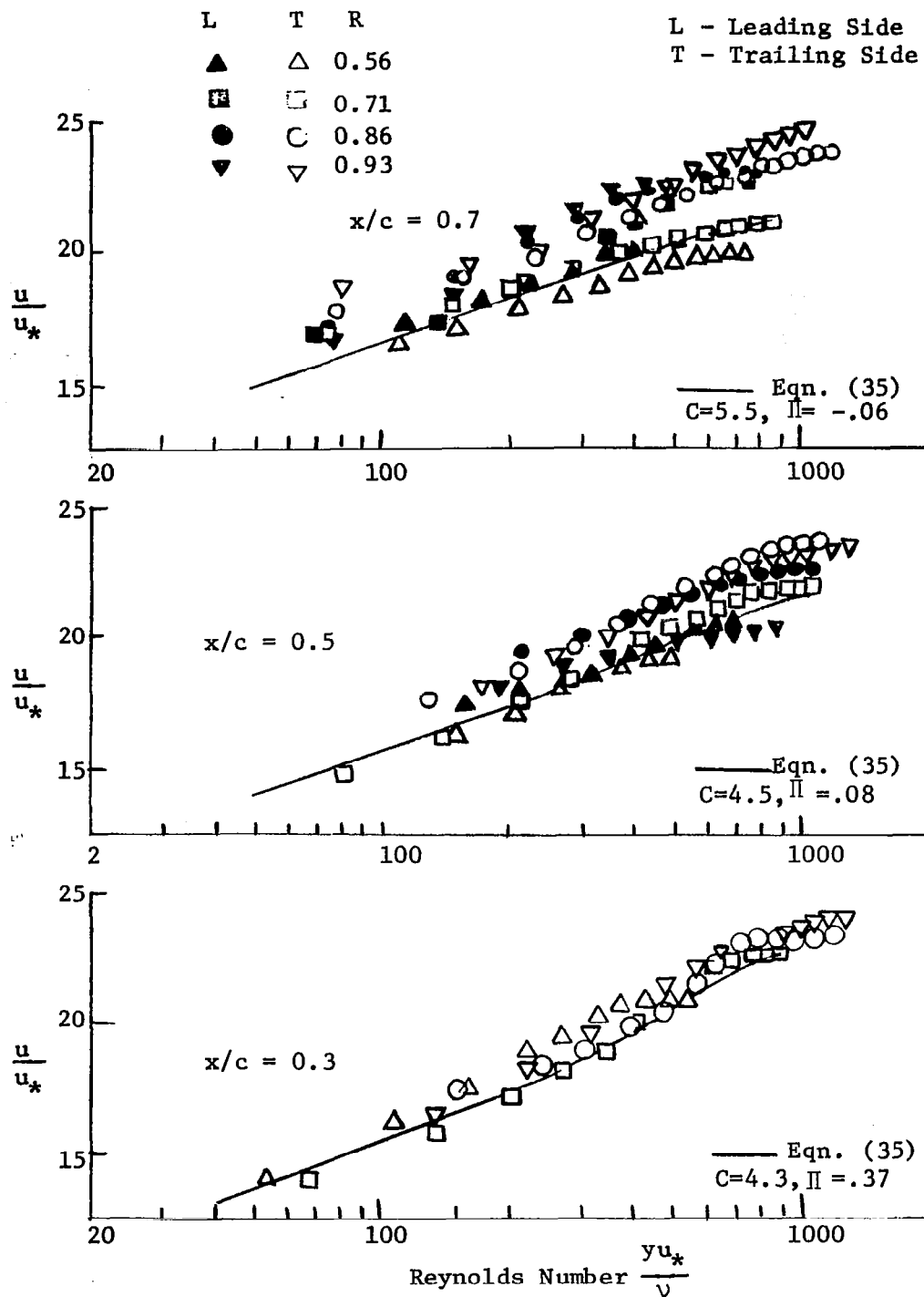Figure 27. Power Law Representation of Streamwise Velocity Component (Open Throttle).

Figure 28. Cole's Plot of Streamwise Velocity Component (Open Throttle).

$$u/u_* = 1/\kappa_1(\log(yu_*/\nu)+\pi\omega(y/\delta)) + C \qquad\qquad (114)$$

where u_* is the friction velocity, κ_1 is von Karman constant, ω is a wake function, π is a parameter to account for the effect of imposed pressure gradients, and C is a constant.

It is seen from the plots that there does exist a law of the wall region ($u/u_* = 1/\kappa \log yu_*/\nu + C$) up to $y^+ \leq 200$-300 depending upon the nature of the blade surface (trailing or leading) and the location of the measuring station. The mean value of constants in the law of the wall vary from $0.40 - 0.42$ for the slope constant κ and 4.5 to 5.5 for the constant C. The wake component $\omega(y/\delta)$ of the Cole's Law has a different form than the sinusoidal form for stationary two-dimensional flows. This may be due to the fact that the entrainment process, which is dominant in the outer part of the boundary layer, is different for the boundary layer on an enclosed rotating surface than for a stationary two-dimensional surface. Value of π which is characteristic of the imposed pressure gradients is found to vary from -0.25 to 0.55. It is positive on the trailing side and has a small negative value on the leading side of the blade. It decreases with x up to $x/c \leq 0.5$ and later increases slowly. This is in accordance with the trend of the observed blade static pressure distribution, as shown in Figure 19. The value of π increases with radius continuously in accordance with the radial pressure gradient.

Distribution of Passage Averaged Chordwise Velocity: In Figure 29 is shown the radial variation of mainstream velocity component averaged across the channel. The passage averaged value of $\bar{u}$ is found to be lower than the free stream velocity that exists in an inviscid flow
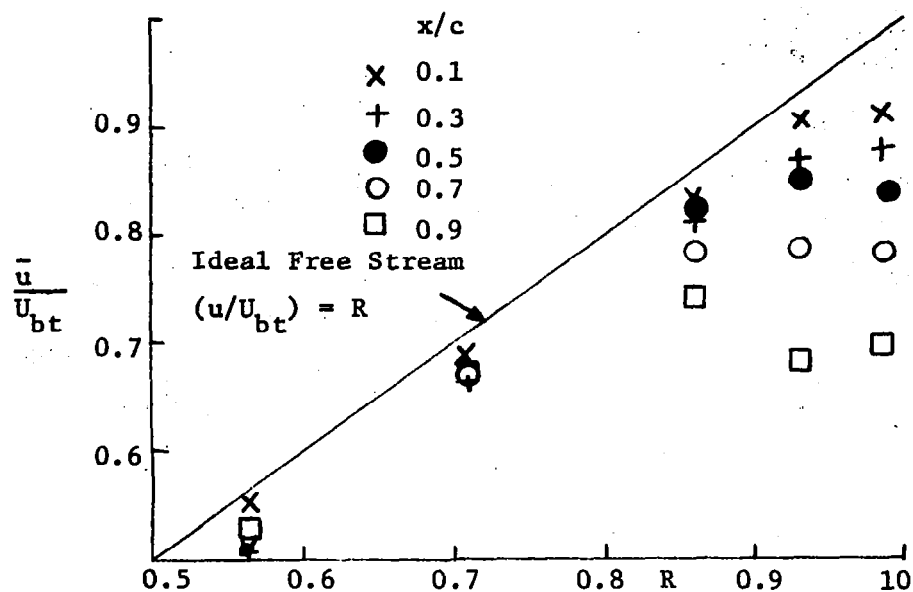
Figure 29. Radial and Chordwise Distribution of Passage Averaged
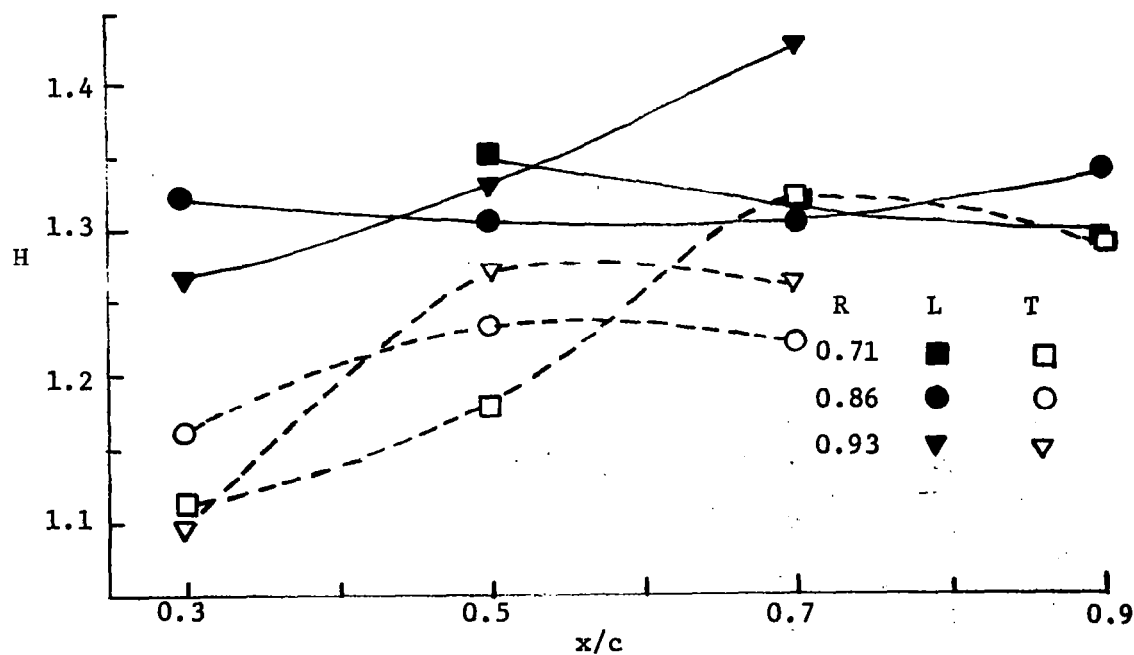Streamwise Velocity Component (Open Throttle).

Figure 30. Distribution of Shape Factor in the Rotating Channel
(Open Throttle).

$(u = \Omega r)$. The difference $(\Omega r - \bar{u})$ increases as the flow proceeds further downstream of the channel, especially after $x/c = 0.5$. The largest difference is near the tip where the two surface boundary layers have interacted with the annulus wall boundary layer, and for $x/c > 0.5$ it extends up to mid radius $(R \sim 0.8)$.

This large reduction in mainstream velocity near the tip is due to the mutual interference of the boundary layers on the two surfaces with the annulus wall boundary layer, which are now completely submerged into each other and is accompanied by radial inward flow in this region. This is in conformity with the increase in radial pressure gradients observed near the tip region. The value of shear stress is not negligible near the center of the passage and the turbulence level in this region is maintained at the expense of mainstream velocity gradient in the normal (y) direction. These results are confirmed by turbulent stress measurements reported in Section 5.3.5

Shape Factor (H): The chordwise distribution of shape factor H obtained from the measurements is plotted in Figure 30. The value of H is higher on the leading side (1.30 to 1.50) compared to that on the trailing side of the channel (1.10 to 1.30). It is nearly constant near the mid radius but changes rapidly at the hub and the tip due to the interference effects of the hub or annulus wall boundary layers. The value is more at higher radii due to larger radial pressure gradient. It should be remarked here that the measured values of H are only qualitative and are liable to some error (due to interpolation of velocity profiles near the blade surface to obtain H) particularly where the boundary layer is thin. Since this set of experimental data has been obtained by running the four-bladed channel at open throttle

and hence with mild pressure gradients, the above results show that it is valid to take H constant in x direction in predicting θ_{11} and ε_w in this case.

5.1.6 Radial Velocity Profile

Figures 31 and 32 show the observed radial velocity distribution across the blade passage. The radial velocity increases as the wall is approached. It should decrease very close to the wall, but since the measurements could not be taken for values of $y^+ < 100$ (due to finite size of the probe), only the outer region of the boundary layer flow has been scanned. Near the centerline of the channel, the radial velocity is small (~ 1 ft/sec) and is within the experimental error (± 1 ft/sec), except near the tip. The radial inward flow is observed near the tip for $x/c > 0.3$. The radial outward flow region is confined to blade boundary layers, being larger near the trailing surface for $x/c < 0.5$. For $x/c > 0.5$, the leading surface boundary layer has larger radial outward component. It is clear that the radial flows are appreciable in the rotating blade channel and are higher than those of a single rotating blade reported by Lakshminarayana et al. (17).

The observed radial velocity component w is plotted in Figure 33 as streamline parameter ε (local radial to mainstream velocity ratio) normalized by the local measured streamline angle (ε_w), i.e. $\varepsilon/\varepsilon_w$, versus nondimensional distance from the wall (y/δ). Measurements near the outer edge of the boundary layer where the radial velocities are of the same order as the experimental error (~ 1 ft/sec) are not shown for clarity. A comparison with Mager's profile (Equation 74) indicates that the experimental data fits this form quite well except near the hub or
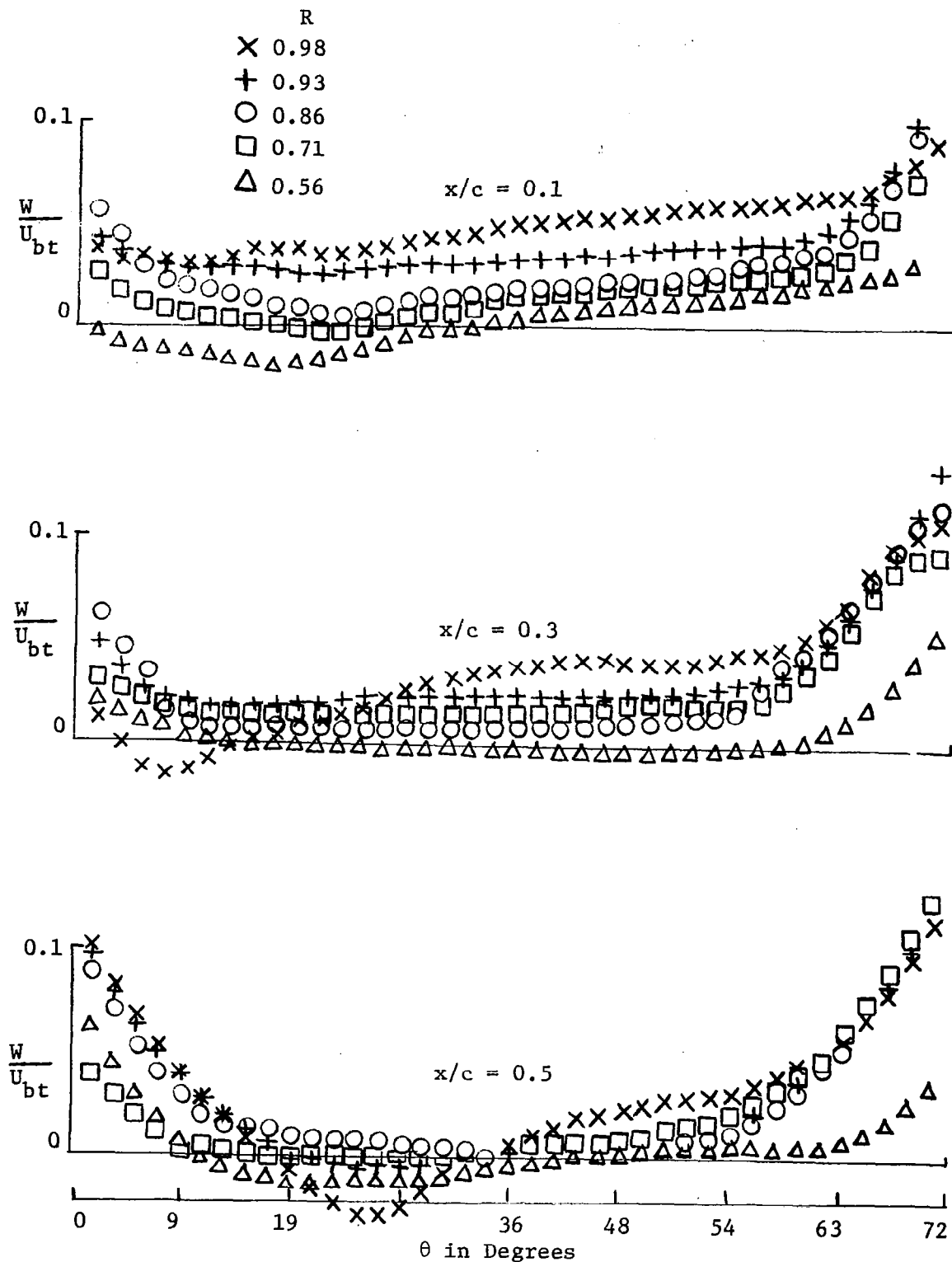
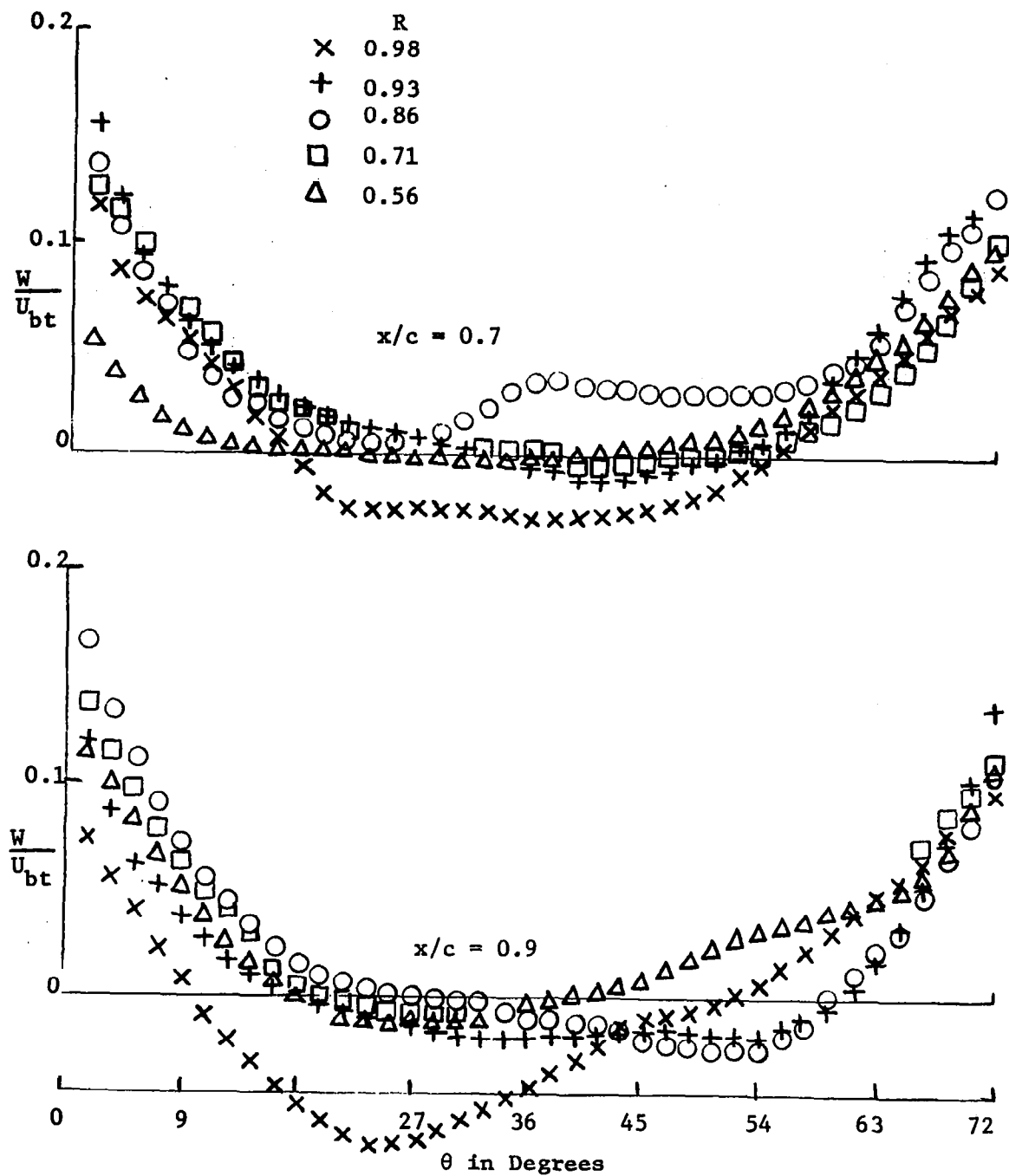Figure 31. Blade to Blade Distribution of Radial Velocity at x/c = 0.1, 0.3, and 0.5 (Open Throttle).

Figure 32. Blade to Blade Distribution of Radial Velocity
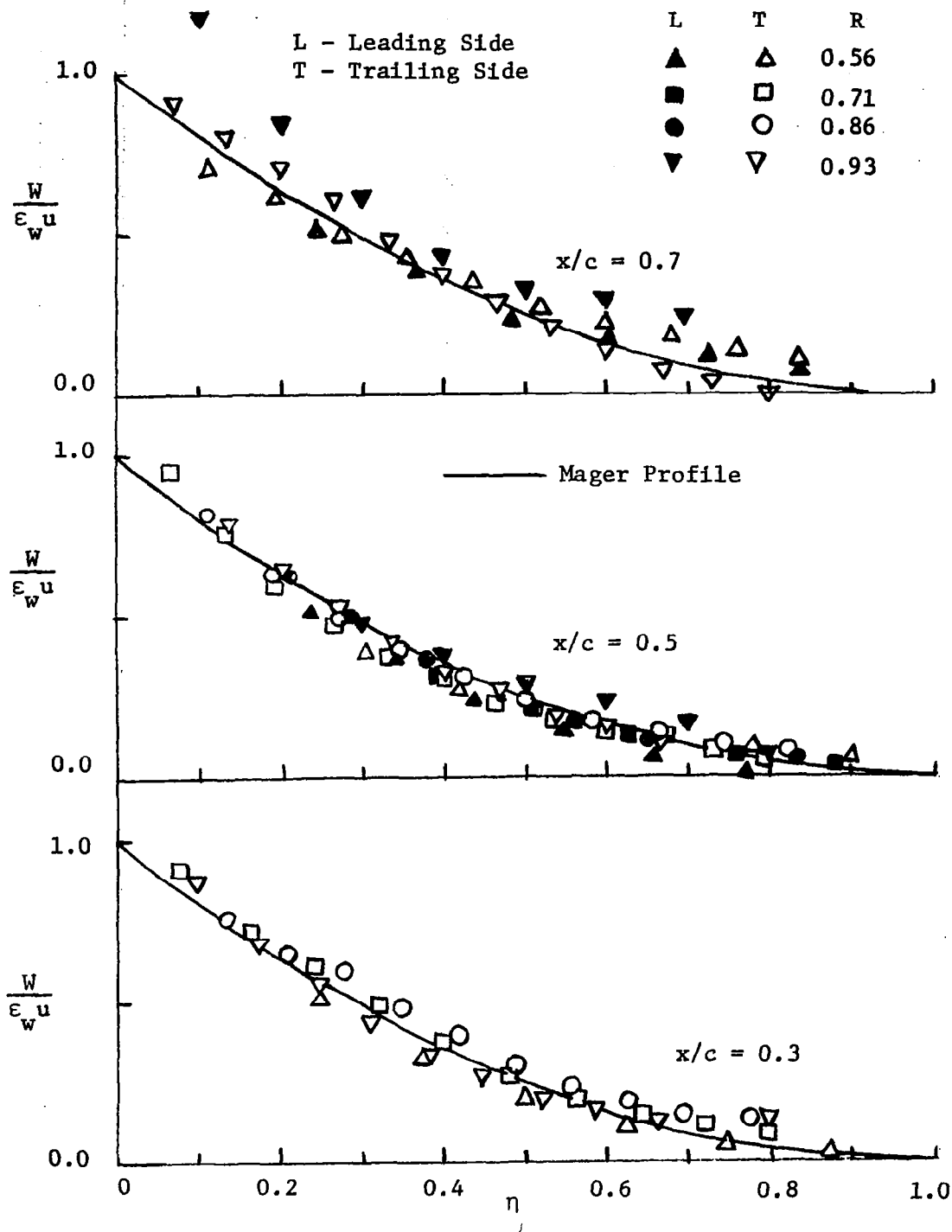at x/c = 0.7 and 0.9 (Open Throttle).

Figure 33. Mager's Representation of the Cross-Flow (Open Throttle).

106

tip. In the interference region the value of $\varepsilon/\varepsilon_w$ is higher than Mager's profile and near the hub the values are, in general, lower. The discrepancy is due to the effects of endwalls which interfere with the blade boundary layer producing complex flows. In the tip region, where the radial inward flows are present, Mager's representation fails because of the reversal of radial velocity profile (s type of profile) inside the boundary layer. This occurs at $x/c = 0.5$, and $R \geq 0.93$, $x/c = 0.7$, and $R \geq 0.86$ and at $x/c = 0.9$ and $R \geq 0.86$.

Plotted in Figures 34 are the hodograph plots of velocities on the leading and trailing surfaces respectively. The radial velocity measurements are inaccurate near the hub for $x/c = 0.3$, since the boundary layer thickness is very small there and therefore this data has been omitted in this polar plot. The data is compared to following predicted forms for the outer layer.

(i) Johnston's Triangular Model $w/U_e = C_2(1 - u/U_e)$ (115a)

(ii) Author's Model $w/U_e = C_1 \sqrt{(2/k-\sin\beta)\sin\beta/RG-(u/U_e)^2}$ (115b)

It is clear from the figure that Johnston's straightline fit 115a doesn't agree with the experimental data (except at some locations near the hub, which is coincidental). The agreement with Equation (115b) is quite good for most of the data, if the value of C_1 is allowed to vary with x. In the region where the two blade boundary layers have not merged i.e. for $x/c \leq 0.5$, it has been experimentally shown in Figures (23) and (24) that the velocity at the edge of boundary layer (U_e) is Ωr and therefore $k = RG \simeq 1.0$ and

$$w/U_e = 0.2 \sqrt{(2-\sin\beta)\sin\beta - (u/U_e)^2}$$
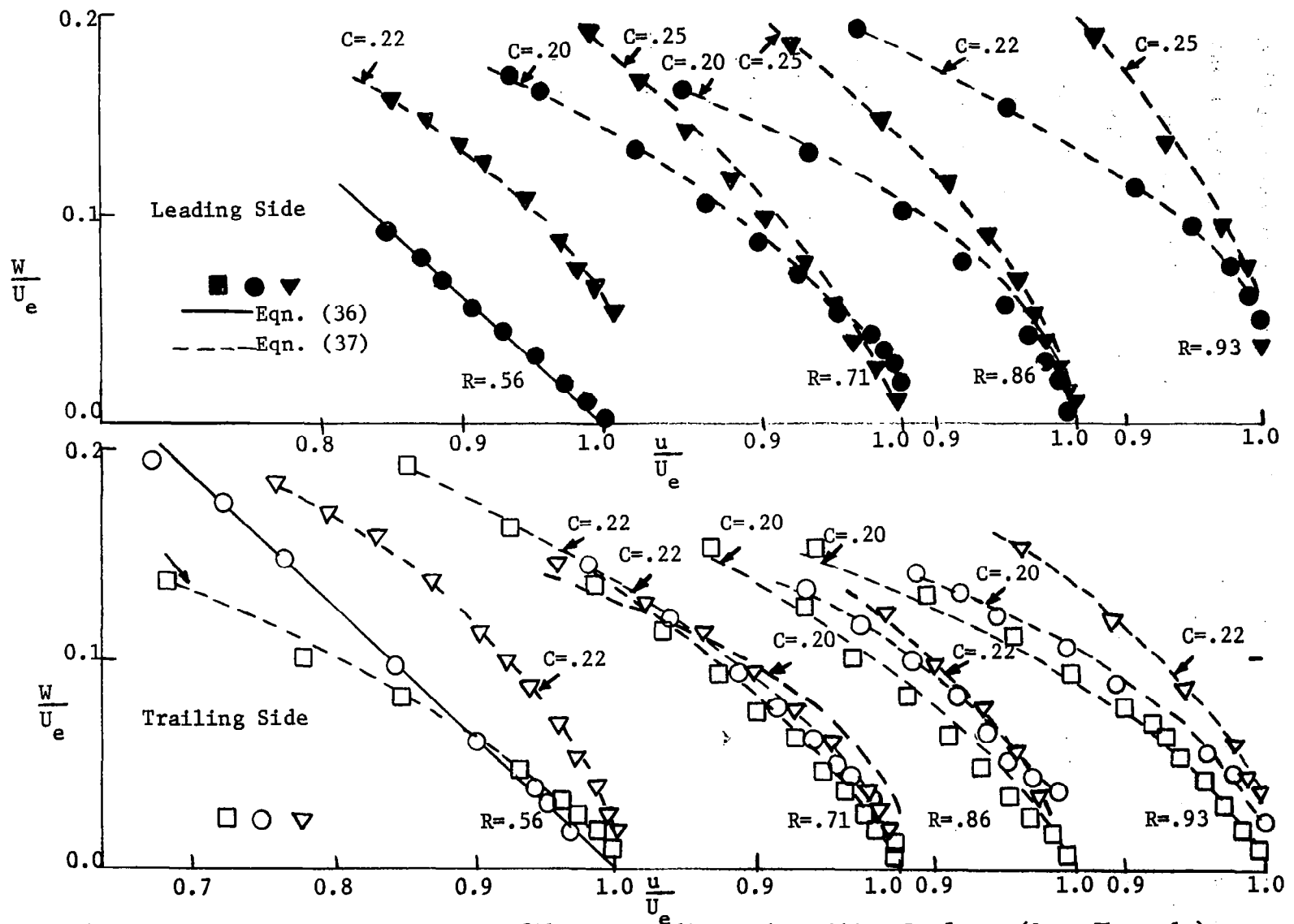
gives the best fit.

107

Figure 34. Hodograph Plot of Velocity Profiles at Leading and Trailing Surfaces (Open Throttle).

Equation (31) as well as the experimental data indicate that it is not necessary for the radial velocity w in the rotating boundary layers in a channel to go to zero when $u = U_e$ and $\partial U_e / \partial y = 0$ as has been observed in the case of boundary layers in the stationary passages. Polar plot of the velocity profiles near the blade tip are shown in Figure 35. Since the radial velocities are comparatively small at $x/c = 0.7$, no definite conclusions can be drawn with regard to the profile shape. However, at $x/c = 0.9$, (interference region – Figure 2), the radial inward velocities as well as the defect in mainstream velocity is appreciable. The data is compared with the Equations (115a) and (115b) with a negative constant in the "interference region". It is evident from the figure that Equation (115b) gives the best fit except near the center of the channel section. The straightline form (115a) is adequate if C_2 is assumed different on the two surfaces.

The existence of such a phenomenon in turbomachinery has not been reported before. It should be remarked here that the mixing losses associated with the interference region has never been taken in to account in developing end loss correlations in turbomachinery. This accounts for some of the discrepancy observed between endwall correlations (based on cascade data) and the endwall losses measured at the exit of turbomachinery rotors.

5.1.7 Comparison of Experimental Results with Theory

The momentum integral technique described in Chapter II has been used to predict the momentum thickness (θ_{11}) and limiting streamline at various r and x locations for the four bladed flat plate inducer. The measured static pressure distribution is used to obtain RG, TG and k.
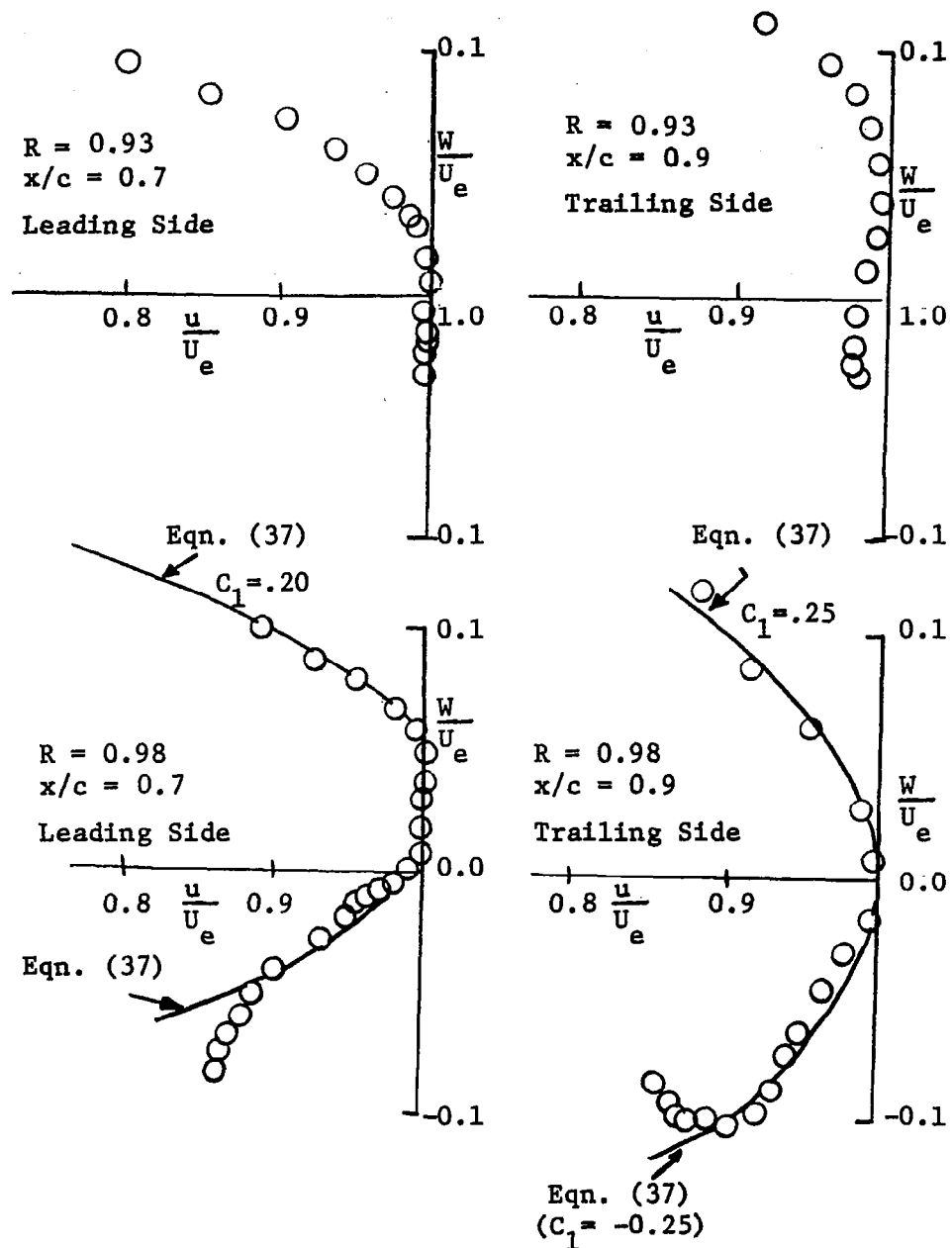
109

Figure 35. Hodograph Plot of the Velocity Profiles in the
Interference Layer (Open Throttle).

The predicted variation of ε_w and θ_{11} for the present case as well as single blade case are also shown in Figures 18 and 36 respectively. For the present case of the flat plate inducer run at open throttle, the values of θ_{11} obtained from the experiments at first increase rapidly up to x/c = 0.3 and decrease or increase slowly further downstream of the channel depending upon the imposed pressure gradients. The values are higher on the trailing surface compared to the leading surface which is due to higher pressure gradients (Figure 19) found on the latter surface. θ_{11} increases with radius for most of the channel, except near the trailing edge of the trailing blade surface. The predictions agree well with the measured values except near the leading edge, where the extent of laminar boundary layer growth is assumed to be known. The location of transition is determined experimentally. Compared to the boundary layer growth on a single blade rotating in stationary fluid, the boundary layer growth is much smaller in a channel due to the presence of radial and chordwise pressure gradients. The difference between the observed and predicted boundary layer growth is partly due to an error in estimating the extent of initial laminar boundary layer and partly due to an error in estimating the momentum thickness θ_{11} from measurements. A study of Equation (70) for θ_{11} shows that the effect of adverse chordwise pressure gradients is to increase the boundary layer thickness, while the effect of positive radial pressure gradients is to decrease it compared to the single blade case plotted in Figure 36. It can therefore be concluded that in the present case, the effect of radial pressure gradient is much larger than the chordwise pressure gradient. This is confirmed by a large decrease in θ_{11} near tip radius
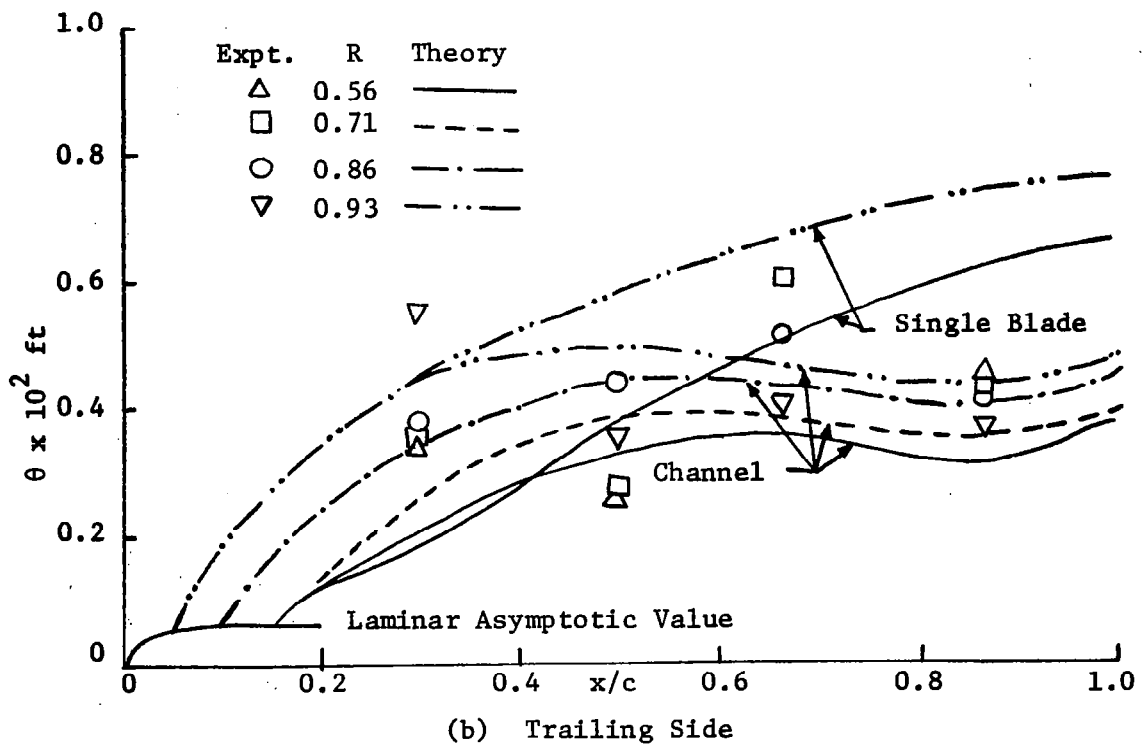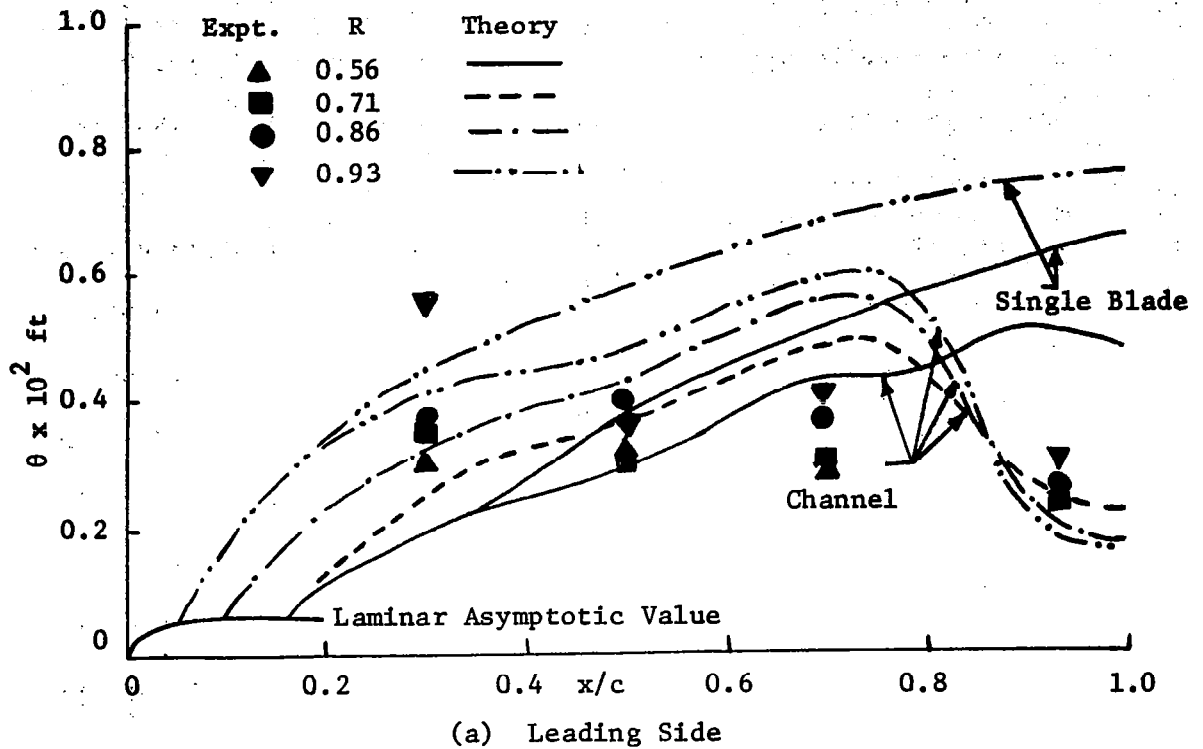
Figure 36. Experimental and Predicted Variation of Momentum Thickness (θ_{11}) in the Channel (Open Throttle).

where the radial pressure gradients are found to be much larger than the chordwise pressure gradients.

The measured and predicted values of the limiting streamline angle are compared in Figure 18. In the turbulent region i.e. $x/c \geq 0.1$ the values increase or decrease with x in accordance with the pressure gradients. The value of ε_w decreases with increase in radius and reaches a minimum at the tip. The magnitude of ε_w is higher on the leading side indicating that the boundary layer is more skewed and that the cross flow is larger compared to that on the trailing side of the channel. The predictions agree reasonably well except near transition. The value of ε_w in the laminar region is obtained from the approximate solution of Banks and Gadd (7). The numerical results are subject to some error because the transition is assumed to be sudden and there is an order of magnitude of difference between the values of limiting streamline angle (ε_w) for laminar and turbulent boundary layers respectively. An important difference between the single blade results of Lakshminarayana et al. (17) and the rotating channel is that the values are higher in a rotating channel and there is a radial variation due to the presence of varying radial pressure gradient.

An examination of Equation (71) indicates that ε_w is very sensitive to pressure gradients and its value increases in the presence of positive radial and chordwise pressure gradients. This accounts for larger values of ε_w measured in a channel as compared to a single blade, plotted in Figure 18. The extent of radial flows and boundary layer growth is very sensitive to radial and chordwise pressure gradients. This conclusion is confirmed by the comparison of boundary layer growth on a single blade and in a channel shown in Figure 36.

5.2 Effect of Throttle and Exit Flow Measurements

In order to investigate the overall performance of the four bladed
flat plate inducer at various flow coefficients, a throttle is installed
at the exit as shown in the test facility (Figure 8). The second
objective is to determine the operating conditions for conducting the
measurements inside the rotor so that the pressure gradients in its
blade passages are of the same order of magnitude as those found in the
actual rocket pump inducers (e.g. Lakshminarayana (21, 45)).

The throttle clearance is varied and annulus wall static pressure
measurements are carried out from inlet to far downstream. The flow
rate, stagnation pressure and flow angle are carried out 14 inches
downstream of the rotor.

Figure 37 shows the static pressure distribution measured on the
annulus wall with different values of throttle clearance. It is seen
that the annulus wall static pressure increases as the throttle
clearance decreases. The negative pressure at the leading edge of the
blade is considered to be caused by the blade blockage effect. Increase
of the blade static pressure at the trailing edge is considered to be
caused by the increase of flow area due to the absence of the blade
thickness. It is seen that the static pressure is constant downstream
of the rotor assembly. It is interesting to note that the axial pressure
gradient on the annulus wall decreases as the throttle clearance
decreases. The stagnation pressure rise coefficients at various throttle
positions are plotted in Figure 38. Even at large throttle openings,
appreciable pressure rise can be seen especially at the tip. This is
caused by considerable boundary layer growth on the blades, and the
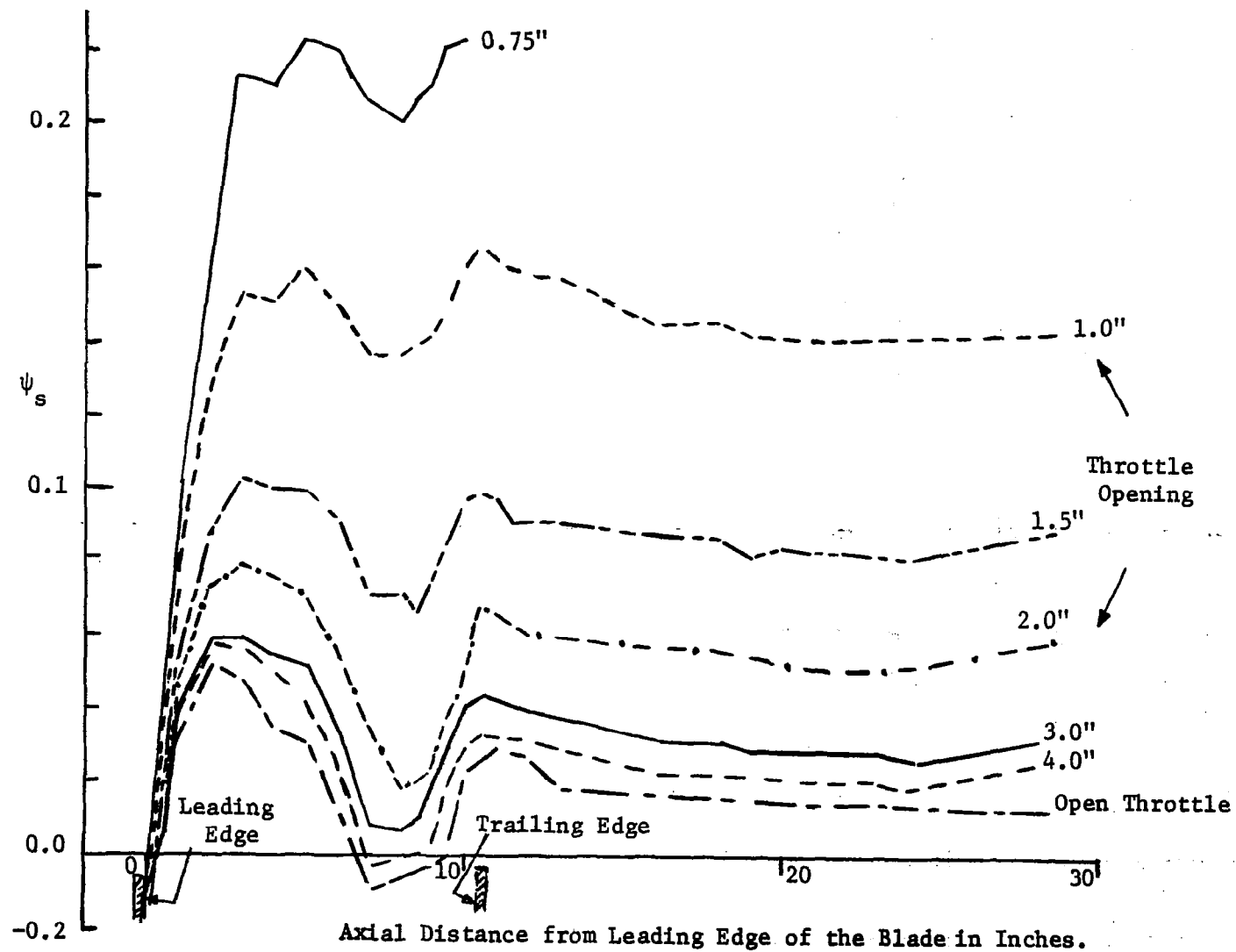shear pumping effect. The outlet angles, measured with respect to

114

Figure 37. Annulus Wall Static Pressure Distribution.

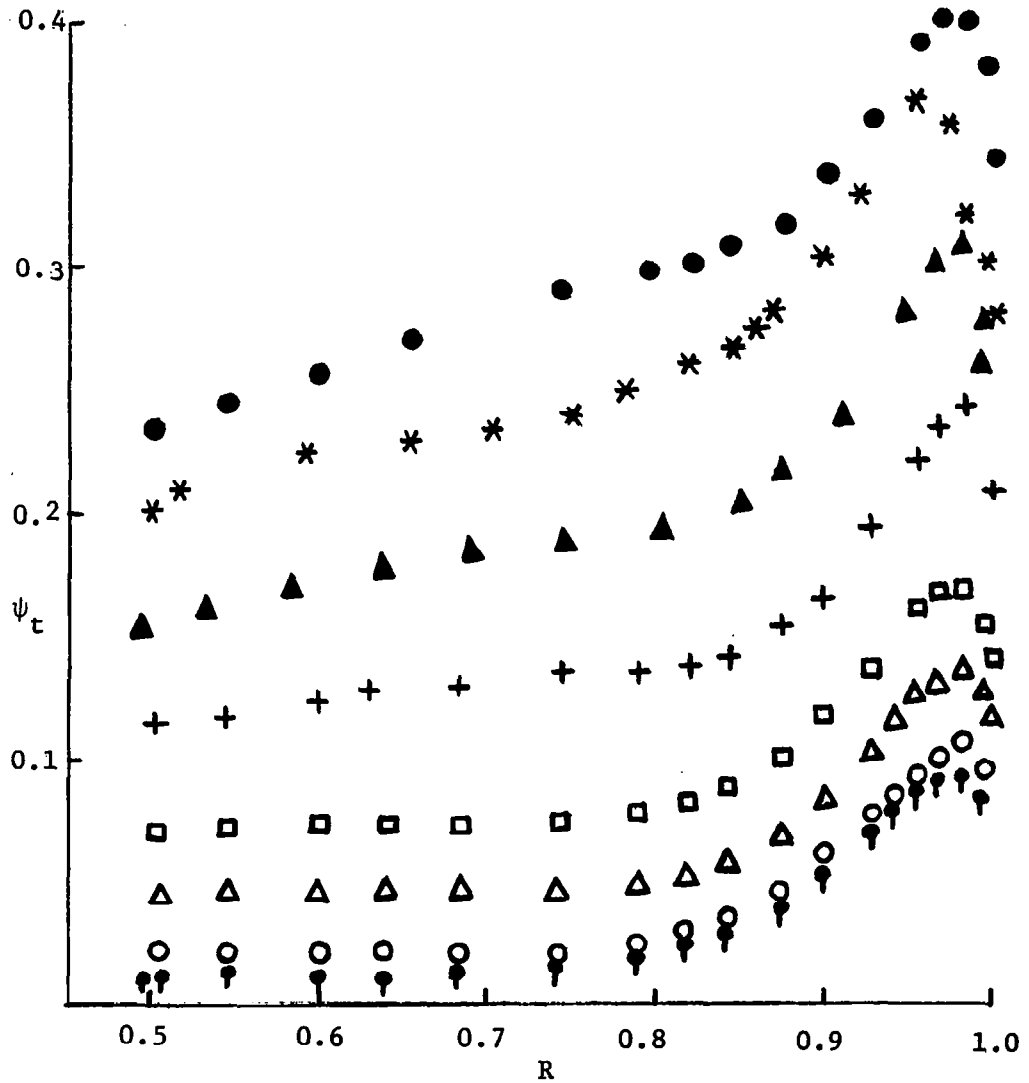| Throttle Opening(O) (inches)	0.5	0.7	0.9	1.0	1.5	2	3	4
Flow Coefficient($\phi \times 10^2$) (mass averaged)	4.1	5	5.6	6	6.5	6.7	6.7	6.7

Figure 38. Distribution of Stagnation Pressure Coefficient (ψ_t) at the Inducer Exit.

tangential directions are derived using a cobra probe. The flow
reversal near the hub, occurs at flow coefficient of 0.0592 or less as
indicated by angle measurements shown in Figure 39. The performance
of the flat plate inducer, plotted in the form of $\bar{\psi}_t - \bar{\phi}$ curve is shown
in Figure 40, where $\bar{\psi}_t$ is mass averaged stagnation pressure coefficient
and $\bar{\phi}$ is passage averaged flow coefficient.

For experiments at large pressure gradients, a throttle clearance
of 0.7 inch corresponding to a flow coefficient of 0.05 and an average
stagnation pressure coefficient $\psi_t \simeq 0.25$, is chosen. Measurement of
stagnation pressure and flow angle are performed at stations 3 and 6
7/16" and 14" downstream of the rotor trailing edge. Static pressure
is measured both at the hub and annulus walls. In Figure 41, ψ_T and ψ_s
distribution is compared to that of a four bladed cambered rocket pump
inducer tested by Lakshminarayana (21, 45). It is seen that the two
rotors have similar characteristics even though the value of ψ_T for the
flat plate rotor is about 25% lower. Axial and radial velocity profile
distribution (Figure 42) show similar trends. However, the backflow
region for the flat plate inducer is more because it is being operated
at lower flow coefficients.

5.3 Experimental Data with Throttle

Actual turbomachinery rotors have large pressure gradients at
design flow conditions. In order to simulate the same flow conditions
in the experimental rotor, the flow is partially throttled at the exit.
A throttle clearance of 0.70 inch corresponding to a flow coefficient
of 0.05 is chosen so that its stagnation pressure distribution (operating
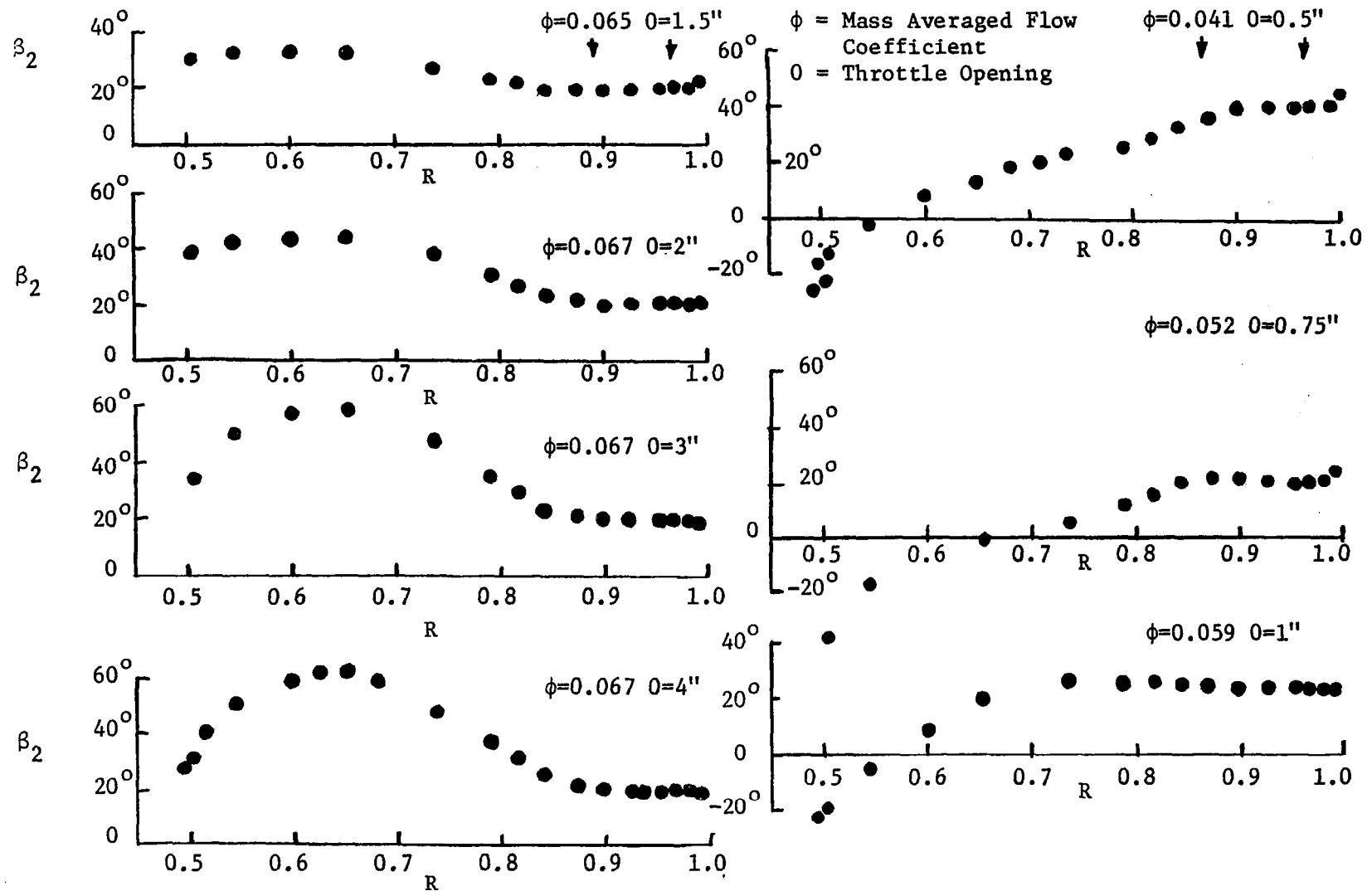characteristics) corresponds to an actual rocket pump inducer operating

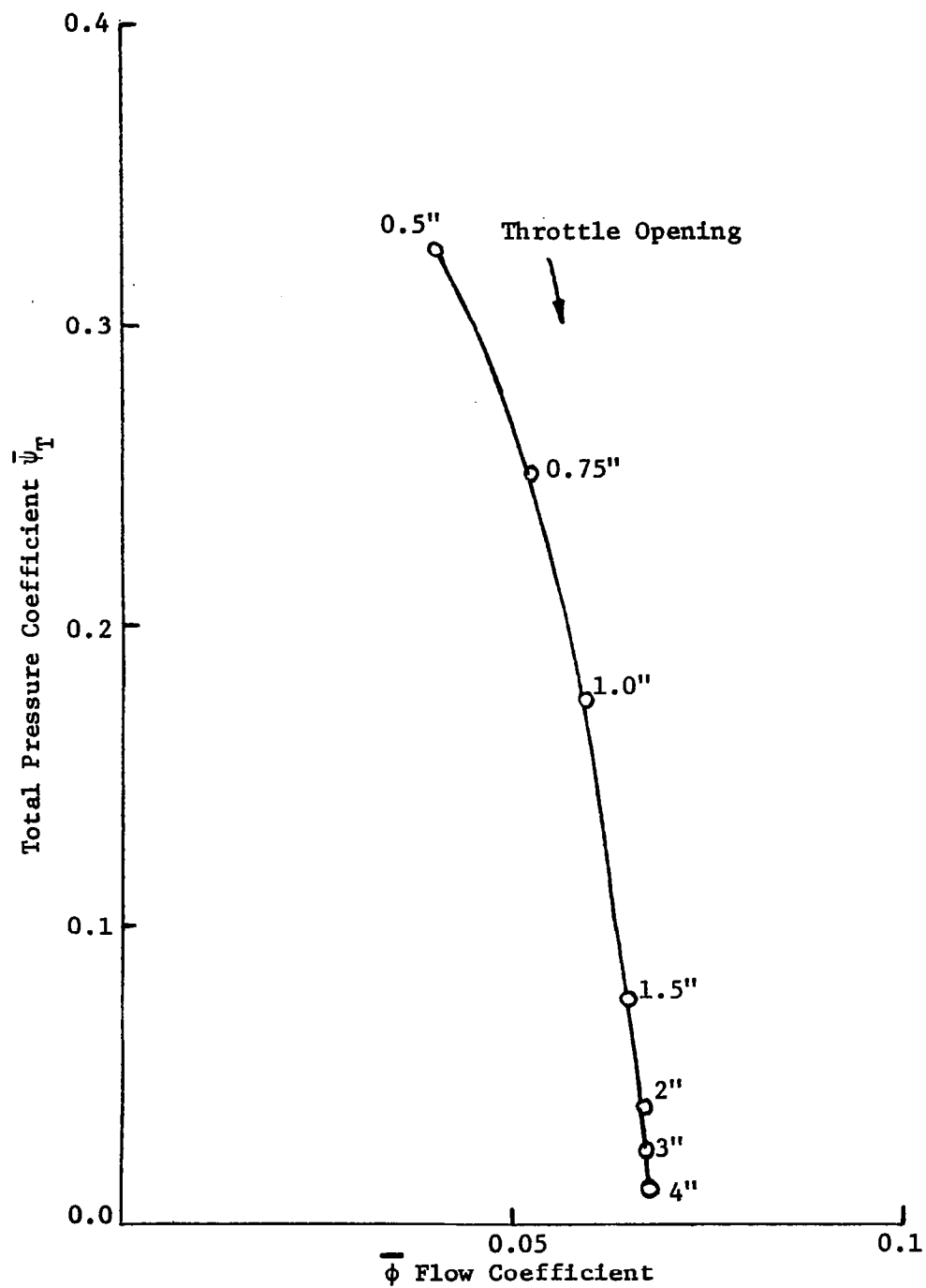Figure 39. Radial Distribution of Outlet Angle (β_2), 14" Downstream of the Trailing Edge.

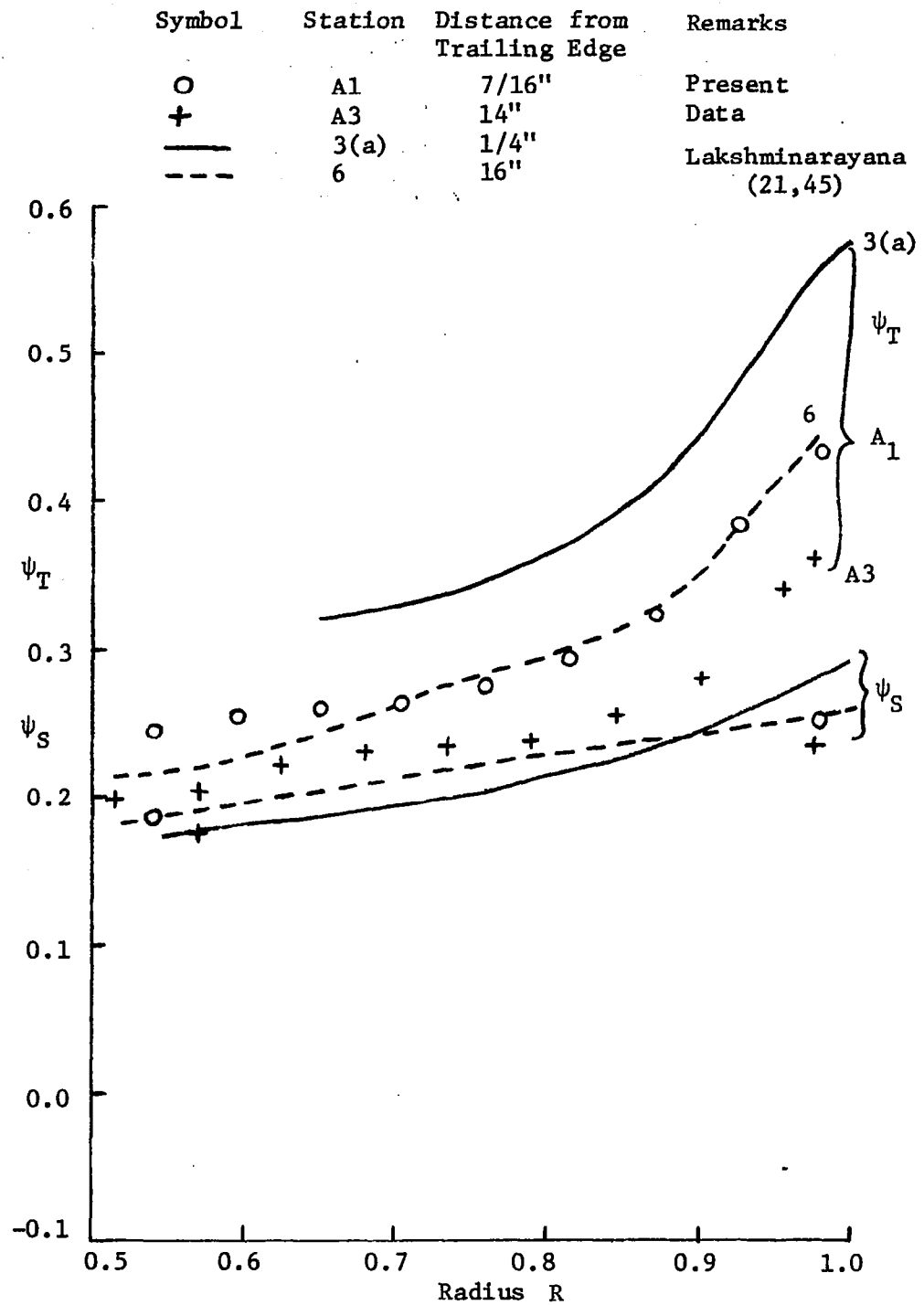Figure 40. Performance Characteristics of Flat Plate Inducer Rotor.

Figure 41. Comparison of Radial Distribution of Stagnation Pressure Coefficient (ψ_T) and Static Pressure Coefficient (ψ_S) for Flat Plate and Cambered Bladed Inducers.
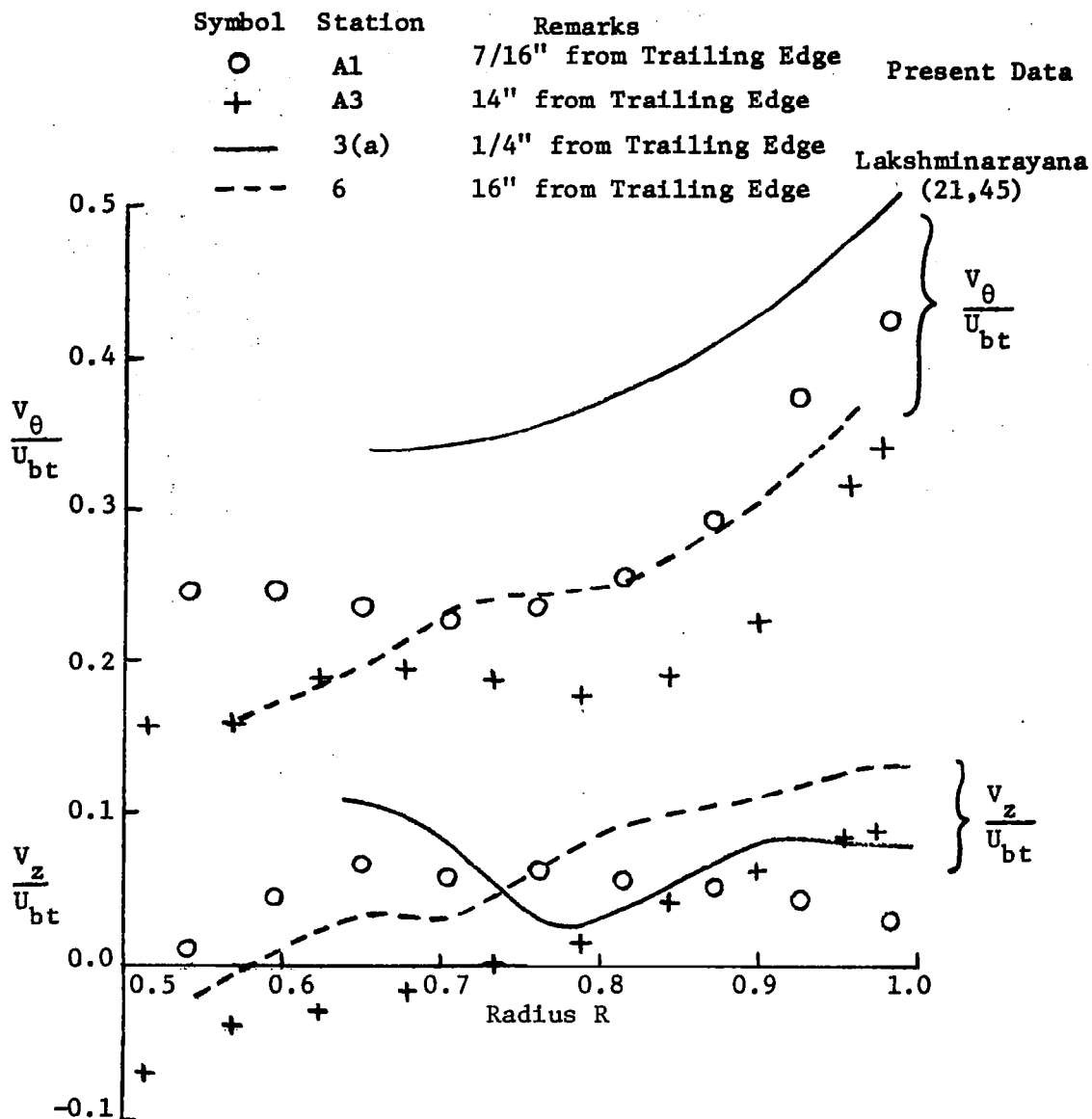
Figure 42. Comparison of Radial Distribution of the Axial
(V_z/U_{bt}) and Tangential (V_θ/U_{bt}) Velocity Profiles
for Throttled Flat Plate Inducer and Cambered Bladed Inducer.

at its design conditions. All the mean flow quantities obtained for rotor operating without throttle are also measured in this case. In addition turbulent intensities and stresses and their spectra are measured to study the effects of rotation on the local turbulent structure of the flow in the rotor channels. A three sensor hotwire probe described earlier in Chapter III is used for all mean velocity and turbulence measurements in a measuring grid of 5 x 5 x 39 in radial, chordwise and blade to blade directions respectively, (except at x/c = 0.1, where measurements are carried out at 3 radii).

Mean velocity profiles are also measured at x/c = 0.9 using the three hole disk probe (Figure 12) to compare the obtained data by two separate methods of measurement. The agreement between two measurements is found to be good. The experimental results of all measurements inside the partially throttled flat plate inducer are described below.

5.3.1   The Limiting Streamline Angle

Figure 43 shows both the radial and the chordwise distribution of the limiting streamline angle both on leading and trailing blade surfaces. The radial distribution shows a continuous decrease of ε_w with radius at all chordwise locations, except near the hub where the interference of the hub wall boundary layer with blade boundary layer is appreciable. At x/c = 0.1, the flow is laminar near the hub on the leading side and consequently results in large values of the limiting streamline angle. The chordwise variation of the limiting streamline angle (Figure 43) shows that in general the magnitude of ε_w increases with x due to adverse chordwise pressure gradients. However, for values of x/c > 0.75, the limiting streamline angle increases on the leading surface and decreases
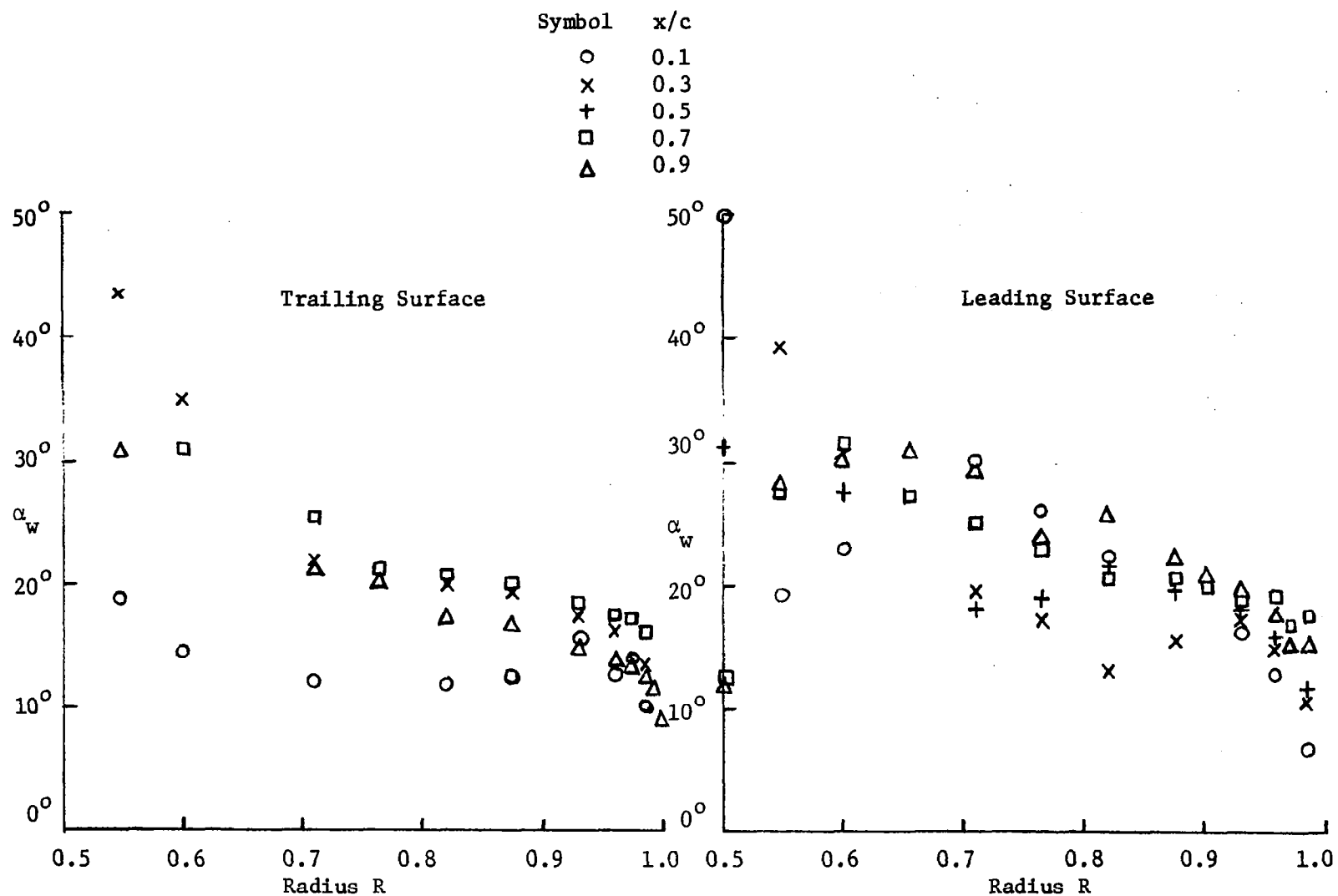
Figure 43. Radial and Chordwise Distribution of Limiting Streamline Angle (α_w)(Throttled Case).

123

on the trailing surface in accordance with the pressure gradients (Figure 44). The magnitude of limiting streamline angles are in general much higher compared to both single blade and open throttle data. This is because the pressure gradients (Figure 44) are much larger in the partially throttled case compared to the open throttle case (Figure 19). The values are comparable to those for actual four bladed cambered rocket pump inducers where the pressure gradients are also of the same order. This confirms an earlier conclusion, based on open throttle data, that the magnitude of the limiting streamline angle is directly affected by the imposed external pressure gradients on the turbulent boundary layers in a rotating passage.

5.3.2 Blade Static Pressures

The radial distribution of blade static pressure at various chordwise locations is shown in Figure 44. The measuring points are the same as in the open throttle case. Unlike the open throttle case (Figure 19),the radial variation of ψ_s is large. Its gradient also increases continuously with the radius to a maximum value at the tip. Except in the entrance region (x/c = 0.1), the static pressure on the leading surface is higher compared to that on the trailing surface. At the entrance, since the inducer is being operated at large incidence (4° at hub to 2° at tip), the leading side has a larger negative value of static pressure than on the trailing side of the blade surface.

It is also clear from Figure 44 that the static pressure rises rapidly with x up to quarter chord. Further downstream, for x/c > 0.25, the static pressure coefficient (ψ_s) remains relatively flat on the leading surface even up to ninety percent of the chord. On the trailing
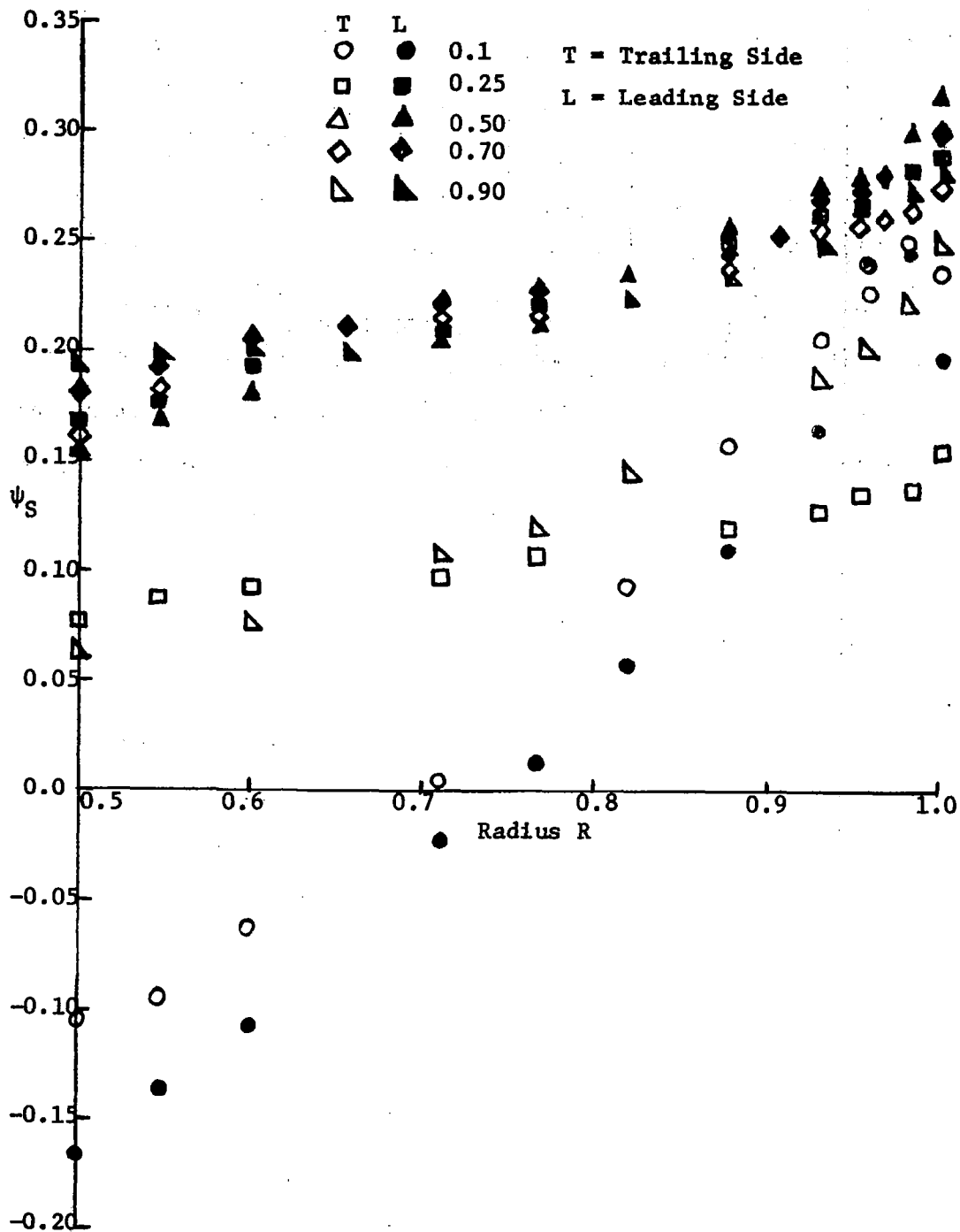
Figure 44. Radial and Chordwise Distribution of the Blade Static
Pressure (ψ_S) on Leading and Trailing Surfaces
(Throttled Case).

side ψ_s increases continuously up to x/c = 0.75 and decreases there onwards. The pressure loading on the surface occurs mainly between x/c = 0.1 and 0.5, and is more pronounced at hub and tip radii. Very near the tip (R > 0.97), ψ_s decreases at x/c = 0.1 on leading side due to the presence of leakage and secondary flows at the tip. Due to large chordwise pressure gradients and incidence, the relative flow near the hub is found to be separated near the leading edge (e.g. at x/c = 0.1).

5.3.3 Mean Velocity Profile

Figures 45 to 49 show the distribution of chordwise and radial flow velocity components at various radial and chordwise locations. Their values are obtained by using three sensor rotating hotwire probe and hotwire equations as described in Chapter IV. The velocity component normal to the blade is found to be very small throughout the channel (< 1 ft/sec) and has not been shown in these figures for the sake of clarity. In order to check the validity and accuracy of hotwire measurements in rotating system, these mean velocity measurements were compared to disk probe measurements at x/c = 0.9 at five radii. The measurements by both methods gave almost identical values of mean velocity profiles within the range of experimental error and hence establish the validity of the hotwire measurements in rotating frame of reference.

Chordwise Velocity Profile: An examination of the streamwise velocity at x/c = 0.1 shows that the flow has already become turbulent over most of the radii. The boundary layer is thin on the leading side and thick on the trailing side. The velocity profiles clearly show that

Figure 45. Blade to Blade Distribution of Mean Velocity Profiles at x/c = 0.1 (Throttled Case).

Figure 46. Blade to Blade Distribution of Mean Velocity Profiles
at x/c = 0.3 (Throttled Case).

Figure 47. Blade to Blade Distribution of Mean Velocity Profiles
at x/c = 0.5 (Throttled Case).
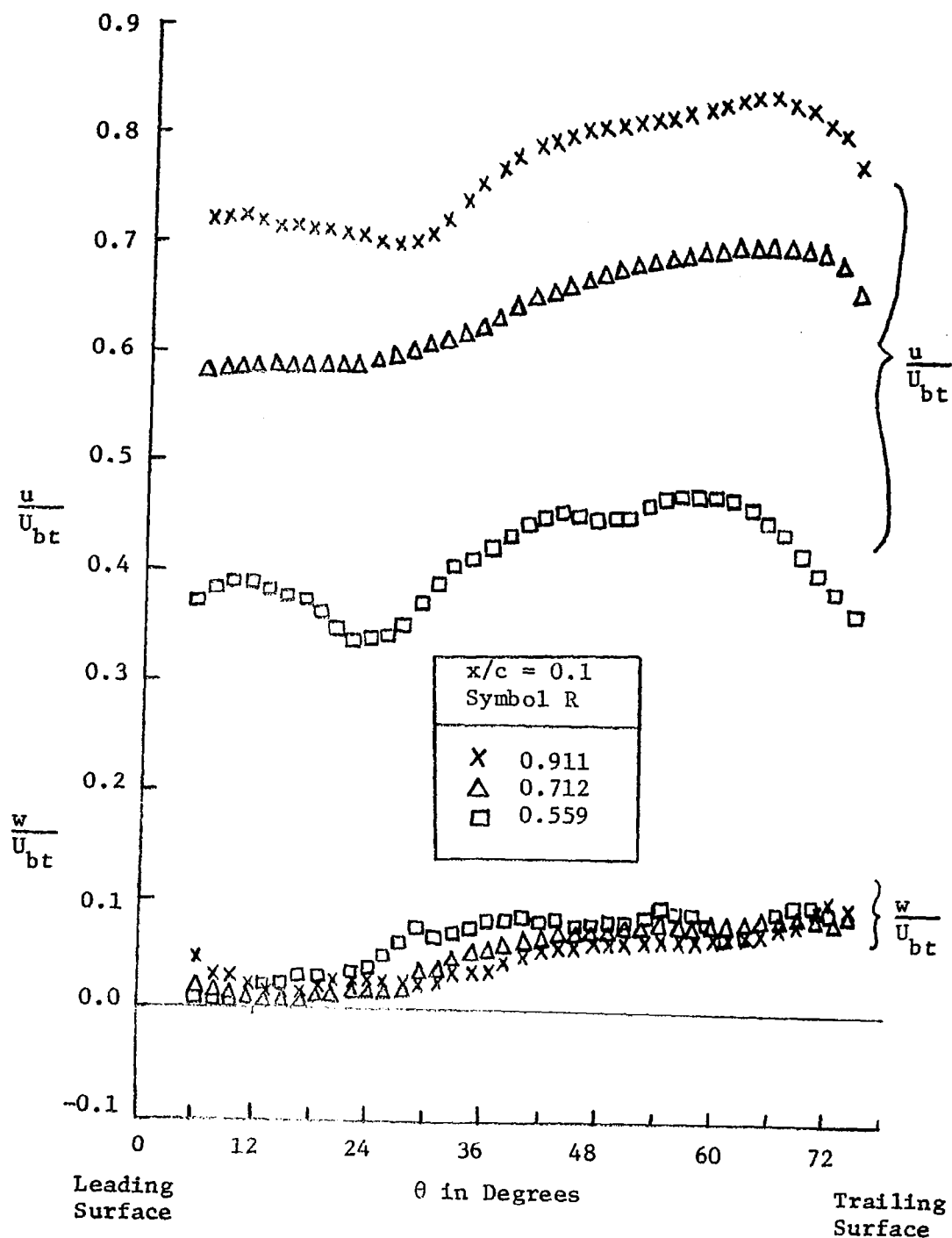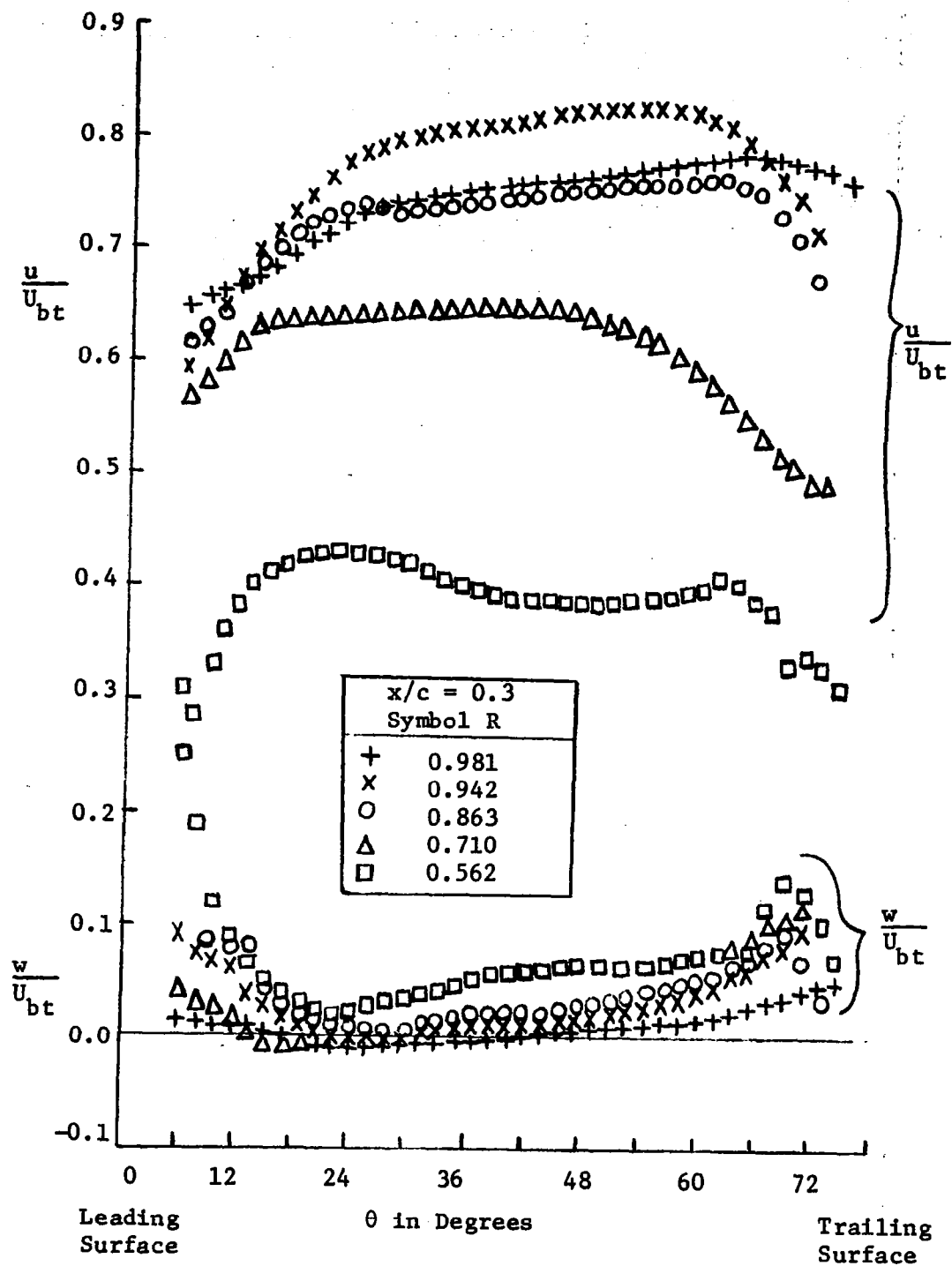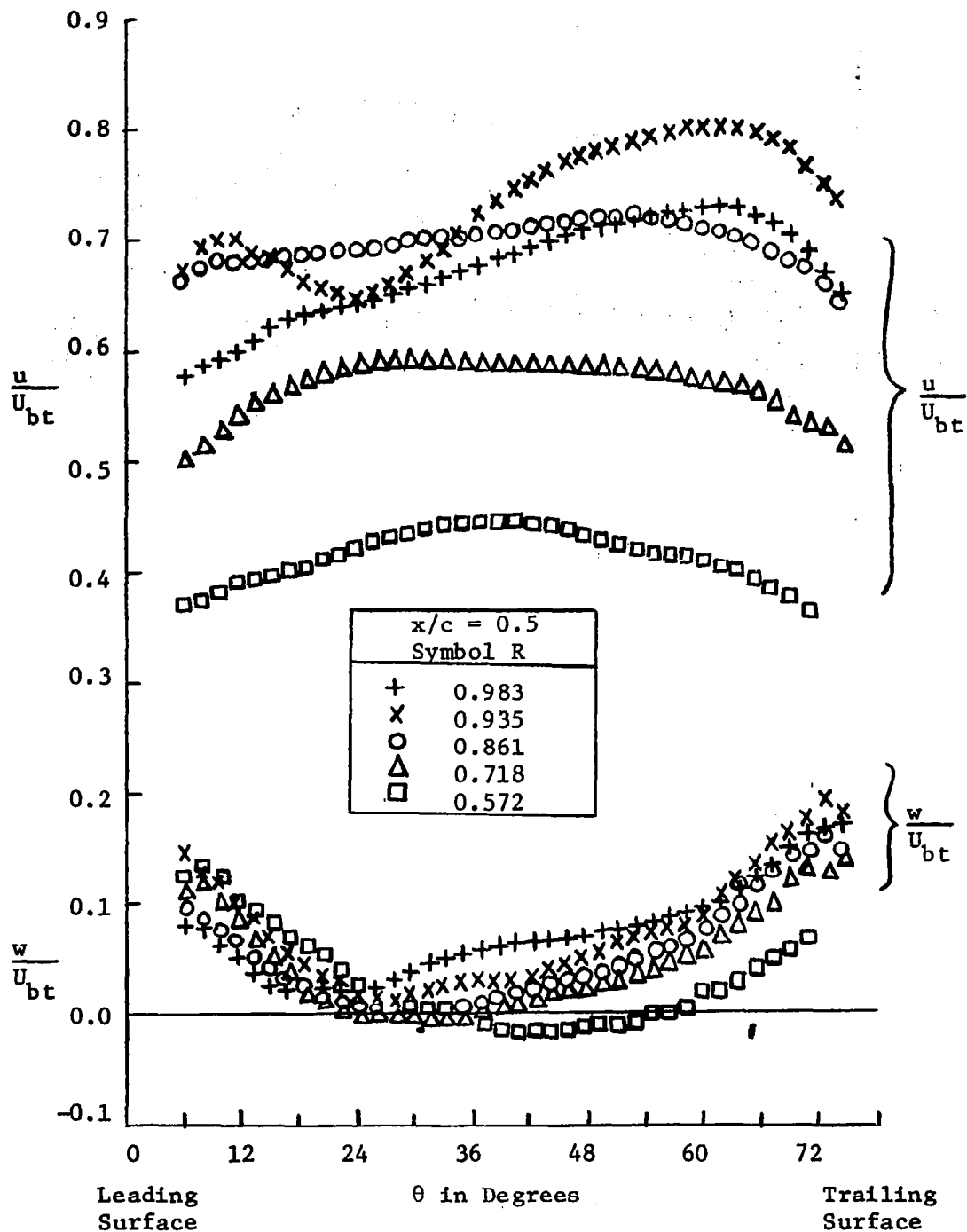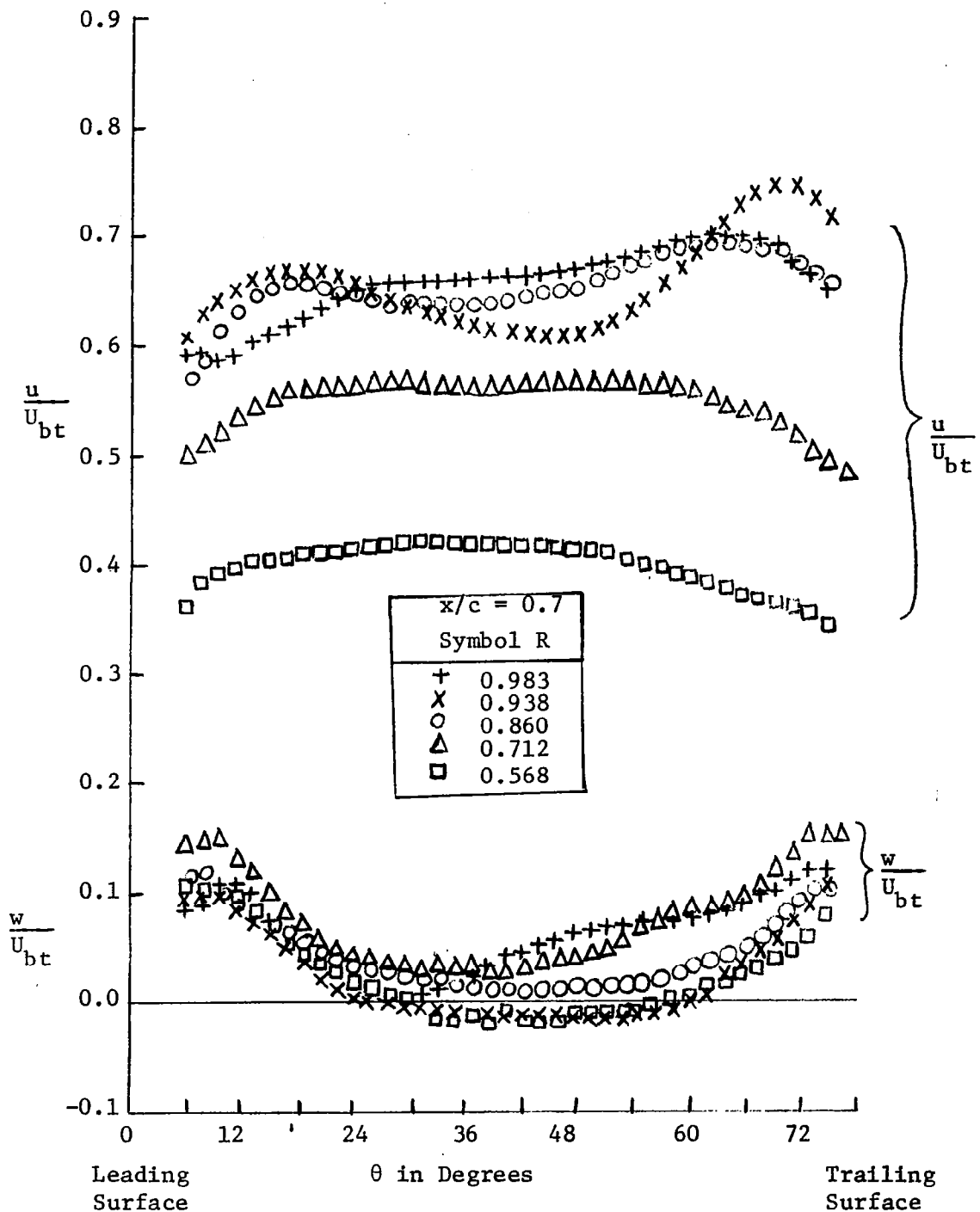
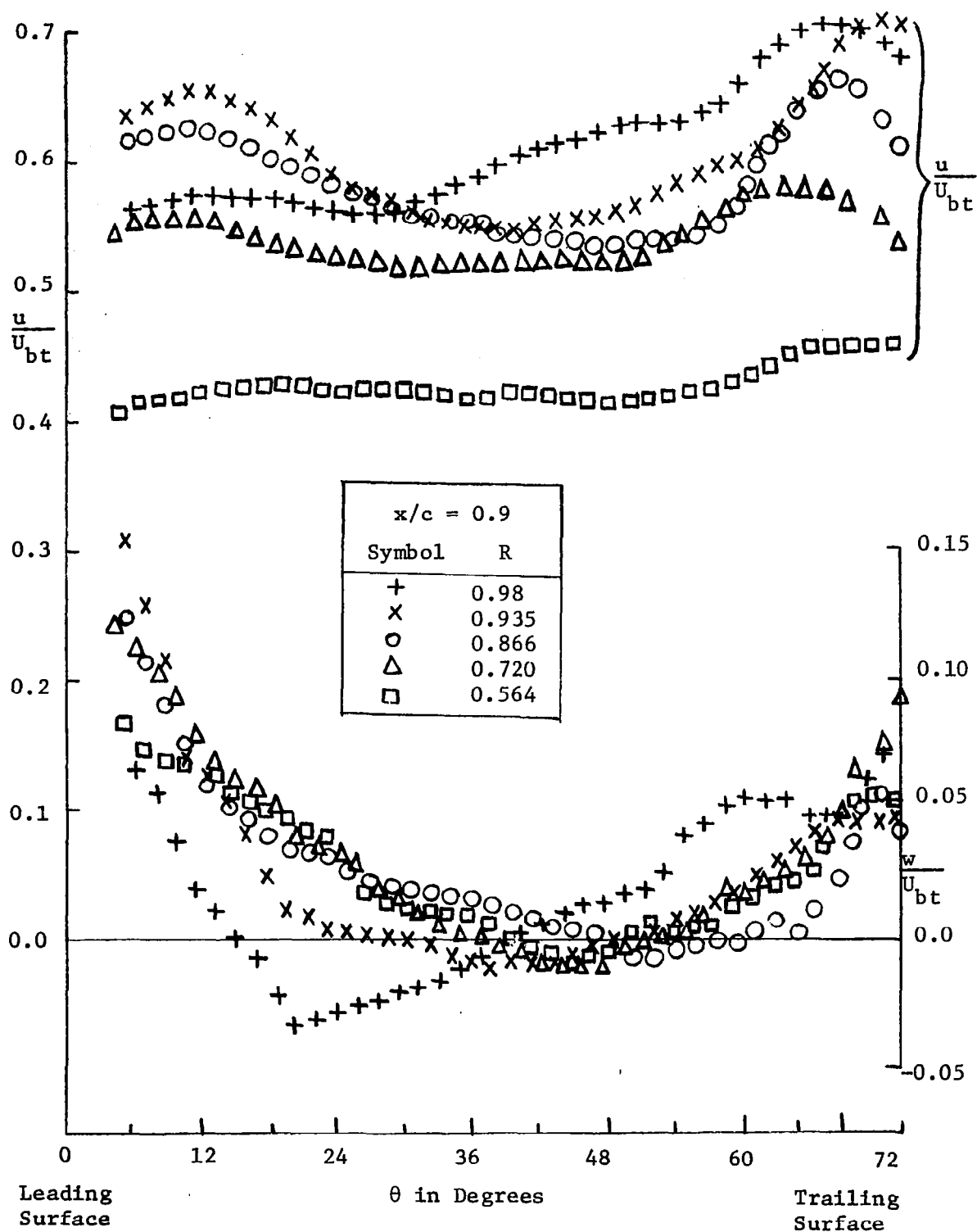Figure 48. Blade to Blade Distribution of Mean Velocity Profiles at x/c = 0.7 (Throttled Case).

Figure 49. Blade to Blade Distribution of Mean Velocity Profiles at x/c = 0.9 (Throttled Case).

the flow is asymmetrical and that large velocity gradients exist across the channel. This is caused by large chordwise and radial pressure gradients that exist near the leading edge (as shown in Figure 44) in the present case. The inducer flow has been throttled to give a large pressure rise at low flow coefficient as shown in the performance curve of Figure 40. The profile distribution at subsequent downstream measuring stations, Figures 45 to 49, show that the boundary layer is turbulent at all radii on both the surfaces and grows rapidly downstream. It should be noted that unlike the open throttle case discussed in Section 5.1, there is a large diffusion of relative flow due to large positive chordwise pressure gradients (Figure 44) in the channel in the entrance region up to x/c = 0.5. Therefore, the streamwise velocity in the inviscid region external to the blade boundary layers is smaller than the blade speed (Ωr).

The boundary layers at tip grow rapidly due to radial flow migration and large unfavorable chordwise pressure gradients. Fully developed flow occurs at x/c = 0.30 for R ≥ 0.94. This region extends inward rapidly. In the interference region (defined in Figure 2), the boundary layer profiles are unconventional, as observed and explained earlier in the open throttle case in Section 5.1. As a result, the boundary layer thickness cannot be defined in a conventional manner and the momentum integral analysis which assumed the monotonically increasing powerlaw profile for the streamwise velocity is inadequate. It gives only a qualitative picture, if the boundary layer thickness is defined as the distance from the surface, where the streamwise velocity component reaches a maximum.

An examination of velocity profiles shows that the boundary layer on the trailing surface is first thicker compared to leading surface up

to midchord. Further downstream, the trend is reversed and at x/c = 0.5, the boundary layer is thicker on the leading side. This behavior is in accordance with the chordwise pressure gradients (Figure 44). The pressure gradients on the leading surface is almost constant after midchord but it has a negative value which results in the acceleration of the mean flow on the trailing surface. The boundary layers on blades are in general thicker in the throttled case compared to those in the open throttle case.

The mainstream velocity is plotted in Figure 50 against non-dimensional distance from the blade wall (y/δ) at x/c = 0.3, 0.5, and 0.7 and at radii R = 0.71, 0.86 and 0.93, both for leading and trailing side boundary layers. Measurements at hub and tip radii have not been plotted in this form, because the boundary layer behavior is unconventional due to end wall effects. As noted in the open throttle case, the measurements fit the power law profile representation well. The value of power index varies from 1/6 to 1/11 depending upon the nature of pressure gradients (Figure 44), the value of power index decreases downstream from x/c = 0.3 to 0.7 particularly on the leading side, which has favorable pressure gradients in this region.

Coles form of streamwise velocity has not been plotted because the measurements in the open throttle case plotted in this form have clearly shown that the usual sinusoidal type of wake profile observed in the outer region of stationary turbulent boundary layers is not observed in rotating turbulent boundary layer data.

In Figure 51, the radial distribution of streamwise velocity at the edge of the boundary layers is plotted, both for leading and trailing side blade boundary layers, at five chordwise locations. Unlike the
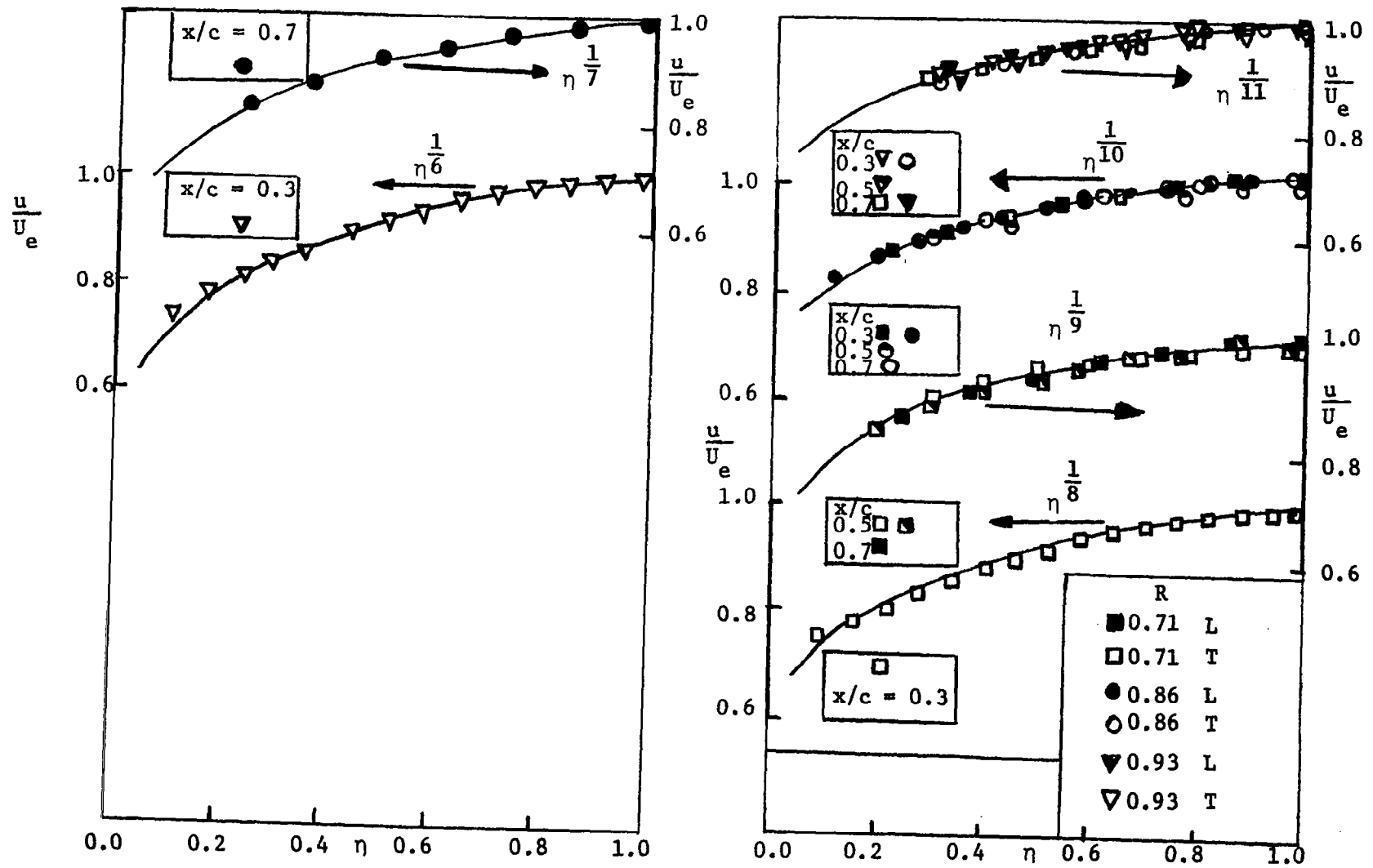
133

Figure 50. Power Law Representation of Velocity Profiles in the Blade Boundary Layer (Throttled Case).
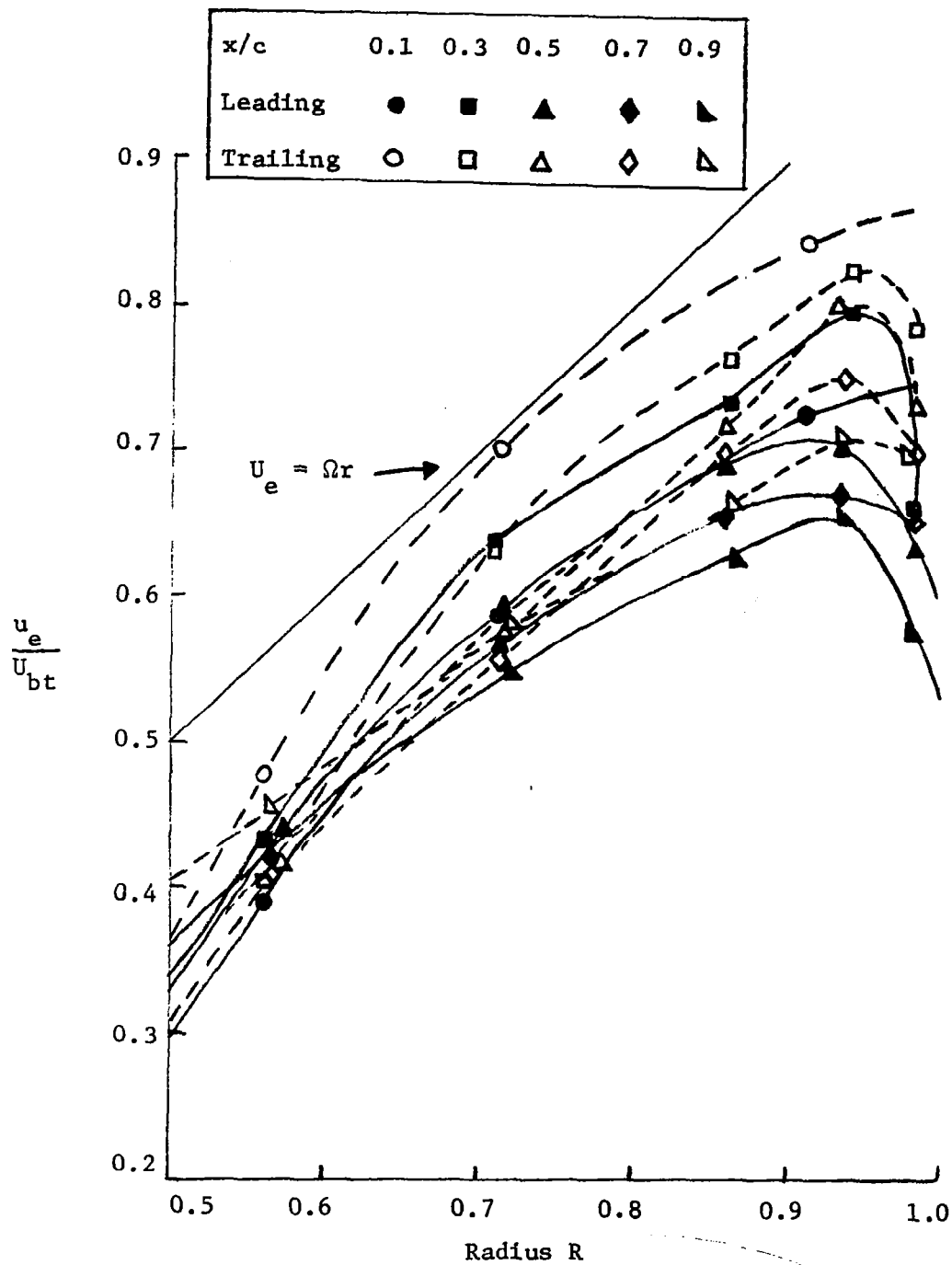
Figure 51. Radial and Chordwise Distribution of Mainstream
Velocity at the Edge of the Boundary Layer
(Throttled Case).

open throttle case, there is a large decrease in the boundary layer
edge velocity even in the entrance region. This is due to the fact
that the inducer in the present case is operated at a lower flow
coefficient (0.05) compared to the open throttle case (0.065), which
results in an appreciable pressure rise as shown in the performance
curve of Figure 40. The difference is larger near the hub and the tip,
where the hub and the annulus walls interfere with the flow. Since
the inducer is operating at a large incidence (4°), the relative flow
is separated at the leading edge and causing the observed reduction
in the streamwise velocity. At the tip, the interference with the
annulus wall produces radial inward flows and a reduction in the
streamwise velocity as described earlier for the open throttle case.
This is accompanied by an increase in radial pressure gradients at
the tip as shown in Figure 44. The decrease is larger on the leading
surface compared to the trailing surface, particularly in the entrance
region, where the leading side encounters larger unfavorable pressure
gradients.

Radial Velocity Profile: The blade to blade distribution of the
radial velocity profiles at different radial and chordwise locations
are also shown in Figures 45 to 49. The radial velocities show the same
behavior as noted in the open throttle case i.e. an increase in
magnitude on approach to the blade surface. The magnitude of radial
flows increase downstream reaching a maximum value near the trailing
edge ($x/c = 0.9$). The radial velocities are first larger in magnitude
on the trailing surface compared to leading surface but after midchord
the trend reverses itself. Similar behavior is observed in the open
throttle case and is due to the fact that the chordwise pressure

gradient on the trailing side is favorable to the flow after the midchord, while on the leading surface, the static pressure is almost a constant. The magnitude of radial flows are larger as compared to both the single blade and the open throttle cases. This can be also discerned by comparison of the plot of limiting streamline angles in Figures 18 and 43. The values in the throttled case are much higher than the other two cases. This is mainly brought about by the presence of larger radial and chordwise pressure gradients in the present case compared to zero pressure gradients in the case of the single blade and mild chordwise pressure gradients in the open throttle case.

The radial velocities are plotted in a hodograph plane in Figure 52, both on the leading and the trailing surfaces and are compared to the theoretically predicted form (Equation 115b). The agreement is quite good at most of the locations. It is seen clearly from the data, that the radial velocity does not go to zero at the location where $u = U_e$. As explained earlier in section 21., this is due to the fact that centrifugal force is larger than the radial pressure gradient force ($\sim V_\theta^2/r$) in the rotor channel and results in outward radial flows even if $\partial u_e/\partial y = 0$, at places where $U_e \sin\beta \neq \Omega r$.

5.3.4 Turbulent Intensities

Blade to blade distribution of all the three turbulent intensity components at various radial and chordwise locations inside the rotor channel are shown in Figures 53 to 73. The turbulent intensity components have been normalized by local total relative flow velocity (U). Figures 53 to 56 show the measurements near the hub. Figures 57 to 65

137
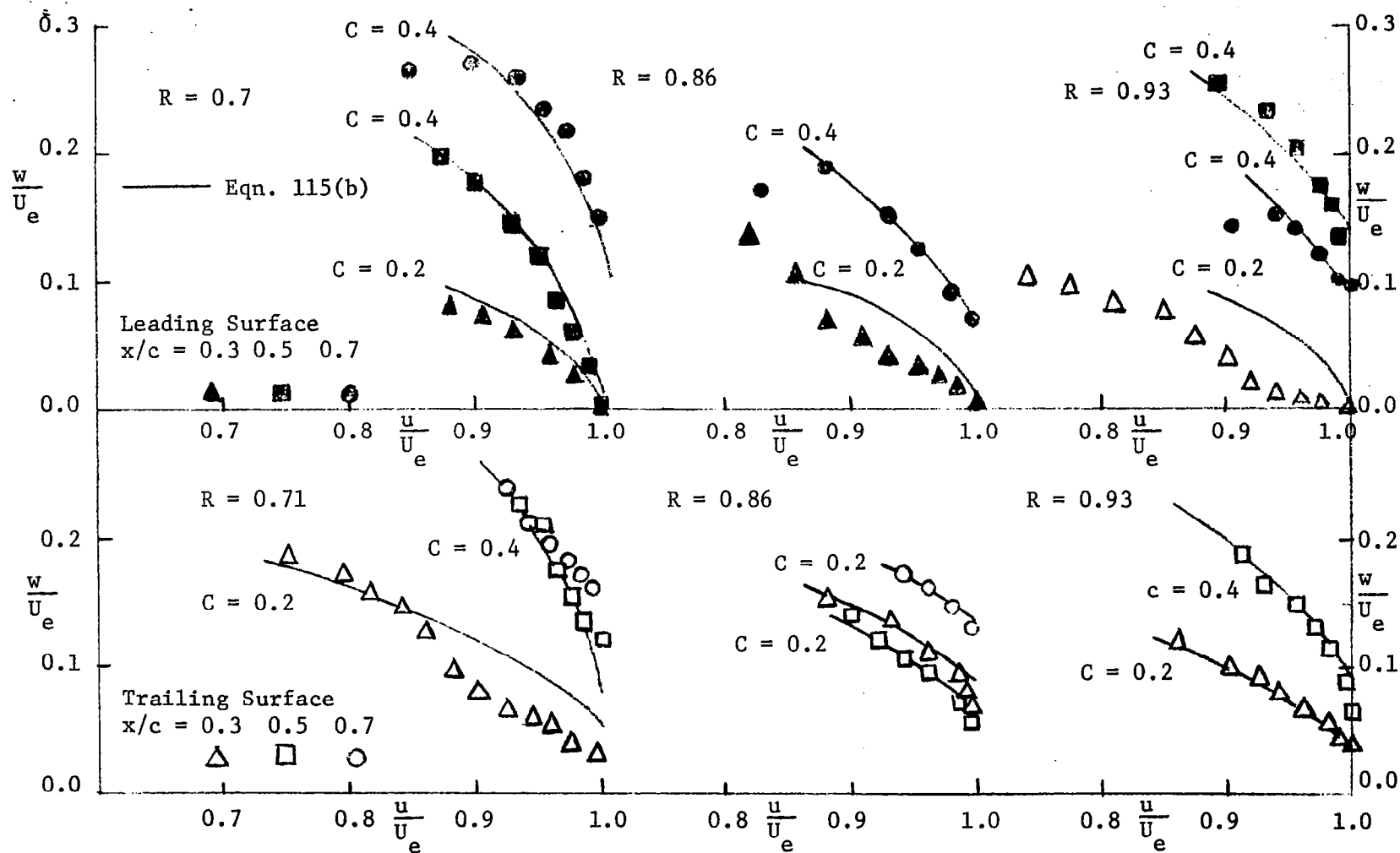
Figure 52.   Hodograph Plot of Velocity Profiles (Throttled Case).

$$\sqrt{\dfrac{\overline{u_i'^2}}{U}}$$

Legend (left plot):
$\sqrt{\overline{u'^2}}/U$ ———
$\sqrt{\overline{w'^2}}/U$ — — —
$\sqrt{\overline{v'^2}}/U$ – – –

0.21
0.20
0.19
0.18
0.17
0.16
0.15
0.14
0.13
0.12

0   12   24   36   48   60   72
Leading   Trailing
Surface   θ in Degrees   Surface

$$\dfrac{\overline{u_i'u_j'}}{U^2} \times 10^2$$

Legend (right plot):
$\overline{u'v'}/U^2$ ———
$\overline{u'w'}/U^2$ — — —
$\overline{v'w'}/U^2$ – – –

2.0
1.5
1.0
0.5
0.0
-0.5
-1.0
-1.5
-2.0

0   12   24   36   48   60   72
Leading   Trailing
Surface   θ in Degrees   Surface

Figure 53.   Blade to Blade Distribution of Turbulent Intensity and Stress Correlations·
at R = 0.52 and x/c = 0.3.

Figure 54. Blade to Blade Distribution of Turbulent Intensity and Stress Correlations at R = 0.572 and x/c = 0.5.

140

Figure 55. Blade to Blade Distribution of Turbulent Intensity and Stress Correlations at R = 0.568 and x/c = 0.7.

141

Figure 56. Blade to Blade Distribution of Turbulent Intensity and Stress Correlations at R = 0.564 and x/c = 0.9.

142

Figure 57. Blade to Blade Distribution of Turbulent Intensity and Stress Correlation at R = 0.712 and x/c = 0.1.

143

Figure 58. Blade to Blade Distribution of Turbulent Intensity and Stress Correlations at R = 0.709 and x/c = 0.3.

Figure 59. Blade to Blade Distribution of Turbulent Intensity and Stress Correlations at R = 0.718 and x/c = 0.5.
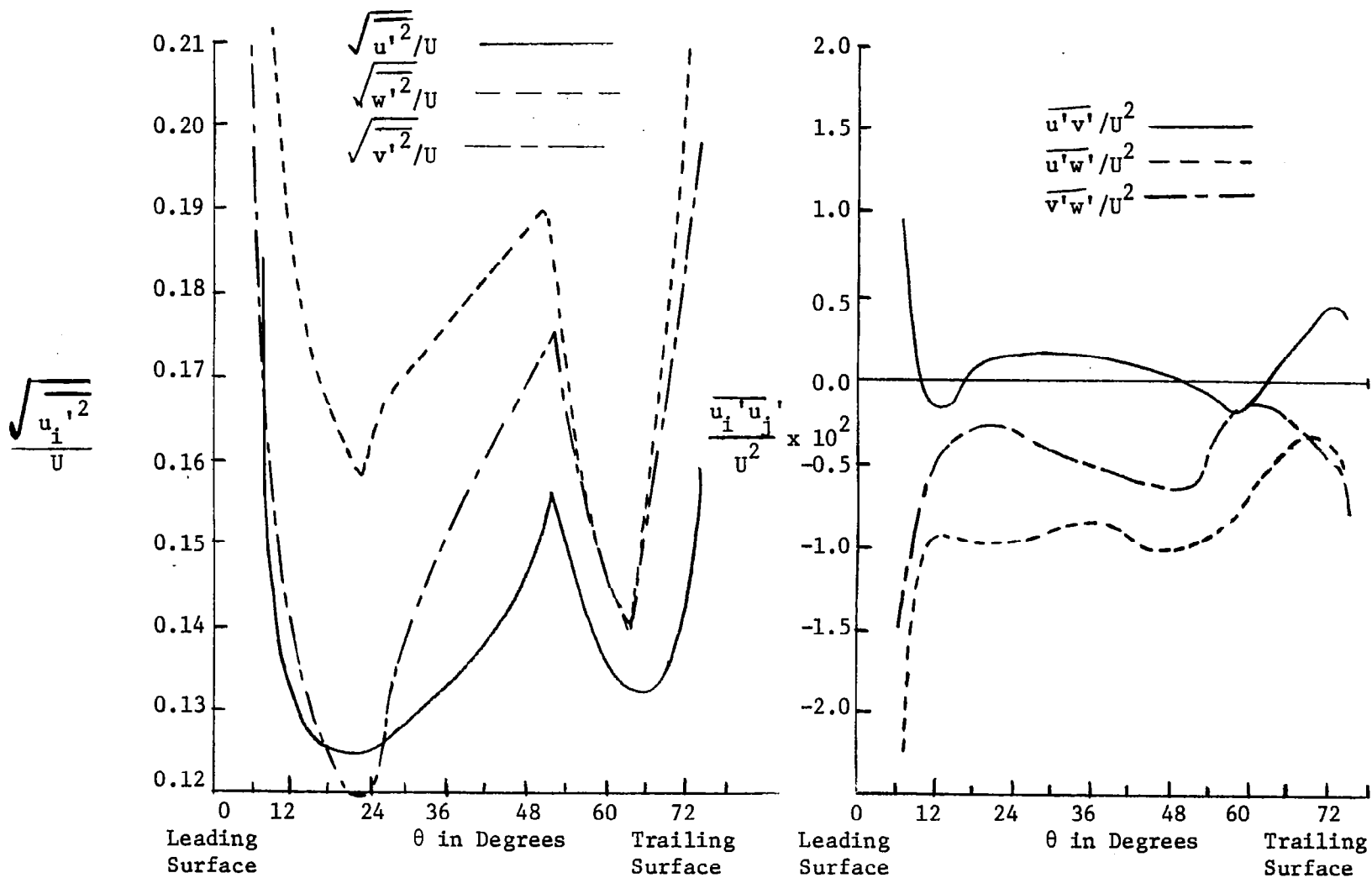
145

Figure 60. Blade to Blade Distribution of Turbulent Intensity and Stress Correlations at R = 0.712 and x/c = 0.7.

Figure 61.   Blade to Blade Distribution of Turbulent Intensity and Stress Correlations at R = 0.719 and x/c = 0.9.

147

Figure 62. Blade to Blade Distribution of Turbulent Intensity and Stress Correlations at R = 0.863 and x/c = 0.3.

Figure 63. Blade to Blade Distribution of Turbulent Intensity and Stress Correlations at R = 0.861 and x/c = 0.5.

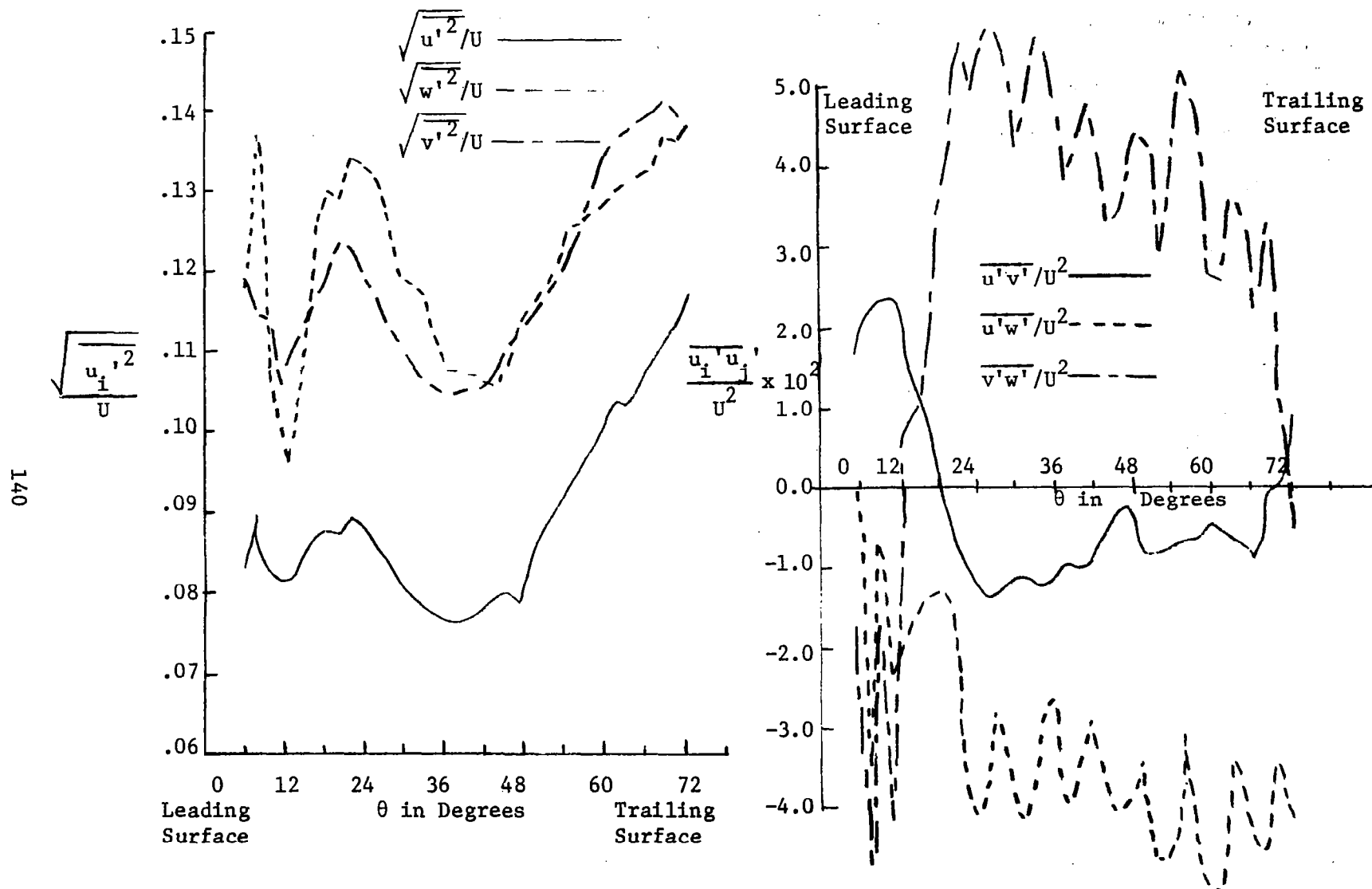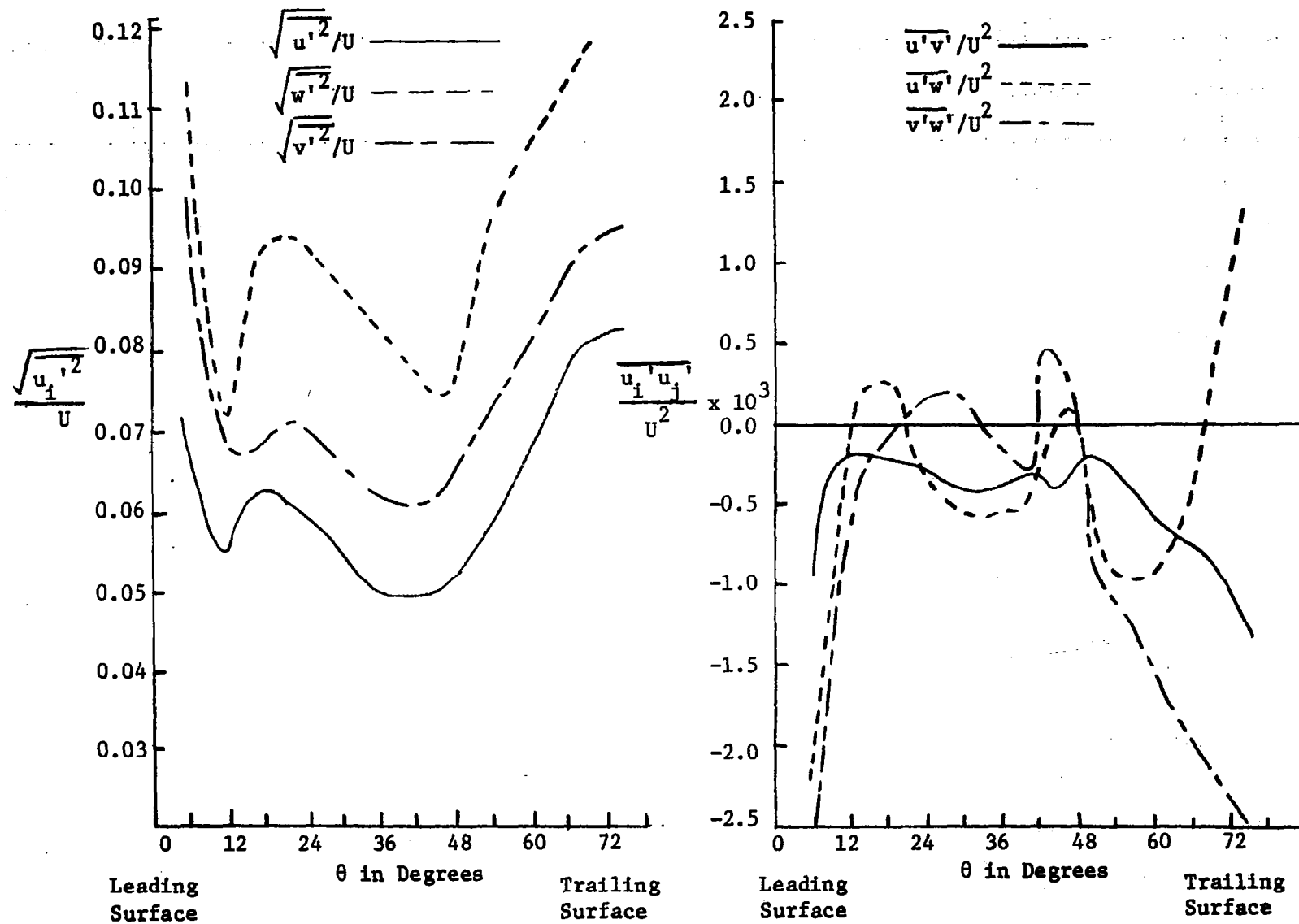Figure 64. Blade to Blade Distribution of Turbulent Intensity and Stress Correlations at R = 0.860 and x/c = 0.7.

Figure 65. Blade to Blade Distribution of Turbulent Intensity and Stress Correlations at R = 0.866 and x/c = 0.9.
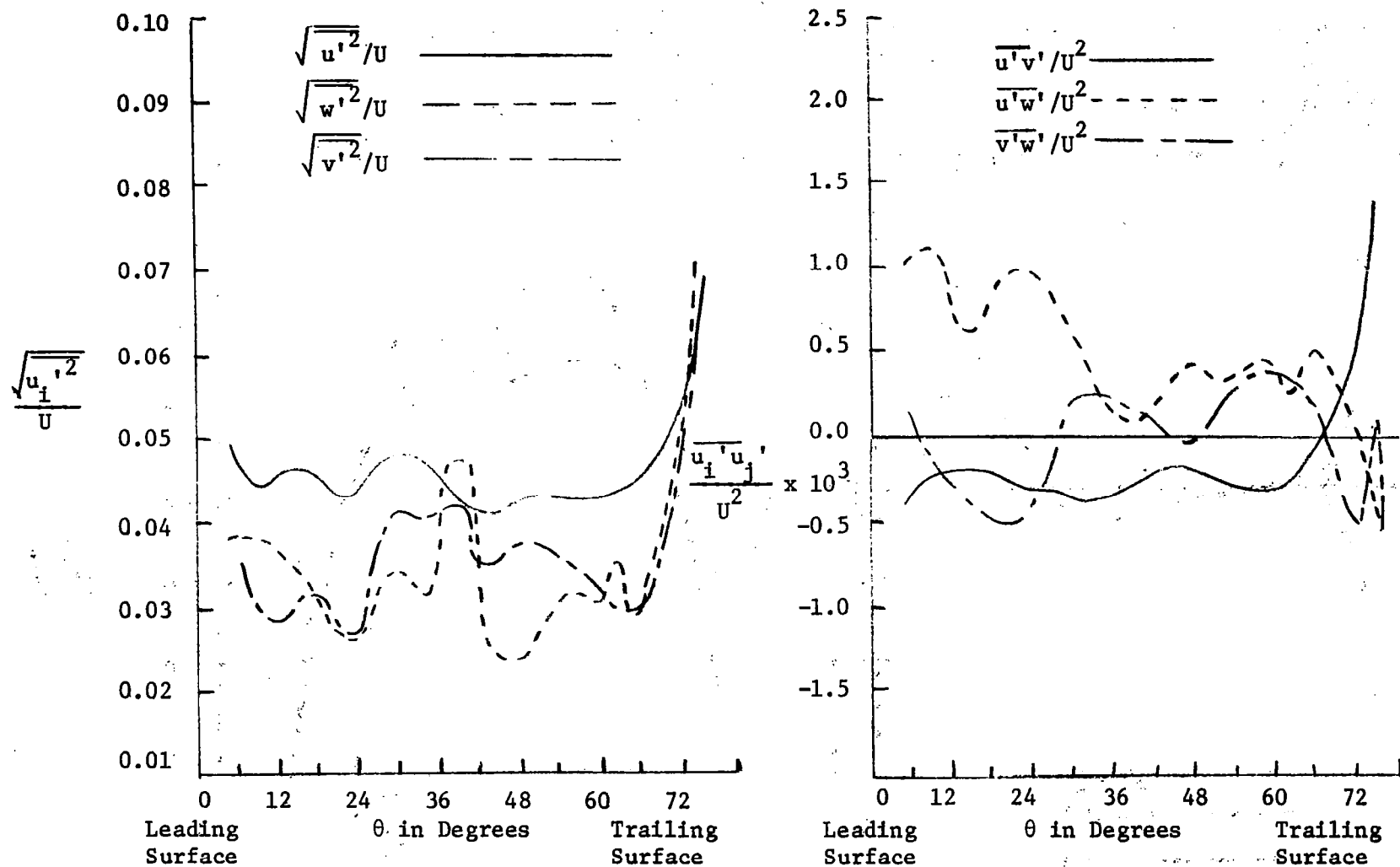
Figure 66. Blade to Blade Distribution of Turbulent Intensity and Stress Correlations at R = 0.911 and x/c = 0.1.
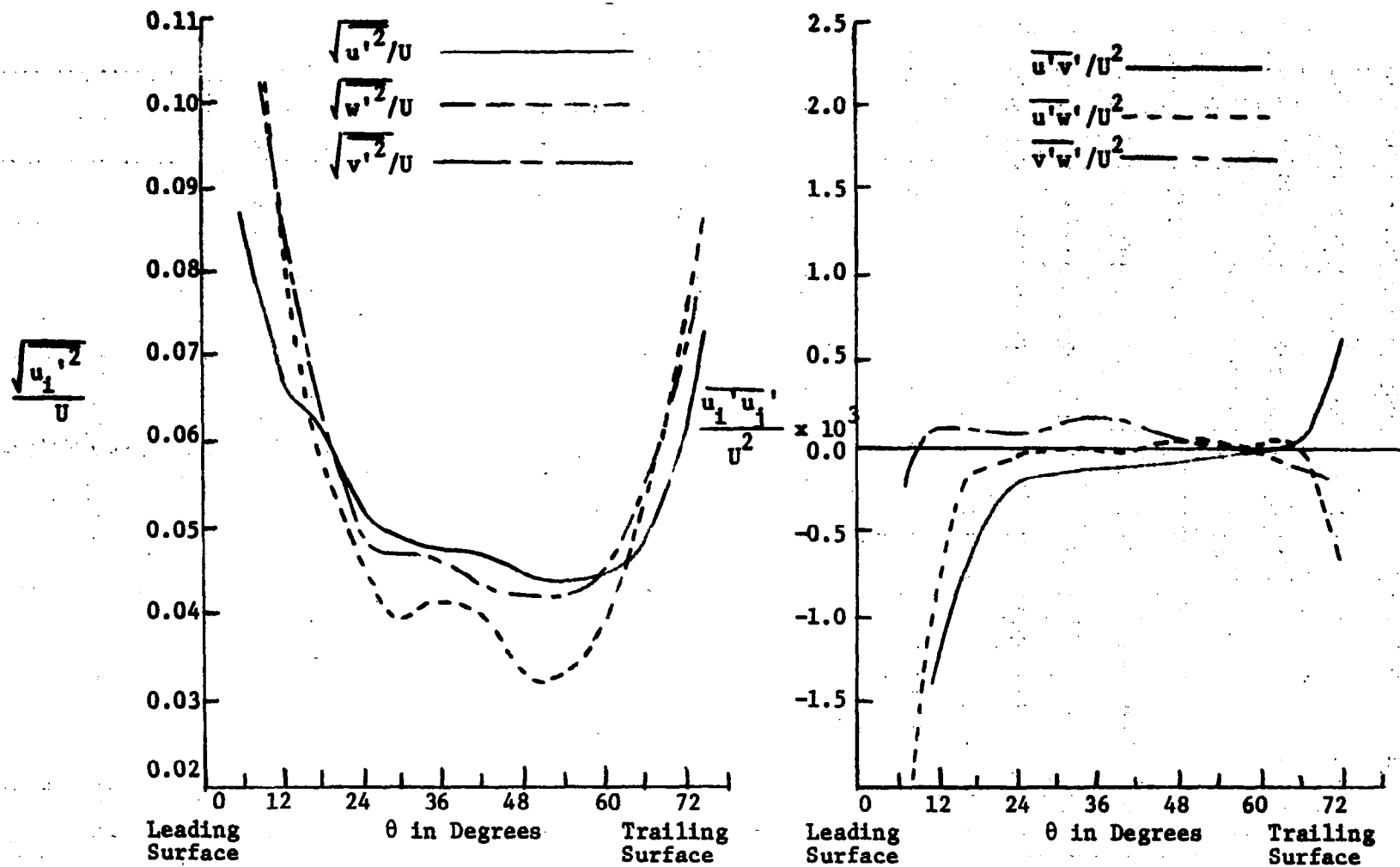
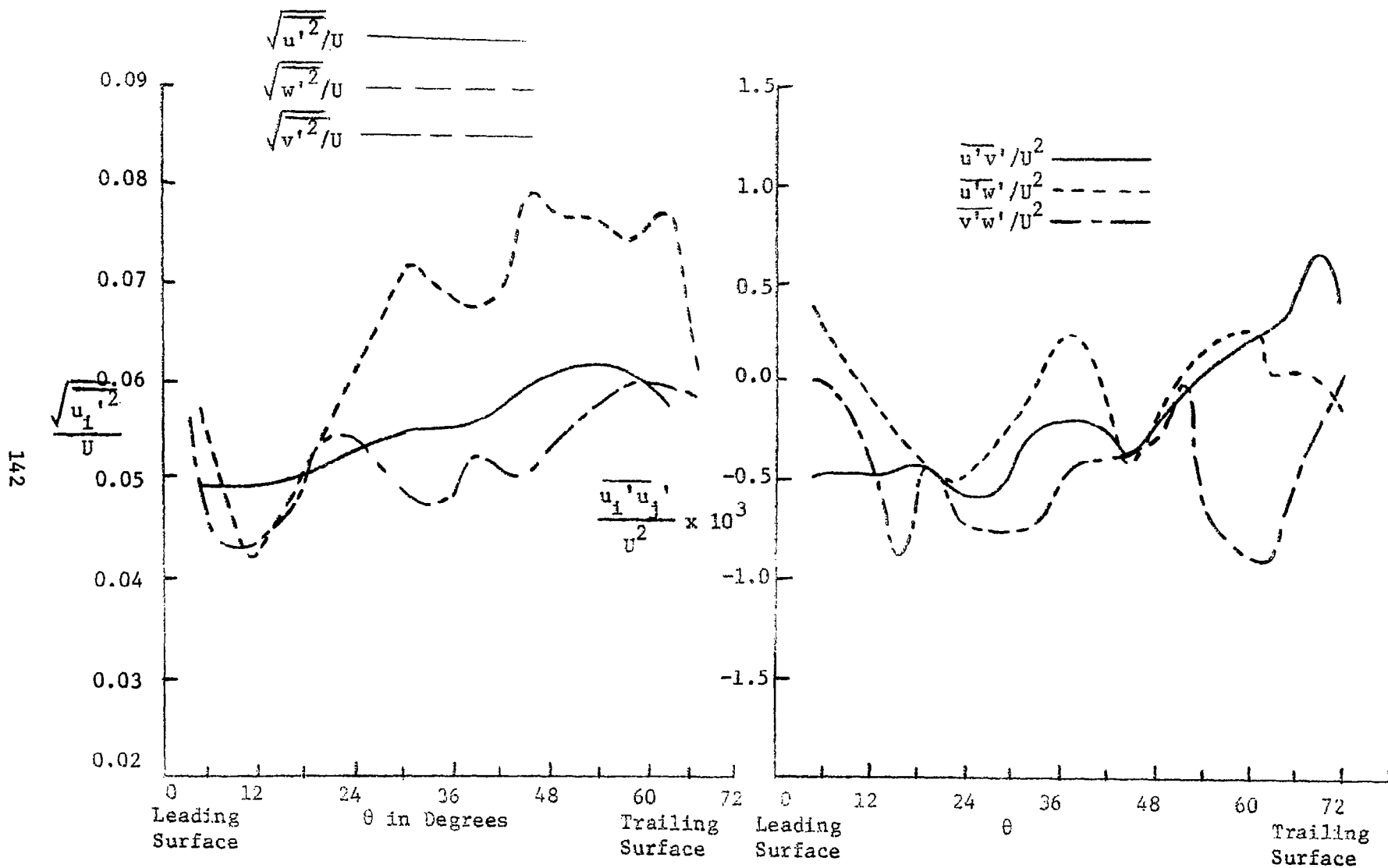Figure 67. Blade to Blade Distribution of Turbulent Intensity and Stress Correlations at R = 0.942 and x/c = 0.3.
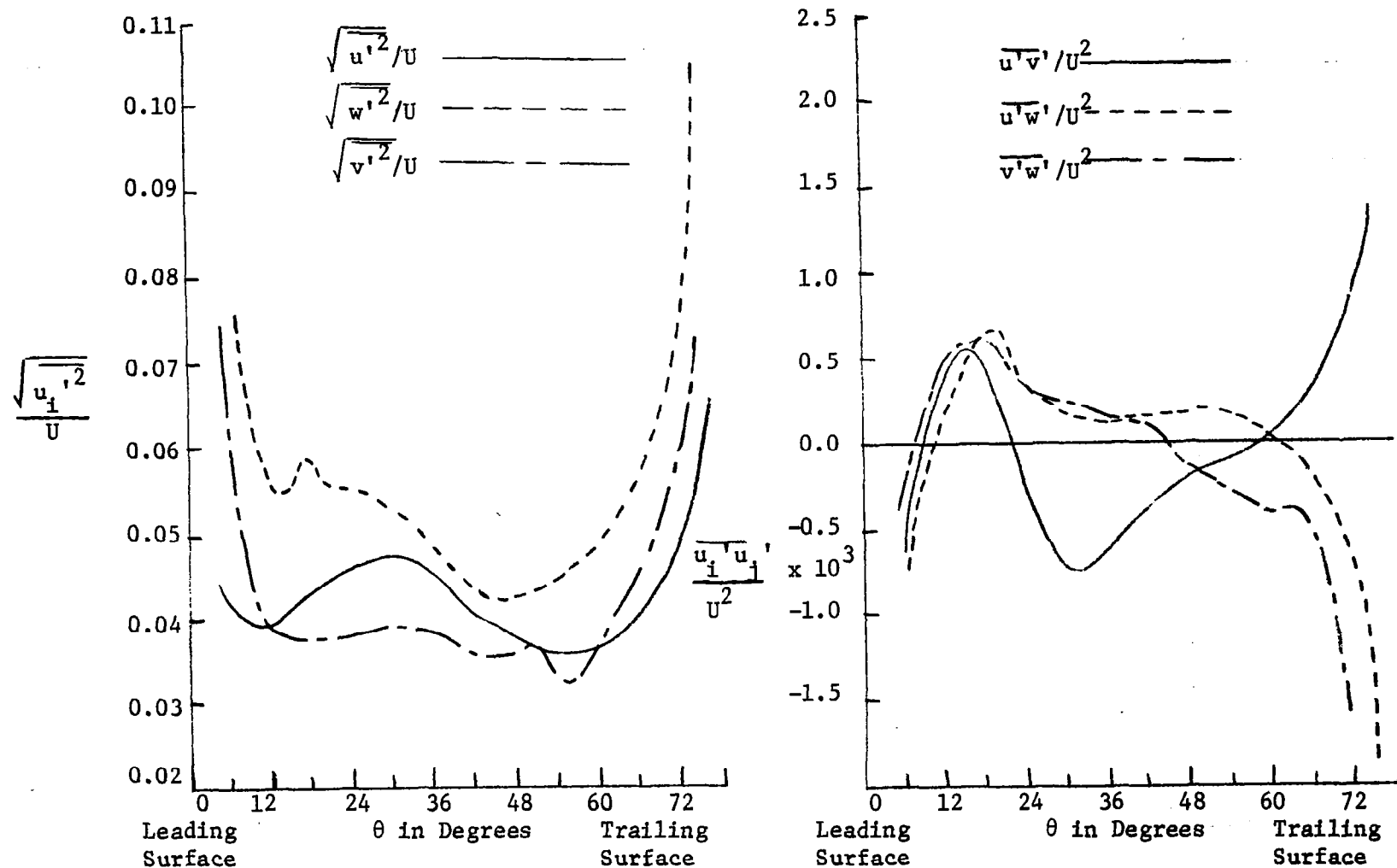
Figure 68.   Blade to Blade Distribution of Turbulent Intensity and Stress Correlations
at R = 0.935 and x/c = 0.5.
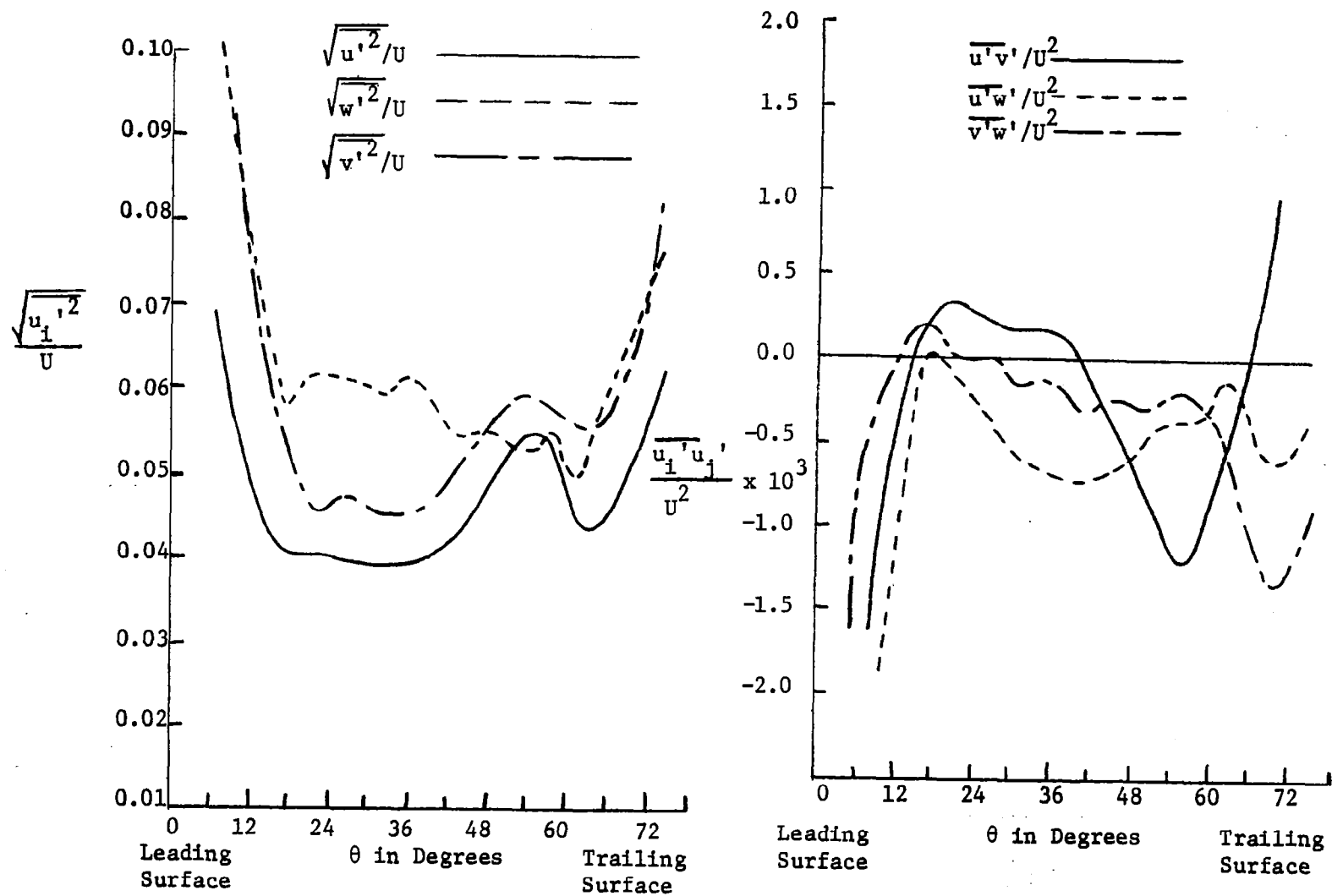
Figure 69. Blade to Blade Distribution of Turbulent Intensity and Stress Correlations at R = 0.938 and x/c = 0.7.
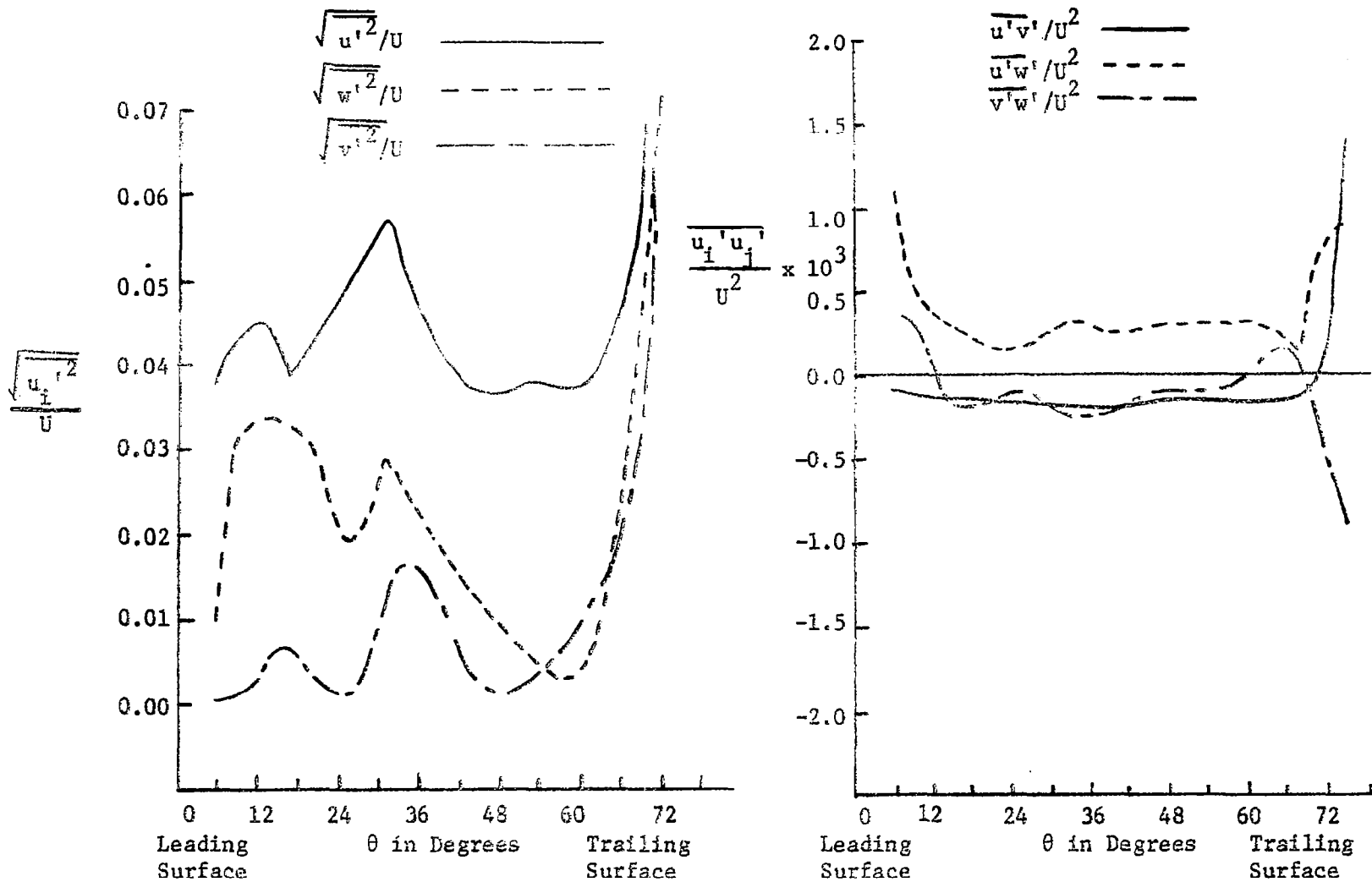
155
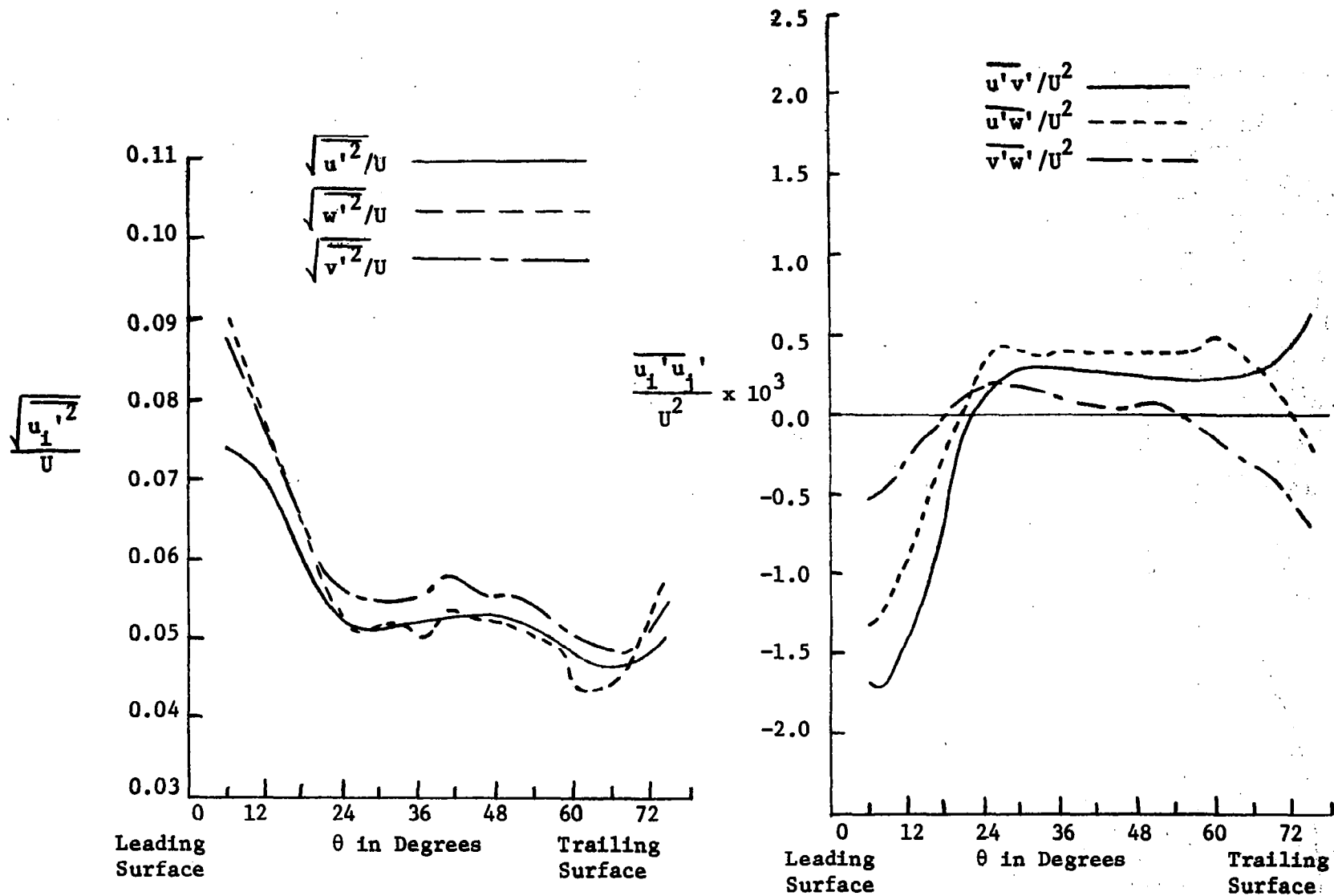
Figure 70. Blade to Blade Distribution of Turbulent Intensity and Stress Correlations at R = 0.981 and x/c = 0.3.

156
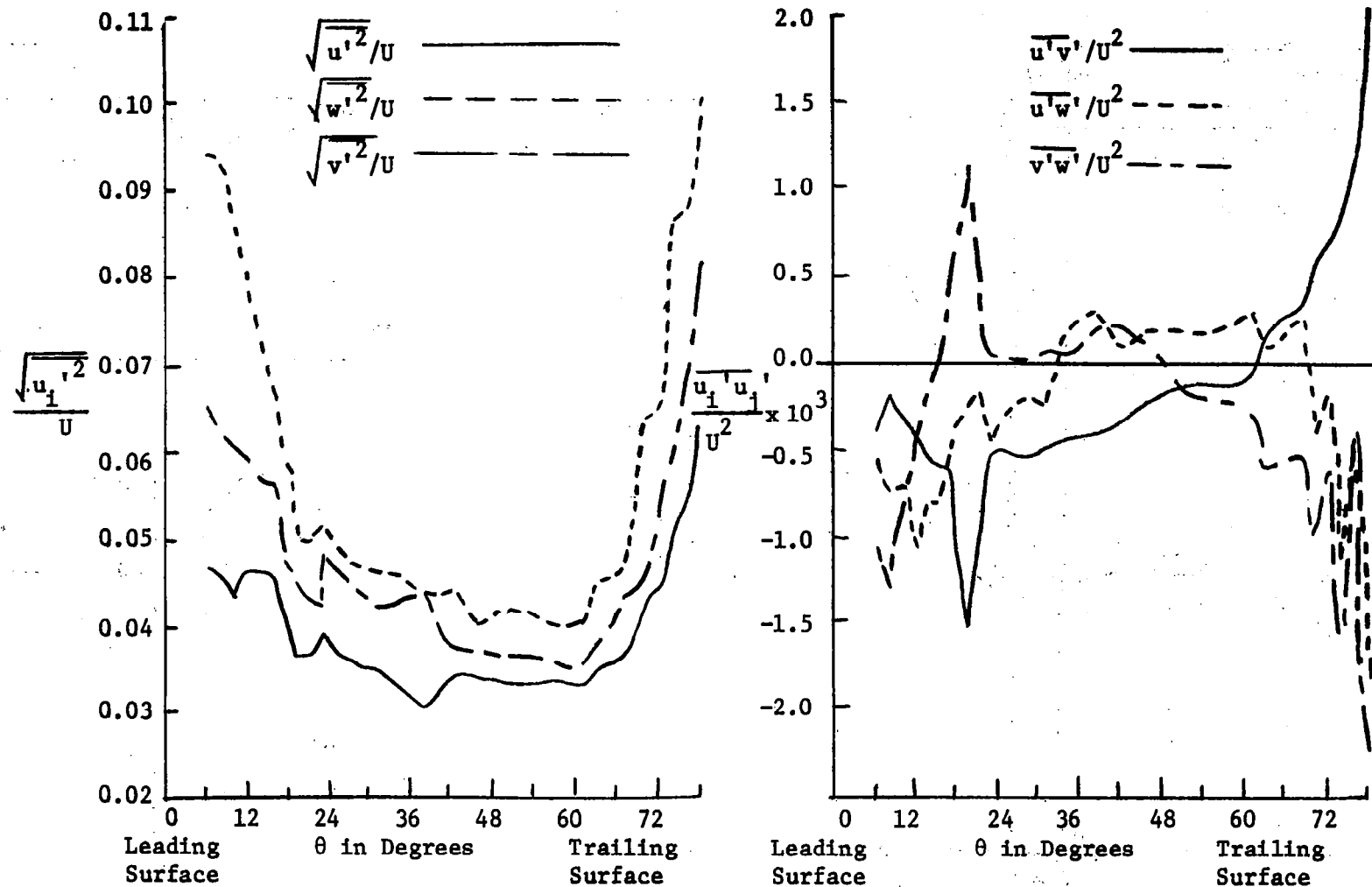
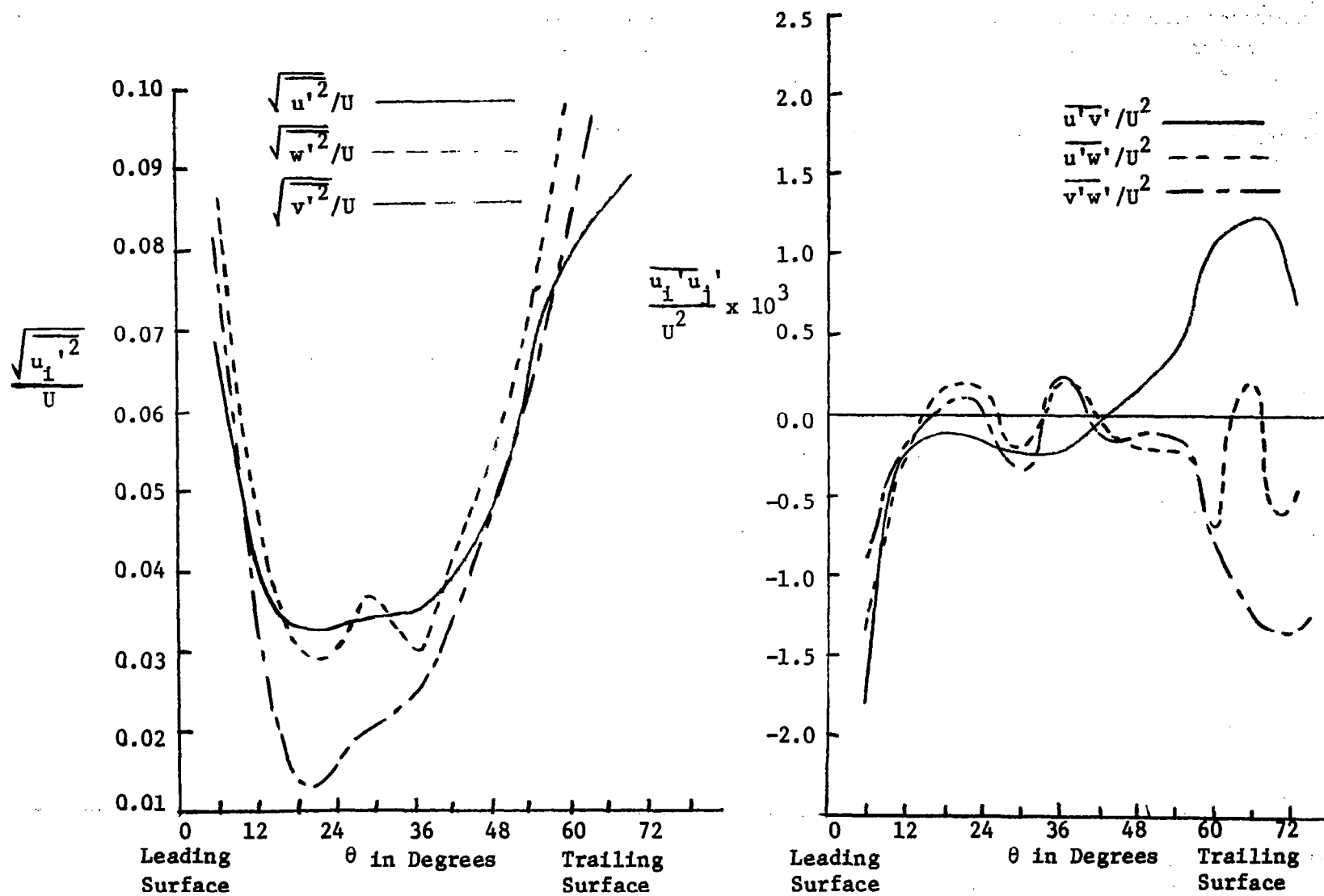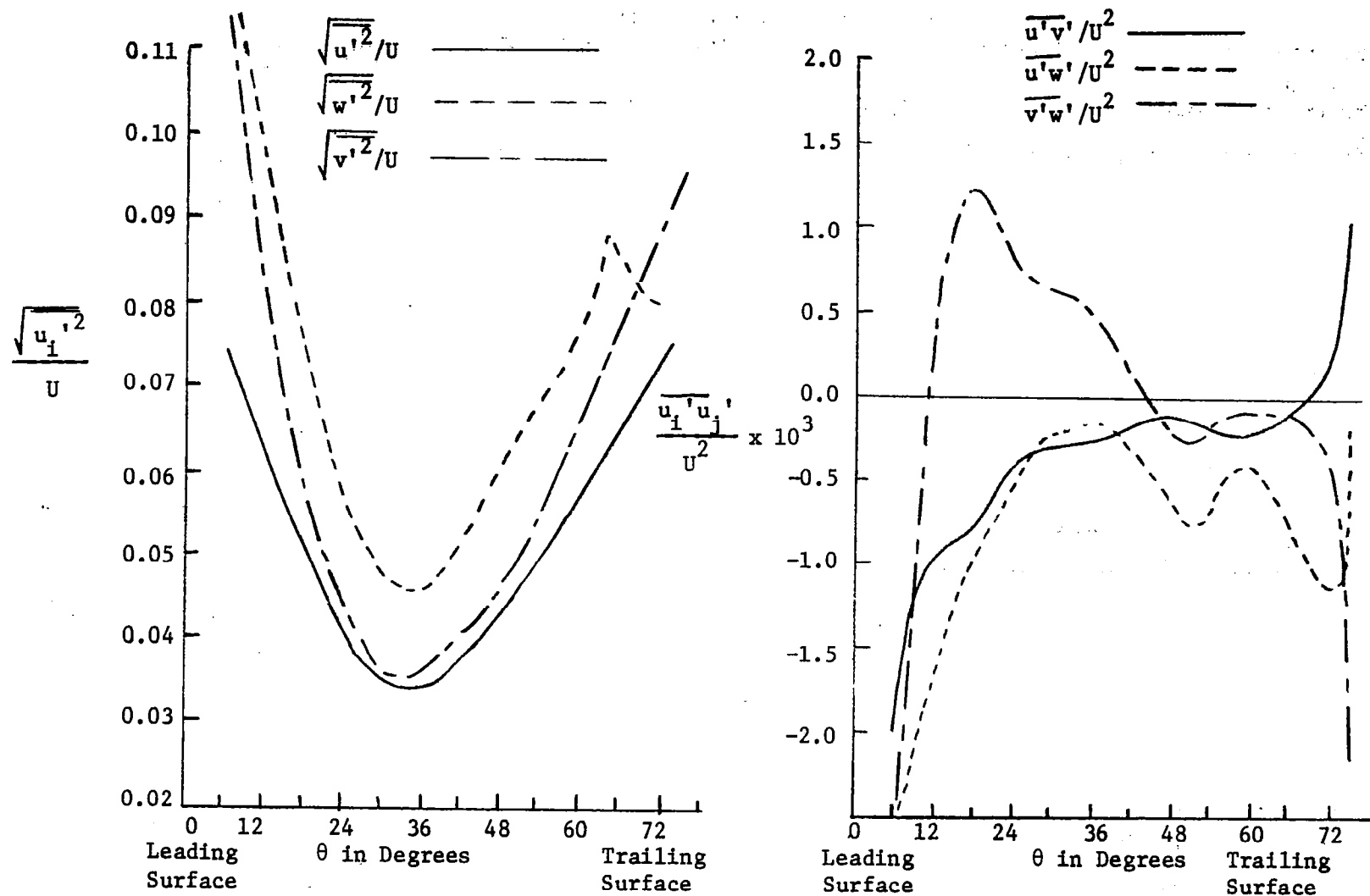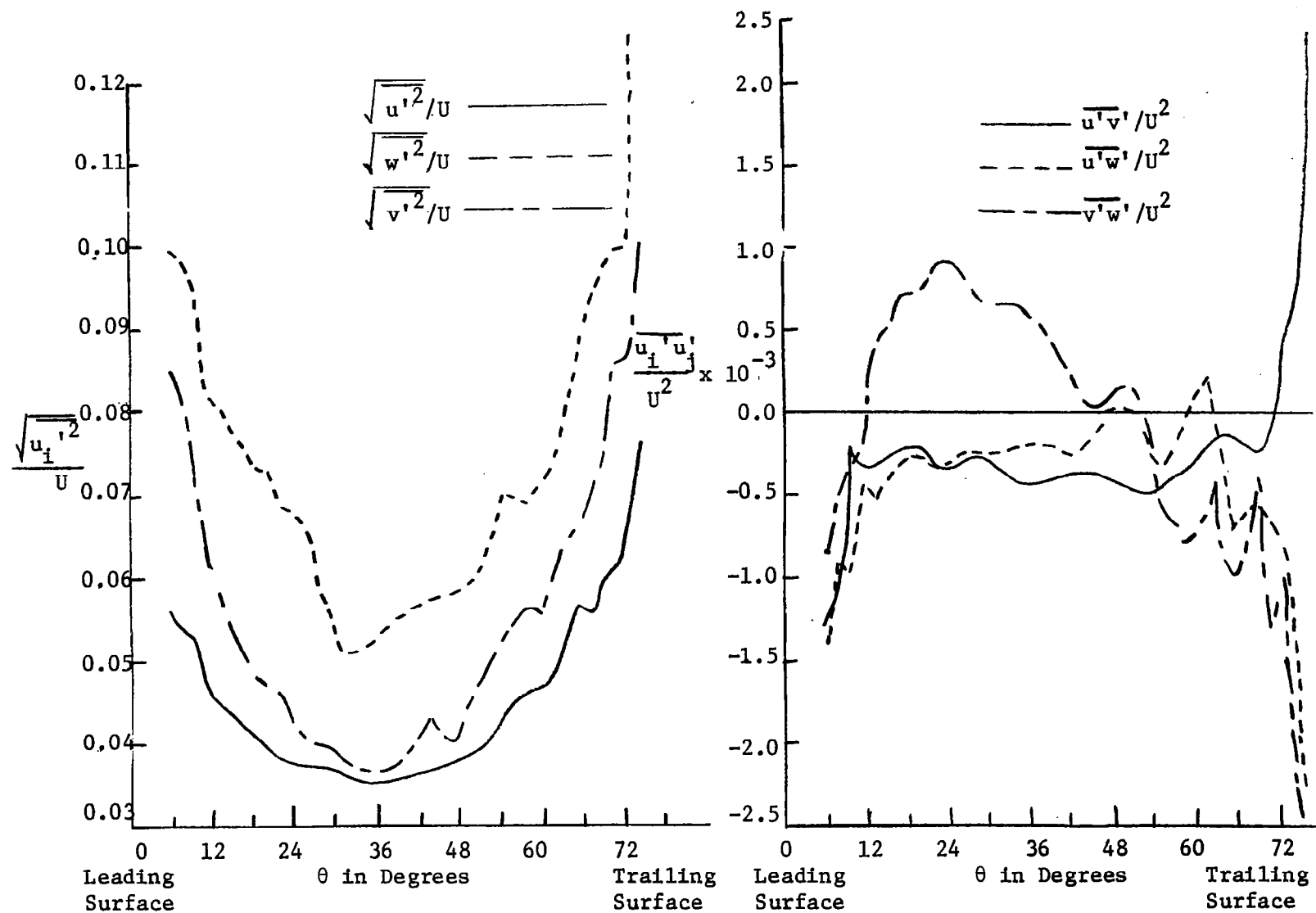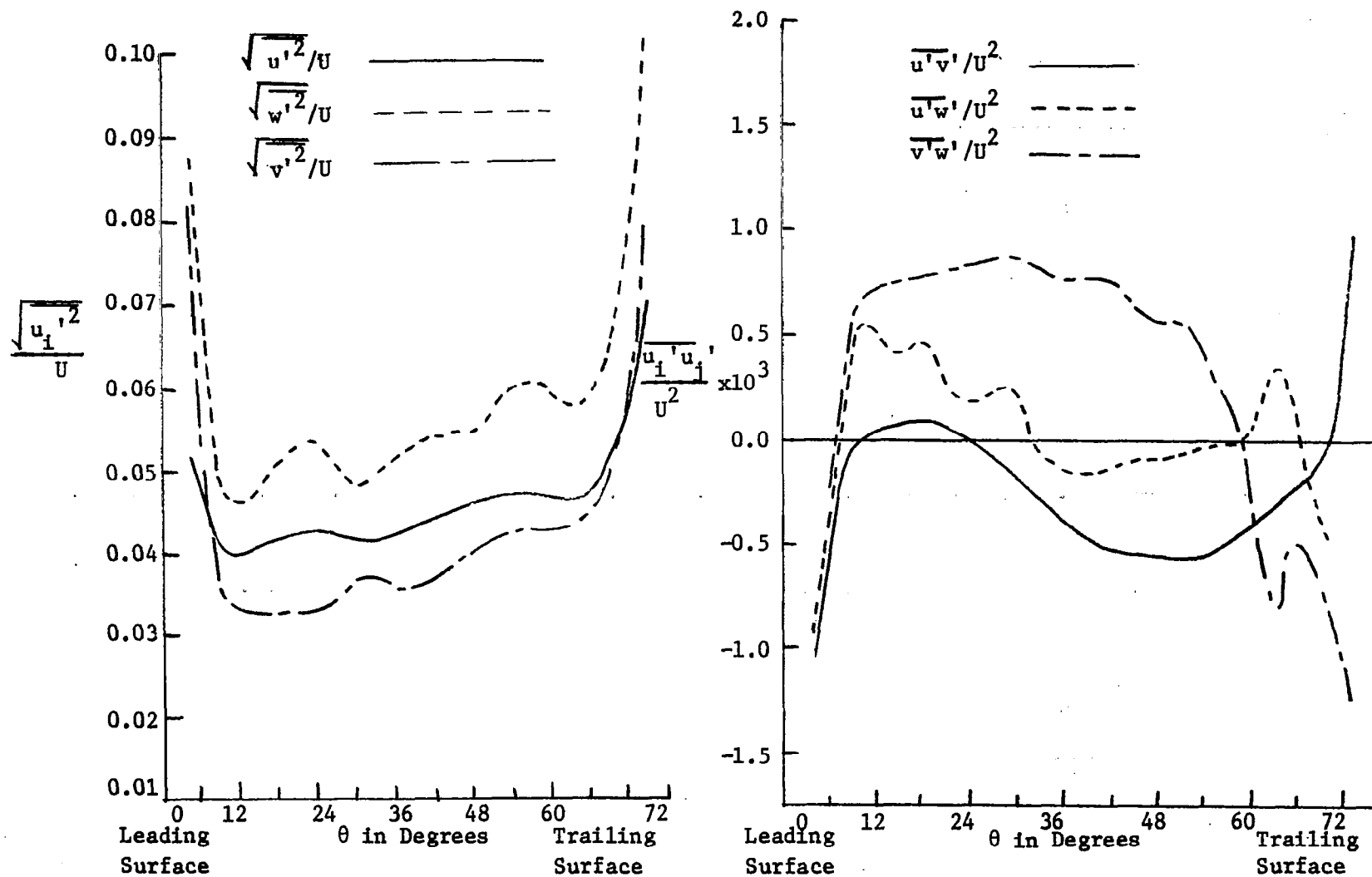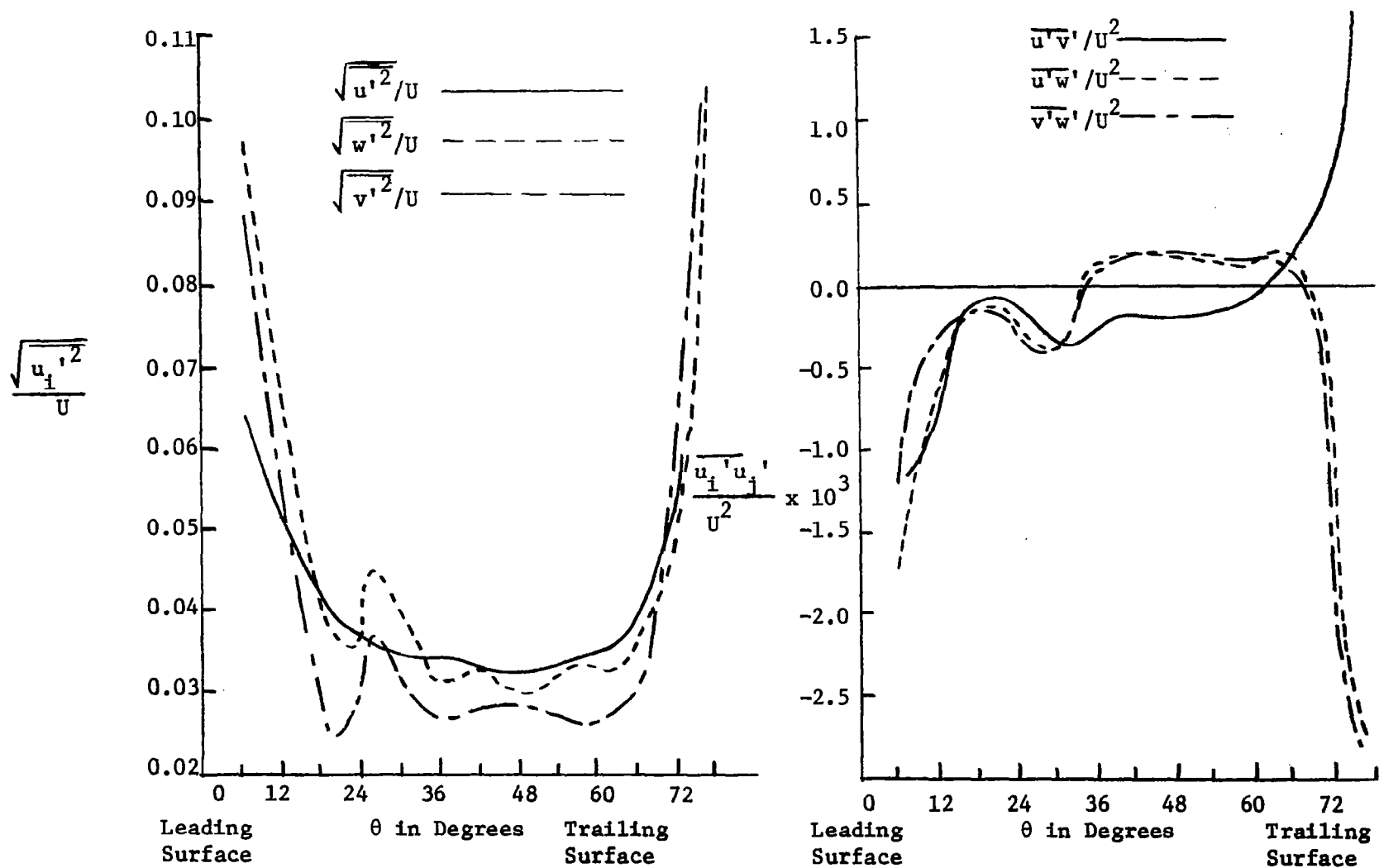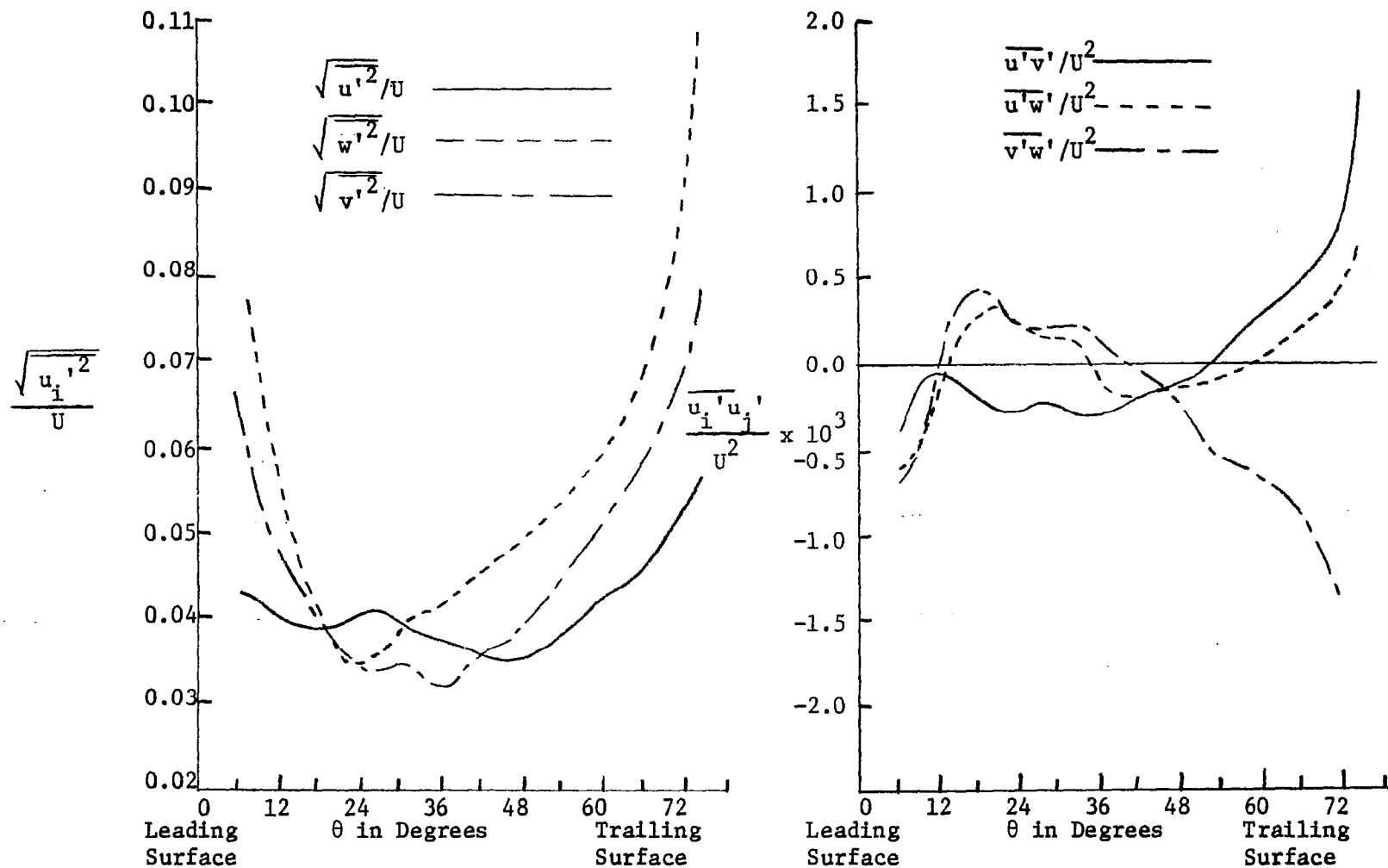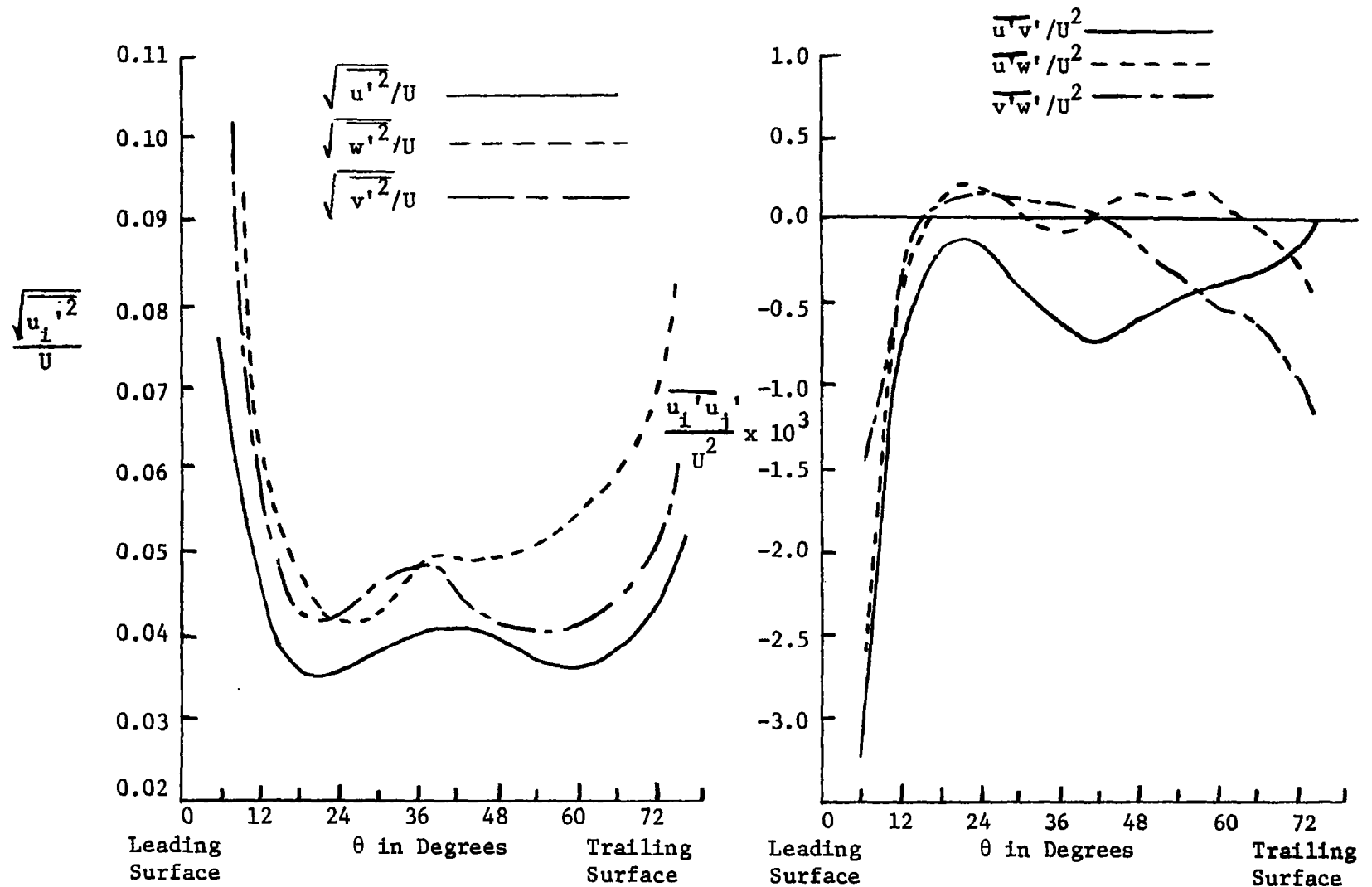Figure 71. Blade to Blade Distribution of Turbulent Intensity and Stress Correlations at R = 0.983 and x/c = 0.5.

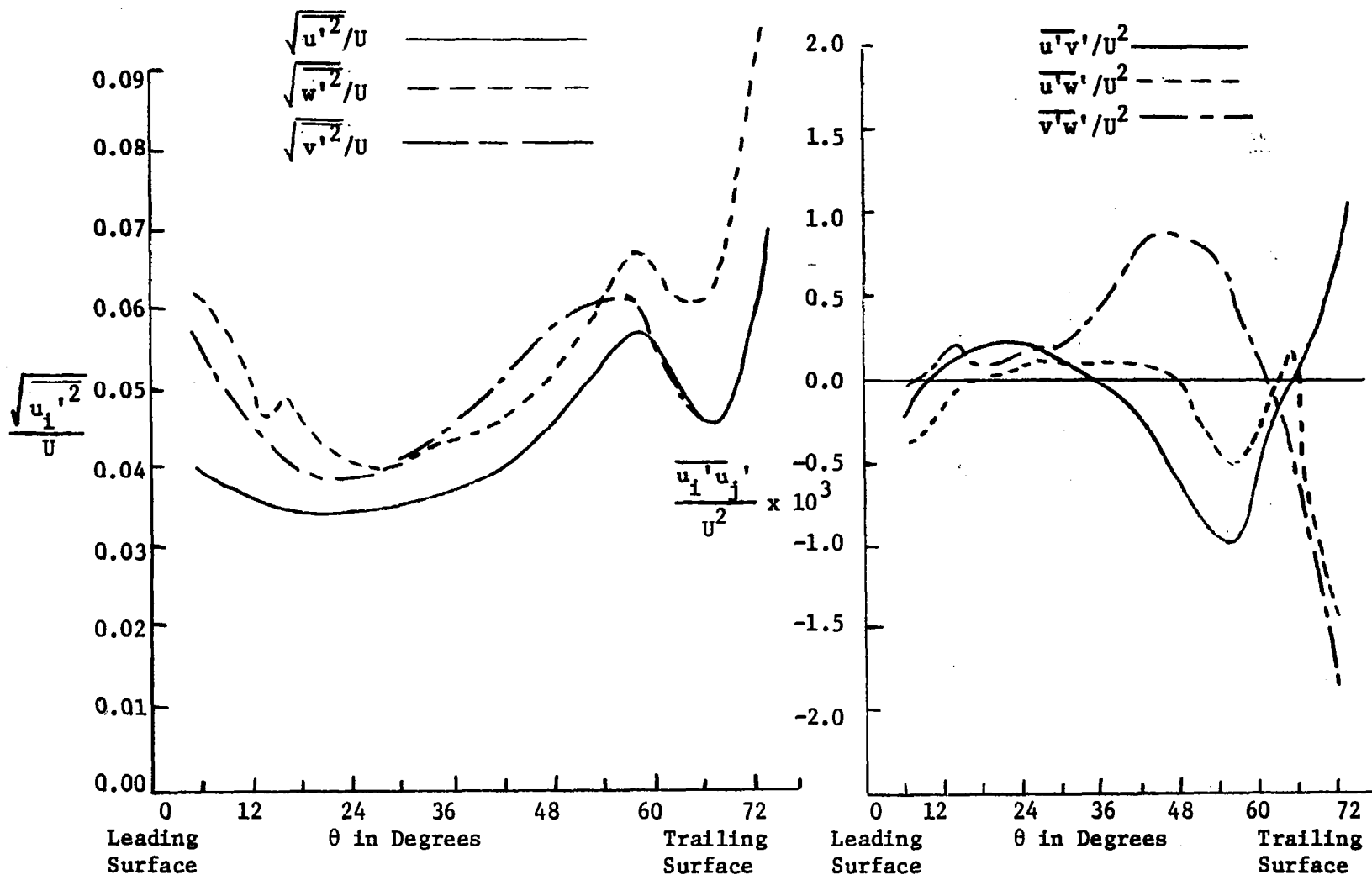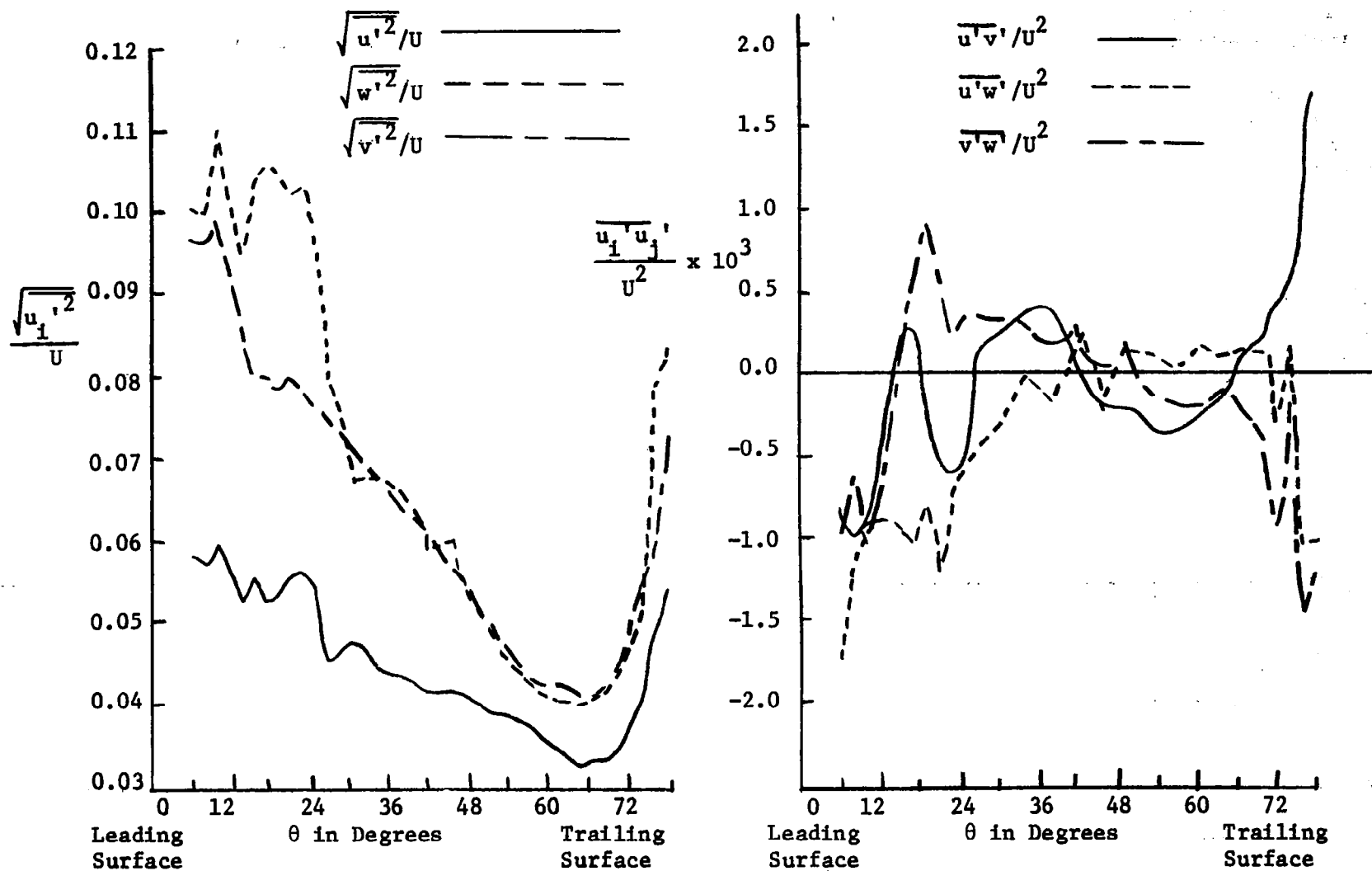Figure 72. Blade to Blade Distribution of Turbulent Intensity and Stress Correlations at R = 0.983 and x/c = 0.7.
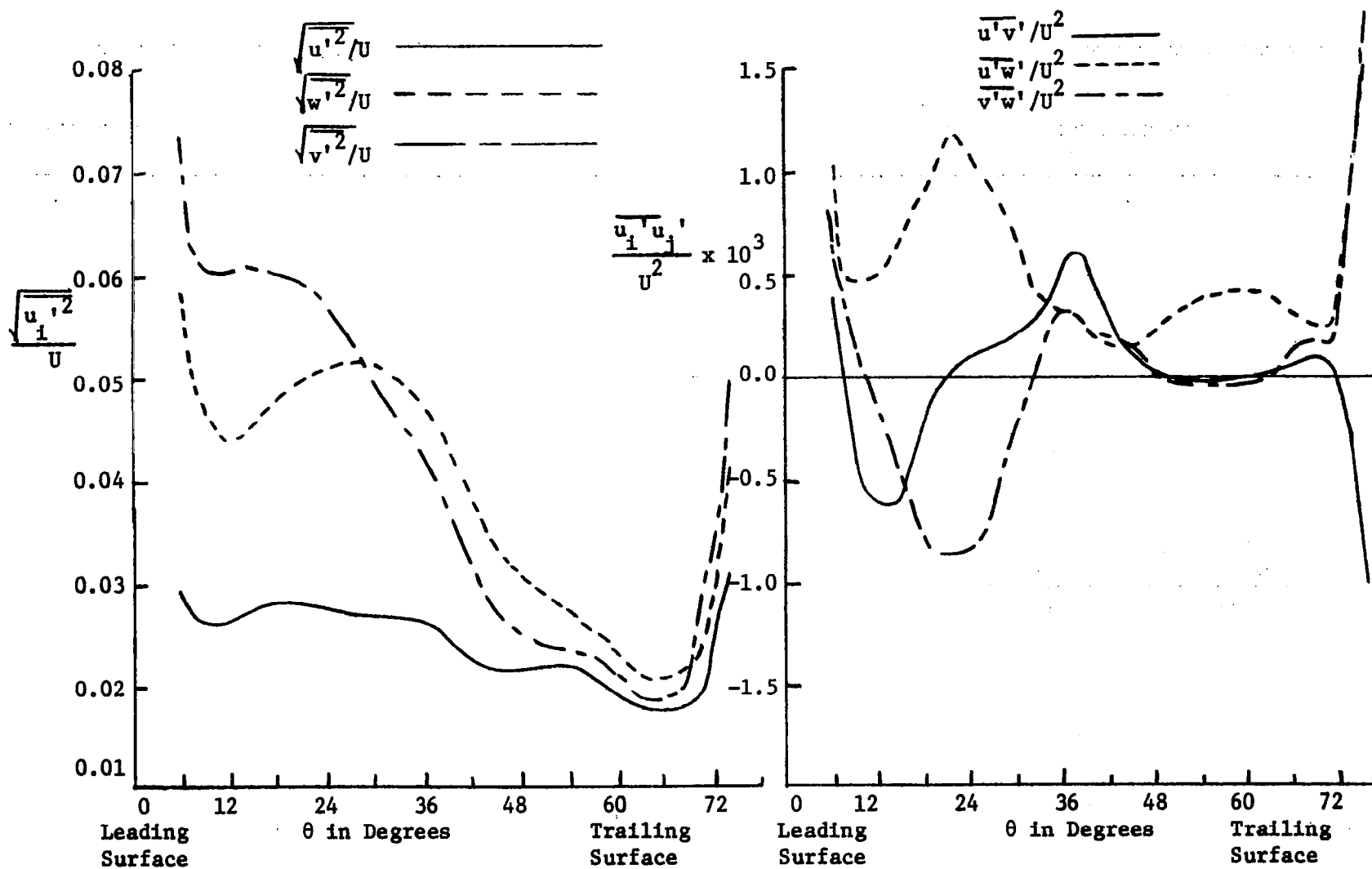
Figure 73. Blade to Blade Distribution of Turbulent Intensity and Stress Correlations at R = 0.98 and x/c = 0.9.

show the measurements near the midradius and Figures 66 to 73 present the data near the tip radius. Experimental accuracy in measurements is estimated to be within 5% for all intensity components. The analysis of errors in turbulence intensities is described in Appendix B (section B.4).

The magnitude of turbulence intensities is higher near the hub and tip regions due to the effect of end walls. The values are highest near the hub ($\sim$16% at x/c = 0.3 as shown in Figure 53) which operates at a maximum flow incidence (4°). The mean velocity profiles (Figs. 45 and 51) have shown the presence of hub wall boundary layer and this may account for the large values of turbulence intensities in this region.

The free stream turbulence level at all radii in the entrance region is quite high. It varies from 20% near the hub to 6% near the tip at x/c = 0.1. The free stream turbulence level is found to decrease with distance inside the rotor channel. It decreases from about 8% (Figure 55) and 4.5% near the tip at x/c = 0.7 (Figure 72). On the other hand, near the mid radius, the free stream turbulence level is almost constant at R = 0.7 (Figures 57 and 61). It increases from 3.5% at x/c = 0.3 (Figure 62) to 5% (Figure 65) at x/c = 0.9 for R $\simeq$ 0.86. This is brought about mainly by the turbulent mixing of the flow in the channel in this region.

The turbulent intensities increase on approach to the blade surfaces. This increase is due to the production of turbulence by mean velocity gradients in the blade boundary layers. They should decrease very near the surface, in the viscous layer but since the measurements could not be taken for distances less than $y^{+} < 50$ (due to

160

finite size of the probe) this phenomenon has not been observed
experimentally.

Except at $x/c = 0.1$, the magnitude of radial intensity component
$(\overline{w'^2})$ is larger than both the streamwise $(\overline{u'^2})$ and blade normal $(\overline{v'^2})$
intensity components. This observed behavior is opposite to known
behavior for stationary two-dimensional boundary layers where $\overline{u'^2} > \overline{w'^2} >$
$\overline{v'^2}$ and clearly indicates that the turbulence characteristics are
markedly changed by the effect by the effect of rotation. Experimental
data of Gorton (23) inside the rotor passage of a three bladed rocket
pump inducer and of Raj (46) in rotor wakes confirm this conclusion.
Qualitatively, it is shown in Appendix C that, in compressors and
pumps where the direction of rotation is opposite to that of the
relative flow, the rotation yields an extra production term in the
transport equation (Appendix C, Equation C-3) of radial intensity
component $(\overline{w'^2})$ and a suppression term in streamwise direction provided
$\overline{u'w'}$ correlation is negative. Shear stress measurements in Figures 53
to 73 show that this is generally true inside the rotating blade
boundary layers in axial flow machinery.

However, at $x/c = 0.1$, Figures 57 and 66 show that $\overline{u'^2} > \overline{w'^2} > \overline{v'^2}$
which is similar to the observed behavior in stationary two-dimensional
boundary layers. An examination of transport equations show that it is
possible to have suppression of $\overline{w'^2}$ and production of $\overline{u'^2}$ if the
correlation $(\overline{u'w'})$ is positive. The turbulent stress data in Figures
57 and 66 indicates that this is true at $x/c = 0.1$.

Turbulence intensity measurements shown in Figures 58 to 65
represent data free of endwall and leading edge effects and is
representative of flows in axial-flow rotors operating at design flow

conditions. It is seen that turbulence intensity components increase downstream with distance from $x/c = 0.3$ to $x/c = 0.9$ on the leading side and decrease on the trailing side. This is mainly brought about by the imposed chordwise pressure gradients (Figure 44) in the passage in this region. These pressure gradients are very small on the leading side and large and favorable on the trailing side.

Near the tip radius in the "interference region" near the trailing edge at $x/c = 0.7$ and 0.9, the turbulent intensities are observed to increase significantly compared to the free stream values (e.g. Figures 65, 69, 73). As explained in the section on Mean Velocity Profiles, the two blade boundary layers have completely merged with each other and their interaction with the annulus wall produces a large turbulent mixing zone in the central region of the passage. Gorton's (23) result also confirms this observed behavior for a three bladed inducer. Unlike the two-dimensional fully developed boundary layers in stationary passages or pipes, the streamwise velocity profile in this interference region shows a dip with inward radial flows. There exist finite mean velocity gradients even in the mid passage as shown in Figures 48 and 49 at $R = 0.98$ and result in an increased production of turbulence in this region.

5.3.5 Turbulent Shear Stresses

Figures 53 to 73 also show the blade to blade distribution of all the three turbulence shear stress correlations derived from the hot wire measurements described earlier in Chapter IV. It should be remarked that the mean velocity, turbulence intensity and shear stresses are measured simultaneously at the same location. Expected error in the

measurement of fluctuating voltage (Appendix B) cross-correlations is less than 6.7% for $\overline{e_1 e_2}$ and $\overline{e_1 e_3}$ and 9.1% for $\overline{e_2 e_3}$ respectively. This should result in a maximum anticipated error of less than 9% in velocity cross-correlations or the turbulent shear stresses. Because of other miscellaneous errors the shear stress data should be used with caution.

The turbulent stresses are small in the center of the channel (except in the interference region) and increase in magnitude on approach to the blade surface, and this trend is similar to turbulence intensity components. This is brought about by the production of these stresses by the mean velocity gradients as shown in transport equations given in Appendix C (Equations C-4 and C-6) and is common to all wall bounded shear flows.

However, unlike two-dimensional boundary layers where only the streamwise turbulent shear stress component $(-\overline{u'v'})$ is present, the data clearly shows that the other two stress components (viz. $(-\overline{u'w'})$ and $(-\overline{v'w'})$) are also of the same order of magnitude as $(-\overline{u'v'})$. In three-dimensional stationary boundary layers the component $(-\overline{v'w'})$ is present due to finite value of the production term in its transport equation (Equation C-6) in Appendix C. However, the correlation $(-\overline{u'w'})$ which represents a cross-correlation normal to boundary layer is found to be negligible because the production term due to mean velocity gradients are small in this direction. In the present case, in addition to mean velocity gradients normal to the boundary layer, there are large mean velocity gradients in radial and chordwise directions (Figures 45 to 49) and result in extra production terms.

It is evident from Equations (C-4), (C-5) and (C-6) of Appendix C, that the effect of rotation in our case (where $\Omega_y = -\Omega\sin\beta$, $\Omega_x = \Omega\cos\beta$,

β varying from 78° at the hub to 84° at the tip) is to increase the streamwise component $(-\overline{u'v'})$ of stress and decrease the other two components $(-\overline{v'w'}$ and $\overline{u'w'})$. The experimental investigation on a single blade (Ref. 17) as well as the present set of data for the streamwise component $(-\overline{u'v'})$ seem to confirm this trend. It is also evident from Equations (C-4) to (C-6) that the curvature terms which are small in this particular case, seem to have effects opposite to that of rotation in the present investigation. The effects of curvature for a swirling jet are discussed by Pratte and Keffer (47).

As explained in the section on turbulent intensities, only the data near the mid radius for $x/c > 0.3$ in Figures 58 to 65 is free from leading edge incidence and end wall effects. It represents the turbulence behavior in the turbulent boundary layers on the blades of turbomachinery rotors operating at designed flow conditions.

It is seen that the correlations $\overline{u'v'}$, $\overline{v'w'}$ and $\overline{u'w'}$ follow the same trend on the leading side which means that the streamwise, radial and blade normal turbulent shear stresses behave similarly. On the trailing side, they follow the opposite trend i.e. $(\overline{u'v'})$ and $(\overline{v'w'})$ correlation has values in between the two. This difference is attributed to the effect of chordwise pressure gradients (Figure 44) in the two cases. On the leading side, for $x/c > 0.3$, the chordwise pressure gradients are small and therefore production terms in Equations (C-4) and (C-6) due to mean velocity gradients in streamwise directions are small and may be neglected. The major shear production terms are $\overline{v'^2}\ \partial u/\partial y$ and $\overline{v'^2}\ \partial w/\partial y$ in (C-4) and (C-6) respectively and normal three-dimensional boundary layer behavior is observed. On the trailing side, the chordwise pressure gradients are favorable and large.

164

This results in production terms of opposite sign in two cases resulting in the observed trend.

In the interference region (Figures 58, 65, and 73), the turbulent stresses become large due to production by mean velocity gradients. The magnitudes of $(-\overline{u'v'})$ and $(-\overline{u'w'})$ are once again opposite in sign. This is due to the fact that streamwise velocity gradient $(\partial u/\partial y)$ has changed sign with increase in distance (y) normal to the blade surface while $(\partial w/\partial y)$ has the same sign because radial flow is inward. The stresses increase almost linearly with y in this region, except where the mean velocity gradients go to zero, i.e. at the position, where u has a minimum value and inward radial flow shows a maximum.

5.3.6 Turbulence Spectra

Spectra of all the six components of Reynolds stresses and turbulent kinetic energy were measured at two stations at x/c = 0.5, R = 0.94 and distances respectively of 3/32 inch ($\theta = 2.7^{\circ}$) and 5/32 inch ($\theta = 4.5^{\circ}$) from the leading side of the blade surface. The main objective of the spectral measurements is to find the cut-off frequency (to eliminate electrical noise signals if any above that frequency) for the 2-channel Butterworth filter used in the hot wire set up in Figure 11. This cut off frequency is characteristic of the flow as well as the limitation of the hot wire anemometer used in the measurement. It was also desired to check the contribution in the hot wire output from any spurious electrical signals at line frequency, blade passing frequency and natural frequency of vibration of the probe. One of the main

165

objectives of this measurement is to discern the influence of rotation on turbulence structure.

Measurements (Figures 74 and 75) clearly show that a cut off frequency of 5 kHz is quite suitable for turbulence intensity and shear stress measurements and the contribution to electrical signal at wave numbers higher than 25 cm^{-1} is negligible in the present flow conditions. Also no spurious electrical signal was observed at line frequency, or blade passing frequency or natural frequency of the probe below 5 kHz. The behavior of turbulent intensity spectra shown in 74 and 75 reveal that the inertial subrange where the spectrum follows a (-5/3) law is very small and the spectra falls rapidly with increase of wave number at large wave numbers. On the other hand, the spectra of turbulent shear stresses shown in Figures 74 and 75 reveal a (-5/3) law behavior between wave numbers 2 to 20. A detailed spectral measurement both on the leading and trailing sides and at various chordwise locations would be required to correlate this behavior with effects of rotation and curvature in rotating blade boundary layers encountered in axial flow turbomachinery.
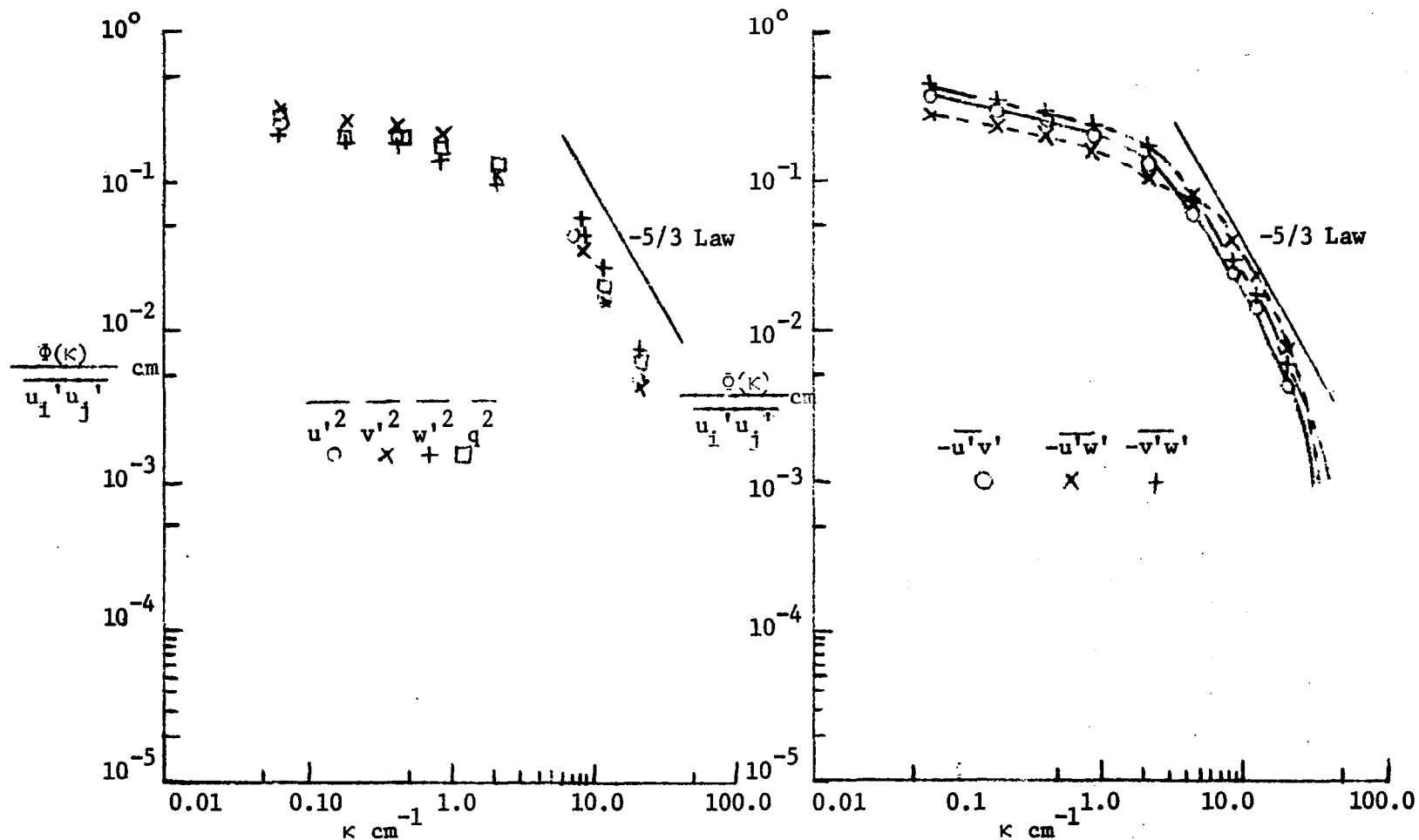
a. Spectrum of Turbulent Intensities   b. Spectrum of Turbulent Stresses

Figure 74.   Spectral Distribution of Turbulent Intensity and Shear Stress Correlations at $R = 0.94$, $x/c = 0.5$, $y^+ \sim 50$ (Throttled Case).

10^0

10^{-1}

10^{-2}

$\dfrac{\Phi(\kappa)}{\overline{u_i'u_j'}}$ cm

10^{-3}

10^{-4}

10^{-5}

| $\overline{u'^2}$ | $\overline{v'^2}$ | $\overline{w'^2}$ | $\overline{q^2}$ |
| O | X | + | □ |

−5/3 Law

$\dfrac{\Phi(\kappa)}{\overline{u_i'u_j'}}$ cm

0.01   0.1   −1 1.0   10.0   100.0

κ cm

a. Spectrum of Turbulent Intensities

10^0

10^{-1}

10^{-2}

10^{-3}

10^{-4}

10^{-5}

−5/3 Law

| $-\overline{u'v'}$ | $-\overline{u'w'}$ | $-\overline{v'w'}$ |
| O | X | + |

0.01   0.1   −1 1.0   10.0   100.0

κ cm

b. Spectrum of Turbulent Stresses
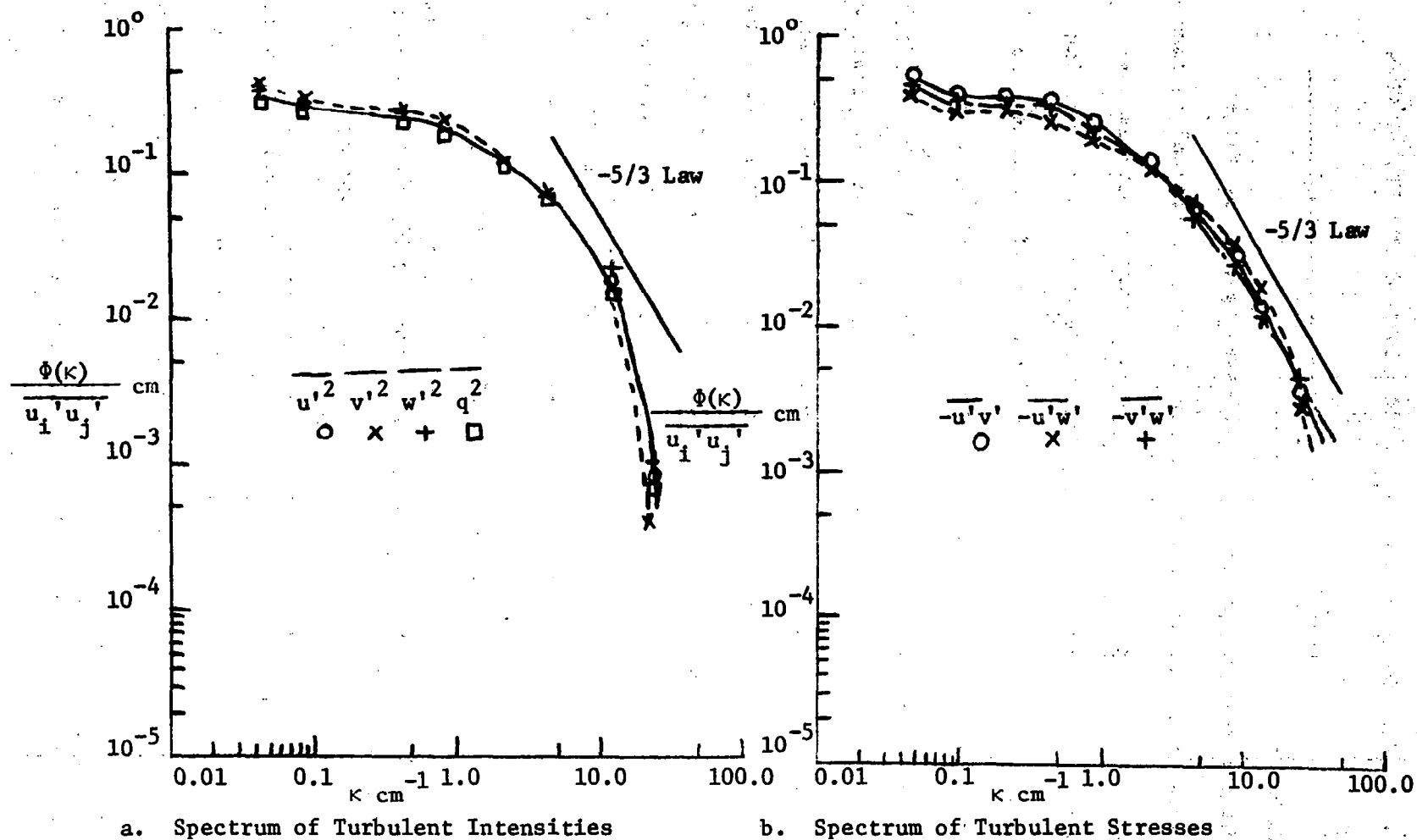
Figure 75. Spectral Distribution of Turbulent Intensity and Shear Stress Correlations
at R = 0.94, x/c = 0.5, $y^+ \sim 100$ (Throttled Case).

6.1 Conclusions

The theoretical and experimental investigation of three dimensional rotating turbulent boundary layer in a helical passage of a turbomachinery rotor show substantial differences between their stationary counterpart as well as from those on a single rotating blade. The rotation induced Coriolis force markedly changes the boundary layer growth, the skin friction, the extent of three-dimensionality and the turbulence flow characteristics in a rotating channel. It should be pointed out that these detailed quantitative measurements on the turbulence and growth characteristics of blade boundary layers in a turbomachine rotor have been performed for the first time. These investigations reveal the inadequacy of the data obtained from cascades in calculating or predicting the performance of a turbomachine. Following important conclusions can be drawn as a result of this investigation.

1. A collateral region exists very near to the wall, even for highly three-dimensional rotating turbulent boundary layers with radial and streamwise pressure gradients. .

2. The law of the wall is found to be valid up to $y^+ \sim 200$.

3. A Power Law representation of the chordwise velocity components fits the data well provided the radial and streamwise variation of the exponent $((H-1)/2)$ in the chordwise velocity profile is taken into account. Cole's representation is possible but the wake function is different from the sinusoidal form used for the stationary turbulent

boundary layers, indicating that the entrainment process in rotating boundary layers is affected by Coriolis and centrifugal forces.

4. Mager's representation of the outward radial velocity (with measured limiting streamline angle) fits the data reasonably well for boundary layers near the mid radius but departs considerably when the annulus wall boundary layer or the boundary layer from adjoining blade interferes.

5. The velocity profiles in the outer part of the boundary layer agree well with the expression,

$$w/U_e = C_1 \sqrt{(2/k - \sin\beta) \sin\beta/RG - (u/U_e)^2}$$

provided the variation of C_1 with x is allowed. In the developing region, for open throttle case, where the boundary layer edge velocity is Ωr, $w/U_e = 0.2 \sqrt{(2-\sin\beta)\sin\beta-(u/U_e)^2}$ gives the best fit. It is also clear that Johnston straight line fit

$$w/U_e = C_2 (1 - u/U_e)$$

is inadequate for rotating axial flow fluid machinery, such as axial flow compressors and turbines. Equation (31) clearly shows that the cross flow is strongly dependent on the stagger angle, local chordwise velocity and the radial pressure gradient.

6. Velocity profiles in the interference region near the tip, where the blade and annulus wall boundary layers produce an intense mixing region, cannot be represented by simple similarity forms. Radial inward flow and appreciable reduction in the streamwise component of velocity characterize this flow. Equation (31) gives the best fit except near the center of the channel section.

7. There is a large reduction in passage averaged streamwise velocity $\bar{u}$ downstream of the channel due to increased radial migration of the flow caused by the pressure gradients. The decrease is very large near the tip in the interference region and is accompanied by radial inward flows and reversal of shear streses. This phenomenon plays an important part in producing increased secondary flow losses in an actual rotor. Its existence and its quantitative measurements have not been reported before. The associated intense mixing and the corresponding increase in end wall losses must be accounted for in calculating the performance of turbomachinery rotors.

8. The observed values of momentum thickness (θ_{11}) are lower than those for a single rotating blade measured by Lakshminarayana et al. (17) due to larger values of the limiting streamline angle (ε_w) and the resulting larger radial velocities. θ_{11} is higher on the trailing side compared to those on leading side. The predictions based on momentum integral solution agree reasonably well.

9. The observed and the predicted values of limiting streamline angle are much higher than the single blade values and agree well except near transition region. This is partly due to errors in the location of transition and partly due to numerical errors involved in assumed sudden transition from laminar to turbulent flow equations.

10. Variation of shape factor (H) is small in open throttle case (1.10-1.3 on the trailing side and 1.25-1.5 on the leading side) except near hub and tip where the end wall boundary layers interfere. For a fully loaded rotor, H varies appreciably. Its variation can be incorporated in the prediction of boundary layer growth by using a modified form (Equation 92) of Head's entrainment equation.

171

11. The skin friction coefficient for the rotating channel is found to vary with three important three-dimensional boundary layer parameters θ_{11}, ε_w and H. The proposed correlation for the skin friction coefficient based on our limited data in rotating channel with mild pressure gradients is

$$C_f = 0.172 \ R_{\theta_{11}}^{-0.268} \ 10^{-0.678H} \ (1+0.52 \ \sqrt{\varepsilon_w(x-x_t)/C} \ )$$

The term in the bracket is due to three-dimensional effects. Variation with $R_{\theta_{11}}$ and H is found to be the same as that for a stationary channel.

12. Turbulence intensity measurements show that the radial component $(\overline{w'^2})$ is larger than the streamwise component $(\overline{u'^2})$ in a rotating turbulent boundary layer. This trend is opposite to that in a stationary channel and is due to rotation.

13. Turbulent shear stress measurements show that in three-dimensional rotating turbulent boundary layers, all the three velocity cross-correlations are of the same order of magnitude inside the boundary layer. They behave similarly if the pressure gradients are negigible and can have opposite signs depending on the nature of chordwise and radial pressure gradients.

14. Both the turbulent intensity and shear stress measurements in the interference region (near the tip) show a large increase in magnitude. The turbulent stresses vary almost linearly in the direction normal to boundary layer and have opposite signs compared to the values near the blade surface. This large gradient in turbulent intensity and shear stresss is due to an intense mixing zone due to interaction of the two boundary layers resulting in increased flow losses in this region.

6.2 Recommendations for Future Work

The present study on the three-dimensional turbulent boundary layers in the rotating blade passages of the four bladed axial flow inducer has shown that there is an urgent need to do both analytical and experimental work in other rotating fluid machinery, such as compressors, turbines and propellers. The turbulent characteristics, the skin friction and the boundary layer growth are significantly affected by both rotation and curvature and quantitative measurements of these effects in rotating frame of reference is essential to predict the losses and the aerodynamic performance of a turbomachinery. As a result of this study, following recommendations are proposed for further research work in the area of rotating turbulent blade boundary layers:

1. A complete solution of mean velocity profiles and the major turbulent stresses in the blade boundary layer using Bradshaw's (25) three-dimensional boundary layer program for stationary flows, modified to include the effects of rotation and curvature as outlined by Anand et al. (20).

2. A prediction method for the boundary layer growth parameters $(\theta_{11}, \varepsilon_w,$ and H) by matching analytical solutions for cross-flow velocity profiles in the inner and outer regions of a turbulent boundary layer, and using the momentum integral solution technique described in Chapter II for arbitrary pressure gradients in a turbo-machinery rotor. The entrainment Equation (92) should be modified to include the effects of free stream turbulence as discussed by Evans and Horlock (48) and the effect of cross-flow on the Head's (32) entrainment coefficient.

3. A comprehensive study of interference effects of annulus wall on the blade boundary layer characteristics both in the stator and the rotor blade row of a turbomachinery.

4. Accurate boundary layer measurements close to the blade surface to verify the extent of collateral region in the inner layer as suggested by Equations (24) and (25).

5. Use of boundary layer probes with high spatial resolution, especially in the measurement of turbulent stresses and the cross-spectra.

REFERENCES

1. Karman, T. V., "Uber laminare und turbulente Reibung", Z. Angen. Math. Mech. I, 233-51, 1921 (Translated as NACA TM 1092, 1946).

2. Barna, S. N., "Secondary Flow in a Rotating Straight Pipe", Proc. Roy. Soc., London, Ser. A., Vol. 227, pp. 133-39, 1954.

3. Benton, G. S., "The Effects of the Earth's Rotation on Laminar Flow in Pipes", Transactions A.S.M.E., J. Applied Mechanics, Vol. 23, pp. 123-27, 1956.

4. Treffethen, L.,"Flow in Rotating Radial Ducts", Report No. 55, GL350-A, General Electric Engineering Laboratory, August, 1957.

5. Chawla, M. D., "The Stability of Boundary Layer Flow Subject to Rotation", Ph.D. Thesis, Michigan State University, 1969.

6. Horlock, J. H., and Wordsworth, J., "The Three-Dimensional Laminar Boundary Layer on a Rotating Helical Blade", J. Fluid Mech., Vol. 23, p. 305, 1965.

7. Banks, W. H., and Gadd, G. E., "A Preliminary Report on Boundary Layers on Screw Propellers and Simpler Rotating Bodies", NPL Report SHR 27/62, Britain, 1962.

8. Fogarty, L. E., "The Laminar Boundary Layer on a Rotating Helical Blade", J. Aero. Sci., p. 247, April 1951.

9. McCroskey, W. J., and Yaggy, P., "Laminar Boundary Layer on Helicopter Rotors in Forward Flight", AIAA Journal, Vol. 6, No. 10, October 1968.

10. Cham, T. S., and Head, M. R., "Turbulent Boundary Layer Flow on a Rotating Disk", J. Fluid Mech., Vol. 37, p. 129, 1969.

11. Lumley, J. L., Panofsky, H., The Structure of Atmospheric Turbulence Interscience, New York, 1964.

12. Blackadar, A. K., and Tennekes, H., "Asymptotic Similarity in Neutral Barotropic Planetary Boundary Layers", J. of Atmospheric Sciences, Vol. 25, p. 1015, 1968.

13. Hill, P. G., and Moon, I., "Effect of Coriolis Forces on Turbulent Boundary Layers in Rotating Fluid Machines", Gas Turbine Lab. Report No. 69, Massachusetts Institute of Technology, June 1962.

14. Moon, I., "Effect of Coriolis Force on the Turbulent Boundary Layer in Rotating Fluid Machines", Gas Turbine Lab. Report No. 74, Massachusetts Institute of Technology, June 1964.

15. Moore, J., "The Development of Turbulent Boundary Layers in Centrifugal Machines", Gas Turbine Lab. Report No. 99, Massachusetts Institute of Technology, June 1969.

16. Haleen, R. M., and Johnston, J. P., "The Influence of Rotation on Flow in a Long Rectangular Channel - An Experimental Study", Report MD-18, Thermosciences Division, Dept. of Mechanical Engr., Stanford University, California, May 1967.

17. Lakshminarayana, B., Jabbari, A., Yamaoka, H., "Three-Dimensional Turbulent Boundary Layer on a Single Rotating Helical Blade", J. Fluid Mechanics, Vol. 51, p. 545, 1972.

18. Bradshaw, P., "The Analogy Between Streamline Curvature and Buoyancy in Turbulent Shear Flow", J. Fluid Mechanics, Vol. 36, Part I, pp. 177-91, 1969.

19. Stratford, B. S., Jawor, Z. M., Smith, M., "The Mixing Between Hot and Cold Air Streams in a Centrifugal Flow Field", British ARC C. P. 793, 1964.

20. Anand, A. K., Gorton, C. A., Lakshminarayana, B., Yamaoka, H., "Investigation of Boundary Layer and Turbulent Characteristics Inside the Passages of an Axial-Flow Inducer", NASA CR 121248, July 1973.

21. Lakshminarayana, B., "Experimental and Analytical Investigation of the Flow Through a Rocket Pump Inducer", NASA SP 304, 1974.

22. Lakshminarayana, B., "Flow Visualization in a Rocket Pump Inducer", Transactions A.S.M.E., J. Basic Engr., p. 777, 1972.

23. Gorton, C. A., "Analytical and Experimental Study of Three-Dimensional Mean Flow and Turbulence Characteristics Inside the Passages of an Axial-Flow Inducer", M.S. Thesis, Department of Aerospace Engineering, The Pennsylvania State University, 1974. (Also as A.S.M.E. Paper 75-GT-4).

24. Cooper, P. and Bosch, H., "Three-Dimensional Analysis of Inducer Fluid Flow", NASA CR-54836, TRW-ER-6673A, February 1966.

25. Bradshaw, P., "Calculation of Three-Dimensional Turbulent Boundary Layers", J. Fluid Mech., 46, p. 417, 1971.

26. Senoo, Y., and Nishi, M., "Equilibrium Three-Dimensional Turbulent Boundary Layer in Curved Duct", Second J.S.M.E. Symposium of Fluid Machinery and Fluidics, Vol. 2, p. 21, 1972.

REFERENCES (continued)

27. Anand, A. K., and Lakshminarayana, B., "Three-Dimensional Turbulent Boundary Layer in a Rotating Helical Channel", J. Fluids Engr., Vol. 97, No. 2, p. 197, June 1975.

28. Ludwieg, H., and Tillman, W., "Untersuchungen uber die Wandschub-spannung in turbulenten Reibungsschichten", Ing. Arch 17, p. 288, 1949.

29. Kline, S. J., Morkovin, M. V., Sovran, G., Cockrell, D. J., (Editors) "Proceedings of Turbulent Boundary Layer - AFOSR-IFP-Stanford Conference", Vol. I, Published by Thermosciences Division, Dept. of Mech. Engr., Stanford University, California, 1968.

30. Mager, A., "Generalization of Boundary Layer Momentum Integral Equations to Three-Dimensional Flow Including Those of Rotating Systems", NACA Report 1067, 1952.

31. Nash, J. F., and Patel, V. C., Three-Dimensional Turbulent Boundary Layers, SBC Book, Inc., 1972.

32. Head, M. R., "Entrainment in the Turbulent Boundary Layers", Aero. Research Council, Rept. and Memo, 3152, 1958.

33. Lewckowicz, A. K., "Two- and Three-Dimensional Incompressible Turbulent Boundary Layers", Ph.D. Thesis, Liverpool University, U.K., 1963.

34. Lakshminarayana B., and Anand, A. K., "Effect of Solidity on Rocket Pump Inducers", Second J.S.M.E. Symposium on Fluid Machinery and Fluidics", p. 157-66, Sept. 1972.

35. Lumley, J. L., "A Simple Constant Temperature Hotwire Anemometer", Ordnance Research Lab., Internal Memo. 503.2471-05, August 1966.

36. Johnston, J. P., "A Wall Trace, Flow Visualization Technique for Rotating Surfaces in Air", ASME, J. Basic Engr., 1964.

37. Jabbari, A., "Turbulent Boundary Layer Characteristics on a Rotating Helical Blade", M.S. Thesis, Department of Aerospace Engineering, The Pennsylvania State University, 1969.

38. Preston, J. H., "The Determination of Turbulent Skin Friction by Means of Pitot Tubes", J. Roy. Aero. Soc. 58, 1954.

39. Pierce, F. J., and Krommenhoek, D., "Wall Shear Diagnostics in Three-Dimensional Turbulent Boundary Layers", ARO-D, Tech. Report No. 2, 1954.

40. Patel, V. C., "Calibration of the Preston Tube and Limitations on its Use in Pressure Gradients", J. Fluid Mechs., Vol. 23, Part I, p. 185, 1965.

41. King, L. V., "On the Convection of Heat from Small Cylinders in a Stream of Fluid", Phil. Trans. Roy. Soc., London, 214A, p. 373, 1914.

42. Wyngaard, J. C., and Lumley, J. L., "A Constant Temperature Hotwire Anemometer", J. of Scientific Instruments, Vol. 44, p. 363-65, 1967.

43. Margolis, D. P., "Further Studies of the Curved Turbulent Mixing Layer", U.S. Army Contract Report #DA-31-124-ARO(D)-153, The Pennsylvania State University, September 1965.

44. Johnston, J. P., "On Three-Dimensional Turbulent Boundary Layers Generated by Secondary Flow", J. Basic Engr., Transactions A.S.M.E., Vol. 82, 1960.

45. Lakshminarayana, B., "Three-Dimensional Flow in a Rocket Pump Inducer", Transactions A.S.M.E., J. Fluid Engr., December 1973.

46. Raj, R., "Characteristics of Cascade and Rotor Wakes", Ph.D. Thesis, Department of Aerospace Engineering, The Pennsylvania State University, 1974.

47. Pratte, B. D., and Keffer, J. F., "The Swirling Turbulent Jet", J. Basic Engr., A.S.M.E., 72-FE-18, 1972.

48. Evans, R. L., and Horlock, J. H., "Calculation of the Development of Turbulent Boundary Layers with a Turbulent Free-Stream", A.S.M.E. Paper 74-FE-24, 1974.

49. Tennekes, H., and Lumley, J. L., A First Course in Turbulence. MIT Press, Cambridge, Massachusetts, 1972.

50. Lighthill, M. J., "Contributions to the Theory of the Pitot-Tube Displacement Effect", J. Fluid Mechs., Vol. 2, p. 493, 1957.

51. Thwaites, B., Incompressible Aerodynamics, Oxford University Press, 1960.

52. Hinze, J. O., Turbulence - An Introduction to Its Mechanism and Theory, McGraw-Hill Book Company, 1959.

53. Bradshaw, P., An Introduction to Turbulence and its Measurement, Pergamon Press, 1971.

54. DISA Electronics, Electronic Measurements of Mechanical Events, DISA Information Journal, No. 7, January 1969.

REFERENCES (continued)

55. Friehe, C. A., Schwarz, W. H., "Deviations from the Cosine Law for Yawed Cylindrical Anemometer Sensors", J. Applied Mech., 68-WA/APM-16, 1968.

56. Lumley, J. L., "On the Interpretation of Time Spectra Measured in High Intensity Shear Flows", Physics of Fluids, Vol. 8, No. 6, 1965.

57. Wyngaard, J. C., "An Experimental Investigation of the Small-Scale Structure of Turbulence in a Curved Mixing Layer", Ph.D. Thesis, The Pennsylvania State University, September 1967.

58. Oka, S., and Kostic, Z., "Influence of Wall Proximity on Hotwire Velocity Measurements", DISA Informational Journal, No. 13, May 1972.

59. Hartog, D., Mechanical Vibrations, McGraw-Hill Book Company, 3rd Edition, 1947.

APPENDIX A

Specifications of Hotwire Probe and Anemometer and

Turbulent Scales of Flow

A.1 Specifications of the Hotwire Probe

All the hotwire measurements reported in Chapter V have been carried out using a miniature triple sensor hotwire probe manufactured by Thermosystems, Inc. The configuration of the probe and its sensors is shown in Figure 14. The probe is specially suited to boundary layer measurements. The probe body is 0.08 inches thick stainless steel tube, eleven inches long and elliptic in section with major and minor axes 0.25 inches and 0.125 inches respectively.

The three hotwire sensors of the probe are supported by six gold plated stainless steel tapered needles, 0.008 inch tip diameter about 0.35 inch away from the probe body facing the direction of the flow, so that the interference effects due to probe body on sensors are minimized. The sensors are made of copper plated tungsten wire, 0.00015 inch in diameter. The total length of each sensor is 0.0624 inch but the etched length varies from 0.025 to 0.040 inch. The properties of hotwire sensors are tabulated in Table I, their direction cosines in Table II and the influence coefficients $\alpha_{\ell i}$ in Table III, below:

Table I

Important Properties of Hotwire Sensor Material

No.	Property	Symbol	Value	Unit
1	Temperature Coefficient of Electrical Resistivity	(b)	5.2×10^{-3}	$/^{\circ}C$
2	Density	ρ_w	19.0	gm/cm^3
3	Specific Heat	c_w	0.032	BTU/lb.
4	Thermal Conductivity	k_w	0.476	gm calorie/ sec $^{\circ}C$

Table II

Direction Cosines of Sensors with Reference Coordinate System of Figure 3.

Angle Orientation	Hotwire 1		Hotwire 2		Hotwire 3	
	Angle in degrees	Direction cosine	Angle in degrees	Direction cosine	angle in degrees	Direction cosine
Ax - x	135°	-0.707	118.5	-0.477	232.5	-0.609
Ax - y	45°	0.707	30.5	0.862	141.9	-0.787
Ax - r	45°	0.707	80.0	0.174	85.0	.087

Ax - x, Ax - y, and Ax - r represent included angles between the wire

axis (Ax) and x, y, and r axes, in the planes formed by wire axis and

x, y, r axes respectively.

Table III

Influence Coefficients ($\alpha_{\ell i}$) of Sensors Used in Hotwire Equation

(99) in Chapter IV for Gorton's (23) Computer Program

Hotwire	$\alpha_{\ell 1}$	$\alpha_{\ell 2}$	$\alpha_{\ell 3}$
1	0.720	0.0	0.670
2	0.882	0.455	0.092
3	0.807	-0.558	0.062

A.2 <u>Specifications of 2-Dual Channel Constant</u>
<u>Temperature Hotwire Anemometers</u>

The anemometry circuitry has been designed to process large

nonlinear fluctuating signals by Wyngaard and Lumley (42) with a flat

frequency response up to 20 kHz. The electronic circuit diagram is

shown in Figure 76 and the details of components are given in Table IV.

Since the spectral measurements show that the magnitude of output

signal reaches the noise level (0.02 mv - anemometer in operation for at

least one hour) for $\omega \leq 5$ kHz in the actual experiment, this anemometer

is found suitable for all the hotwire measurements reported in Chapter V.

Figure 76. Electrical Circuit Diagram of the Multi-Channel Hotwire Anemometer Used in The Experiment.

Table IV

Anemometer Components

Resistor No.	Value Ω	Watt	Composition	Number required for two-channel
R_1	100Ω pot	1 turn		2
R_3, R_5	100	1-min	wire wound	4
R_6	5000	1/2	metal film	2
R_7	2000	1-min	wire would	2
R_8	1000	1-min	metal film	2
R_9	10K	1/2	metal film	3
R_{10}	50K	1/2	metal film	3
R_{11}	1000	1/2	metal film	3
R_{12}	2000	1/2	metal film	3
R_{13}	500	1/2	metal film	2
R_{14}	10 K Potentiometer	10 turn		2
R_4	100K	1/4	carbon	2

Capacitor	Value	Quantity
C_1, C_6	1 µf	4
C_2	560 µf	2
C_3	.002 µf	2
C_4	2.2 µf	3
C_5	68 µf	3
C_7	1500 µf	2
filter capacitor 6.8 µf-35V		16
filter capacitor .01 µf-low volt.		16

184

A.3 Scales of the Flow

The relevant range of flow parameters for estimating various scales of turbulence for the present flow study are:

1. Free stream velocity in a relative frame of reference = 30 to 60 ft/sec.

2. Boundary layer thickness = 0.04 ft at x/c = 0.1 to 0.12 ft at x/c ≥ 0.5.

3. Skin friction velocity = 2 to 3 ft/sec.

4. Overall turbulence level = 5% to 15% inside the blade boundary layers.

5. Reynolds number based on tip radius and peripheral velocity at the tip = 6.67×10^5.

An estimation of turbulent length scales is very important from the point of view of categorizing the type of turbulent flow, understanding its basic structure and in calculating the various errors involved in the measurement of turbulent flow correlations, which are described in Appendix B. The three important scales of turbulence are:

1. Large eddy length scale (ℓ)

2. Taylor's microscale (λ_g)

3. Kolmogorov scale (η)

Following Tennekes and Lumley (49), the large eddy length scale is proportional to the mean flow strain rate. It is of the order of the mixing length in the case of turbulent boundary layer flows. ℓ is therefore ∿ 0.2 inch at x/c = 0.1 and ∿ 0.6 inch at x/c ≥ 0.5.

The Reynolds number ($u'\ell/\nu$) is an important parameter in determining the structure of turbulent flow. For the present case its value lies between 500 at x/c ≤ 0.5 to 1500 at x/c > 0.5. Here u' represents the turbulent intensity.

185

Taylor's microscale (λ_g) is defined as:

$$\epsilon = 15 \, \nu u'^2 / \lambda_g^2 \qquad \text{(A-1)}$$

where ϵ is the turbulent dissipation rate (ϵ). An estimate of ϵ according to Tennekes and Lumley (50) is obtained by

$$\epsilon = u'^3 / \ell \qquad \text{(A-2)}$$

Therefore ϵ is $\sim$ 1000 ft^2/sec^3 to 1500 ft^2/sec^3 and λ_g is $\sim$ 0.04 inch to $\sim$ 0.07 inch at $x/c = 0.1$ and $x/c \geq 0.5$ respectively.

Kolmogorov scale (η) which represents the small scale eddies in the dissipation range is defined as

$$\eta = (\nu^3/\epsilon)^{1/4} \qquad \text{(A-3)}$$

The Kolmogorov scale is $\sim$ 3 - 4 x 10^{-3} inch.

In the spectral representation of Reynolds stress tensor components, the concept of wave number is very useful. The wave number is defined as

$$\kappa = 2\pi\omega/u \simeq 1/\ell_e \qquad \text{(A-4)}$$

where ω is the frequency at which the contribution due to a correlation between two fluctuating velocity components to the Reynolds stress is being considered. u is the mean flow velocity at which an eddy of length ℓ_e, corresponding to that wave number is convected.

The wave number is usually represented in centimeter units. The wave number corresponding to an eddy of wire length is 13 cm^{-1} and the wave numbers corresponding to an eddy equal to distance between wires 1 and 2 or wires 1 and 3 (Figure 14) is 10 cm^{-1}. The wave number corresponding to distance between wires 2 and 3 is 6.4 cm^{-1}. These wave numbers are required in calculating errors in Reynolds stress correlations described in Appendix B.

APPENDIX B

Experimental Error Analysis and Accuracy of Data

The various sources of error in the measurements and methods of incorporating them in the data are described in this Appendix.

B.1 Limiting Streamline Angles

The following are the sources of errors in the measurement of limiting streamline angles by the ammonia trace technique.

1. Finite velocity of the injected ammonia and extent of collateral region.

2. Finite dimensions of the static pressure tap through which the ammonia is injected.

3. Misalignment of the ozalid paper strip with reference direction.

4. Inaccuracy in measuring angles from the ammonia trace due to increased blurredness in the trace with distance due to turbulent diffusion effects.

Items 1 to 3 are controllable and are minimized by experience and proper design of the ammonia transfer device. However item 4 is the main source of inaccuracy. An error in angles up to $\pm 2^\circ$ is possible. Therefore the percentage error in the small cross flow case (where the limiting streamline angle is $\sim 10^\circ$) can be as high as 20%.

B.2 Skin Friction Coefficient

The Preston tube measurements for the blade surface shear stress are liable to the following errors:

1. The inner diameter of the probe should be small compared to the exterior law of the wall region. Near the leading edge the 'law of the wall' region is very small and results in some error.

2. Misalignment of probe compared to the actual flow direction at the wall.

3. Measurement of effective radius of the probe location from the rotor axis, when the probe is inclined.

Error due to item 1 is found negligible, as demonstrated by the measurements with different tube diameters. The error due to item 2 is minimized by using a rounded tip Preston tube. The last error due to inclination of Preston tube depends upon the magnitude of limiting streamline angle and the radius of measurement. It is maximum at the hub for large pressure gradient cases. For a one inch tube, tilted up to 45°, the total anticipated error in measurement at hub is $\sim 6\%$.

B.3 Mean Velocity Profiles

The sources of error and experimental accuracy depend both on the type and geometry of the probe and its sensors. Both the three hole disk probe and the three sensor hot wire probe, have been used for mean velocity measurements. Probable sources of error from disk-type probe measurements are:

1. Nonuniformity in the flow.

2. Proximity of the probe to the blade surface.

3. Finite dimensions of the sensor area.

4. Inclination of the streamline to the total pressure hole.

5. Misalignment in reference direction (x), which is parallel to the blade surface.

All errors except (5) are due to inherent characteristics of the flow or the probe. They are minimized by incorporating the following corrections to the data:

1. Correction due to nonuniform plane shear flow in the radial direction (Figure 77): Since the calibration of the probe is conducted in a wind tunnel where the flow is uniform, an error due to shear flow arises, when the probe scans through the blade boundary layer. The magnitude of this error in angle measurements depends upon the stagnation pressure gradient in the relative flow and the distance between the two pressure holes used for the flow angle measurements. Error in angle measurements (e_α) due to shear flow in radial direction at any measuring point can be proved to be

$$e_\alpha \propto k_1 \frac{\partial u}{\partial r} \cdot \frac{\ell}{u} = k_1 \frac{\ell}{r} \qquad (B-1)$$

where ℓ is the radial distance between the two holes and k_1 is a constant, which is found to be nearly equal to 1.0. For the present case, ℓ = 0.175 inch, $u \sim \Omega r$ and r varies from 9 inches at hub to 18.25 inches at tip. Hence the error in angle measurement (e_α) $\sim 1.0°$ at hub and $0.5°$ at tip.

The error due to finite dimensions of the sensor area is directly related to the distance between the holes. From the practical point of view, for 1/32 inch diameter holes, a minimum distance of 5/32 inch is required and the design value of 0.175 inch is quite appropriate. Maximum anticipated error in the velocity profile measurements $\sim$ 1% at the hub. It is partly corrected by using Equation (B-1).

The second source of error due to shear flow is the displacement of total stagnation pressure point from its true position. Lighthill's (50) expression for the displacement (Δ) of the effective center of pressure from the probe axis for a cylindrical probe of diameter d is
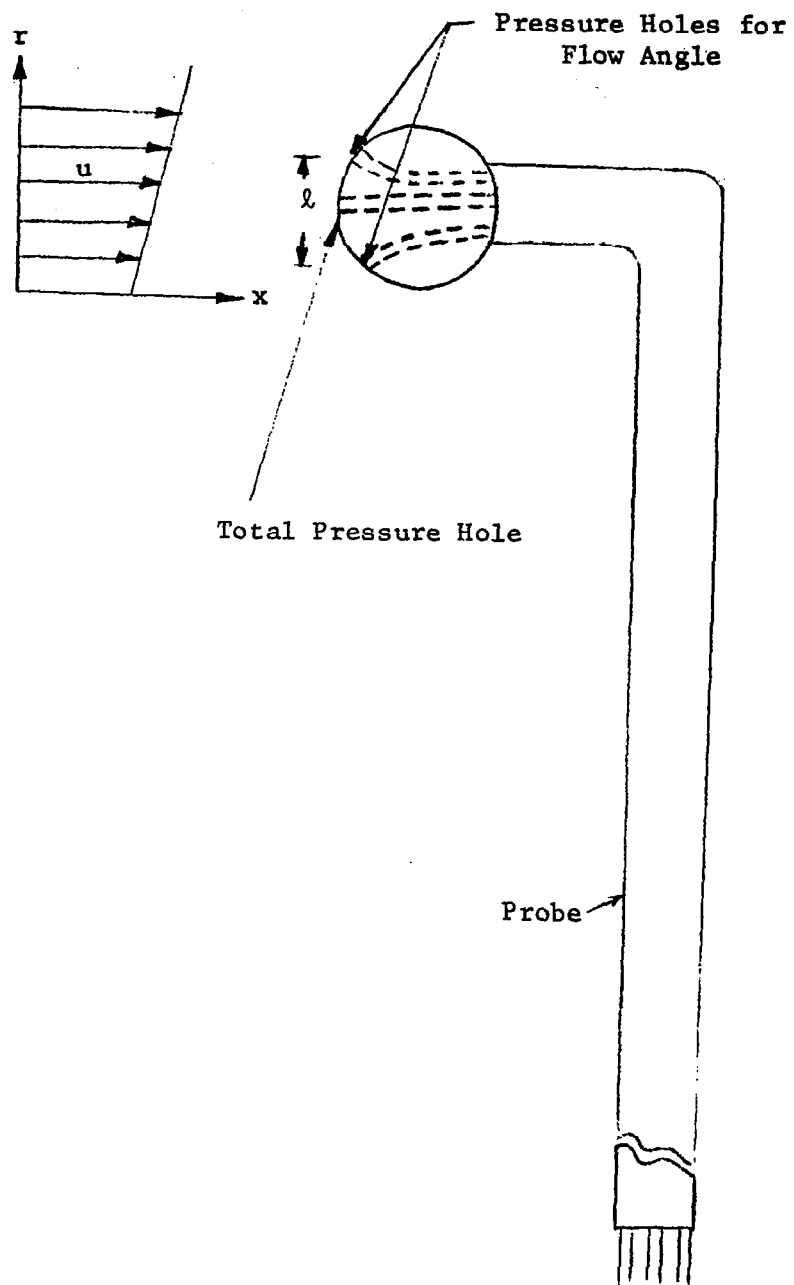
189

Figure 77.   Disk Probe in Radial Shear Flow.

190

$$\frac{\Delta}{d} = f \left[\frac{\frac{\partial u}{\partial y} d}{2u}\right] = 0.45\, \zeta - 3.05\, \zeta^3, \text{ where } \zeta = \frac{\partial u}{\partial y}\left(\frac{d}{2u}\right) \qquad \text{(B-2)}$$

Here the shear gradient in the direction (y) normal to the boundary layer is used, because $\frac{\partial u}{\partial y} \gg \frac{\partial u}{\partial r}$. In the present case, d = 0.031 inch, $\zeta \approx 0.02$, $\frac{\Delta}{d} \sim 0.009$. The traversing step in boundary layer measurement is 0.06 inch. The error due to this shift is therefore at the most 1.8%.

2. Correction due to proximity of the blade surface: The effect of the blade wall on probe measurements is to displace the effective center of measurement from its true position in the direction of increasing distance from the blade. According to Thwaites (51) the maximum displacement (Δ) due to this effect is given by $\frac{\Delta}{t} \leq 0.5$ where t is the thickness of the probe. The disk probe is 0.03 inch thick. Therefore the maximum displacement is $\Delta \leq 0.015$ inch. Even though it is small, its affect must be accounted for the measurement closest to the wall. This correction has been incorporated in the final analysis of the data.

4. Error due to inclination of the streamline to the total pressure hole: Total pressure measurements will be in error if the streamline is inclined to the total pressure hole of the disk probe. This error is eliminated by using a calibration curve for the total pressure measurements. This is carried out by traversing the probe inside the potential core of a 1 foot diameter open jet. The total pressure is measured for different angular positions with respect to jet axis. The normalized difference between true and observed total pressure is plotted against flow angle for different values of flow velocities in the tunnel. The single correction curve obtained by this procedure (Figure 78) is used to correct the total pressure measurements as follows:
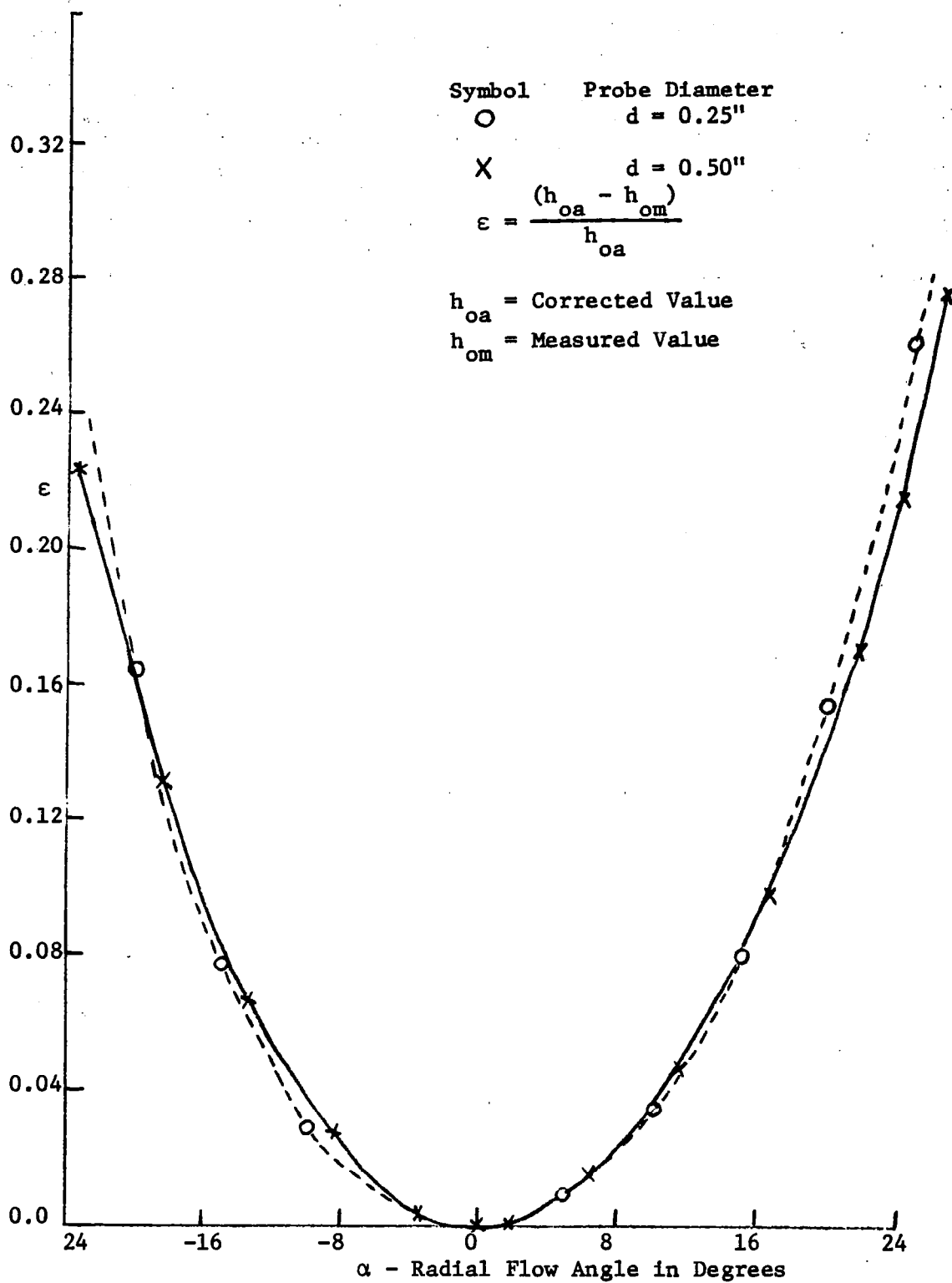
Figure 78. Correction Curve to Measured Stagnation Pressure
for Disk Probe.

$$\frac{h_{o\Delta}}{h_{om}} = 1 + \Delta_{hc} \qquad\qquad (B-3)$$

where h_{om} and h_{oc} are, respectively, the measured and actual values of total pressure head of air in inches of water and Δ_{hc} is the correction from the calibration curve at any given angle α (Figure 78). It is to be noted that the flow angle is also to be corrected because the normalizing dynamic head in the angle calibration curve (Figure 13) uses the uncorrected measured head (h_{om}) to calculate the dynamic head. Thus both α and h_{om} values are corrected by iterative procedure. It may be remarked that the error in total pressure for a flow angle $\leq 10^{o}$, is less than 3% and hence the correction may be neglected.

B.4   Errors in Hotwire Measurements

In the case of measurements with the three-sensor hotwire probe, the following sources of errors may occur.

1.   Inclination of the wire to the flow streamline (deviation from cosine law).

2.   Geometry of prongs and probe body (inviscid flow and heat transfer effects).

3.   Finite distances between wires (spatial resolution of the probe).

4.   Finite dimensions of individual wires (ℓ/d, end effect, spatial resolution, etc.).

5.   Temporal resolution or thermal inertia of the wires.

6.   Aging, oxidation and contamination of the wires.

7.   Ambient temperature drift.

8.   Proximity of wire to the wall.

9. Probe body vibration due to rotation and flow induced excitation.

10. Spurious signals from the power line (60 Hz) and blade passing frequency.

11. Finite sampling time.

12. Measurement of wire angles with respect to the reference coordinate system.

13. Misalignment of the probe with respect to the reference axis.

Errors 1, 7, and 8 are eliminated by using correction factors from available hotwire literature (52, 53, 54) and calibration in a wind tunnel. The probe and sensor errors 2 to 6 are minimized by proper selection of the probe dimensions, support needles and the sensors. Error 9 is eliminated by proper clamping, error 10 is minimized by reducing the number of ground loops to a minimum. Error 11 is inherent and can only be reduced by increasing the sampling time. Errors 12 and 13 depend on the accuracy of angle measuring equipment and aligning devices respectively.

Estimation and minimization of all the above mentioned errors and methods of correcting the data are described below.

1. Inclination of wire to the flow streamline: Inclination of a hotwire to the flow streamline causes a change in effective cooling velocity on the wire and is expressed by Hinze (52) as,

$$U_{eff}^2 = U_N^2 + K^2 U_a^2 \qquad (B-4)$$

where U_N and U_a are components of total flow velocity vector respectively in normal and axial directions of the wire respectively. K is a correction factor, which according to Friehe and Schwarz (55) depends mainly on the ℓ/d ratio of the hotwire.

2. Geometry of prongs and probe body: The prongs and the probe body affect the hotwire measurements in two ways. Firstly, they change the flow velocity vector near the wire due to obstruction of the flow (inviscid effect) and secondly it affects heat transfer rate. The major design parameters which influence this error are prong to wire diameter ratio, prong length to diameter ratio and spacing between the prongs. From Appendix A, the values of these are respectively 20, 40 to 50 and 2mm. Following DISA (54), the maximum anticipated error for 45° inclination of streamline from the calibrated position ($\alpha = 0$) is 1.5%. Since the flow vector inclination from calibrated position in the measurement is less than 45°, this error is negligible.

3. Spatial resolution of the probe: The finite distance between the wires or the total sensing area, can be a large source of error, particularly in nonuniform three-dimensional flows. Since the hotwire measurements by individual wires are made at 40 points from one blade to the other, it is easy to interpolate the measurement at a single point from the observed measurements at adjacent data points. Since wire 1 in Figure 14 coincides with one of the reference axis (x) the measurements of the other two wires are interpolated to this point. Since the distances between wires is small (maximum value is 0.060 inch) as compared to measured boundary layer thickness ($\sim$ 0.5 inch), a linear interpolation scheme is used. Unfortunately this correction cannot be applied to the measurements of cross-correlations and the corresponding error in their measurements is derived as follows:

The error in a cross-correlation due to spatial resolution is nothing but the minimum eddy size the probe can correlate because of

195

separation of the two wires. The wave numbers (κ) corresponding to these distances are $\kappa_{12} = \kappa_{13} = 10.0$ cm^{-1} and $\kappa_{13} = 6.4$ cm^{-1} as defined and described in Appendix B. The error e in the correction is given by Lumley (56) as

$$e(\overline{u_i'u_j'}) = \frac{\int\limits_{\kappa}^{\infty} E_{ij}(\kappa)\ d\kappa}{\int\limits_{o}^{\infty} E_{ij}(\kappa)\ d\kappa} = \frac{\overline{u_i'u_j'} - \overline{u_i'u_j'}(\kappa)}{\overline{u_i'u_j'}} \qquad (B-5)$$

The turbulence can be taken to be locally isotropic for $\kappa_m \sim 5$ cm^{-1}. An estimate of correlation and hence the error may be obtained by assuming that the spectrum of E follows the following expressions as discussed by Wyngaard (57),

$$\begin{aligned} E_{ij}(\kappa) &= \text{constant } C_1 (0 < \kappa < 0.1) \\ &= \text{constant } C_2/\kappa\ (0.1 < \kappa < 5.0) \qquad (B-6) \\ &= \text{constant } \varepsilon^{2/3}\kappa^{-5/3}(5.0 < \kappa < \infty) \end{aligned}$$

The correlations $\overline{u_i'u_j'}$ are directly related to measured fluctuating voltage correlation $(\overline{e_ie_j})$ as described in Chapter IV. Using these relations, the maximum anticipated errors in the measured voltage correlations are:

Error in $\overline{e_1e_2}$, $\overline{e_1e_3}$ correlations = 6.7%

Error in $\overline{e_2e_3}$ correlation = 9.1%

So the anticipated maximum error in cross-correlations due to spatial distance is $\sim$ 9%.

4. Spatial resolution of the wire: The finite dimensions of the hotwire cause the following errors:

a. Error in heat transfer rate parallel to axis of the wire (ℓ/d) ratio).

b. Error in heat transfer rate due to cold length effect $(\ell/_c)$.

c. Error in measurements due to spatial resolution in turbulence data.

d. Error in measurement of mean velocities in nonuniform flow.

e. Thermal inertia error in fluctuation levels at different frequencies.

The first error investigated by Friehe and Schwarz (55) can be incorporated as outlined in Equation (B-4) by making K as a function of ℓ/d ratio, where ℓ and d are respectively the etched length and diameter of the wire. The ℓ/d ratio varies from 133-300. Following Friehe and Schwarz (55), K ranges from 0.25 to 0.15 respectively.

The cold length effect or end effect is due to transfer of heat to prongs at the end of the wire. Following Hinze (53), the cold length is given by

$$\ell_c = \frac{d}{2} \sqrt{\frac{e_c \pi k_w}{bR_o (A+B\sqrt{U}-I^2)}} \tag{B-7}$$

where e_c is a conversion constant between heat and electrical units. For heat in calories and electrical energy in joules, its value is 4.2 k_w is the heat conductivity of the wire material. b is the temperature coefficient of the electrical resistivity of the wire. R_o is the electrical resistance of the wire at $0^\circ C$. A and B are hotwire constants. I is the value of electric current flowing in the wire to maintain a constant temperature, when the fluid flow velocity is U. For A = 0.35, $A + B \sqrt{U} = E = 0.45$, I = 80 m A and using the specifications of the wire from Appendix B, the cold length ℓ_c is given by

$$\frac{\ell_c}{d} = 60 \quad \text{and} \quad \frac{\ell_c}{\ell} = 0.25 \text{ to } 0.45$$

197

This error is eliminated by calibration of each wire over the complete flow range and using the local values of slope B in the King's law.

The error due to spatial resolution of wire is discussed by Wyngaard (57). Since the Kolmogorov length scale η varies from 0.003 inch to 0.005 inch. The corresponding wire length to Kolmogorov length scale ratio (ℓ/η) is ~ 6. This gives about 10% error in intensity spectrum at a wave number given by $\kappa_{im} \ell = 1.2$ or $\kappa_{im} = 10$ cm^{-1} where κ_{im} is the wave number where the measured spectrum of mean turbulent energy falls by 10%. Since the magnitude of spectrum falls to very small values for $\kappa > 10$ cm^{-1}, and area under spectrum for $\kappa_{im} \leq 10$ is about 90%, the total error in turbulence intensities is $\leq 1\%$.

Since the sensor wires are in a nonuniform three-dimensional flow field the effective cooling velocity varies over the entire length due to their finite length. The calibration curve, on the other hand is based on uniform velocity field over the wire. The measured output voltage therefore doesn't correspond to mean velocity at the center of the wire. Similarly an error is also made in turbulence measurements. The error in turbulence measurements due to nonuniform flow is given by Hinze (52) as

$$\overline{e^2} = C \, (\overline{e^2}) \text{ measured} \tag{B-8}$$

where $\overline{e^2}$ is the corrected voltage and C is the correction factor given by

$$C \simeq (1 - \frac{\ell^2}{6\lambda_g^2})^{-1} \quad (\text{for } \ell/\lambda_g < 1) \tag{B-9}$$

where ℓ is the sensor length and λ_g is the Taylor's micro-scale of turbulence. For the present case, $\ell \simeq 0.030$ inch and $\lambda_g = 0.040$ to 0.068 inch. Therefore the correction factor to rms voltages varies from 1.03

to 1.09. This factor if neglected introduces a maximum error of 4.5% in the intensity measurements.

5. Thermal inertial of the wire: The temporal error due to thermal inertia at any frequency ω is given by Hinze (52) as,

$$e(\omega) = 1/\sqrt{1 + \omega^2 M^2}$$ where M is the time constant of the wire

$$M = \frac{e_c C_w (R_W - R_f)}{b\, I^2 R_o R_f} = \frac{e_c C_w (\theta_w - \theta_f)}{I^2 R_f} \qquad (B-10)$$

where C_w is the heat capacity of the entire wire, R_w and R_f are the values of wire electrical resistance at temperatures θ_w and θ_f respectively. θ_w is the temperature to which the wire is heated and θ_f is the fluid temperature.

For tungsten wires used in the experiments with over heat ratio of 0.8, and using the specification data from Appendix A, $M \sim 1.4 \times 10^{-4}$ secs. Therefore Thermal inertia error in measured fluctuation levels for 1 kHz and 5 kHz are,

$$e\ (1\ kHz) = 0.98\%$$

$$e\ (5\ kHz) = 25\%$$

6. Aging, oxidation and contamination of the wire: The errors due to aging, oxidation and contamination depend on the total operation time, over heat ratio and the flow environments respectively. These errors are minimized by calibrating the probe before and after the experiment, and incorporating the changes in calibration constants by interpolating according to the fraction of total time used in each measurement.

7. Ambient temperature drift: Change in ambient temperature causes changes ih the heat transfer rate of sensors resulting in corresponding

change in measured output voltages from the anemometer. This effect can be corrected in the following manner.

The constants in the hot wire equation $E_m^2 = A + B \sqrt{U}$ are given by Hinze (52) as,

$$A = A_o \, k_f (Pr_m)^{0.20} (\theta_w - \theta_f) \qquad (B-11)$$

and

$$B = B_o \, k_f Re_d^{0.5} (Pr_m)^{0.33} (\theta_w - \theta_f)$$

where θ_w is the wire temperature when heated, subscript m refers to values at mean temperature equal to $(\theta_w + \theta_f)/2$, and θ_f is fluid temperature. k_f is thermal conductivity of wire at fluid temperature. A_o and B_o are functions of wire dimensions and those properties of the wire that are independent of fluid temperature. For common range of variation of fluid temperatures of $\pm 10^\circ F$, Prandtl number (Pr) is also a constant. The thermal conductivity (k_m) increases linearly with temperature as $k_m = a + a_1 \, \theta_m$ but $k_m Re_d^{0.5}$ is almost independent of temperature. Following Hinze (52), the effect of ambient temperature on two coefficients is given by

$$A = A_1 (1 + \alpha \theta_f) (\theta_w - \theta_f)$$

$$\qquad (B-12)$$

$$B = B_1 (\theta_w - \theta_f)$$

where A_1 and A_2 are constants, $\alpha = a_1/2 \, (a + a_1/2 \, \theta_w) = $ constant for a constant temperature hotwire anemometer. The effect of ambient temperature θ_f can therefore be written as

$$A = A_{f_o} (1 + \frac{\alpha}{1 + \alpha \theta_{fo}})(1 - \frac{\Delta \theta_f}{\theta_w - \theta_{fo}})$$

$$\qquad (B-13)$$

$$B = B_{f_o} (1 - \frac{\Delta \theta_f}{\theta_w - \theta_{fo}})$$

where $\Delta\theta_f = \theta_f - \theta_{fo}$ is a small quantity $\sim \pm 10^o F$, subscript o refers to zero flow conditions. For an over heat ratio of 0.8, $\theta_f = 533^o R$, $\alpha = 0.0024$, $\alpha/(1+\alpha\theta_{fo}) = 0.001$ and $(1/(\theta_w - \theta_{fo})) = 0.0024$ respectively. The coefficients A and B are

$$A = A_{fo}(1 + 0.001\ \Delta\theta_f)(1 - 0.0024\ \Delta\theta_f) = A_{fo}(1 - 0.0014\ \Delta\theta_f) \quad (B\text{-}14)$$

$$B = B_{fo}\ (1 - 0.0024\ \Delta\theta_f) \quad\quad\quad\quad\quad (B\text{-}15)$$

The correction factors given by Equations (B-14) and (B-15) have been incorporated in the computer program for processing hotwire data.

8. Proximity of the wire to a wall: The proximity of a hotwire to the blade surface causes an error in measurements by increasing the heat transfer rate. The increase in heat transfer gives effective cooling velocity higher than those in the absence of wall. According to Oka and Kostic (58), the dimensionless difference between apparent and true velocity has the form

$$\frac{\Delta u}{u_*} = f(u_* y/\nu) \ . \quad\quad\quad\quad (B\text{-}16)$$

The influence of a wall has been shown by them to be less than $(0.1u_*)$ for $y^+ = u_* y/\nu > 6$. Since the nearest measurement is taken at $y^+ \geq 50$, error due to this effect is negligibly small.

9. Probe body vibrations: The vibrations of probe body due to rotation or flow induced excitation, if present, can add significant amount of spurious signal to the measurements. Even though the probe was securely clamped and no visible or other indications of vibrations were found (e.g., the wires would break if the probe is vibrating), the spectra of the correlation tensor are analyzed at natural frequency and its multiple harmonics (lower than 5 kHz) at few representative cases

(near the tip radius where the natural frequency of the probe is lowest O(1 kHz)). *The spectral measurements reported in Chapter V clearly show that there is no spurious signal due to vibrations of the probe.*

The natural frequencies of the probe body at various radii are obtained by assuming the probe to be supported at one end like a uniformly loaded cantilever of elliptic cross-section (Figure 79), with *a weight equivalent to the portion of the probe bent at right angle to* the probe length and supporting the sensors. The effect of probe rotation is also included. The natural frequencies in bending mode are given by Hartog (59) as,

$$\omega_n^2 = (\omega_n^2)_{\Omega=0} + a\,\Omega^2 \tag{B-17}$$

where $(\omega_n)_{\Omega=0} = 3.03\ EI/\ell_o^3\ (M+0.023m)$

E = Elastic Modulus = 30×10^6 psi

m = mass per unit length of the probe = $0.0018\ \ell_o$

M = Point load = 0.00225 lb mass

I = Moment of Area = 1.74×10^{-4} in^4

a is a constant. Its value according to Hartog (59) is 1.5 for first mode of vibration. The natural frequencies based on Equation (B-17) at various radii are given by,

radius (inches) = 18.0, 17.0, 15.75, 14.0

ω_n (kHz) = 0.835, 1.4, 1.75, 5.8

Therefore, for radii lower than 14 inches, natural frequency is greater than the cut off frequency (5 kHz) and so does not affect the measurements. Spectral measurements at tip reveal no spurious signal due to vibrations of the probe, if any.
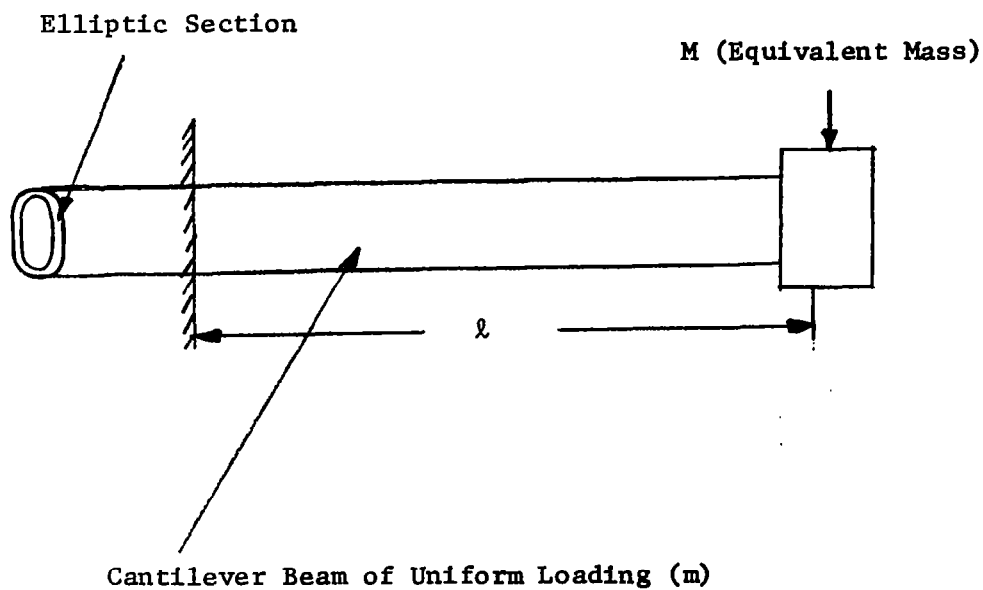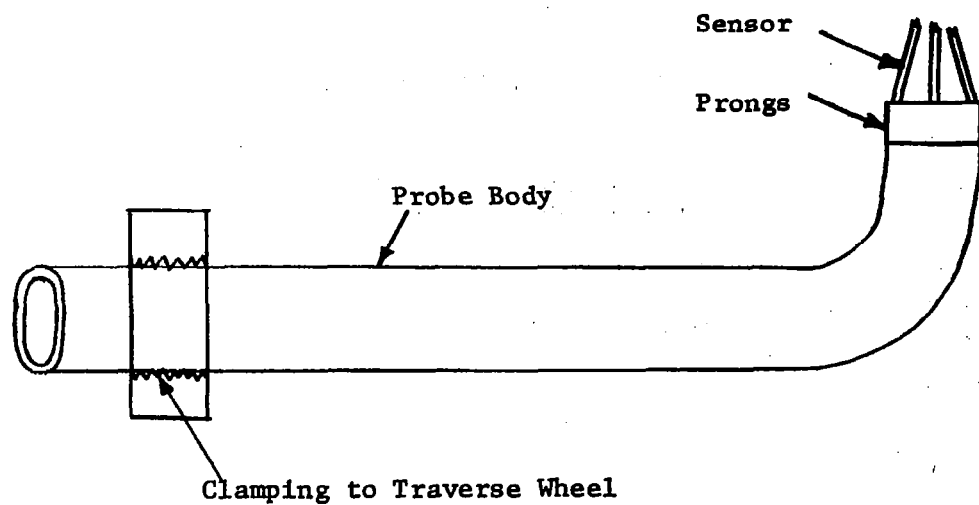
Figure 79. Cantilever Model for Calculation of Natural Frequency
of Vibration of Hotwire Probe.

10. Stray signals from power line and blade passing frequency: Stray signals at line frequency (60 Hz) could be present in the output, if there are too many ground loops in the electronic circuitry. The number of ground loops is reduced to a minimum and the spectrum measurements are carried out at 60 Hz. It is found that no significant error is present due to this source. The spectrum is also measured at blade passing frequency (190 Hz) and no spike is noticed in the spectrum.

11. Finite sampling time: The error in hotwire measurements due to finite sampling time is discussed by Tennekes and Lumley (49). The root mean square error in true mean value U is given by,

$$e_{rms} = \sqrt{\overline{(U_T - U)^2}} \simeq \sqrt{\overline{2u'^2} \, \tau_E/T} \qquad (B-18)$$

where T is the averaging time and τ_E is the integral time scale defined by

$$\tau_E = \int_0^\infty \rho(t) \, dt \qquad (B-19)$$

where $\rho(t)$ is the correlation coefficient between two values of U separated by a time t. According to Tennekes and Lumley (49) the integral time scale is of the order of large eddy turnover time,

$$\tau_E \sim 0.4 \, \delta/U = 2.7 \text{ to } 8.0 \times 10^{-4} \text{ secs.}$$

Also from Hinze (52), for stationary processes, an estimate of the integral time scale is given by

$$\tau_E = 2\Lambda_g/U \simeq 0.7 \text{ to } 1.75 \times 10^{-4} \text{ seconds}$$

where Λ_g is Taylor's integral scale. The maximum error in the measurement of mean velocities for an averaging time (T) is,

$$\% \text{ Error} = (100u'/U)\sqrt{2\tau_E/T} \sim 10 \times \sqrt{2 \times 8 \times 10^{-4}/T}$$

$$= 0.40/\sqrt{T} = 0.07\%, \, 0.06\%, \, 0.05\% \text{ respectively for } T = 30,$$

45, 60 secs. Similarly the root mean square error for turbulent components which are almost guassian with zero mean is given by Margolis (43) as,

$$\%(\varepsilon)_{rms} = 100\sqrt{\frac{4\tau_E}{T}} \leq 100\sqrt{\frac{32 \times 10^{-4}}{T}} \leq \sqrt{\frac{32}{T}} \qquad (B-20)$$

From Equation (B-20), the error in turbulence intensity is 1%, 0.85%, and 0.7% respectively for T = 30, 34, and 60 seconds.

12. Measurement of wire angles with respect to reference coordinate system: An optical projector of Applied Research Laboratory, The Pennsylvania State University, which has a least count in angle measurements of 0.08° (5') was used. For angle measurements in the range 45° – 60° the anticipated error in velocity measurement is

$$e = \Delta\alpha \tan\alpha = 0.14\% - 0.25\%$$

13. Misalignment of the probe with respect to the reference axis (x): The probe misalignment with the reference axis, introduces a significant error in the blade normal velocity component v. The measured value of v_m is related to true value by

$$v_m = v_{true} \pm u \sin \delta\alpha \qquad (B-21)$$

where $\delta\alpha$ is the misalignment angle. The maximum anticipated misalignment is $\pm4^{\circ}$. This can therefore add or subtract an error equal to 6.6% of the streamwise velocity component u. Since the velocity component v is very small and goes to zero at the blade surface, the error due to probe misalignment is minimuzed by assuming that v ≡ 0 at the first data point nearest to the blade and the corresponding value of misalignment angle is used to correct the measurements.

Equations of Reynolds Stresses in Rotating Coordinate System

The transport equations of Reynolds stresses in rotating coordinate frame of reference (x, y, r) are obtained from Nash and Patel (31) by retaining the principal curvature term $k_{xr} = \sin^2\beta/r$ and including the additional terms due to rotation. The equations are:

$$\frac{D}{Dt}\left(\overline{\frac{u'^2}{2}}\right) = \left(\frac{\partial}{\partial t} + u\frac{\partial}{\partial x} + v\frac{\partial}{\partial y} + w\frac{\partial}{\partial r} + k_{xr}w\right)\left(\overline{\frac{u'^2}{2}}\right)$$

$$= -\frac{\partial u}{\partial x}\overline{u'^2} + \frac{\partial u}{\partial y}(\overline{-u'v'}) + (\overline{-u'w'})(2\Omega_y + k_{xr}u + \frac{\partial u}{\partial r})$$

$$\qquad\quad \text{II} \qquad\qquad \text{I} \qquad\qquad \text{IV} \quad\ \text{V} \qquad \text{III}$$

$$-\frac{\partial}{\partial y}\left(\overline{\frac{u'^2 v'}{2}}\right) + \overline{\frac{p'}{\rho}\left(\frac{\partial u'}{\partial x}\right)} + \nu\ \overline{u'\nabla^2 u'} \qquad\qquad (C\text{-}1)$$

$$\qquad\quad \text{VI} \qquad\qquad \text{VII} \qquad\qquad \text{VIII}$$

$$\frac{D}{Dt}\left(\overline{\frac{v'^2}{2}}\right) = \left(\frac{\partial}{\partial t} + u\frac{\partial}{\partial x} + v\frac{\partial}{\partial y} + w\frac{\partial}{\partial r}\right)\left(\overline{\frac{v'^2}{2}}\right)$$

$$= -\frac{\partial v}{\partial y}\overline{v'^2} - \frac{\partial}{\partial y}\left(\overline{\frac{v'^3}{2}} + \overline{\frac{p'v'}{\rho}}\right) + \overline{\frac{p'}{\rho}\frac{\partial v'}{\partial y}}$$

$$\qquad\quad \text{I} \qquad\qquad\qquad \text{VI} \qquad\qquad\qquad \text{VII}$$

$$+ \nu\ \overline{v'\nabla^2 v'} + 2\ \Omega_x\overline{v'w'} \qquad\qquad\qquad (C\text{-}2)$$

$$\qquad\quad \text{VIII} \qquad\quad \text{IV}$$

$$\frac{D}{Dt}\left(\overline{\frac{w'^2}{2}}\right) = \left(\frac{\partial}{\partial t} + u\frac{\partial}{\partial x} + v\frac{\partial}{\partial y} + w\frac{\partial}{\partial r}\right)\left(\overline{\frac{w'^2}{2}}\right)$$

$$= (-2k_{xr}u - 2\Omega_y + \frac{\partial w}{\partial x})(\overline{-u'w'}) + (+2\Omega_x + \frac{\partial w}{\partial y})(\overline{-v'w'}) - \frac{\partial w}{\partial r}\overline{w'^2}$$

$$\quad\quad\quad\quad V \quad\quad IV \quad\quad\quad\quad IV \quad\quad\quad I \quad\quad\quad III$$

$$- \frac{\partial}{\partial y}\left(\overline{\frac{v'w'^2}{2}}\right) + \overline{\frac{p'}{\rho}\frac{\partial w'}{\partial r}} + \nu\,\overline{w'\nabla^2 w'} \quad\quad\quad (C\text{-}3)$$

$$\quad\quad\quad\quad VI \quad\quad\quad\quad VII \quad\quad\quad VIII$$

where $\Omega_y = -\Omega \sin\beta$, $\Omega_x = \Omega \cos\beta$ and $\Omega_r = 0$ for the flat plate inducer. It should be noticed that the turbulent energy equation (sum of Equations C-1, C-2, and C-3) would contain no terms due to rotation. This is due to the fact that the coriolis force has no component in the chordwise direction. The turbulent stress equations are,

$$\frac{D}{Dt}(\overline{-u'v'}) = \left(\frac{\partial}{\partial t} + u\frac{\partial}{\partial x} + v\frac{\partial}{\partial y} + w\frac{\partial}{\partial r} + k_{xr}w\right)(\overline{-u'v'})$$

$$= \overline{v'^2}\frac{\partial u}{\partial y} - \left(\frac{\partial u}{\partial x} + \frac{\partial v}{\partial y}\right)(\overline{-u'v'}) - \left(k_{xr}u + 2\Omega_y + \frac{\partial u}{\partial r}\right)(\overline{-w'v'}) - 2\Omega_x\overline{u'w'}$$

$$\quad I \quad\quad II \quad\quad\quad\quad I \quad\quad\quad V \quad\quad IV \quad\quad\quad III \quad\quad\quad IV$$

$$- \nu(\overline{u'\nabla^2 v'} + \overline{v'\nabla^2 u'}) + \frac{\partial}{\partial y}(\overline{u'v'^2} + \overline{\frac{p'u'}{\rho}}) - \overline{\frac{p'}{\rho}\left(\frac{\partial u'}{\partial y} + \frac{\partial v'}{\partial x}\right)}$$

$$\quad\quad\quad\quad VIII \quad\quad\quad\quad\quad VI \quad\quad\quad\quad\quad VII$$

$$(C\text{-}4)$$

207

$$\frac{D}{Dt}(\overline{-u'w'}) = (\frac{\partial}{\partial t} + u\frac{\partial}{\partial x} + v\frac{\partial}{\partial y} + w\frac{\partial}{\partial r} + k_{xr}w)(\overline{-u'w'})$$

$$= (-2k_{xr}u + \frac{\partial w}{\partial x})\overline{u'^2} + \overline{w'^2}(k_{xr}u + \frac{\partial u}{\partial r}) - 2\Omega_y(\overline{u'^2} - \overline{w'^2})$$

$$VIIVIIIIV$$

$$-[\frac{\partial w}{\partial y}(\overline{-u'v'}) + \frac{\partial u}{\partial y}(\overline{-v'w'}) + (\frac{\partial u}{\partial x} + \frac{\partial w}{\partial r})(\overline{-u'w'})] + \frac{\partial}{\partial y}(\overline{u'v'w'})$$

$$IIIIIIVI$$

$$-\overline{\frac{p'}{\rho}(\frac{\partial w'}{\partial x} + \frac{\partial u'}{\partial r})} - \nu(\overline{u'\nabla^2 w'} + \overline{w'\nabla^2 u'}) \text{(C-5)}$$

$$VIIVIII$$

and

$$\frac{D}{Dt}(\overline{-v'w'}) = (\frac{\partial}{\partial t} + u\frac{\partial}{\partial x} + v\frac{\partial}{\partial y} + w\frac{\partial}{\partial r})(\overline{-v'w'})$$

$$= \overline{v'^2}\frac{\partial w}{\partial y} + (2k_{xr}u - \frac{\partial w}{\partial x} + 2\Omega_y)(\overline{-u'v'}) - (\frac{\partial w}{\partial r} + \frac{\partial v}{\partial y})(\overline{-v'w'})$$

$$IVIIIVIIII$$

$$-2\Omega_x(\overline{w'^2} - \overline{v'^2}) + \frac{\partial}{\partial y}(\overline{v'^2 w'} + \overline{\frac{w'p'}{\rho}}) - \overline{\frac{p'}{\rho}(\frac{\partial w'}{\partial y} + \frac{\partial v'}{\partial r})}$$

$$VIVII$$

$$- \nu(\overline{v'\nabla^2 w'} + \overline{w'\nabla^2 v'}) \text{(C-6)}$$

$$VIII$$

These equations are valid for both compressor and turbine rotors. For a compressor, Ω_x is +ve, Ω_y is -ve and for a turbine rotor, Ω_x is -ve and Ω_y is + ve.

The term on the left hand side is the total convective derivative of a Reynolds stress, terms I to III on right hand side represent production of Reynolds stress by mean velocity gradients, term IV is due

to rotation, term V is due to curvature, term VI represents diffusion of Reynolds stress due to gradients of pressure velocity and triple velocity correlations, term VII is the pressure strain or equalizing term and the last term VIII represents viscous diffusion and dissipation of the Reynolds stress. The qualitative effects of rotation terms in the transport of a Reynolds stress depends on the directions of rotation and are tabulated below for decelerating relative flow in compressors and pumps and accelerating relative flow in turbines.

Table V

Effect of Rotation

Transport Equation	Rotation Term Effect		
	Term	Compressor and Pump	Turbine
C-1 $\overline{u^2}/2$	$2\Omega_y(\overline{-u'w'})$	Suppression	Production
C-2 $\overline{v'^2}/2$	0	No Effect	No Effect
C-3 $\overline{w'^2}/2$	$-2\Omega_y(\overline{-u'w'})$	Production	Suppression
C-4 $\overline{-u'v'}$	$-2\Omega_y(\overline{-w'v'})$	Production	Suppression
C-5 $\overline{-u'w'}$	$+2\Omega_y(\overline{w'^2}-\overline{u'^2})$	Suppression (if $(\overline{w'^2} - \overline{u'^2})$ is positive) Production (if $(\overline{w'^2} - \overline{u'^2}$ is negative)	Production Suppression
C-6 $\overline{-v'w'}$	$+2\Omega_y(\overline{-u'v'})$	Suppression	Production